



HAL
open science

High pressure synthesis in materials science

Alain Largeteau

► **To cite this version:**

Alain Largeteau. High pressure synthesis in materials science. *Materials*, 14 (7) / 14(15) / 15(6), pp.1-91, 2022. hal-03831281

HAL Id: hal-03831281

<https://hal.science/hal-03831281v1>

Submitted on 26 Oct 2022

HAL is a multi-disciplinary open access archive for the deposit and dissemination of scientific research documents, whether they are published or not. The documents may come from teaching and research institutions in France or abroad, or from public or private research centers.

L'archive ouverte pluridisciplinaire **HAL**, est destinée au dépôt et à la diffusion de documents scientifiques de niveau recherche, publiés ou non, émanant des établissements d'enseignement et de recherche français ou étrangers, des laboratoires publics ou privés.



Distributed under a Creative Commons Attribution - NonCommercial - NoDerivatives 4.0 International License



High Pressure Synthesis in Materials Science

Guest Editor:

Dr. Alain Largeteau

Department of High Pressure,
CNRS, Univ. Bordeaux, ICMCB,
UMR 5026, F-33600 Pessac,
France

alain.largeteau@u-bordeaux.fr

Deadline for manuscript
submissions:

closed (31 March 2021)

Message from the Guest Editor

High pressure (HP) is an integral part of various domains of science. The combination of temperature with pressure results in applications in several already existing fields, to sinter/consolidate/densify for obtaining solid material. Innovative HP processes were designed for the high pressure syntheses.

Recently, innovative high pressure processes have emerged by the combination of different technologies opening new possibility for obtaining these advanced functional inorganic materials such as: high pressure & spark plasma sintering, cold isostatic pressure & minus temperature, hydrothermal synthesis & sintering.

The upcoming Special Issue, entitled “High Pressure Synthesis in Materials Science” aims to cover an overview of the innovation in high pressure processes/technologies for the synthesis of advanced functional inorganic materials. To this end, it is my pleasure to invite you to submit a manuscript for this Special Issue. Full papers, communications, and reviews are welcome.

Keywords

- sintering
- densification
- consolidation
- crystallization
- polymorphism
- innovative high pressure processes



mdpi.com/si/45504

Special Issue

Published Papers (4 papers)

Analysis of the Temperature Distribution on the Surface of Saddle-Shaped Briquettes Consolidated in the Roller Press

by Michał Bembenek and Andrzej Uhryński

Materials 2021, 14(7), 1770; <https://doi.org/10.3390/ma14071770> - 03 Apr 2021

A Review of Binderless Polycrystalline Diamonds: Focus on the High-Pressure-High-Temperature Sintering Process

by Jérémy Guignard, Mythili Prakasam and Alain Largeteau

Materials 2022, 15(6), 2198; <https://doi.org/10.3390/ma15062198> - 16 Mar 2022

In Situ High-Pressure Synthesis of New Outstanding Light-Element Materials under Industrial P-T Range

by Yann Le Godec and Alexandre Courac

Materials 2021, 14(15), 4245; <https://doi.org/10.3390/ma14154245> - 29 Jul 2021

Metastable Materials Accessed under Moderate Pressure Conditions ($P \leq 3.5$ GPa) in a Piston-Cylinder Press

by Javier Gainza, Federico Serrano-Sánchez, João Elias F. S. Rodrigues, Norbert Marcel Nemes, José Luis Martínez and José Antonio Alonso

Materials 2021, 14(8), 1946; <https://doi.org/10.3390/ma14081946> - 13 Apr 2021

Article

Analysis of the Temperature Distribution on the Surface of Saddle-Shaped Briquettes Consolidated in the Roller Press

Michał Bembenek  and Andrzej Uhryński

Faculty of Mechanical Engineering and Robotics, AGH University of Science and Technology, A. Mickiewicza 30, 30-059 Krakow, Poland; uhrynski@agh.edu.pl

* Correspondence: bembenek@agh.edu.pl

Abstract: The unit pressure in the fine-grained material consolidation process in the roller press can reach over hundred MPa and is a parameter which results, among other things, from the properties of the consolidated material and the compaction unit geometry. Its value changes depending on the place on the molding surface. Generating different pressure on the surface of briquettes makes their compaction different. One's own and other researchers' experience shows that, in the case of exerting high pressure on the merged fine-grained material, the higher unit pressure exerted on the material, the higher temperature of the consolidated material is. The temperature distribution on the surface of the briquettes can testify the locally exerted pressure on the briquette. The stress distribution in the briquetting material is still a subject of research. The article includes thermography studies of the briquetting process of four material mixtures. Thermal images of briquettes were taken immediately after they left the compaction zone as well as forming rollers. The obtained thermograms and temperature variability at characteristic points of the surface of briquettes were analyzed. The correlation between the temperature distribution and the stress distribution in the briquettes was determined.



Citation: Bembenek, M.; Uhryński, A. Analysis of the Temperature Distribution on the Surface of Saddle-Shaped Briquettes Consolidated in the Roller Press. *Materials* **2021**, *14*, 1770. <https://doi.org/10.3390/ma14071770>

Academic Editor: Alain Largeteau

Received: 22 February 2021

Accepted: 31 March 2021

Published: 3 April 2021

Publisher's Note: MDPI stays neutral with regard to jurisdictional claims in published maps and institutional affiliations.



Copyright: © 2021 by the authors. Licensee MDPI, Basel, Switzerland. This article is an open access article distributed under the terms and conditions of the Creative Commons Attribution (CC BY) license (<https://creativecommons.org/licenses/by/4.0/>).

Keywords: briquetting; roller press; temperature distribution; thermography; briquetting pressure

1. Introduction

Thermography is a non-destructive, non-contact method of detecting, registering, processing, and then visualizing infrared radiation. The obtained thermogram is a representation of the temperature distribution on the surface of the observed object. The non-contact and non-invasive measurement of the tested objects in most applications is the basic criterion for the use of thermal imaging techniques.

One of the first fields that successfully used thermography has been construction in its broadest sense. It is used to analyze the thermal tightness of buildings, defects in the heating system [1], as well as to identify areas which are at risk of moisture condensation and mold [2]. This technique (due to its non-invasiveness) has also been well received in medicine and scientific research related to it [3–5]. Thermography is also used in the machining of materials. This applies not only to the control of the workpiece temperature [6], but also to the general control of the temperature increases and distribution in the machining zone [7], or the chip surface temperature [8]. It has also been mentioned that the use of thermography occurs in the diagnosis of the welding process and the assessment of the quality of these joints [9,10]. Thermography is used in the widely understood diagnostics of machines and their components, starting from CNC (Computer Numerical Control) machine tools [11], through mechanical expanders [12], rotating machines [13], belt conveyors [14], internal combustion engines (catalytic reactors) [15,16], bearings and bearing nodes [17,18], brakes [19], up to electrical devices and machines [20–23]. Attempts have been made to correlate strength tests and stresses in the material with the amount of heat generated [24]. Loaded ropes and steel chains were examined in order to determine

their weak points [25]. Plastic strains and cavitation of polypropylene under tension were analyzed [26], and a system for comprehensive thermomechanical analysis of materials was suggested [27]. Strength tests were also performed during a bending test of thin-walled composite beams made of matrix composites [28]. A methodology for the use of thermal imaging techniques to assess the extent of fatigue degradation of polymeric materials (in particular epoxy composite) was also developed [29]. In addition to passive thermography, active thermography is also known. It is a method of stimulating the object of research, for example, by providing a thermal impulse [30] or inducing this effect by means of acoustic activation [31], including ultrasound [32] or microwaves [33], and then observing the path of its propagation by a thermal imaging camera in the facility. This type of thermography is especially used in defectoscopy [34,35].

Thermal phenomena are a rich source of information about technological processes and changes or irregularities occurring during them [36], which allows for the control of process parameters and the necessary modification. Thermography was used, among others, to control the stability of the extrusion process of poly (vinyl chloride) [37], textiles [38–40], tire vulcanization [41], production of casting molds [42], the process of casting and cooling steel [43] iron ores (with biomass) [44], the quality of moldings made of loose materials (microcrystalline cellulose) leaving the compaction zone [45], and even in the process of cooling of natural rock materials [46]. Another field of application for thermography has become research on materials and their structure [45,47]. The possibilities of using the thermography method in the analysis of the degree of destruction of metal-fiber laminates subjected to dynamic impacts at low speed were described [48]. A prototype of a thermographic apparatus for non-destructive testing of composites was also developed [49].

Despite such a wide application of thermographic research, it is very rarely used to study agglomeration processes [45]. The pressurized agglomeration is the key process that is presently employed in the power [50–54], heavy [55–58], chemical [59,60], and pharmaceutical industry [61–63]. Industries have willingly used roller presses rather than other briquetting machines, for example, screw or punch briquette machines [50,53], due to constant operability with a relatively low demand for energy [64,65]. A standard roller press design usually contains the following subassemblies: drive system, working rollers cage, roller support system, and compaction unit. The compaction unit is a particularly important unit among the systems for pressurized agglomeration [54,61,66]. A very important element of a properly conducted agglomeration is effective preparation of the material and its dosing [67,68]. The briquette forming process takes place between two rollers, which rotate in mutually opposite directions and on the surfaces of which there are molding cavities distributed in a proper way [69]. In traditional roller presses, working surfaces of rollers are provided with cavities which are arranged so as to be their mutual mirror images on both rollers [64]. The compaction unit of this type is referred to in the literary sources as symmetrical [64,65]. Mutual differentiation of the working surfaces of both rolls prevents unfavorable phenomena from occurring during material consolidation [55]. In this way, an asymmetric compaction unit is established. The briquettes manufactured in a traditional asymmetrical compaction unit are in the shape of a saddle. This is particularly useful for materials that are difficult to briquette in a roller press, i.e., those that are characterized by a high moisture, high compaction degree necessary for consolidation, low bulk density, the presence of hydrophobic grains, those that tend to be suspended in hoppers and dispensers, and those with a high elastic deflection after pressure is removed. The use of an asymmetric compaction unit enables an increase in the moisture range within which the material can be briquetted [64,65]. It also eliminates briquettes from cracking in half along the plane of mutual closure of cavities on both rolls [55,64]. The unit pressure in the fine-grained material consolidation process often reaches several hundred MPa and is a parameter which results, among other things, from the properties of the material being consolidated and the compaction system geometry [54,61,70]. Its value changes depending on the place on the molding surface [71,72]. This is one of the reasons that the briquette

compaction is not uniform throughout its volume, as shown by the research presented in the works [70,73]. It was also proved in simulation studies using the Finite Element Method [74]. In the case of the gravity feeder for the symmetrical compaction unit, the lowest unit pressure value occurs in the lower area of the cavity (Figure 1). A similar stress distribution can be expected for an asymmetric compaction system; however, such tests were not carried out with gravity feeding.

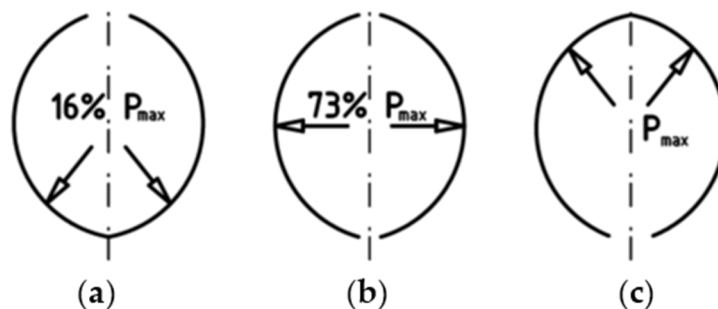


Figure 1. Unit pressure value distribution during the briquetting process in a roller press. P_{max} , maximum unit pressure [64]: (a–c) the successive compaction phases during the rotation of the rollers.

Our own experiments carried out during the determination of the compaction level, characteristics of fine-grained materials [69,75] performed in a closed die, show that the compacted material heats up when high pressure is exerted on it. This is also confirmed by the experiments done by Litstera et al. [45]. Based on the microcrystalline cellulose, they proved the temperature distribution in a roller compaction process (briquetting with a flat rollers) across the width of the ribbon is not uniform. There are temperature differences between the central area and the edges of the ribbon. It is related to the inter alia with a different degree of material compaction (higher density in the middle of the part), which is caused by uneven material flow in the press feeder. During consolidation, due to inner friction and work, heat is generated between the particles of the merged material which causes a temperature change in a certain volume of the briquette. The higher unit pressures exerted on the material, the higher the temperature of the consolidated material is. The temperature distribution on the surface of the briquettes can also be related to locally exerted pressure on the briquette. The stress distribution in the briquetting material is still the subject of research. Therefore, the IR thermography studies of the briquetting process were conducted in order to verify the use of thermography to study the course of the briquetting process in a roller press.

2. Materials and Methods

The thermographic research of briquetting process in the roller press was done using a roller press (AGH University of Science and Technology, Krakow, Poland) (Figure 2) with a 450 mm roller pitch diameter with an installed compaction unit for production of the saddle-shaped briquettes with a size of $31 \times 30 \times 13$ mm and a rated capacity of 6.5 cm^3 (Figure 3). The outline view of the molding surface used to consolidate the material is presented in Figure 4. The press was equipped with a cycloidal gear motor with a power of 22 kW and a frequency converter that enabled infinitely variable control of the revolutionary speed of the rolls. All materials were briquetted using a gravity feeder with a roller revolutionary speed of 0.85 RPM, which corresponded to the peripheral speed of the rolls equal to 0.02 m/s with an inter-roll gap of 1 mm, which caused each briquette in the forming row to fall out approximately 1.6 s.

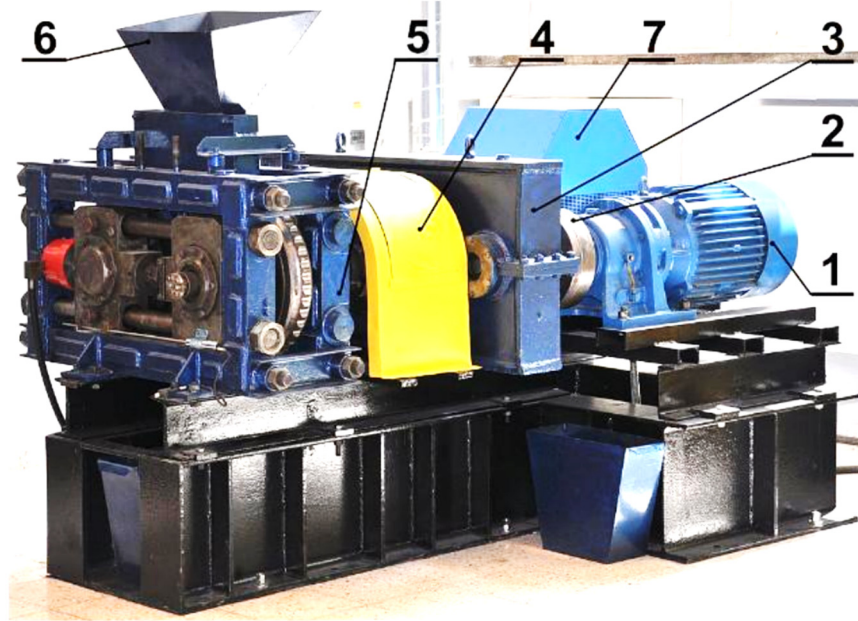


Figure 2. LPW 450 laboratory roller press: (1) gear motor with a cycloidal transmission; (2) flexible clutch; (3) gearbox; (4) enclosure of Oldham couplings and friction clutch; (5) molding rollers cage; (6) gravity feeder; (7) hydraulic system of sliding roller support [69].



Figure 3. Molding rings used in roller press compaction unit with a saddle-shaped briquette [69].

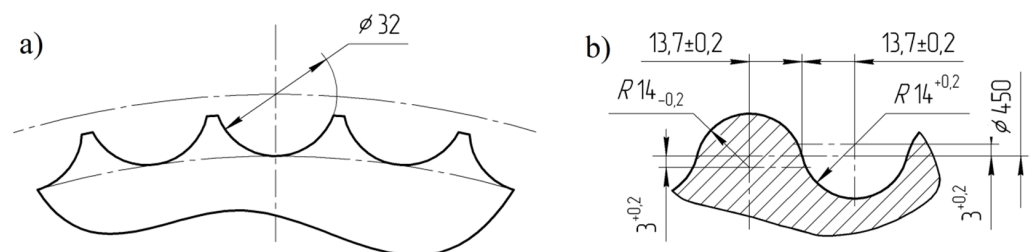


Figure 4. Geometry of molding cavities on the working surface of rolls used for tests: (a) front view and (b) cross section through the groove [69].

Materials of three various origins and various chemical compositions and structures were selected for the tests:

- material of inorganic origin—hydrated lime,
- material of organic origin/fuels: charcoal,
- heavy industry waste: electric arc furnace dust (EAFD) mixtures.

Before the consolidation process, four mixtures of the materials referred to above were prepared. They were thoroughly mixed and brought to a proper moisture, enabling them to be consolidated in a roller press. Binders were added. Moisture was determined by the weight method at 105 °C until constant weight was obtained. The Vibra AJH 420 CE (Tokyo, Japan) scale was used.

Mixture 1. (M1)

The mixture contained 47.7% of EAFD, 36.7% of scale, 7.3% fine coke breeze, 5.5% 80° Bx molasses, and 2.8% calcium hydroxide. The last two ingredients acted as a binder [7]. The mixture was mixed approximately 10 min in the double-arm Z-blade mixer with four rectangular mixing elements with dimensions 190 × 90 mm and the shaft rotating speed 55 RPM (Figure 5). Its moisture content was 4.6%.



Figure 5. The view of Z-blade mixer used in the test for material preparation.

Mixture 2. (M2)

The charcoal fines with a grain size down to 3 mm were mixed in the Z-blade mixer for approximately 10 min. with a 4% of starch. The moisture content of the mixture was 26.9%.

Mixture 3. (M3)

The pre-compacted charcoal fines were mixed with a 4% of starch. The moisture content of the mixture was 26.9%. The pre-compacted process involves briquetting and crushing the consolidated briquettes to a size below 10 mm.

Mixture 4. (M4)

Its composition was 83.3% calcium hydroxide manufactured by Lhoist (EN 459-1 CL 90-S) (Lhoist, Limelette, Belgium) and 16.7% water. The mixture was mixed in Z-blade mixer for about 30 min. The moisture content of the mixture was 16.9%.

The FLIR T335 Thermal Imaging Camera (Wilsonville, OR, USA) was used for the tests. The operating temperature range of the camera is: −20 to +650 °C, and the temperature measurement error: ± 2 °C or ± 2% of the measurement value. The camera is equipped with a microbolometric matrix with a resolution of 320 × 240 pixels, a 25° × 18.75° lens, and a 0.05 °C Noise Equivalent Temperature Difference sensitivity. Before the tests, it was necessary to calibrate the camera. The ambient temperature during tests was 18.6 °C. In the laboratory, access to daylight and artificial light to the measuring station was eliminated. In addition, a light-tight imaging station was made to block the inflow of the light to the working area of the thermal imaging camera (Figure 6), which eliminated the reflection

of radiation disturbing the test result and ensuring repeatability of the distance between the camera and the tested briquette. Each time, two briquettes were ejected from the roller press at a time, and were caught and transferred to a cardboard plate in heat-insulating gloves immediately after leaving the compaction unit. Then, the briquettes and the pad were placed in a measuring station and thermal images were taken. The time between catching the briquettes and taking the photo was about 3 s. After each test, the cardboard pad was changed to make the test conditions reproducible as the pads got hotter (the pads got hotter from the briquettes as time went on). Due to the low peripheral speed of the rollers (0.02 m/s), it was possible to transfer the briquette to the pad directly after it was removed from the compaction unit, while maintaining a precise control of briquette top-bottom, front-back orientation. Briquetting tests with the faster peripheral speeds were unsuccessful as it was not possible to catch the briquettes in a controlled and reproducible orientation. The photos of the briquettes were taken in such a way that their “top” (Figure 7) was always located up the top edge of the image. Two briquettes were placed on the pads in two positions: “front” and “back”, as it shown in Figure 4b.

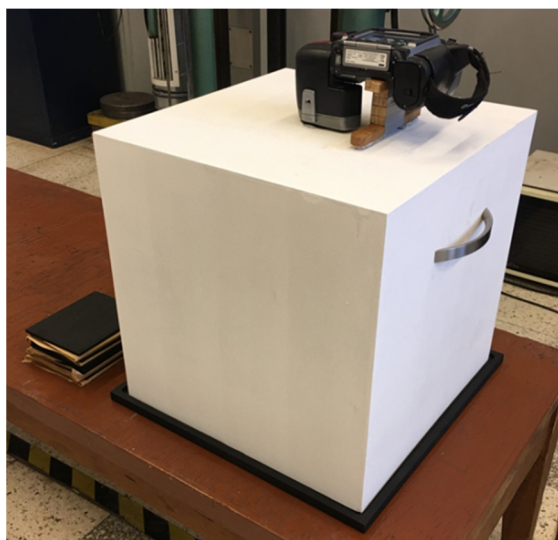


Figure 6. The view of the light-tight imaging station for taking photos during measurements, eliminating the effects of external radiation.

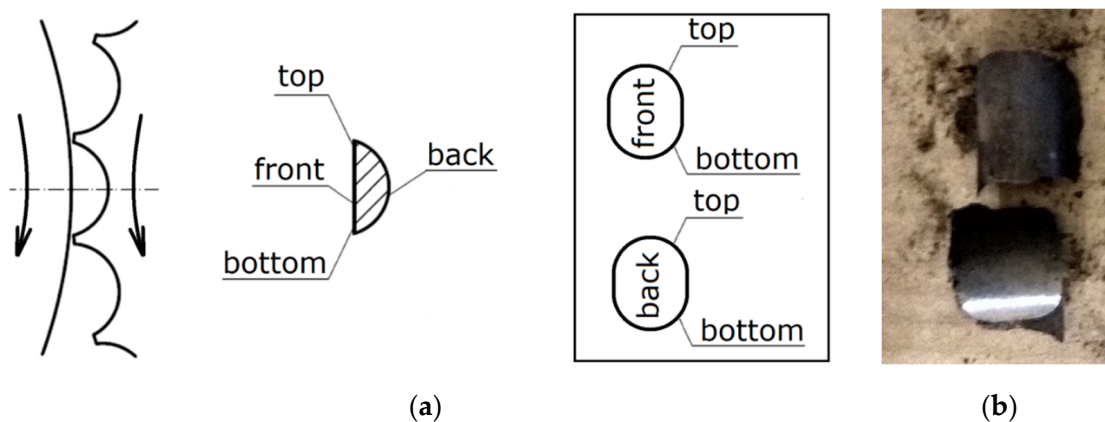


Figure 7. The briquettes arrangement: (a) in the compaction unit, (b) on the cardboard pad.

From 3 to 10 thermal images were taken of the briquettes from each of the mixtures, out of which 3 with the highest maximum temperature were selected for further analysis (Figure 8a). The photos were analyzed using the FLIR Quick Report program v. 1.2 SP1

(Wilsonville, OR, USA). First of all, the maximum temperature was determined for each type of briquette, both at the front and back, and their measurements were averaged.

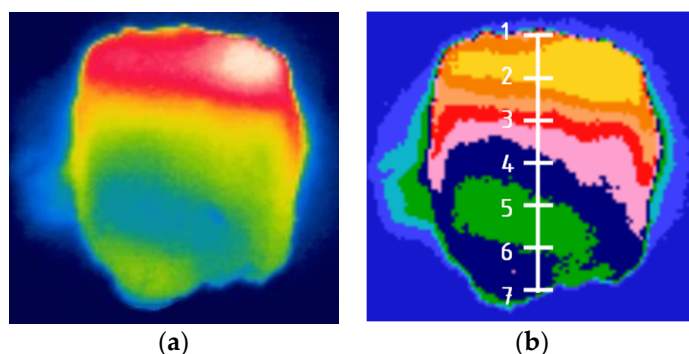


Figure 8. Thermogram: (a) unprocessed, (b) processed in FLIR Quick Report with measuring points where temperature readings were taken to prepare the temperature distribution on the briquette surfaces.

In order to examine the temperature distribution on the briquette surfaces, into the thermograms, the grid shown in Figure 8a was fitted. The measuring points were spaced 5 mm from each other (Figure 8b). For each thermogram, 7 temperature values were read at points in the vertical axis of the briquette.

The next stage of the research was attempts to determine the temperature distribution on the rollers immediately after the consolidation process. The thermographic images of the rollers were taken with and without an additional anti-reflective coating. The rollers were coated with an anti-glare spray containing talcum powder CRC Crick 130 (CRC Industries Europe, Belgium). The thermographic images of rollers stored in the laboratory at ambient temperature were also taken.

3. Results and Discussion

Good quality briquettes which did not crumble were obtained from all the materials used in the tests. In tests where fine-grained charcoal was merged, the shape of the edge of briquettes was more irregular; hence, the images of the briquettes on the thermograms had less-clear edges. However, it did not hinder their thermal imaging analysis.

The first stage of the research was to produce a pilot batch of briquettes from each of the mixtures. The briquettes were then seasoned at ambient temperature for 6 h and then thermal images of all four types of briquettes were taken together. The analysis of the images showed that the briquettes have the same temperature as the ambient temperature. The temperature of all briquettes was the same on the surfaces of each of the briquettes and no differences were noticed in the temperature distribution. For briquettes from each mixture, images were also taken after the next 5, 10, 15 s briquetting in order to analyze the cooling process of the briquettes. Based on the analysis of the briquette cooling gradient on subsequent images, it was found that the time between making the briquettes, their transfer to the station, and taking the first photo did not significantly affect the temperature changes. Then the actual tests began.

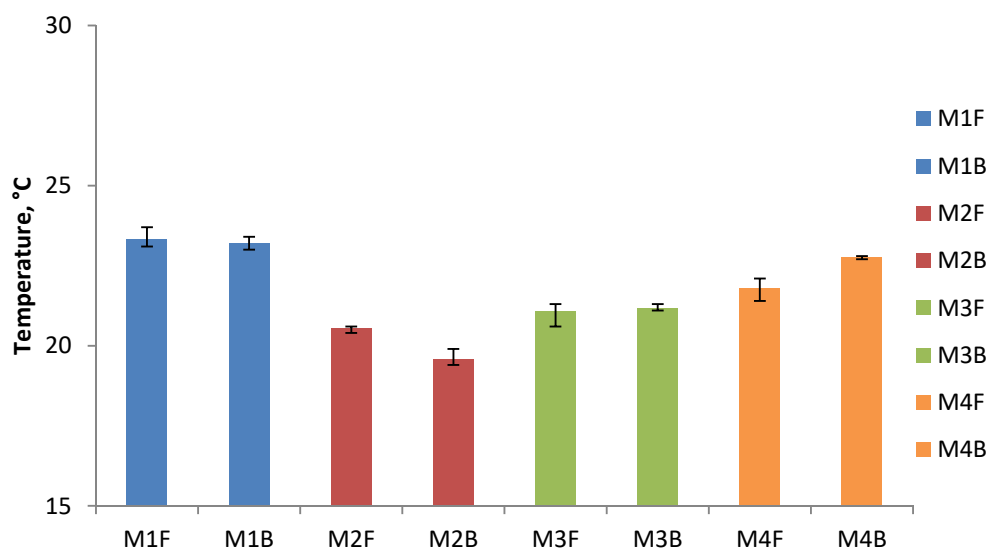
The results of the minimum and maximum temperature for each type of briquettes on the front and back sides and their average values are presented in Tables 1 and 2 and in the Figures 9 and 10.

Table 1. The results of minimum temperature measurements on the surface of briquettes after briquetting.

Side	M1, °C		M2, °C		M3, °C		M4, °C	
Front	23.1		20.4		20.6		21.4	
	23.2	23.3	20.6	20.5	21.3	21.1	21.9	21.8
	23.7		20.6		21.3		22.1	
Back	23.0		19.4		21.1		22.7	
	23.2	23.2	19.4	19.6	21.1	21.2	22.8	22.8
	23.4		19.9		21.3		22.8	

Table 2. The results of maximum temperature measurements on the surface of briquettes after briquetting.

Side	M1, °C		M2, °C		M3, °C		M4, °C	
Front	26.9		22.4		22.6		23.9	
	26.7	26.6	22.2	22.2	22.6	22.6	24.1	24.3
	26.3		22.0		22.5		25.0	
Back	27.6		22.3		22.7		24.3	
	27.0	27.0	22.0	22.1	22.6	22.6	24.4	24.4
	26.4		22.0		22.6		24.5	

**Figure 9.** The results of average minimum temperature measurements on the surface of briquettes after briquetting: F—front, B—back.

The summary graph of the minimum surface temperatures (Figure 9) shows that the lowest temperature, both on the front and back surfaces, is obtained for the briquettes made of Mixture 2 (charcoal fines mixed with a 4% of starch without pre-compaction). The minimum temperature of these briquettes is 1.0 °C higher than the ambient temperature.

The summary graph of the maximum surface temperatures (Figure 10) shows that the highest temperature, both on the front and back surfaces, is obtained for the briquettes made of Mixture 1 (47.7% of EAFD, 36.7% of scale, 7.3% fine coke breeze, 5.5% 80° Bx molasses, and 2.8% calcium hydroxide). The maximum temperature of these briquettes is 9.4 °C higher than the ambient temperature. The briquettes made of calcium hydroxide are also characterized by a similar maximum temperature on the surface. The highest temperature on the surface of briquettes made of fine charcoal (M2 and M3) is lower than both of the above samples (M1 and M4). It amounts to 22.2 °C for non-compacted briquettes and 22.6 °C for compacted briquettes, respectively. The difference of 0.4 °C between the two samples can be explained by the heating of Mixture 3 during its pre-compaction. The maximum temperatures on both sides of the briquette are very similar to each other. The

biggest difference between the front side and the back side was recorded for Mixture 1 and it amounts to 0.4 °C. The differences between the maximum and minimum temperatures measured on the briquette surface are 3.8 °C for the Mixture 1, 2.5 °C for the Mixture 2, 1.5 °C for the Mixture 3, and 2.5 °C for the Mixture 4.

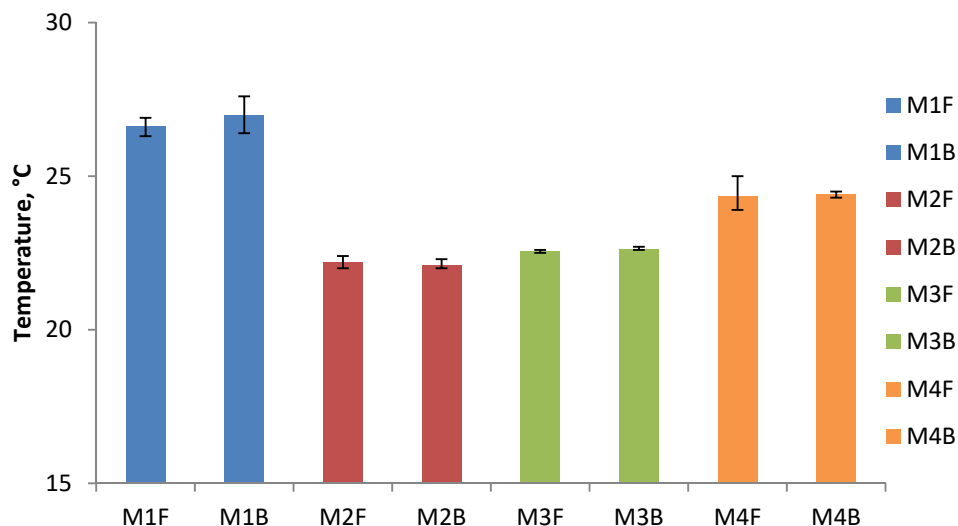


Figure 10. The results of average maximum temperature measurements on the surface of briquettes after briquetting: F—front, B—back.

The results of the temperature distribution on the briquette surfaces for each type of briquette on the front and the back sides and its average value are presented in Tables 3 and 4 and in the Figures 11 and 12.

Table 3. The temperature distribution on the front side briquette surfaces in the characteristic points.

Point	M1, °C		M2, °C		M3, °C		M4, °C	
1	23.9		20.6		21.3		23.7	
	23.8	23.9	20.8	20.9	21.3	21.3	23.5	23.6
	24.1		21.4		21.4		23.7	
2	25.5		22.2		22.3		24.0	
	26.7	26.4	22.0	22.2	22.0	22.3	23.8	23.9
	26.9		22.4		22.6		24.0	
3	24.9		21.6		22.6		23.8	
	26.3	25.6	21.3	21.6	22.0	22.4	23.4	23.7
	25.7		22.0		22.5		23.8	
4	24.4		21.2		22.4		23.5	
	25.6	25.0	20.8	21.0	21.7	22.1	23.2	23.4
	25.0		21.1		22.1		23.5	
5	24.0		21.1		22.1		23.3	
	24.7	24.3	20.4	20.8	21.5	21.9	23.0	23.1
	24.2		20.9		22.0		23.1	
6	23.9		20.7		21.8		23.0	
	23.9	23.8	21.1	20.8	21.4	21.6	22.8	22.9
	23.7		20.7		21.7		22.9	
7	23.7		20.6		21.4		22.3	
	23.1	23.3	20.6	20.6	20.6	21.1	22.0	22.2
	23.2		20.6		21.3		22.4	

Table 4. The temperature distribution on the back side briquette surfaces in the characteristic points.

Point	M1, °C		M2, °C		M3, °C		M4, °C	
1	23.9		21.2		21.9		24.2	
	24.2	24.1	22.0	21.7	21.9	21.9	24.1	24.2
	24.3		21.9		21.9		24.2	
2	27.6		22.3		22.6		23.7	
	27.0	27.0	21.6	22.0	22.2	22.5	23.6	23.7
	26.4		22.0		22.7		23.9	
3	25.9		21.4		22.6		23.5	
	25.6	25.8	21.5	21.3	22.0	22.3	23.2	23.4
	25.9		21.1		22.2		23.4	
4	24.0		21.1		22.2		23.2	
	24.2	24.3	21.0	21.0	21.9	22.0	22.9	23.1
	24.7		21.0		22.0		23.2	
5	23.4		20.3		22.0		23.1	
	23.2	23.4	20.0	20.2	21.6	21.8	22.8	23.0
	23.6		20.4		21.9		23.0	
6	23.0		19.9		21.8		22.9	
	23.6	23.4	19.4	19.8	21.3	21.6	23.0	22.9
	23.5		20.0		21.7		22.8	
7	23.7		20.2		21.4		22.8	
	23.7	23.7	19.4	19.9	21.1	21.2	23.0	22.9
	23.6		20.0		21.1		22.8	

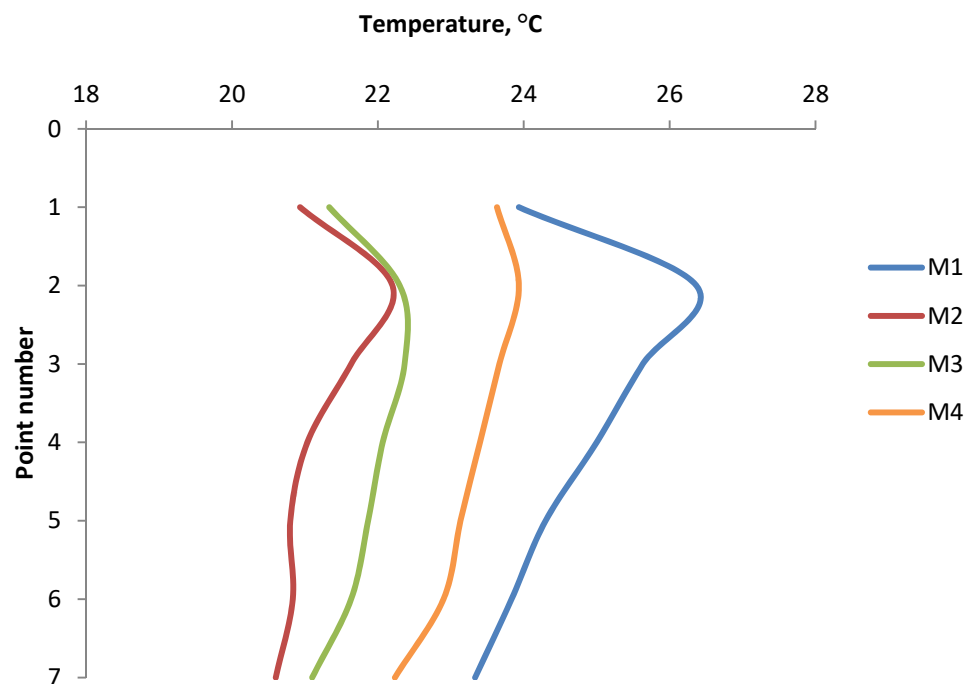


Figure 11. The temperature distribution on the front side briquette surfaces.

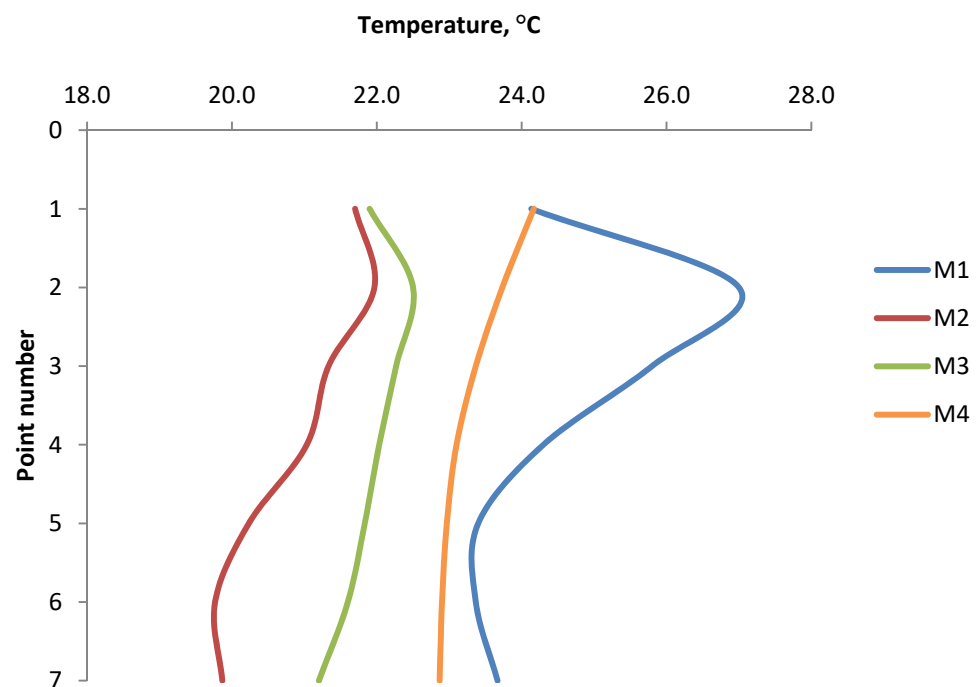


Figure 12. The temperature distribution on the back side briquette surfaces.

Analyzing the graphs of temperature distribution on both the front and back surfaces of the briquettes (Figures 11 and 12), it can be concluded that the characteristics of the temperature variation curve are similar for all the tests. The temperature values increase from point 1 to the maximum value in point 2 or 3, and then decrease to point number 7. The maximum temperature values in all cases were obtained in point 2, except for the temperature distribution on the front part of the Mixture 3 briquette, where the highest temperature was recorded in point 3. The conclusion is that the areas with maximum temperature are in the upper and middle upper parts of the briquette. In the temperature distribution in the front side of the briquettes, the temperature values at measuring points 1 and 7 are similar to each other. These points lie at the border edges of the briquette. On the back sides of the briquettes, the temperatures in point 1 are slightly higher than in point 7. The lowest temperatures at all the measurement points were recorded on the surfaces of briquettes made of a mixture of charcoal without pre-compaction (M2). Despite the smaller range of temperature values, the thermograms clearly show that the shape of the temperature gradients is analogous to the thermograms obtained in other mixtures. Tests carried out on Mixture 2 and Mixture 3 (the same mixture of charcoal, only prepared differently for consolidation) show that the temperature distribution on the surface of briquettes depends primarily on the geometry of the compaction unit and on the preparation of the material.

The first tests to take the thermographic images of the working rollers before the briquetting process are shown in Figure 13. In that case, the reflection of radiation was recorded, and therefore, they were considered unsuccessful. This is also confirmed by the control tape stuck to the roller which was not reflected. The next step was to eliminate all reflections. The thermogram of the roller after briquetting clearly shows that its surface was heated up during the process and the temperature distribution was not uniform. Despite eliminated access to daylight and artificial light in the laboratory, the reflection was still visible. The control tape after the briquetting was destroyed due to very high pressure on the rollers surface.

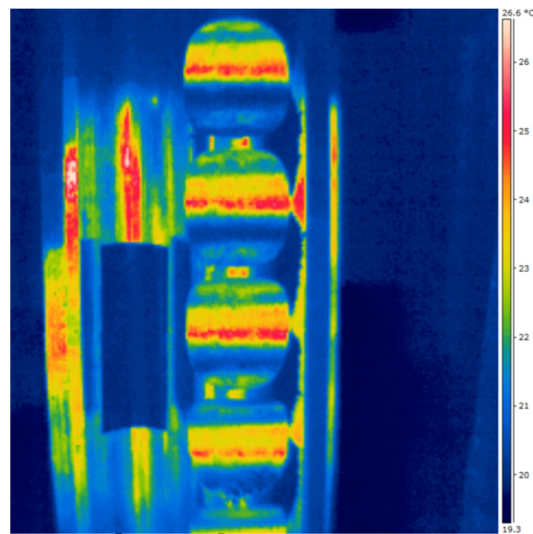


Figure 13. Working roller thermogram with reflections of radiation before briquetting process.

Then, thermal images of the rollers stored and not used in the laboratory at ambient temperature were taken. Despite eliminated access to daylight and artificial light in the laboratory, the reflections were still visible. Despite their constant temperature, the thermograms showed variation in their surface temperature by about 1 °C, which made the accuracy of the measurements too low for the correct analysis of the results. In subsequent tests, the rolls were coated with an anti-reflex spray CRC Crick 130 (CRC Industries Europe, Zele, Belgium). The attempts were also considered unsuccessful. The spraying of the aerosol after the briquetting process cooled the surface of the rollers and made it impossible to record the actual temperature gradients. The coating applied before consolidation, after the briquetting process, was destroyed. Despite the observance of the strict test conditions, attempts to measure the temperature distribution on the surface of working rollers did not bring positive results.

4. Conclusions

The conducted research allows to conclude that a thermograph is an interesting research method in the context of using it to analyze the processes of briquetting fine-grained materials. At the same time, this method requires very good preparation of the test stand in order to eliminate the influence of undesirable external factors, like radiation sources that may prevent the reliable processing of the obtained results. The attempts to measure the temperature distribution on the surface of working rollers did not bring positive results. Despite the observance of the strict test conditions, the external disturbances on the roller surface could not be eliminated. For each type of the merged material, the temperature in the upper part of the briquette was the highest. The obtained temperature distributions coincide with the bulk material deformation in the forming cavity during briquetting process in asymmetrical compaction unit presented in the work [70]. From the analysis of both distributions, it can be concluded that higher local briquette temperatures in a given place correspond to better local density. Therefore, in the case of saddle-shaped briquette in the upper part of the briquette, the stresses and strain are greater, and those in the lower part—smaller, which is also confirmed by the recent research presented in the paper [76].

The study of the temperature distribution presented in the paper can also be related to the actual types of pressure exerted on the bottom (central part) of the forming cavity presented in the literature. They amount to approximately 65 MPa for the M1 mixture [69], while for the M4 mixture it is approximately 30 MPa [77]. Different pressure generated on both materials also correlates with the temperatures obtained on the briquette surface in their central part. For mixture M1, the measured temperature at the center of the forming

cavity (point 4) is higher, and so is the pressure. It should be noted that each material may have a different temperature response to pressure. This was proved by the own research of the pressure exerted on M2 and M3 materials during briquetting in the roller press. The pressures measured for these materials are 45 and 50 MPa, respectively. This corresponds to the difference of measured temperatures on the briquette surfaces of M2 and M3 materials (higher pressure, higher temperature). However, it was proved that materials do not directly correlate with pressures and temperatures for each other. On the basis of thermography studies, it is concluded that measuring the pressure in the central part is not the maximum pressure exerted on the briquette during forming; however, from the point of view of measurement technology, a different arrangement of the pressure sensor is difficult to implement in technical conditions.

It can be concluded that testing the temperature in the briquette can be an indirect method of testing its degree of compaction and the pressure generated on its surface during briquetting. This method can be widely used to select the right forming volume and geometry to obtain properly compacted briquettes. This method can also be very useful for examining the correction of the shape of forming cavities, because on its basis, it can be seen which part of briquette is not compacted properly, thus which area of the surface forming the cavities should be corrected because in this place, the local temperature will be lower than in other places [69].

Author Contributions: Conceptualization, M.B. and A.U.; formal analysis, M.B. and A.U.; methodology, M.B. and A.U.; investigation, M.B. and A.U.; writing—original draft, M.B. and A.U.; writing—review and editing, M.B. All authors have read and agreed to the published version of the manuscript.

Funding: Printing of the publication was funded by Subsidy grant number 16.16.130.942/KPiEM.

Institutional Review Board Statement: Not applicable.

Informed Consent Statement: Not applicable.

Data Availability Statement: The data presented in this study are available on request from the corresponding author.

Acknowledgments: We would like to thank Klara Brendel for her help during the research.

Conflicts of Interest: The authors declare no conflict of interest.

References

1. Gomółka, Z.; Kwiatkowski, B.; Twaróg, B. Thermovision measurements in diagnostic systems [Pomiary termowizyjne w systemach diagnostycznych]. *Eduk. Tech. Inform.* **2014**, *5*, 598–604. (In Polish)
2. Stachniewicz, R. Use of thermography for determining places in danger of the mold growth in residential buildings. *Ekon. Sr.* **2018**, *3*, 142–156.
3. Damijan, Z.; Uhryński, A. Systemic cryotherapy influence of low temperatures on selected physiological parameters. *Acta Phys. Pol. A* **2012**, *121*, 38–41. [[CrossRef](#)]
4. Damijan, Z.; Uhryński, A. The influence of driver's working environment on thermal changes of their organism. *Acta Phys. Pol. A* **2010**, *118*, 35–40. [[CrossRef](#)]
5. Damijan, Z.; Uhryński, A. The effect of general low frequency vibration on energy balance of a human being. *Acta Phys. Pol. A* **2013**, *123*, 970–973. [[CrossRef](#)]
6. Kaczmarek, J. Using a thermovision method for measuring temperatures of a workpiece during abrasive cut-off operation. *Adv. Manuf. Sci. Technol.* **2011**, *35*, 85–95.
7. Molenda, J.; Charchalis, A. Using thermovision for temperature measurements during turning process. *J. KONES Powertrain Transp.* **2018**, *25*, 293–298.
8. Bartoszek, M. Thermovision measurements of temperature on the tool-chip upper side in turning of aisi 321 steel. *Tech. Sci.* **2020**, *23*, 69–80.
9. Nowacki, J.; Wypych, A. Application of thermovision method to welding thermal cycle analysis. *J. Achiev. Mater. Manuf. Eng.* **2010**, *40*, 131–137.
10. Piecuch, G.; Madera, M.; Żabiński, T. Diagnostics of welding process based on thermovision images using convolutional neural network. In *IOP Conference Series: Materials Science and Engineering, Proceedings of the IV International Conference of Computational Methods in Engineering Science—CMES'19, Kazimierz Dolny, Poland, 21–23 November 2019*; IOP Publishing: Bristol, UK, 2019, p. 012042; Volume 710.

11. Struzikiewicz, G.; Sioma, A. Application of infrared and high-speed cameras in diagnostics of CNC milling machines: Case study. In *Proceedings of SPIE, Proceedings of the Photonics Applications in Astronomy, Communications, Industry, and High-Energy Physics Experiments, Wilga, Poland, 27 May–2 June 2019*; Romaniuk, R.S., Linkzug, M., Eds.; SPIE: Bellingham, WA, USA, 2019; Volume 11176, p. 111760C.
12. Macrea, T.; Macrea, D.; Cepisca, C. Thermovision lubrication monitoring system for a mechanical expander. In *Proceedings of the 7th International Symposium on Advanced Topics in Electrical Engineering, ATEE, Bucharest, Romania, 12–14 May 2011*; pp. 1–4.
13. Fidal, M. Identification of machine technical state on the basis of fourier analysis of infrared images. *Diagn. Struct. Health Monit.* **2011**, *2*, 25–30.
14. Michalik, P.; Zajac, J. Use of thermovision for monitoring temperature conveyor belt of pipe conveyor. *Appl. Mech. Mater.* **2014**, *683*, 238–242. [[CrossRef](#)]
15. Worsztynowicz, B.; Uhryński, A. The analysis of heating process of catalytic converter using thermo-vision. *Combust. Engines* **2015**, *54*, 41–51.
16. Worsztynowicz, B.; Uhryński, A.; Borkowski, B.; Pluta, M. The analysis of thermal state of catalytic converter depending on fuel supply and engine load using thermo-vision. *Combust. Engines* **2017**, *56*, 30–36. [[CrossRef](#)]
17. Zywicka, G.; Baginski, P.; Banaszek, S. Experimental studies on foil bearing with a sliding coating made of synthetic material. *J. Tribol.* **2016**, *138*, 11301. [[CrossRef](#)]
18. Gabrhelová, L.; Jurman, J. Temperature of bearings of rotating machines as a result of vibration. *Trans. VŠB Tech. Univ. Ostrava Saf. Eng. Ser.* **2010**, *56*, 1747.
19. Baranowski, P.; Damaziak, K.; Malachowski, J.; Mazurkiewicz, L.; Polakowski, H.; Piatkowski, T.; Kastek, M. Thermovision in the validation process of numerical simulation of braking. *Metrol. Meas. Syst.* **2014**, *21*, 329–340. [[CrossRef](#)]
20. Simko, M.; Chupac, M.; Gutten, M. Thermovision measurements on electric machines. In *Proceedings of the 2018 International Conference on Diagnostics in Electrical Engineering (Diagnostika), Pilsen, Czech Republic, 4–7 September 2018*; pp. 1–4.
21. Janura, R.; Gutten, M.; Korenciak, D.; Sebok, M. Thermal processes in materials of oil transformers. *Diagn. Electr. Mach. Insul. Syst. Electr. Eng.* **2016**, *2016*, 81–84.
22. Kuchynkova, H.; Hajek, V. Measurement of temperature of electrical machines using thermovision camera. *Zesz. Probl. Masz. Elektr.* **2010**, *87*, 139–144.
23. Wyleciał, T.; Urbaniak, D. Research on thermal contact resistance in a bed of steel square bars using thermovision. *Acta Phys. Pol. A* **2019**, *135*, 263–269. [[CrossRef](#)]
24. Sharkeev, Y.; Vavilov, V.; Skripnyak, V.A.; Belyavskaya, O.; Legostaeva, E.; Kozulin, A.; Chulkov, A.; Sorokoletov, A.; Skripnyak, V.V.; Eroshenko, A.; et al. Analyzing the deformation and fracture of bioinert titanium, zirconium and niobium alloys in different structural states by the use of infrared thermography. *Metals* **2018**, *8*, 703. [[CrossRef](#)]
25. Krešák, J.; Peterka, P.; Kropuch, S.; Novák, L. Measurement of tight in steel ropes by a mean of thermovision. *Measurement* **2014**, *50*, 93–98. [[CrossRef](#)]
26. Pawlak, A.; Rozanski, A.; Galeski, A. Thermovision studies of plastic deformation and cavitation in polypropylene. *Mech. Mater.* **2013**, *67*, 104–118. [[CrossRef](#)]
27. Košťál, P.; Ružiak, I.; Jonšta, Z.; Kopal, I.; Hrehuš, R.; Kršková, J. Experimental method for complex thermo-mechanical material analysis. *Int. J. Thermophys.* **2010**, *31*, 630–636. [[CrossRef](#)]
28. Piekłak, K.; Mikołajczyk, Z. Strength tests of 3D warp-knitted composites with the use of the thermovision technique. *Fibres Text. East. Eur.* **2011**, *19*, 100–105.
29. Rojek, M.; Wróbel, G. Thermographic method of fatigue assessment of polymeric materials. *J. Achiev. Mater. Manuf. Eng.* **2010**, *42*, 88–93.
30. Grochalski, K.; Peta, K. Diagnostic methods of detecting defects within the material with the use of active infrared thermovision. *Arch. Mech. Technol. Mater.* **2017**, *37*, 41–44. [[CrossRef](#)]
31. Bazaleev, N.I.; Bryukhovetskiy, V.V.; Klepikov, V.F.; Litvinenko, V.V. Thermovision acoustic thermography construction materials defectoscopy. *Vopr. At. Nauk. Tekhn. Fiz. Radiatsion Pov. Radiatsion Materialoved.* **2011**, *2*, 178–185.
32. Wierzbicki, Ł.; Stabik, J.; Wróbel, G.; Szczepanik, M. Efficiency of two non-destructive testing methods to detect defects in polymeric materials. *J. Achiev. Mater. Manuf. Eng.* **2010**, *38*, 163–170.
33. Durka, T.; Stefanidis, G.; Van Gerven, T.; Stankiewicz, A. On the accuracy and reproducibility of fiber optic (FO) and infrared (IR) temperature measurements of solid materials in microwave applications. *Meas. Sci. Technol.* **2010**, *21*, 045108. [[CrossRef](#)]
34. Lahiri, B.B.; Bagavathiappan, S.; Reshmi, P.R.; Philip, J.; Jayakumar, T.; Raj, B. Quantification of defects in composites and rubber materials using active thermography. *Infrared Phys. Technol.* **2012**, *55*, 191–199. [[CrossRef](#)]
35. Róžański, L.; Ziopaja, K. Detection of material defects in reinforced concrete slab using active thermography. *Meas. Autom. Monit.* **2017**, *63*, 82–85.
36. Miękina, W.; Madura, H. Podstawy teoretyczne pomiarów termowizyjnych. *Pomiary termowizyjne w praktyce. Agenda Wydawnicza PAKu* **2004**, 10–26.
37. Tor-Świątek, A.; Samujło, B. Use of thermo vision research to analyze the thermal stability of microcellular extrusion process of poly (vinyl chloride). *Maint. Reliab.* **2013**, *15*, 58–61.

38. Kašiković, N.; Novaković, D.; Milić, N.; Vladić, G.; Zeljković, Ž.; Stančić, M. Thermovision and spectrophotometric analysis of ink volume and material characteristics influence on colour changes of heat treated printed substrates. *Tech. Gaz.* **2015**, *22*, 33–41. [[CrossRef](#)]
39. Michalak, M. Bezkontaktowe badania właściwości cieplnych wyrobów włókienniczych. Cz. 1. [Non-contact tests of thermal properties of textiles, Part 1]. *Przegląd Włókienniczy Włókno Odzież Skóra* **2010**, *2*, 31–33. (In Polish)
40. Michalak, M. Bezkontaktowe badania właściwości cieplnych wyrobów włókienniczych. Cz. 2. [Non-contact tests of thermal properties of textiles, Part 2]. *Przegląd Włókienniczy Włókno Odzież Skóra* **2010**, *3*, 25–27. (In Polish)
41. Hynek, M.; Votapek, P. Thermal analysis of tyre curing process. In Proceedings of the 17th International Conference on Structural Mechanics in Nuclear Engineering, Svratka, Czech Republic, 9–12 May 2011; pp. 223–226.
42. Žaba, K.; Nowak, S.; Kwiatkowski, M.; Nowosielski, M.; Kita, P.; Sioma, A. Application of non-destructive methods to quality assessment of pattern assembly and ceramic mould in the investment casting elements of aircraft engines. *Arch. Metall. Mater.* **2014**, *59*, 1517–1525. [[CrossRef](#)]
43. Lepiarczyk, D.; Uhryński, A. Thermo-vision analysis of iron foundry production process concerning secondary usage of heat. *Pol. J. Environ. Stud.* **2014**, *23*, 1017–1023.
44. Legemza, J.; Fröhlichová, M.; Findorák, R. The thermovision measurement of temperature in the iron-ore sintering process with the biomass. *Acta Metall. Slovaca Conf.* **2014**, *4*, 56–65. [[CrossRef](#)]
45. Litstera, J.D.; Omara, C.; Salman, A.D.; Yua, M.; Weidemann, M.; Schmidt, A. Roller compaction: Infrared thermography as a PAT for monitoring powder flow from feeding to compaction zone. *Int. J. Pharm.* **2020**, *578*, 119114.
46. Stempkowska, A.; Izak, P.; Mastalska-Popławska, J.; Staszewska, M. The analysis of thermal properties of selected rock materials by thermovision methods. *J. Pol. Miner. Eng. Soc.* **2018**, *2*, 337–344.
47. Zou, J.; Rubio, V.; Binner, J. Thermoablative resistance of ZrB₂-SiC-WC ceramics at 2400 °C. *Acta Mater.* **2017**, *133*, 293–302. [[CrossRef](#)]
48. Jakubczak, P.; Bienias, J.; Surowska, B. Impact damage live-time analysis of modern composite materials using thermography. *Compos. Theory Pract.* **2014**, *14*, 219–223.
49. Vavilov, V.P.; Billard, S.; Ayvazyan, V.M. A thermal tomographic unit for testing composite materials. *Russ. J. Nondestruct. Test.* **2014**, *50*, 679–683. [[CrossRef](#)]
50. Wilczyński, D.; Malujda, I.; Górecki, J.; Jankowiak, P. Research on the process of biomass compaction in the form of straw. *MATEC Web Conf.* **2019**, *254*, 05015. [[CrossRef](#)]
51. Ajimotokan, H.A.; Ehindero, A.O.; Ajao, K.S.; Adeleke, A.A.; Ikubanni, P.P.; Shuaib-Babata, Y.L. Combustion characteristics of fuel briquettes made from charcoal particles and sawdust agglomerates. *Sci. Afr.* **2019**, *6*, e00202. [[CrossRef](#)]
52. Florentino-Madiedo, L.; Díaz-Faes, E.; Barriocanal, C. Mechanical strength of bio-coke from briquettes. *Renew. Energy* **2020**, *146*, 1717–1724. [[CrossRef](#)]
53. Obidziński, S. Pelletization process of postproduction plant waste. *Int. Agrophysics* **2012**, *3*, 279–284. [[CrossRef](#)]
54. Baiul, K.V. Synthesis of roller press rational design for composite solid fuel production. *Probl. Reg. Energetics* **2019**, *2*, 103–116.
55. Polyanskii, V.I.; Kobelev, M.V.; Vetoshkin, A.V. (Оборудование для брикетирования отсева металлургической извести). [The equipment for the press compacting of the metallurgical lime screenings]. *New Refract. Sci. Eng. J.* **2014**, *3*, 99–100. (In Russian)
56. Khudyakov, A.; Vashchenko, S.V.; Baiul, K.V.; Semenov, Y.S. Kaolin raw material briquetting for lump chamotte production. *Refract. Ind. Ceram.* **2018**, *4*, 333–337. [[CrossRef](#)]
57. Magdziarz, A.; Kuźnia, M.; Bembenek, M.; Gara, P.; Hryniewicz, M. Briquetting of EAF dust for its utilisation in metallurgical processes. *Chem. Process. Eng.* **2015**, *36*, 263–271. [[CrossRef](#)]
58. Ulus, A.; Ekici, H.; Güler, E. Optimization of recovery efficiency for briquetted aluminum chips up to briquetting parameters. In *Light Metals 2017*; Ratvik, A., Ed.; Springer: Cham, Switzerland, 2017; pp. 925–932.
59. Bembenek, M.; Wdaniec, P.; Baran, E. Production of a granulated mineral fertilizer from waste gypsum in a flat-matrix granulator. *Przem. Chem.* **2020**, *99*, 236–238. (In Polish)
60. Bembenek, M.; Wdaniec, P. Effect of crusher type and its parameters on the dry granulation of powders. *Przem. Chem.* **2019**, *98*, 310–313. (In Polish)
61. Michrafy, A.; Zavaliangos, A.; Cunningham, J.C. Dry granulation process modelling. *Predict. Modeling Pharm. Unit Oper.* **2017**, *1*, 71–97.
62. Bindhumadhavan, G.; Seville, J.P.K.; Adams, M.J.; Greenwood, R.W.; Fitzpatrick, S. Roll compaction of a pharmaceutical excipient: Experimental validation of rolling theory for granular solids. *Chem. Eng. Sci.* **2005**, *60*, 3891–3897. [[CrossRef](#)]
63. Schiano, S.; Chen, L.; Wu, C.-Y. The effect of dry granulation on flow behaviour of pharmaceutical powders during die filling. *Powder Technol.* **2018**, *337*, 78–83. [[CrossRef](#)]
64. Hryniewicz, M. Metoda Doboru Pras Walcowych Oraz Opracowania Założeń do Ich Modernizacji Lub Konstrukcji [Method of Selection of Roll Presses and Elaboration of Design Criteria for Their modernization or Construction]. Ph.D. Thesis, AGH University of Science and Technology, Kraków, Poland, 1997. (In Polish).
65. Bembenek, M. Badania i perspektywy nowych obszarów stosowania pras walcowych. [Research and prospects for new areas of using roller presses]. *Przem. Chem.* **2017**, *9*, 1845–1847. (In Polish)
66. Baiul, K.V.; Solodka, N.; Khudyakov, A.; Vashchenko, S.V. Selection of rational surface configuration For roller press tires. *Powder Metall. Met. C+* **2020**, *59*, 9–21. [[CrossRef](#)]

67. Kruszelnicka, W.; Kasner, R.; Bałdowska-Witos, P.; Flizikowski, J.; Tomporowski, A. The integrated energy consumption index for energy biomass grinding technology assessment. *Energies* **2020**, *13*, 1417. [[CrossRef](#)]
68. Karwat, B.; Rubacha, P.; Stańczyk, E. Simulational and experimental determination of the exploitation parameters of a screw conveyor. *Eksploat. Niezawodn.* **2020**, *22*, 741–747. [[CrossRef](#)]
69. Bembenek, M. Exploring efficiencies: Examining the possibility of decreasing the size of the briquettes used as the batch in the electric arc furnace dust processing line. *Sustainability* **2020**, *12*, 6393. [[CrossRef](#)]
70. Loginov, Y.N.; Bourkine, S.P.; Babaliyov, N.A. Cinematics and volume deformations during roll press briquetting. *J. Mater. Process. Technol.* **2001**, *118*, 151–157. [[CrossRef](#)]
71. Bembenek, M.; Krawczyk, J.; Pańcikiewicz, K. The wear on roller press rollers made of 20Cr4/1.7027 steel under conditions of copper concentrate briquetting. *Materials* **2020**, *13*, 5782. [[CrossRef](#)]
72. Baiul, K.; Vashchenko, S.V.; Khudyakov, A.; Krot, P.; Solodka, N. Optimisation of wastes compaction parameters in case of gradual wear of the briquetting press rolls. In Proceedings of the First Virtual Conference on Mechanical Fatigue VCMF2020, University of Porto (FEUP, Portugal), Wroclaw University of Science and Technology (Poland), ESIS/TC12 Technical Committee (European Structural Integrity Society–ESIS), Cracow, Poland, 9–11 September 2020; pp. 9–11.
73. Loginov, J.N.; Babajłow, N.A.; Pierwuchina, D.N. Physical modeling of roll pressing at asymmetric effect on the sealing material. *Izvestijawysshich Uchebnych Zawiedienij Czernaja Metailurgija* **2015**, *58*, 186–191. (In Russian) [[CrossRef](#)]
74. Zavaliangos, A.; Dec, R. Powder processing in the roller press—Theory and practice. *Powder Handl. Process.* **2007**, *1*, 23–28.
75. Bembenek, M. Modeling of loads in the drive system of a roller press on an example of a press for briquetting brown coal. *Mech. Adv. Technol.* **2018**, *84*, 113–124. [[CrossRef](#)]
76. Bembenek, M.; Krawczyk, J.; Frocisz, Ł.; Śleboda, T. The analysis of the morphology of the saddle-shaped bronze chips briquettes produced in the roller press. *Materials* **2021**, *14*, 1455. [[CrossRef](#)]
77. Gara, P. Research on the Selection of Parameters for Compaction and Grinding Calcium Hydroxide to Obtain a Specific Sorbent. Ph.D. Thesis, AGH University of Science and Technology, Kraków, Poland, 2005. (In Polish).

Review

Metastable Materials Accessed under Moderate Pressure Conditions ($P \leq 3.5$ GPa) in a Piston-Cylinder Press

Javier Gainza ¹, Federico Serrano-Sánchez ¹, João Elias F. S. Rodrigues ¹, Norbert Marcel Nemes ², José Luis Martínez ¹ and José Antonio Alonso ^{1,*}

¹ Instituto de Ciencia de Materiales de Madrid (ICMM), Consejo Superior de Investigaciones Científicas (CSIC), Sor Juana Inés de la Cruz 3, E-28049 Madrid, Spain; jgainza@ucm.es (J.G.); fserrano@icmm.csic.es (F.S.-S.); rodrigues.joaolias@gmail.com (J.E.F.S.R.); martinez@icmm.csic.es (J.L.M.)

² Departamento de Física de Materiales, Universidad Complutense de Madrid, E-28040 Madrid, Spain; nmnemes@fis.ucm.es

* Correspondence: ja.alonso@icmm.csic.es

Abstract: In this review, we describe different families of metastable materials, some of them with relevant technological applications, which can be stabilized at moderate pressures 2–3.5 GPa in a piston-cylinder press. The synthesis of some of these systems had been previously reported under higher hydrostatic pressures (6–10 GPa), but can be accessed under milder conditions in combination with reactive precursors prepared by soft-chemistry techniques. These systems include perovskites with transition metals in unusual oxidation states (e.g., RNiO₃ with Ni³⁺, R = rare earths); double perovskites such as RCu₃Mn₄O₁₂ with Jahn–Teller Cu²⁺ ions at A sites, pyrochlores derived from Tl₂Mn₂O₇ with colossal magnetoresistance, pnictide skutterudites M_xCo₄Sb₁₂ (M = La, Yb, Ce, Sr, K) with thermoelectric properties, or metal hydrides Mg₂MH_x (M = Fe, Co, Ni) and AMgH₃ (A: alkali metals) with applications in hydrogen storage. The availability of substantial amounts of sample (0.5–1.5 g) allows a complete characterization of the properties of interest, including magnetic, transport, thermoelectric properties and so on, and the structural characterization by neutron or synchrotron X-ray diffraction techniques.

Keywords: high-pressure synthesis; RNiO₃ perovskites; metal-insulator transitions; CaCu₃Mn₄O₁₂; colossal magnetoresistance; SeNiO₃; SeCoO₃; NaMgH₃; Tl₂Mn₂O₇; CoSb₃



Citation: Gainza, J.; Serrano-Sánchez, F.; Rodrigues, J.E.F.S.; Nemes, N.M.; Martínez, J.L.; Alonso, J.A. Metastable Materials Accessed under Moderate Pressure Conditions ($P \leq 3.5$ GPa) in a Piston-Cylinder Press. *Materials* **2021**, *14*, 1946. <https://doi.org/10.3390/ma14081946>

Academic Editor: George Kenanakis

Received: 22 March 2021

Accepted: 9 April 2021

Published: 13 April 2021

Publisher's Note: MDPI stays neutral with regard to jurisdictional claims in published maps and institutional affiliations.



Copyright: © 2021 by the authors. Licensee MDPI, Basel, Switzerland. This article is an open access article distributed under the terms and conditions of the Creative Commons Attribution (CC BY) license (<https://creativecommons.org/licenses/by/4.0/>).

1. Introduction

Many interesting materials (oxides, chalcogenides, pnictides, hydrides) with exceptional electronic properties are metastable under ambient conditions and require special synthesis conditions such as high pressure, or the use of strongly oxidizing or reducing conditions or, in general, the utilization of moderate treatment temperatures. Some of these metastable materials, given the difficulty of their preparation, had been little studied so far, in spite of their interesting properties. This is the case, for example, of new oxides of transition metals in unusual oxidation states (e.g., V(IV), Cr(IV), Mo(V), Fe(IV), Ni(III), Cu(III)) or intermediate valence states (such as Cu(II)-Cu(III), Mn(III)-Mn(IV), Fe(II)-Fe(III)), some of which present strong electronic correlations that are responsible for interesting properties such as the superconductivity, the metallic behaviour and the metal-to-insulator transitions or the colossal magnetoresistance phenomenon. As a brief overview, the high hydrostatic pressure favours the formation of the short and strongly covalent chemical bonds characterizing the high oxidation states; on the other hand, the high pressure applied by a reactive gas such as oxygen provides the highly oxidizing conditions necessary for the stabilization of some of the mentioned valence states. Additionally, pressure prevents the decomposition of unstable reactants at the synthesis temperature (e.g., Tl₂O₃, CrO₂); it helps to increase the coordination numbers and it favours the denser phases, in perovskite-like materials [1–4], skutterudites, pyrochlores and so on. Finally, high pressure enhances

the reaction kinetics substantially. Thus, high pressure is a good choice to prepare new compounds with a low stability or a metastable character.

In the past 20 years, our group at the Instituto de Ciencia de Materiales de Madrid (CSIC) has been dealing with the stabilization of several families of metastable materials, which have been accessed with a simple piston-cylinder hydrostatic press, under moderate pressure conditions in the 2.0–3.5 GPa range. The synthesis of some of these systems was previously described to proceed at superior pressures (6–10 GPa); in our case the combination of wet chemistry procedures to obtain reactive precursors, or the choice of the reactants, was key to succeed under moderate pressure conditions. In the following we will describe some results corresponding to the families of $RNiO_3$ perovskites (R = rare-earths), $Tl_2Mn_2O_7$ pyrochlores and derivatives, $CaCu_3Mn_4O_{12}$ double perovskites and derivatives, $M_xCo_4Sb_{12}$ skutterudites (M = alkali, alkali earth or rare earth elements), $(Se,Te)MO_3$ (M = Ni, Mn, Co) perovskites and $AMgH_3$ hydrides (A = alkali metals).

2. Materials and Methods

In all cases, the high-pressure reactions were carried out in a piston-cylinder Rockland Research press (Rockland Research Corporation, West Nyack, NY, USA), attaining maximum pressures of 3.5 GPa (piston of $\frac{1}{2}$ ") or 2 GPa (piston $\frac{3}{4}$ "). The samples were introduced in gold, platinum or niobium capsules, depending on the chemical nature of the reactants. These capsules were set in graphite cylinders acting as heaters, with Pyrex sleeves acting as pressure medium (Figure 1). The final pressure was applied in cold; the temperature was increased at 20 °C/min. Pressurization and depressurization rates were 2 GPa/h. After the heating period (20–60 min), the sample was rapidly cooled (100 °C/s) and then the pressure was slowly released. Therefore, the high-pressure products were quenched to a metastable state, where they were kinetically stable for long times. The reactants and experimental details for each system were as follows:

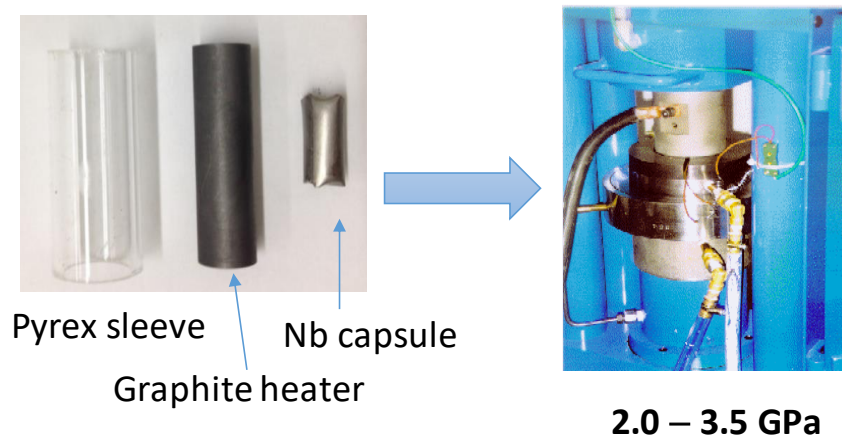


Figure 1. (Left): Graphite heater, Pyrex sleeve and Nb capsule (made of an Nb foil). (Right): view of the piston-cylinder press, including the power cable, thermocouple wiring and water cooling systems.

RNiO₃ perovskites. Stoichiometric mixtures of analytical grade $Ni(OH)_2$ (99%, Aldrich Chemical Company Inc., St. Louis, MO, USA) and R_2O_3 (R = rare earths) (99.9%, Alfa Aesar, Karlsruhe, Germany) were ground in an agate mortar with 30% $KClO_4$ (>99.5%, Fluka Chemika, Buchs, Switzerland), incorporated to provide an in situ high-oxygen pressure to promote the oxidation of nickel to Ni^{3+} . The precursor mixture was introduced into a gold capsule of 5 mm diameter. A hydrostatic pressure of 2 or 3.5 GPa was applied; the sample was then heated at 900 °C for 20 min, followed by quenching. The KCl resulting from the decomposition of $KClO_4$ and traces of R_2O_3 and NiO was subsequently eliminated by washing the resulting powder in a diluted HNO_3 solution (65%, J.T. Baker, Schwerte, Germany) at 60 °C. The sample was then dried at 150 °C for 1 h in air.

RCu₃Mn₄O₁₂ double perovskite derivatives. Stoichiometric amounts of analytical grade, R₂O₃ (R = rare earths), Cu(NO₃)₂·3H₂O and MnCO₃ (99.9+%, Aldrich, Steinheim, Germany) were dissolved in citric acid. For R = Ce, Pr, Tb, Th, Ce(NO₃)₃, Pr₆O₁₃ or Tb₄O₇ or Th(NO₃)₄·5H₂O were used, respectively, instead of R₂O₃. For Fe-substituted samples, FeC₂O₄ was used as reactant. The citrate solution turned into a resin by slow evaporation and drying at 120 °C. Afterwards, all the organic materials and nitrates were eliminated by heating at 600 °C for 12 h. This precursor was mixed with KClO₄ (30% in weight) and thoroughly ground, sealed in a gold capsule (8 mm diameter, 10 mm length) and inserted in a cylindrical graphite heater. Hydrostatic pressure of 2 GPa and 1000 °C temperature were applied for 60 min to carry out the reaction. The in situ decomposition of KClO₄ provides the high O₂ pressure required to stabilize Mn⁴⁺ cations. Subsequently, the product was ground and washed in a dilute HNO₃ aqueous solution, in order to eliminate small amounts of unreacted CuO and dissolve KCl remaining from the decomposition of KClO₄; then the powder was dried in air at 150 °C for 1 h.

(Se,Te)MO₃ (M = Ni, Co, Mn) perovskites. A thoroughly ground stoichiometric mixture of TeO₂/H₂SeO₃ and Ni(OH)₂/CoO/MnO (99%, Alfa Aesar, Kandel, Germany) was sealed in a platinum capsule (6 mm dia.), and loaded in a cylindrical graphite heater. The reaction occurred at a pressure of 3.5 GPa at 850 °C for 1 h. After quenching to room temperature the pressure was released.

Metal hydrides, Mg₂MH_x (M = Fe, Co, Ni) and AMgH₃ (A: Li, Na, K). Polycrystalline samples of these nominal compositions were synthesized from stoichiometric mixtures of LiH, NaH, KH, MgH₂ and metal Fe, Co or Ni (Alfa Aesar, 99.9%, Kandel, Germany). The precursors were handled in inert atmosphere in an N₂-filled glove box, since the reactants are highly sensitive to air and moisture. The reactants were mixed and ground in a mortar and then sealed in a gold capsule (8 mm diameter, 10 mm length), and loaded in a cylindrical graphite heater. The reactions occurred at moderate conditions of 2 GPa and 775 °C for short reaction times, less than 45 min, followed by quenching to room temperature under pressure and finally releasing the pressure slowly. The gold capsule with the reaction products was opened inside the glove box, yielding dense pellets, which were ground to perform the structural characterization.

Tl₂Mn₂O₇ pyrochlore derivatives. Tl₂Mn₂O₇, Tl_{2-x}Bi_xMn₂O₇ (x = 0.1, 0.2), Tl_{2-x}Cd_xMn₂O₇ (x = 0.1, 0.2), and Tl₂Mn_{1.8}Sb_{0.2}O₇ pyrochlores were synthesized from Tl₂O₃, CdO/Bi₂O₃/Sb₂O₃ and MnO₂ (Alfa Aesar, 99%, Germany) powders. The oxide mixtures were sealed in an 8 mm-diameter gold capsule, and loaded in a cylindrical graphite heater. The reaction occurred in a piston-cylinder press, at a pressure of 2 GPa at 1000 °C for 1 h.

Skutterudites M_xCo₄Sb₁₂ (M = alkali, alkali-earth, rare-earth elements). The samples with different compositions M_xCo₄Sb₁₂ (M = K, Sr, Y, La, Ce, Yb, Mm (mischmetal)) have been prepared by a solid-state reaction under moderate temperature and pressure conditions. The reagents used were analytical grade KH, Sr, Y, La, Ce, Yb, Co and Sb in powder form. About 1.1 g of the starting elements was mixed according to the stoichiometric amount and sealed in a 5 mm dia. niobium capsule in an N₂-filled glove box, which was placed inside the graphite cylinder used as a heater. Reactions were carried out at a pressure of 3.5 GPa at 800 °C for 1 h. Afterwards, the products were quenched, and the pressure was released.

In all cases, the nature of the resulting powder was assessed by laboratory X-ray diffraction (XRD) in a Bruker-AXS D8 diffractometer (Bruker-AXS, Karlsruhe, Germany) (40 kV, 30 mA), with Cu K α radiation ($\lambda = 1.5418 \text{ \AA}$). NPD patterns collected at the high resolution D2B neutron diffractometer of ILL-Grenoble were used for structural refinement. Although only a relatively small amount of sample was obtained from the high-pressure experiments (about 0.5 g), good quality patterns could be collected with the high-flux mode and a counting time of 4 h. A wavelength of 1.594 Å was selected from a Ge monochromator. Synchrotron X-ray diffraction (SXR) experiments were carried out in transmission mode on the BL04-MSPD beamline of the ALBA synchrotron (Barcelona, Spain) using the highest angular resolution mode as provided by the MAD setup [5]. The samples were sealed in

0.7 mm diameter quartz capillaries that were rotating during acquisition time to increase powder averaging. The beam energy was 28 keV ($\lambda = 0.4427 \text{ \AA}$) or 32 keV ($\lambda = 0.38776 \text{ \AA}$), selected to optimize absorption. The analysis of the diffraction data was performed by the Rietveld method, using the FullProf Suite [6]. The diffraction peak shape was defined with a pseudo-Voigt function; a linear interpolation between points devoid of reflections was considered as background. The final refinement included the scale factor, zero-point shift, width and asymmetry parameters, unit-cell parameters, atomic positions, and isotropic or anisotropic displacement factors. No regions were excluded from the refinements.

3. Results and Discussion

3.1. RNiO₃ Perovskites (R = Rare Earths)

The detailed and systematic study of the metal-to-insulator (MI) transitions in the RNiO₃ (R = rare earths) perovskites has been a long-standing topic, since these perovskites, containing Ni³⁺, are paradigmatic examples of charge-transfer materials that undergo abrupt metal-insulator transitions as a function of temperature and the size of the rare-earth cation. Torrance et al. [7] interpreted such transitions in terms of the reduction and closing of the charge-transfer gap between O²⁻ and Ni³⁺ ions. The presence of trivalent nickel makes it difficult to prepare these materials, particularly with smaller lanthanide radius. Thus, the transport properties (and MI transitions) had only been reported for R between La to Eu, prepared under high-oxygen pressures of 200 bar. There are examples of Ni perovskites synthesized at elevated pressures (~6 GPa) and temperatures (1000–1200 °C) in the literature [8–10], such as BiNiO₃. However, the preparation of the phases for R = Y, Gd, Tb, Dy, Ho, Er, Tm, Yb, Lu, not synthesized again since the pioneering work by Démazeau in 1971 [11], was demonstrated to be possible using moderate pressures of 2 GPa. Sufficient amounts of samples were obtained to perform accurate neutron and synchrotron X-ray diffraction studies across the transitions. A charge disproportionation in YNiO₃ associated with the MI transition was described for the first time [12,13]. In the monoclinic *P2₁/n* crystal structure, Ni atoms occupy two independent crystallographic sites with slightly different charge, $3 + \delta$ and $3 - \delta$, in such a way that there are alternating small and large octahedra along the 3 directions of the crystal (Figure 2).

This effect is extensive to other small rare-earth members, from R = Ho to R = Lu [14,15], for which the MI transition temperatures progressively increase as the R³⁺ size decreases (Figure 2). The access to these metastable materials made it possible to investigate a number of unexplored physical phenomena, which are mentioned hereafter: (i) High-pressure studies across the MI transitions by different techniques showed a metallization of the high-T phase for LuNiO₃ [16]; (ii) Mössbauer results in ⁵⁷Fe-doped Ni perovskites combined with neutron studies offered additional evidence of the charge disproportionation in RNiO₃ (R = Sm, Eu, Gd, Dy) [17–19]; (iii) Transport measurements in sintered NdNiO₃ yielded new features of the metallic state [20–22]; (iv) The investigation of absorbing DyNiO₃ in double-walled sample holders allowed the establishment of charge disproportionation and the resolution of the magnetic structure of DyNiO₃ [23]; (v) The observation, for the first time, of magnetic peaks by synchrotron soft X-ray resonant magnetic powder diffraction was possible in SmNiO₃ samples [24]; and (vi) the study of the evolution of the charge transfer between Ni^{3+ δ} and Ni^{3- δ} for the whole RNiO₃ series was possible from X-ray absorption data [25].

More results concern (i) the study of magnetic and electronic properties of RNiO₃ (R = Pr, Nd, Eu, Ho and Y) from resonant X-rays [26]; (ii) the magnetism and magnetic structures of the perovskite series NdNi_{1-x}Mn_xO₃ from neutron powder diffraction [27]; (iii) Mössbauer results in ⁵⁷Fe-doped Ni perovskites combined with neutron studies offering additional evidence of the charge disproportionation in RNiO₃ (R = Tm and Yb) [28], and allowing us to complete the phase diagram for these materials (Figure 2); (iv) the stability of the Ni sites across the pressure-induced insulator-metal transition in YNiO₃, previously prepared at 2 GPa [29]; and (v) the spin-canted magnetism and decoupling of the charge and spin-orbit coupling in NdNiO₃ [30]. Recently, the extremely high angular resolution

of the MSPD diffractometer at ALBA synchrotron X-ray source allowed us to observe the characteristic peak splitting in the (2,2,4) and (-2,2,4) twin reflections in SmNiO₃ (Figure 2), thus confirming the monoclinic distortion and charge disproportionation in this perovskite with Sm³⁺ ion with a relatively large size [31].

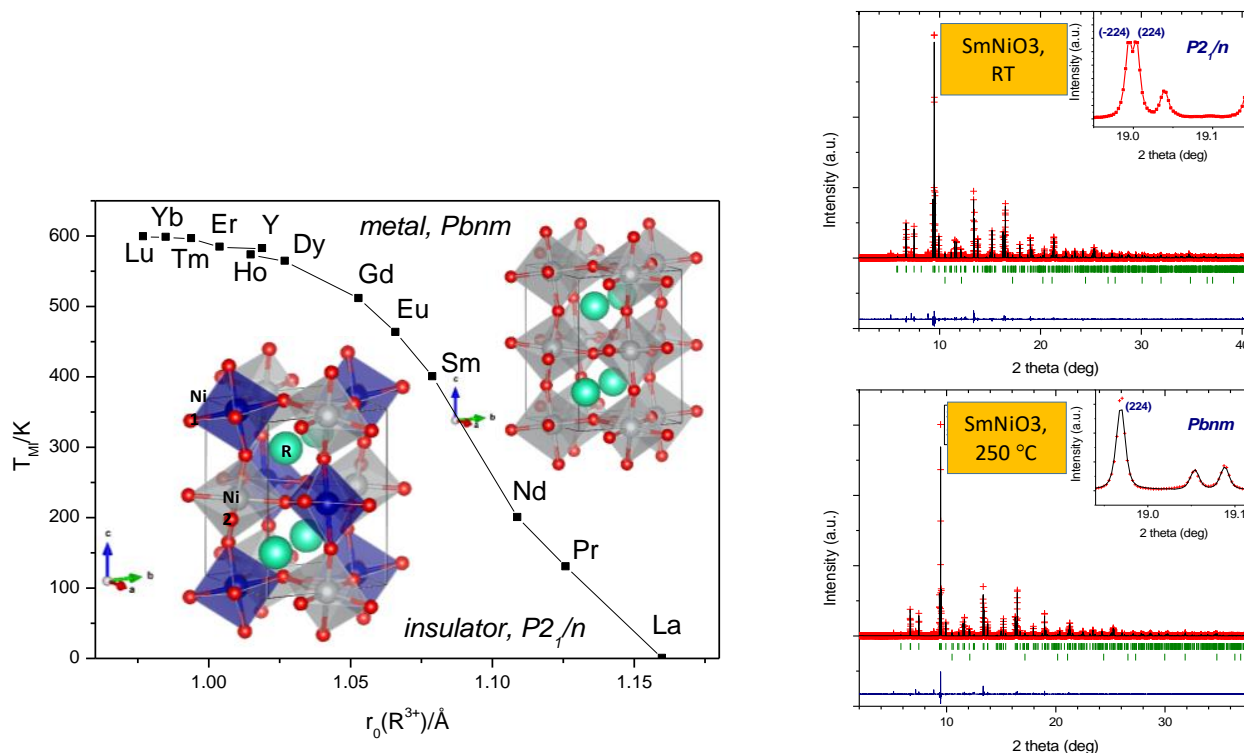


Figure 2. (Left): Phase diagram regarding the metal-insulator transitions experienced by RNiO₃ perovskites as a function of temperature and the R³⁺ ionic size. The monoclinic structure corresponding to the insulating state (space group $P2_1/n$) contains two types of crystallographically independent Ni atoms, whereas the orthorhombic structure (space group $Pbnm$) only contains one type of NiO₆ octahedron. (Right): Characteristic splitting of the (2,2,4)/(-2,2,4) reflections observed by synchrotron X-ray diffraction ($\lambda = 0.4427 \text{ \AA}$), due to the monoclinic symmetry only in the insulator regime, below the MI transition in SmNiO₃.

3.2. CaCu₃Mn₄O₁₂

Magneto-resistant (MR) materials experience an abrupt reduction in resistivity upon the application of an external magnetic field [32]. Its interest is induced, on one hand, by the wide panoply of technological applications in the field of magnetic sensors and read-head for magnetic disks. On the other hand, its study is also driven by more basic reasons, concerning the microscopic mechanisms that control these properties and, surprisingly, are related to other behaviours of the condensed matter such as the metallic state in oxides or the superconductivity.

In particular, we focus on a family of oxides that must be prepared under high-pressure conditions: the perovskites derived from CaCu₃Mn₄O₁₂. This oxide is among the ferrimagnetic materials that have been “rediscovered” in light of their MR properties [33,34]. This complex perovskite with a T_c = 360 K, shows a considerable MR at low field: at room temperature MR is almost saturated for magnetic fields as low as 0.03 T. Therefore, its response upon an external field is much more abrupt than for other more conventional systems. In spite of these encouraging properties, this oxide has been very little studied due to its metastable character, which requires high-pressure preparation conditions. The synthesis of this family of materials had been described, up to now, to proceed at 5–6 GPa [33,35], yet we managed to synthesize CaCu_{2.5}Mn_{4.5}O₁₂ at moderate pressures of 2 GPa, with comparable properties to those previously reported [36]. On the other hand, we have

checked that the replacement of Ca for La or other rare-earths in $\text{RCu}_3\text{Mn}_4\text{O}_{12}$ [37–39] has noticeable effects on the increment of T_C , besides observing a significant increase of the low-field MR, up to 3% at RT in 1 T [40].

These oxides can be considered as a 4-fold superstructure of perovskite $(\text{ABO}_3)_4$, with long-range order of R(Ca) and Cu at the A sites. The crystal structure exhibits the peculiarity of containing Cu^{2+} or Mn^{3+} , which are Jahn–Teller ions [41], at the A positions of the perovskite, in square planar coordination, as shown in Figure 3. This is due to the strong tilting of MnO_6 octahedra, defined in the $Im\bar{3}$ cubic space group.

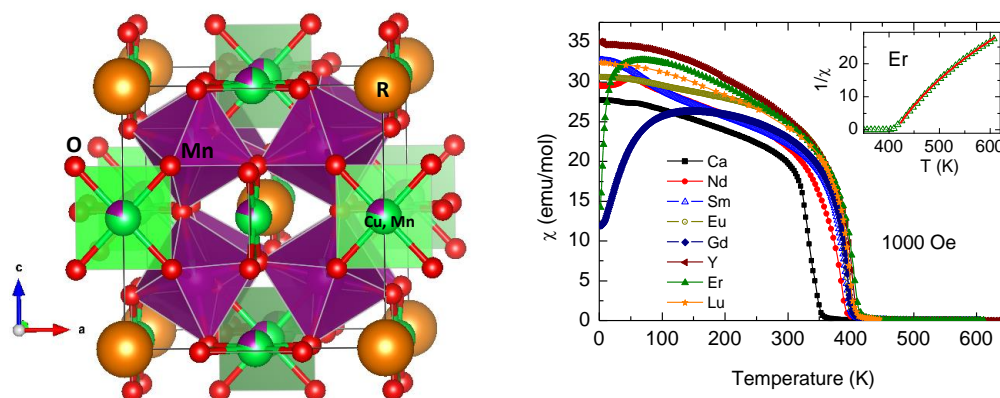


Figure 3. (Left): Crystal structure of $(\text{Ca,R})_3\text{Mn}_4\text{O}_{12}$, defined in the $Im\bar{3}$ space group, with the MnO_6 octahedra heavily tilted configuring a square planar oxygen coordination around Cu^{2+} (or Mn^{3+}). (Right): Evolution of the Curie temperature for the long-range ferrimagnetic ordering of Cu^{2+} and Mn^{4+} spins, enhanced by the decrease of the R^{3+} ionic size. The inset shows the reciprocal susceptibility above T_C for the sample with Er, characteristic of ferrimagnetic systems.

The peculiar magnetic structure of some members such as $\text{TbCu}_3\text{Mn}_4\text{O}_{12}$ has also been studied by NPD [42]. There is an interesting correlation between some structural parameters and the magnetic properties, which was discovered from neutron or synchrotron X-ray diffraction studies of all the series. By replacing Ca^{2+} with R^{3+} cations in the parent $\text{CaCu}_3\text{Mn}_4\text{O}_{12}$ oxide, there is a strong increase of the ferrimagnetic Curie temperature (T_C), shown in Figure 3, due to electron injection. The ionic radii of R^{3+} cations from La to Lu along the rare-earth series decrease, creating an internal or chemical pressure: The accompanying compression of the MnO_6 octahedral units with small rare earths brings about progressively shorter Mn–O distances and enhances the overlap between Mn and O orbitals, thus strengthening superexchange and increasing T_C by 50 K [43]. A transition from Pauli-paramagnetism to ferromagnetism was also observed in $\text{CaCu}_3(\text{Ru}_{4-x}\text{Mn}_x)\text{O}_{12}$ ($0 \leq x \leq 3$) perovskites [44], also prepared under moderate pressure conditions.

3.3. SeMO_3 ($M = \text{Mn}, \text{Co}, \text{Ni}$)

In classical ABO_3 oxides of the perovskite structure, at the A position usually an alkaline, alkaline-earth or rare-earth cation resides, with transition metals at the B sites. Much rarer are perovskite oxides containing *p-block* elements with an inert electron pair at the A positions, such as Tl^+ , Sn^{2+} , Sb^{3+} , Bi^{3+} , Se^{4+} and Te^{4+} . In order to stabilize perovskitelike oxides with these rather small cations, high-pressure conditions are typically required [1]. Two important examples are SeCuO_3 [45] and BiMnO_3 [46–49]. The large structural distortion bends the superexchange Cu–O–Cu or Mn–O–Mn angles and promotes the ferromagnetic interactions, according to the Goodenough–Kanamori rules [50]. We recently prepared and studied SeCoO_3 [51], SeMO_3 ($M = \text{Ni}, \text{Mn}$) [52], and TeNiO_3 [53], which warrants the accessibility to these systems under moderate pressure conditions. There are several examples in the literature where this synthesis process has also been proven useful, such as the $\text{SeCo}_{1-x}\text{Mn}_x\text{O}_3$ material prepared at ~ 4 GPa and ~ 1100 K for 1 h [54], and the SeMO_3 ($M = \text{Mn}, \text{Ni}$) compounds synthesized at 3.5 GPa and 1123 K [55].

In addition, the lone electron pair induces cationic shifts that favour ferroelectricity: together with their magnetism, these materials are magnetoelectric, useful for multiple-memory devices (storage of information by both electric and magnetic means) or memory elements written with electric field using its ferroelectricity but read magnetically as a ferromagnetic bit. In particular, in TeNiO_3 [53] the extremely distorted crystal structure shapes a trigonal-pyramidal environment for the Te, where it is effectively coordinated to three oxygen atoms at Te–O distances of 1.92 Å (Figure 4). The 3-fold oxygen coordination is remarkably anomalous in perovskite-type structures, accounting for the required stabilization of these materials under high pressure conditions.

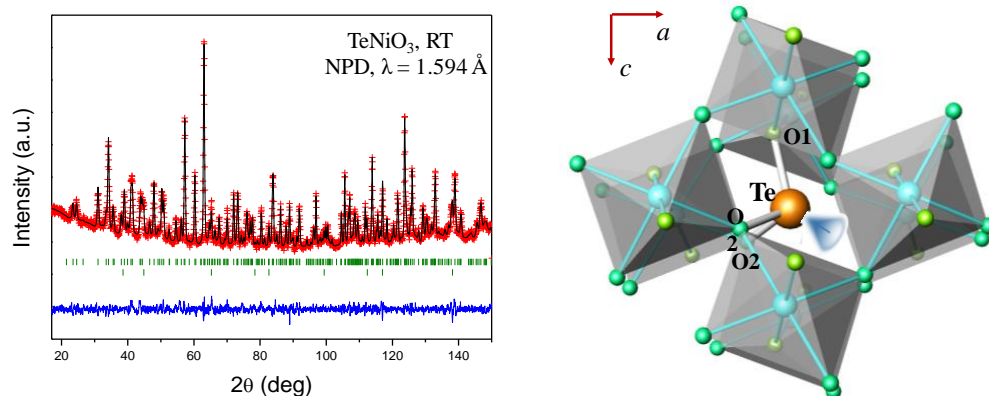


Figure 4. (Left): Neutron powder diffraction pattern of TeNiO_3 perovskite, collected at D2B diffractometer (ILL-Grenoble) from a single-batch sample obtained at 3.5 GPa. A reactive mixture of $\text{Ni}(\text{OH})_2$ and TeO_2 , contained in a sealed platinum capsule under the reaction conditions (850 °C for 2 h), was essential to succeed. (Right): the extremely distorted environment for Te^{4+} ions leaves room for the electron lone pair of this p element, schematically represented in this structural view, highlighting the tilting of NiO_6 octahedra.

3.4. Metal Hydrides

The utilization of hydrogen as energy vector in the coming decades has boosted the research and improvement of hydrogen storage procedures. Although the use of compressed hydrogen is the immediate choice in electrical vehicles, safety considerations in case of a crash advise delving into the research of the ideal hydrogen storage material, still undiscovered. A classic example of metal hydride with hydrogen storage properties is LaNi_5 and derivatives [56], able to form hydrides with composition LaNi_5H_6 . New classes of materials composed of much lighter constituents (Li, Be, B, C, N, O, Na, Mg, Al, Si, P, S) have shown a much superior hydrogen storage capacity per weight than the conventional LaNi_5 materials. Especially interesting are the Mg-based hydrides, given their high mass-storage capacity; as a drawback MgH_2 is thermally stable, with decomposition temperatures above 450 °C, which prevents applications. The destabilization of MgH_2 by doping with different metals has been an active research field in recent years.

In this line, we have been successful in preparing several derivatives of the Mg_2MH_x family ($\text{M} = \text{Fe}, \text{Co}, \text{Ni}$) [57,58] by direct reaction between the simple hydride MgH_2 and the transition metals under high-pressure conditions, in gold capsules at 2 GPa. It is worth mentioning that Mg_2FeH_6 has one of the best H mass capacity ever described, almost 6%. Figure 5 shows the crystal structure of the novel Mg_2FeH_6 hydride, where Fe is octahedrally coordinated to hydrogen atoms. Figure 5 (right) also illustrates the cyclic hydrogen release-uptake of Mg_2NiH_4 , prepared under moderate-pressure conditions.

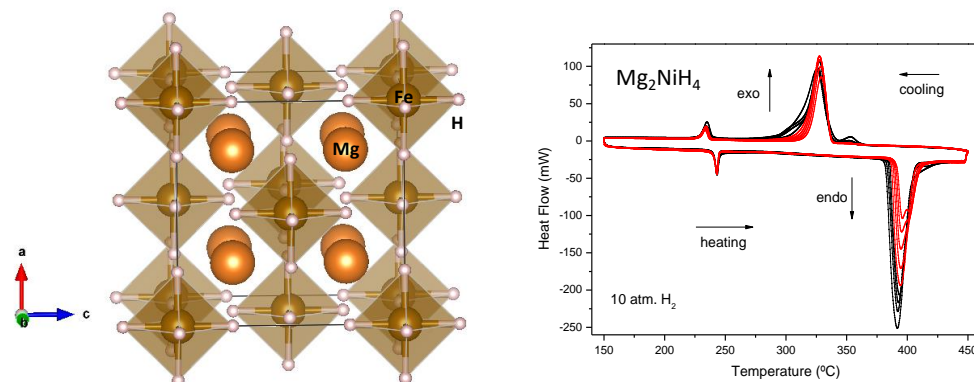


Figure 5. (Left): View of the crystal structure of Mg_2FeH_6 , where Fe is octahedrally coordinated to 6 H atoms, while Mg is in 12-fold coordination, with Mg–H distances of 2.28 Å. (Right): Cyclic DSC curves of Mg_2NiH_4 in 10 bar of H_2 at $10\text{ }^\circ\text{C min}^{-1}$, showing a reduced temperature for H release with respect to MgH_2 hydride, and a moderate reversibility. 20 cycles are shown; the endothermic peaks correspond to H_2 release, and the exothermic ones to H_2 uptake.

This success in the preparative protocol has stimulated the synthesis of novel complex hydrides by direct reaction of simple hydrides under high-pressure conditions, which prevent the thermal decomposition of the reactants: we successfully prepared new hydride perovskites, of formula $\text{Na}_{1-x}\text{Li}_x\text{H}_3$, by reaction under pressure of Na(Li)H and MgH_2 [59], as well as $\text{Na}_{1-x}\text{K}_x\text{MgH}_3$ [60]. In all these compounds, the location of H atoms, the study of the tilting of the BH_6 octahedra, the presence of H vacancies and so on are also key knowledge to interpret the sorption/desorption kinetics.

Neutron diffraction techniques were powerful (and unique) tools to localize hydrogen atoms in these hydrides; Figure 6 shows the tilting of MgH_6 octahedra in NaMgH_3 perovskite, defined in the space group $Pbnm$, and exhibiting similar topology as the standard perovskite oxides [58]. This study demonstrated that it is not strictly necessary to study deuterated samples with neutrons, given the available flux in modern reactors or spallation sources.

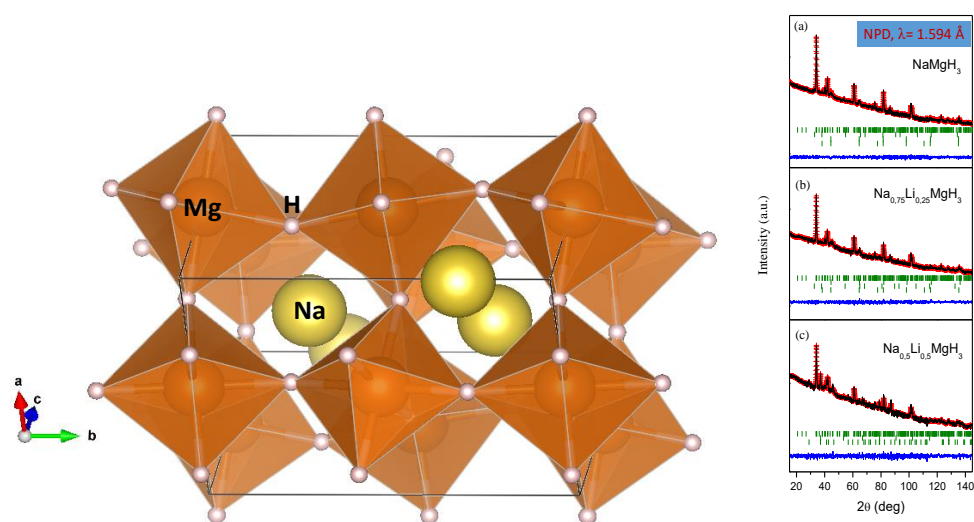


Figure 6. (Left): crystal structure of NaMgH_3 , exhibiting an orthorhombic superstructure of perovskite, space group $Pbnm$, with tilted MgH_6 octahedra. (Right): neutron diffraction patterns for $\text{Na}_{1-x}\text{Li}_x\text{MgH}_3$, displaying in the strong background the incoherent scattering of H. (a): $x = 0$; (b): $x = 0.25$; (c): $x = 0.5$.

3.5. $Tl_2Mn_2O_7$

$Tl_2Mn_2O_7$ pyrochlore, with tetravalent valence for Mn, does not seem to follow the conventional model of Double Exchange that is formally accepted for mixed-valence perovskites [61–63]; more research demonstrates that the magnetic superexchange may be mediated by the conduction electrons [64]. $Tl_2Mn_2O_7$ is among the few metal oxides that simultaneously present ferromagnetic and metallic properties. This oxide is metastable at ambient conditions, and must be prepared under high-pressure conditions, at 2 GPa. Many efforts have been made to optimize the magnetoresistive properties of this singular material, in chemically doped derivatives. In addition, under moderate pressure conditions, diverse doped series were stabilized for the first time. The Tl sublattice of this pyrochlore has been doped with Bi, Pb and Cd, exhibiting very distinct physical properties. The Mn sublattice has been, alternatively, doped with Sb, Te and Ti [65–68]. In the Bi-doped phases, $Tl_{2-x}Bi_xMn_2O_7$, with $x = 0.05, 0.1, 0.2, 0.3$ [65], the presence of competitive FM and AFM interactions gives rise to a “cluster-glass-type” behaviour, and promotes the magnetoresistance (MR) by several orders of magnitude above the undoped material. Moreover, the most spectacular results were obtained for the Cd-doped pyrochlore [66], with an MR up to $10^6\%$ at 2 K, and 20% at room temperature for magnetic field up to 0.5 T: this result has no precedents in the literature of magnetoresistive materials, and allowed proposing this material as a candidate for technological applications. Figure 7 illustrates the MR behaviour of $Tl_{2-x}Cd_xMn_2O_7$ pyrochlores, showing MR values up to 10^6 for $x = 0.2$.

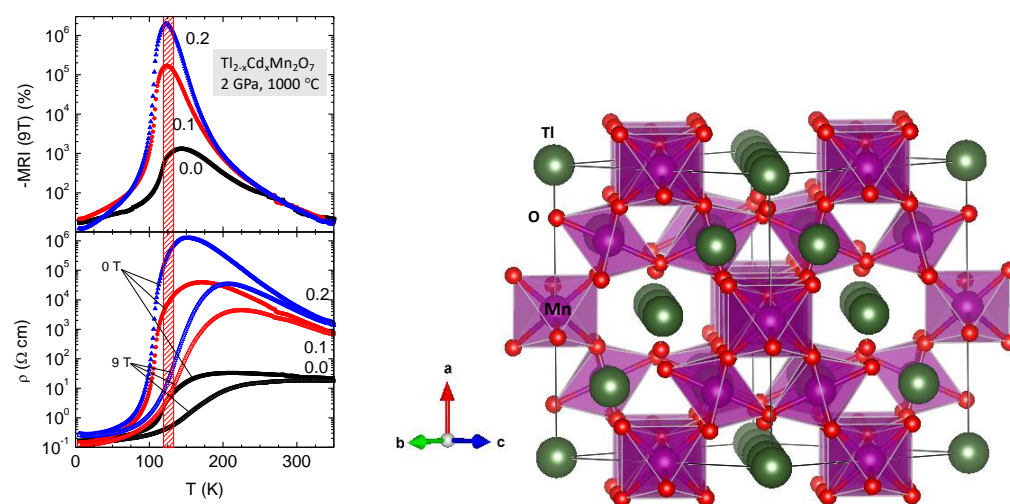


Figure 7. (Left): evolution of the magnetoresistance of the $Tl_{2-x}Cd_xMn_2O_7$ family, showing maxima coinciding with the insulator-to-metal transitions (lower panel) in the 120–140 K temperature range. (Right): Structural view of the pyrochlore structure, defined in the cubic $Fd-3m$ space group.

Also extremely interesting has been the study by neutron diffraction of the structural evolution under pressure of different doped pyrochlores, depending on the chemical nature of the different bonds, Tl–O and Mn–O, for the diverse studied families [69]. Figure 7 illustrates the crystal structure of the $Tl_2Mn_2O_7$ pyrochlore, consisting of a framework of MnO_6 octahedra sharing corners with Mn–O–Mn angles of about 133° , leaving large cages where Tl ions are located.

3.6. Skutterudites $M_xCo_4Sb_{12}$ ($M = \text{Alkali, Alkali-Earth, Rare-Earth Elements}$)

Globally, about two-thirds of energy is dissipated as waste heat, providing an important niche for thermoelectric materials (TM). TMs can directly transform a temperature difference into electric energy [70–72]. However, a good TM must possess three antagonistic properties, hindering the design and development of novel materials: it requires a high Seebeck voltage (S , thermoelectric power), low electrical resistivity (ρ) and low thermal conductivity (κ). Most materials have a coupled thermal and electronic conductivity, since the same carriers

are involved in both mechanisms to a large extent. TMs are characterized by a Figure of Merit (ZT) defined as ($ZT = S^2T/\rho\kappa$); the best ZT is around 1–2, depending on the T range. To date, the best TMs are strongly doped semiconductors such as PbTe or Bi_2Te_3 .

The possibility of preparing thermoelectric specimens under HP conditions was recently demonstrated [73–76], in particular in skutterudites. MX_3 skutterudites derive their name from Skutterud, a small town in Norway, where a mineral based on CoAs_3 was discovered in 1845, and their structure can host different transition metals (Fe, Co, Rh, Ir) at M position, and p-block semimetals (P, As, Sb) as X atoms [72]. A prominent feature is the existence of two relatively large voids that can be filled with additional atoms. Filled skutterudites contain lanthanide, or alkali-earth ions interstitially occupying these voids [77], with large thermal vibration parameters indicating that they can “rattle” or participate in a soft phonon mode of the crystal structure. This “ball in a cage” configuration of filled skutterudites directly determines the basic conditions for high ZT values. The effect of the atomic void fillers in oversized cages drastically reduces κ and thereby maximizes ZT [78,79]. The stabilization of such metastable compounds is possible, for example, for the parent, unfilled CoSb_3 pnictide, which can be successfully stabilized at 3.5 GPa, with exceptionally low thermal conductivities that were ascribed to partial Sb deficiency, the Sb vacancies acting as phonon scatterers [80]. We also stabilized $\text{La}_{1-x}\text{CoSb}_3$, with different rattling La contents, optimizing the charge carrier concentration [81], as well as Ce, Yb [82] and even with Mischmetal [83] as rattling elements (cocktail of Ce, La and other rare earths) also at 3.5 GPa. A key finding to succeed in these HP syntheses was the use of capsules made of Nb sheets, instead of the conventional Au or Pt capsules: Nb is inert with respect to Sb, and the handmade cylinders are perfectly sealed under pressure, avoiding contact with air, which would oxidize this element or the rare-earth metal fillers. There are several additional works in the literature related to the high-pressure synthesis of skutterudites, but most of them are performed at very high pressures ($\sim 6\text{--}8$ GPa) [84] or in several steps [85–88]. Figure 8 shows a view of the cubic $\text{M}_x\text{Co}_4\text{Sb}_{12}$ skutterudite structure, defined in the cubic space group $Im\bar{3}$, containing strongly rotated CoSb_6 octahedra (Co–Sb–Co $\sim 126^\circ$) that, in fact, is very similar to the $\text{CaCu}_3\text{Mn}_4\text{O}_{12}$ crystal structure (Figure 3), defined in the same space group, and also containing tilted MnO_6 octahedra. In the present case, the strong rotation in the space conforms square Sb_4 units (see Figure 8) that develop important role as traps for phonons, thus reducing the thermal conductivity.

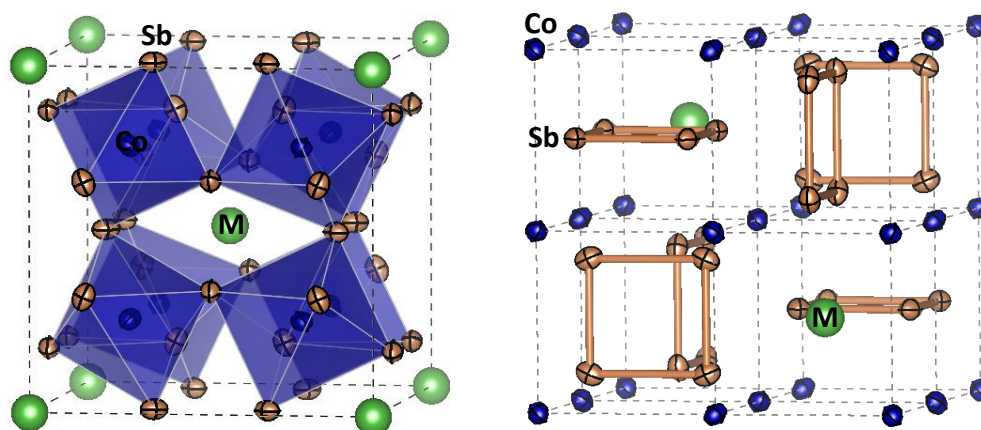


Figure 8. Two views of the skutterudite structure $\text{M}_x\text{Co}_4\text{Sb}_{12}$ (M = filler element), defined in the cubic $Im\bar{3}$ space group. The strongly tilted CoSb_6 octahedra (left view) determine the presence of Sb_4 rings (right view), of importance in the electronic properties. The M filler elements (alkali, alkali-earths, rare-earths) occupy the large 8a voids, where the rattling diminishes the thermal conductivity.

In La-filled skutterudites, it has been additionally discovered that HP reactions favour fluctuations in the filling fraction, leading to glass-like ultralow thermal conductivity in caged skutterudites [81]. This is in line with recent discoveries by ab initio calculations and synthesis of multiscale filling-fraction fluctuation in the $\text{RFe}_4\text{Sb}_{12}$ system [89]. HP

brings about the separation into phases higher and lower La filler contents, leading to multiscale strain field fluctuations. The filling fraction fluctuation reduces the lattice thermal conductivity, via strain-field scattering of high-energy phonons. This strategy of favouring the uneven filling factor under HP conditions has been extended to other elements, such as K, Sr, Y and more [90].

4. Conclusions

Moderate-pressure conditions have been demonstrated to be a powerful tool for the stabilization of metastable materials with technological applications, sometimes in combination with a pertinent choice of the reactants or by elaborating suitable precursors by wet-chemistry procedures. Systems as different as transition-metal oxides in unusual oxidation states, metal pnictides or hydrides can be accessed in substantial amounts enabling a complete characterization. Besides favouring the short bonding distances of high oxidation states in densely packed structures such as perovskites, the reactions occur in laboratory-made sealed capsules avoiding the oxidation (e.g., Sb), or volatilization (e.g., SeO₂), or decomposition (e.g., NaH, MgH₂) of certain reactants, making it possible for the desired reactions in short times and controlled atmospheres (e.g., high O₂ pressure). Those findings are to be applied in novel metastable systems as upcoming research directions: Some oxides with unusual oxidation states (e.g., Fe⁴⁺, in (Ca,Sr)FeO₃ derivatives), and novel pnictides and chalcogenides such as SnSe derivatives and MM'₂S₄ (M, M' = transition metals) thiospinels, accessible under moderate-pressure conditions, are to be exploited in the near future.

Author Contributions: Conceptualization, J.A.A., N.M.N. and J.L.M.; methodology, J.G., F.S.-S. and J.E.F.S.R.; writing—original draft preparation, J.A.A. and J.G.; writing—review and editing, N.M.N.; funding acquisition, J.A.A., N.M.N. and J.L.M. All authors have read and agreed to the published version of the manuscript.

Funding: This research was funded by the Spanish Ministry of Science, Innovation, and Universities for funding the project number: MAT2017-84496-R.

Institutional Review Board Statement: Not applicable.

Informed Consent Statement: Not applicable.

Data Availability Statement: No new data were created or analyzed in this study. Data sharing is not applicable to this article.

Acknowledgments: J.G. thanks MICINN for granting the contract: PRE2018-083398.

Conflicts of Interest: The authors declare no conflict of interest.

References

1. Goodenough, J.B.; Kafalas, J.A.; Longo, J.M. *Preparative Methods in Solid State Chemistry*; Hagenmüller, P., Ed.; Academic Press: New York, NY, USA, 1972.
2. Demazeau, G. New problems in solid-state chemistry solved by high pressure conditions: An exciting perspective for preparing new materials. *Chim. Scr.* **1988**, *28*, 21–24. [[CrossRef](#)]
3. Demazeau, G. High pressure in solid-state chemistry. *J. Phys. Condens. Matter* **2002**, *14*, 11031–11035. [[CrossRef](#)]
4. Rodgers, J.A.; Williams, A.J.; Atfield, J.P. High-pressure/High-temperature Synthesis of Transition Metal Oxide Perovskites. *Zeitschrift für Naturforschung B* **2006**, *61*, 1515–1526. [[CrossRef](#)]
5. Fauth, F.; Boer, R.; Gil-Ortiz, F.; Popescu, C.; Vallcorba, O.; Peral, I.; Fullà, D.; Benach, J.; Juanhuix, J. The crystallography stations at the Alba synchrotron. *Eur. Phys. J. Plus* **2015**, *130*, 160. [[CrossRef](#)]
6. Rodríguez-Carvajal, J. Recent advances in magnetic structure determination by neutron powder diffraction. *Phys. B Phys. Condens. Matter* **1993**, *192*, 55–69. [[CrossRef](#)]
7. Torrance, J.; Lacorre, P.; Nazzari, A.; Ansaldo, E.; Niedermayer, C. Systematic study of insulator-metal transitions in perovskites RNiO₃ (R = Pr, Nd, Sm, Eu) due to closing of charge-transfer gap. *Phys. Rev. B* **1992**, *45*, 8209–8212. [[CrossRef](#)]
8. Inaguma, Y.; Yoshida, M.; Tsuchiya, T.; Aimi, A.; Tanaka, K.; Katsumata, T.; Mori, D. High-pressure synthesis of novel lithium niobate-type oxides. *J. Phys. Conf. Ser.* **2010**, *215*, 012131. [[CrossRef](#)]
9. Ishiwata, S.; Azuma, M.; Takano, M.; Nishibori, E.; Takata, M.; Sakata, M.; Kato, K. High pressure synthesis, crystal structure and physical properties of a new Ni(ii) perovskite BiNiO₃. *J. Mater. Chem.* **2002**, *12*, 3733–3737. [[CrossRef](#)]

10. Inaguma, Y.; Katsumata, T. High Pressure Synthesis, Lattice Distortion, and Dielectric Properties of a Perovskite $\text{Bi}(\text{Ni}_{1/2}\text{Ti}_{1/2})\text{O}_3$. *Ferroelectrics* **2003**, *286*, 111–117. [[CrossRef](#)]
11. Demazeau, G.; Marbeuf, A.; Pouchard, M.; Hagenmuller, P. Sur une série de composés oxygènes du nickel trivalent dérivés de la perovskite. *J. Solid State Chem.* **1971**, *3*, 582–589. [[CrossRef](#)]
12. Alonso, J.A.; Martínez-Lope, M.J.; Casais, M.T.; Aranda, M.A.G.; Fernández-Díaz, M.T. Metal–Insulator Transitions, Structural and Microstructural Evolution of RNiO_3 (R = Sm, Eu, Gd, Dy, Ho, Y) Perovskites: Evidence for Room-Temperature Charge Disproportionation in Monoclinic HoNiO_3 and YNiO_3 . *J. Am. Chem. Soc.* **1999**, *121*, 4754–4762. [[CrossRef](#)]
13. Alonso, J.A.; García-Muñoz, J.L.; Fernández-Díaz, M.T.; Aranda, M.A.G.; Martínez-Lope, M.J.; Casais, M.T. Charge Disproportionation in RNiO_3 Perovskites: Simultaneous Metal-Insulator and Structural Transition in YNiO_3 . *Phys. Rev. Lett.* **1999**, *82*, 3871–3874. [[CrossRef](#)]
14. Alonso, J.A.; Martínez-Lope, M.J.; Casais, M.T.; García-Muñoz, J.L.; Fernández-Díaz, M.T. Room-temperature monoclinic distortion due to charge disproportionation in RNiO_3 perovskites with small rare-earth cations (R = Ho, Y, Er, Tm, Yb, and Lu): A neutron diffraction study. *Phys. Rev. B* **2000**, *61*, 1756–1763. [[CrossRef](#)]
15. Alonso, J.A.; Martínez-Lope, M.J.; Casais, M.T.; García-Muñoz, J.L.; Fernández-Díaz, M.T.; Aranda, M.A.G. High-temperature structural evolution of RNiO_3 (R = Ho, Y, Er, Lu) perovskites: Charge disproportionation and electronic localization. *Phys. Rev. B* **2001**, *64*, 094102. [[CrossRef](#)]
16. Mazin, I.I.; Khomskii, D.I.; Lengsdorf, R.; Alonso, J.A.; Marshall, W.G.; Ibberson, R.M.; Podlesnyak, A.; Martínez-Lope, M.J.; Abd-Elmeguid, M.M. Charge Ordering as Alternative to Jahn-Teller Distortion. *Phys. Rev. Lett.* **2007**, *98*, 176406. [[CrossRef](#)]
17. Presniakov, I.; Baranov, A.; Demazeau, G.; Rusakov, V.; Sobolev, A.; Alonso, J.A.; Martínez-Lope, M.J.; Pokholok, K. Evidence through Mössbauer spectroscopy of two different states for ^{57}Fe probe atoms in RNiO_3 perovskites with intermediate-size rare earths, R = Sm, Eu, Gd, Dy. *J. Phys. Condens. Matter* **2007**, *19*, 036201. [[CrossRef](#)]
18. Caytuero, A.; Micklitz, H.; Abd-Elmeguid, M.M.; Litterst, F.J.; Alonso, J.A.; Baggio-Saitovitch, E.M. Evidence for charge disproportionation in monoclinic EuNiO_3 from ^{57}Fe Mössbauer spectroscopy. *Phys. Rev. B* **2007**, *76*, 193105. [[CrossRef](#)]
19. Alonso, J.A.; Martínez-Lope, M.J.; Demazeau, G.; Fernández-Díaz, M.T.; Presniakov, I.A.; Rusakov, V.S.; Gubaidulina, T.V.; Sobolev, A.V. On the evolution of the DyNiO_3 perovskite across the metal–insulator transition through neutron diffraction and Mössbauer spectroscopy studies. *Dalton Trans.* **2008**, *46*, 6584–6592. [[CrossRef](#)] [[PubMed](#)]
20. García-Muñoz, J.L.; Aranda, M.A.G.; Alonso, J.A.; Martínez-Lope, M.J. Structure and charge order in the antiferromagnetic band-insulating phase of NdNiO_3 . *Phys. Rev. B* **2009**, *79*, 134432. [[CrossRef](#)]
21. Kumar, D.; Rajeev, K.P.; Alonso, J.A.; Martínez-Lope, M.J. Slow dynamics in hard condensed matter: A case study of the phase separating system NdNiO_3 . *J. Phys. Condens. Matter* **2009**, *21*, 185402. [[CrossRef](#)]
22. Kumar, D.; Rajeev, K.P.; Alonso, J.A.; Martínez-Lope, M.J. Evidence of kinetically arrested supercooled phases in the perovskite oxide NdNiO_3 . *J. Phys. Condens. Matter* **2009**, *21*, 485402. [[CrossRef](#)]
23. Muñoz, A.; Alonso, J.A.; Martínez-Lope, M.J.; Fernández-Díaz, M.T. On the magnetic structure of DyNiO_3 . *J. Solid State Chem.* **2009**, *182*, 1982–1989. [[CrossRef](#)]
24. Staub, U.; García-Fernández, M.; Mulders, A.M.; Bodenthin, Y.; Martínez-Lope, M.J.; Alonso, J.A. Soft x-ray resonant magnetic powder diffraction on PrNiO_3 . *J. Phys. Condens. Matter* **2007**, *19*, 092201. [[CrossRef](#)]
25. Medarde, M.; Dallera, C.; Grioni, M.; Delley, B.; Vernay, F.; Mesot, J.; Sikora, M.; Alonso, J.A.; Martínez-Lope, M.J. Charge disproportionation in RNiO_3 perovskites (R = rare earth) from high-resolution x-ray absorption spectroscopy. *Phys. Rev. B* **2009**, *80*, 245105. [[CrossRef](#)]
26. Bodenthin, Y.; Staub, U.; Piamonteze, C.; García-Fernández, M.; Martínez-Lope, M.J.; Alonso, J.A. Magnetic and electronic properties of RNiO_3 (R = Pr, Nd, Eu, Ho and Y) perovskites studied by resonant soft x-ray magnetic powder diffraction. *J. Phys. Condens. Matter* **2011**, *23*, 036002. [[CrossRef](#)]
27. Sánchez-Benítez, J.; Martínez-Lope, M.J.; Alonso, J.A.; García-Muñoz, J.L. Magnetic and structural features of the $\text{NdNi}_{1-x}\text{Mn}_x\text{O}_3$ perovskite series investigated by neutron diffraction. *J. Phys. Condens. Matter* **2011**, *23*, 226001. [[CrossRef](#)]
28. Alonso, J.A.; Martínez-Lope, M.J.; Presniakov, I.A.; Sobolev, A.V.; Rusakov, V.S.; Gapochka, A.M.; Demazeau, G.; Fernández-Díaz, M.T. Charge disproportionation in RNiO_3 (R = Tm, Yb) perovskites observed in situ by neutron diffraction and ^{57}Fe probe Mössbauer spectroscopy. *Phys. Rev. B* **2013**, *87*, 184111. [[CrossRef](#)]
29. Ramos, A.Y.; Piamonteze, C.; Tolentino, H.C.N.; Souza-Neto, N.M.; Bunau, O.; Joly, Y.; Grenier, S.; Itié, J.-P.; Massa, N.E.; Alonso, J.A.; et al. Stability of Ni sites across the pressure-induced insulator-to-metal transition in YNiO_3 . *Phys. Rev. B* **2012**, *85*, 045102. [[CrossRef](#)]
30. Kumar, D.; Rajeev, K.P.; Alonso, J.A.; Martínez-Lope, M.J. Spin-canted magnetism and decoupling of charge and spin ordering in NdNiO_3 . *Phys. Rev. B* **2013**, *88*, 014410. [[CrossRef](#)]
31. Serrano-Sánchez, F.; Fauth, F.; Martínez, J.L.; Alonso, J.A. Experimental Observation of Monoclinic Distortion in the Insulating Regime of SmNiO_3 by Synchrotron X-ray Diffraction. *Inorg. Chem.* **2019**, *58*, 11828–11835. [[CrossRef](#)]
32. Rao, C.N.R.; Raveau, B. *Colossal Magnetoresistance and Other Related Properties in 3d Oxides*; World Scientific: Singapore, 1998; ISBN 9789810232764.
33. Zeng, Z.; Greenblatt, M.; Subramanian, M.A.; Croft, M. Large Low-Field Magnetoresistance in Perovskite-type $\text{CaCu}_3\text{Mn}_4\text{O}_{12}$ without Double Exchange. *Phys. Rev. Lett.* **1999**, *82*, 3164–3167. [[CrossRef](#)]

34. Sánchez-Benítez, J.; Prieto, C.; de Andrés, A.; Alonso, J.A.; Martínez-Lope, M.J.; Casais, M.T. Evidence of two different Mn states in $\text{CaCu}_3\text{Mn}_4\text{O}_{12}$ derivatives with colossal magnetoresistance. *Phys. Rev. B* **2004**, *70*, 024419. [[CrossRef](#)]
35. Chenavas, J.; Joubert, J.C.; Marezio, M.; Bochu, B. The synthesis and crystal structure of $\text{CaCu}_3\text{Mn}_4\text{O}_{12}$: A new ferromagnetic-perovskite-like compound. *J. Solid State Chem.* **1975**, *14*, 25–32. [[CrossRef](#)]
36. Sánchez-Benítez, J.; Alonso, J.A.; Martínez-Lope, M.J.; Casais, M.T.; Martínez, J.L.; de Andrés, A.; Fernández-Díaz, M.T. Preparation, Crystal and Magnetic Structure, and Magnetotransport Properties of the Double Perovskite $\text{CaCu}_2.5\text{Mn}_{4.5}\text{O}_{12}$. *Chem. Mater.* **2003**, *15*, 2193–2200. [[CrossRef](#)]
37. Sánchez-Benítez, J.; Alonso, J.A.; Falcón, H.; Martínez-Lope, M.J.; De Andrés, A.; Fernández-Díaz, M.T. Preparation under high pressures and neutron diffraction study of new ferromagnetic $\text{RCu}_3\text{Mn}_4\text{O}_{12}$ (R = Pr, Sm, Eu, Gd, Dy, Ho, Tm, Yb) perovskites. *J. Phys. Condens. Matter* **2005**, *17*, S3063–S3068. [[CrossRef](#)]
38. Sánchez-Benítez, J.; Martínez-Lope, M.J.; Alonso, J.A. Preparation at moderate pressures, crystal and magnetic structure and magnetotransport of the ferrimagnetic $\text{CeCu}_3\text{Mn}_4\text{O}_{12}$ perovskite. *J. Appl. Phys.* **2010**, *107*, 103904. [[CrossRef](#)]
39. Sánchez-Benítez, J.; Martínez-Lope, M.J.; Alonso, J.A. Magnetism, Magnetotransport and Magnetic Structure of $\text{ThCu}_3\text{Mn}_4\text{O}_{12}$, Prepared at Moderate Pressures. *Zeitschrift für Naturforschung B* **2008**, *63*, 655–660. [[CrossRef](#)]
40. Alonso, J.A.; Sánchez-Benítez, J.; De Andrés, A.; Martínez-Lope, M.J.; Casais, M.T.; Martínez, J.L. Enhanced magnetoresistance in the complex perovskite $\text{LaCu}_3\text{Mn}_4\text{O}_{12}$. *Appl. Phys. Lett.* **2003**, *83*, 2623–2625. [[CrossRef](#)]
41. Jahn-Teller Distortions. (2020, August 15). Available online: <https://chem.libretexts.org/@go/page/519> (accessed on 8 April 2021).
42. Sánchez-Benítez, J.; Alonso, J.A.; de Andrés, A.; Martínez-Lope, M.J.; Martínez, J.L.; Muñoz, A. Peculiar Magnetic Behavior of the $\text{ThCu}_3\text{Mn}_4\text{O}_{12}$ Complex Perovskite. *Chem. Mater.* **2005**, *17*, 5070–5076. [[CrossRef](#)]
43. Sánchez-Benítez, J.; Alonso, J.A.; Martínez-Lope, M.J.; de Andrés, A.; Fernández-Díaz, M.T. Enhancement of the Curie Temperature along the Perovskite Series $\text{RCu}_3\text{Mn}_4\text{O}_{12}$ Driven by Chemical Pressure of R^{3+} Cations (R = Rare Earths). *Inorg. Chem.* **2010**, *49*, 5679–5685. [[CrossRef](#)]
44. de la Calle, C.; Sánchez-Benítez, J.; Barbanson, F.; Nemes, N.; Fernández-Díaz, M.T.; Alonso, J.A. Transition from Pauli-paramagnetism to ferromagnetism in $\text{CaCu}_3(\text{Ru}_{4-x}\text{Mn}_x)\text{O}_{12}$ ($0 \leq x \leq 3$) perovskites. *J. Appl. Phys.* **2011**, *109*, 123914. [[CrossRef](#)]
45. Subramanian, M.A.; Ramirez, A.P.; Marshall, W.J. Structural Tuning of Ferromagnetism in a 3D Cuprate Perovskite. *Phys. Rev. Lett.* **1999**, *82*, 1558–1561. [[CrossRef](#)]
46. Kimura, T.; Kawamoto, S.; Yamada, I.; Azuma, M.; Takano, M.; Tokura, Y. Magnetocapacitance effect in multiferroic BiMnO_3 . *Phys. Rev. B* **2003**, *67*, 180401. [[CrossRef](#)]
47. Belik, A.A.; Yokosawa, T.; Kimoto, K.; Matsui, Y.; Takayama-Muromachi, E. High-Pressure Synthesis and Properties of Solid Solutions between BiMnO_3 and BiScO_3 . *Chem. Mater.* **2007**, *19*, 1679–1689. [[CrossRef](#)]
48. Toulemonde, P.; Darie, C.; Goujon, C.; Legendre, M.; Mendonca, T.; Álvarez-Murga, M.; Simonet, V.; Bordet, P.; Bouvier, P.; Kreisel, J.; et al. Single crystal growth of BiMnO_3 under high pressure–high temperature. *High Press. Res.* **2009**, *29*, 600–604. [[CrossRef](#)]
49. Montanari, E.; Righi, L.; Calestani, G.; Migliori, A.; Gilioli, E.; Bolzoni, F. Room Temperature Polymorphism in Metastable BiMnO_3 Prepared by High-Pressure Synthesis. *Chem. Mater.* **2005**, *17*, 1765–1773. [[CrossRef](#)]
50. Goodenough, J.B. *Magnetism and the Chemical Bond*; Interscience-Wiley: New York, NY, USA, 1963.
51. Muñoz, A.; Alonso, J.A.; Martínez-Lope, M.J.; Morán, E.; Escamilla, R. Synthesis and study of the crystallographic and magnetic structure of SeCoO_3 . *Phys. Rev. B* **2006**, *73*, 104442. [[CrossRef](#)]
52. Muñoz, A.; Alonso, J.A.; Martínez-Lope, M.J.; Falcón, H.; García-Hernández, M.; Morán, E. High-pressure synthesis and study of the crystal and magnetic structure of the distorted SeNiO_3 and SeMnO_3 perovskites. *Dalton Trans.* **2006**, *41*, 4936–4943. [[CrossRef](#)]
53. Martínez-Lope, M.J.; Retuerto, M.; Alonso, J.A.; Sánchez-Benítez, J.; Fernández-Díaz, M.T. High-pressure synthesis and neutron diffraction investigation of the crystallographic and magnetic structure of TeNiO_3 perovskite. *Dalton Trans.* **2011**, *40*, 4599. [[CrossRef](#)]
54. Ridley, C.J.; Knight, K.S.; Wilson, C.W.; Smith, R.I.; Bull, C.L. Structure and physical properties of $\text{SeCo}_{1-x}\text{Mn}_x\text{O}_3$. *J. Phys. Condens. Matter* **2019**, *31*, 395402. [[CrossRef](#)] [[PubMed](#)]
55. Cabuk, S. Magnetic, electronic and mechanical properties of SeXO_3 (X = Mn, Ni) with the LSDA + U framework. *J. Alloys Compd.* **2021**, *850*, 156674. [[CrossRef](#)]
56. Liang, G.; Huot, J.; Schulz, R. Hydrogen storage properties of the mechanically alloyed LaNi_5 -based materials. *J. Alloys Compd.* **2001**, *320*, 133–139. [[CrossRef](#)]
57. Retuerto, M.; Sánchez-Benítez, J.; Alonso, J.A.; Leardini, F.; Ares, J.R.; Fernández, J.F.; Sánchez, C. Deuteration properties of $\text{CaNi}_{5-x}\text{Cu}_x$ system. *J. Power Sources* **2011**, *196*, 4342–4346. [[CrossRef](#)]
58. Martínez-Coronado, R.; Retuerto, M.; Torres, B.; Martínez-Lope, M.J.; Fernández-Díaz, M.T.; Alonso, J.A. High-pressure synthesis, crystal structure and cyclability of the Mg_2NiH_4 hydride. *Int. J. Hydrogen Energy* **2013**, *38*, 5738–5745. [[CrossRef](#)]
59. Martínez-Coronado, R.; Sánchez-Benítez, J.; Retuerto, M.; Fernández-Díaz, M.T.; Alonso, J.A. High-pressure synthesis of $\text{Na}_{1-x}\text{Li}_x\text{MgH}_3$ perovskite hydrides. *J. Alloys Compd.* **2012**, *522*, 101–105. [[CrossRef](#)]
60. Andrada-Chacón, A.; Alonso, J.A.; Pomjakushin, V.; Sánchez-Benítez, J. High-pressure synthesis and structural characterization of $\text{Na}_{1-x}\text{K}_x\text{MgH}_3$ perovskite hydrides. *J. Alloys Compd.* **2017**, *729*, 914–920. [[CrossRef](#)]
61. Shimakawa, Y.; Kubo, Y.; Manako, T. Giant magnetoresistance in $\text{Ti}_2\text{Mn}_2\text{O}_7$ with the pyrochlore structure. *Nature* **1996**, *379*, 53–55. [[CrossRef](#)]

62. Subramanian, M.A.; Toby, B.H.; Ramirez, A.P.; Marshall, W.J.; Sleight, A.W.; Kwei, G.H. Colossal Magnetoresistance Without Mn^{3+}/Mn^{4+} Double Exchange in the Stoichiometric Pyrochlore $Tl_2Mn_2O_7$. *Science* **1996**, *273*, 81–84. [[CrossRef](#)]
63. Shimakawa, Y.; Kubo, Y.; Hamada, N.; Jorgensen, J.D.; Hu, Z.; Short, S.; Nohara, M.; Takagi, H. Crystal structure, magnetic and transport properties, and electronic band structure of $A_2Mn_2O_7$ pyrochlores ($A = Y, In, Lu$ and Tl). *Phys. Rev. B* **1999**, *59*, 1249–1254. [[CrossRef](#)]
64. Núñez-Regueiro, M.D.; Lacroix, C. Origin and pressure dependence of ferromagnetism in $A_2Mn_2O_7$ pyrochlores ($A = Y, In, Lu$ and Tl). *Phys. Rev. B* **2000**, *63*, 014417. [[CrossRef](#)]
65. Alonso, J.A.; Martínez, J.L.; Martínez-Lope, M.J.; Casais, M.T.; Fernández-Díaz, M.T. Room Temperature Magnetoresistance and Cluster-Glass Behavior in the $Tl_{2-x}BixMn_2O_7$ ($0 \leq x \leq 0.5$) pyrochlore series. *Phys. Rev. Lett.* **1999**, *82*, 189–192. [[CrossRef](#)]
66. Alonso, J.A.; Velasco, P.; Martínez-Lope, M.J.; Casais, M.T.; Martínez, J.L.; Fernández-Díaz, M.T.; de Paoli, J.M. Unprecedented magnetoresistance in Cd-substituted $Tl_2Mn_2O_7$ pyrochlores. *Appl. Phys. Lett.* **2000**, *76*, 3274–3276. [[CrossRef](#)]
67. Alonso, J.A.; Martínez-Lope, M.J.; Casais, M.T.; Velasco, P.; Martínez, J.L.; Fernández-Díaz, M.T.; de Paoli, J.M. Enhancement of ferromagnetic coupling in Sb-substituted $Tl_2Mn_2O_7$ pyrochlores. *Phys. Rev. B* **1999**, *60*, R15024–R15027. [[CrossRef](#)]
68. Alonso, J.A.; Martínez-Lope, M.J.; Casais, M.T.; Martínez, J.L.; Fernández-Díaz, M.T. Large Increase in Magnetoresistance and Cluster-Glass Behavior in Defect $Tl_{2-x}Mn_2O_{7-y}$ Pyrochlores. *Chem. Mater.* **2000**, *12*, 1127–1133. [[CrossRef](#)]
69. Velasco, P.; Alonso, J.A.; Tissen, V.G.; Marshall, W.G.; Casais, M.T.; Martínez-Lope, M.J.; de Andrés, A.; Prieto, C.; Martínez, J.L. Pressure effect in the structure, transport properties, and magnetic interactions of $Tl_2Mn_2O_7$ pyrochlores derivatives. *Phys. Rev. B* **2003**, *67*, 104403. [[CrossRef](#)]
70. Li, J.-F.; Liu, W.-S.; Zhao, L.-D.; Zhou, M. High-performance nanostructured thermoelectric materials. *NPG Asia Mater.* **2010**, *2*, 152–158. [[CrossRef](#)]
71. Snyder, G.J.; Toberer, E.S. Complex thermoelectric materials. *Nat. Mater.* **2008**, *7*, 105–114. [[CrossRef](#)]
72. Nolas, G.S.; Morelli, D.T.; Tritt, T.M. SKUTTERUDITES: A Phonon-Glass-Electron Crystal Approach to Advanced Thermoelectric Energy Conversion Applications. *Annu. Rev. Mater. Sci.* **1999**, *29*, 89–116. [[CrossRef](#)]
73. Serrano, F.; Gharsallah, M.; Cherif, W.; Martínez, J.L.; Cascos, V.; Troncoso, L.; Alonso, J.A. Facile Preparation of State-of-the Art Thermoelectric Materials by High-pressure Synthesis. *Mater. Today Proc.* **2015**, *2*, 661–668. [[CrossRef](#)]
74. Li, X.; Zhang, Q.; Kang, Y.; Chen, C.; Zhang, L.; Yu, D.; Tian, Y.; Xu, B. High pressure synthesized Ca-filled $CoSb_3$ skutterudites with enhanced thermoelectric properties. *J. Alloys Compd.* **2016**, *677*, 61–65. [[CrossRef](#)]
75. Kang, Y.; Yu, F.; Chen, C.; Zhang, Q.; Sun, H.; Zhang, L.; Yu, D.; Tian, Y.; Xu, B. High pressure synthesis and thermoelectric properties of Ba-filled $CoSb_3$ skutterudites. *J. Mater. Sci. Mater. Electron.* **2017**, *28*, 8771–8776. [[CrossRef](#)]
76. Yang, J.; Zhang, L.; Liu, Y.; Chen, C.; Li, J.; Yu, D.; He, J.; Liu, Z.; Tian, Y.; Xu, B. Investigation of skutterudite $MgyCo_4Sb_{12}$: High pressure synthesis and thermoelectric properties. *J. Appl. Phys.* **2013**, *113*, 113703. [[CrossRef](#)]
77. Slack, G.A. *CRC Handbook of Thermoelectrics*; Rowe, D.M., Ed.; CRC Press: Boca Raton, FL, USA, 1995; ISBN 0849301467.
78. Rull-Bravo, M.; Moure, A.; Fernández, J.F.; Martín-González, M. Skutterudites as thermoelectric materials: Revisited. *RSC Adv.* **2015**, *5*, 41653–41667. [[CrossRef](#)]
79. Liu, Z.-Y.; Zhu, J.-L.; Tong, X.; Niu, S.; Zhao, W.-Y. A review of $CoSb_3$ -based skutterudite thermoelectric materials. *J. Adv. Ceram.* **2020**, *9*. [[CrossRef](#)]
80. Prado-Gonjal, J.; Serrano-Sánchez, F.; Nemes, N.M.; Dura, O.J.; Martínez, J.L.; Fernández-Díaz, M.T.; Fauth, F.; Alonso, J.A. Extra-low thermal conductivity in unfilled $CoSb_3$ - δ skutterudite synthesized under high-pressure conditions. *Appl. Phys. Lett.* **2017**, *111*, 1–6. [[CrossRef](#)]
81. Serrano-Sánchez, F.; Prado-Gonjal, J.; Nemes, N.M.; Biskup, N.; Varela, M.; Dura, O.J.; Martínez, J.L.; Fernández-Díaz, M.T.; Fauth, F.; Alonso, J.A. Low thermal conductivity in La-filled cobalt antimonide skutterudites with an inhomogeneous filling factor prepared under high-pressure conditions. *J. Mater. Chem. A* **2017**, *6*, 118–126. [[CrossRef](#)]
82. Serrano-Sánchez, F.; Prado-Gonjal, J.; Nemes, N.M.; Biskup, N.; Dura, O.J.; Martínez, J.L.; Fernández-Díaz, M.T.; Fauth, F.; Alonso, J.A. Thermal Conductivity Reduction by Fluctuation of the Filling Fraction in Filled Cobalt Antimonide Skutterudite Thermoelectrics. *ACS Appl. Energy Mater.* **2018**, *1*, 6181–6189. [[CrossRef](#)]
83. Gainza, J.; Serrano-Sánchez, F.; Prado-Gonjal, J.; Nemes, N.M.; Biskup, N.; Dura, O.J.; Martínez, J.L.; Fauth, F.; Alonso, J.A. Substantial thermal conductivity reduction in mischmetal skutterudites $Mm_xCo_4Sb_{12}$ prepared under high-pressure conditions, due to uneven distribution of the rare-earth elements. *J. Mater. Chem. C* **2019**, *7*, 4124–4131. [[CrossRef](#)]
84. Takizawa, H.; Okazaki, K.; Uheda, K.; Endo, T.; Nolas, G.S. High Pressure Synthesis of New Filled Skutterudites. *MRS Proc.* **2001**, *691*, G2.3. [[CrossRef](#)]
85. Liu, Y.; Li, X.; Zhang, Q.; Zhang, L.; Yu, D.; Xu, B.; Tian, Y. High Pressure Synthesis of p-Type $CeyFe_{4-x}Co_xSb_{12}$ Skutterudites. *Materials* **2016**, *9*, 257. [[CrossRef](#)] [[PubMed](#)]
86. Zhao, P.; Sun, H.; Yu, F.; Wang, B.; Zhao, H.; Wang, D.; Yu, D.; Tian, Y.; Xu, B. Thermoelectric performance of p-type $CaFe_{1.3}Co_{2.7}Sb_{12}$ skutterudites from high pressure synthesis. *J. Alloys Compd.* **2021**, *851*, 156928. [[CrossRef](#)]
87. Zhang, J.; Xu, B.; Wang, L.-M.; Yu, D.; Yang, J.; Yu, F.; Liu, Z.; He, J.; Wen, B.; Tian, Y. High-pressure synthesis of phonon-glass electron-crystal featured thermoelectric $LixCo_4Sb_{12}$. *Acta Mater.* **2012**, *60*, 1246–1251. [[CrossRef](#)]
88. Chen, C.; Zhang, L.; Li, J.; Yu, F.; Yu, D.; Tian, Y.; Xu, B. Enhanced thermoelectric performance of lanthanum filled $CoSb_3$ synthesized under high pressure. *J. Alloys Compd.* **2017**, *699*, 751–755. [[CrossRef](#)]

-
89. Ren, W.; Geng, H.; Zhang, Z.; Zhang, L. Filling-Fraction Fluctuation Leading to Glasslike Ultralow Thermal Conductivity in Caged Skutterudites. *Phys. Rev. Lett.* **2017**, *118*, 1–6. [[CrossRef](#)] [[PubMed](#)]
 90. Gainza, J.; Serrano-Sánchez, F.; Rodrigues, J.E.; Prado-Gonjal, J.; Nemes, N.M.; Biskup, N.; Dura, O.J.; Martínez, J.L.; Fauth, F.; Alonso, J.A. Unveiling the Correlation between the Crystalline Structure of M-Filled CoSb₃ (M = Y, K, Sr) Skutterudites and Their Thermoelectric Transport Properties. *Adv. Funct. Mater.* **2020**, *30*, 2001651. [[CrossRef](#)]

Review

In Situ High-Pressure Synthesis of New Outstanding Light-Element Materials under Industrial P-T Range

Yann Le Godec ^{1,*} and Alexandre Courac ^{1,2}

¹ Institut de Minéralogie, de Physique des Matériaux et de Cosmochimie (IMPMC), Sorbonne Université, UMR CNRS 7590, Muséum National d'Histoire Naturelle, IRD UMR 206, 75005 Paris, France; alexandre.courac@sorbonne-universite.fr

² Institut Universitaire de France, IUF, 75005 Paris, France

* Correspondence: yann.le_godec@sorbonne-universite.fr

Abstract: High-pressure synthesis (which refers to pressure synthesis in the range of 1 to several GPa) adds a promising additional dimension for exploration of compounds that are inaccessible to traditional chemical methods and can lead to new industrially outstanding materials. It is nowadays a vast exciting field of industrial and academic research opening up new frontiers. In this context, an emerging and important methodology for the rapid exploration of composition-pressure-temperature-time space is the in situ method by synchrotron X-ray diffraction. This review introduces the latest advances of high-pressure devices that are adapted to X-ray diffraction in synchrotrons. It focuses particularly on the “large volume” presses (able to compress the volume above several mm³ to pressure higher than several GPa) designed for in situ exploration and that are suitable for discovering and scaling the stable or metastable compounds under “traditional” industrial pressure range (3–8 GPa). We illustrated the power of such methodology by (i) two classical examples of “reference” superhard high-pressure materials, diamond and cubic boron nitride c-BN; and (ii) recent successful in situ high-pressure syntheses of light-element compounds that allowed expanding the domain of possible application high-pressure materials toward solar optoelectronic and infrared photonics. Finally, in the last section, we summarize some perspectives regarding the current challenges and future directions in which the field of in situ high-pressure synthesis in industrial pressure scale may have great breakthroughs in the next years.

Keywords: high pressure; synthesis; in situ; X-ray diffraction; synchrotron



Citation: Le Godec, Y.; Courac, A. In Situ High-Pressure Synthesis of New Outstanding Light-Element Materials under Industrial P-T Range. *Materials* **2021**, *14*, 4245. <https://doi.org/10.3390/ma14154245>

Academic Editor: Dirk Lehmkus

Received: 15 June 2021

Accepted: 19 July 2021

Published: 29 July 2021

Publisher's Note: MDPI stays neutral with regard to jurisdictional claims in published maps and institutional affiliations.



Copyright: © 2021 by the authors. Licensee MDPI, Basel, Switzerland. This article is an open access article distributed under the terms and conditions of the Creative Commons Attribution (CC BY) license (<https://creativecommons.org/licenses/by/4.0/>).

1. Introduction

Achieving sustainable growth on a finite planet is a challenge of this century. The needs of societies are changing rapidly and the role of new smart materials in ensuring such transformations is paramount. This challenge requires new kind of materials and, for this, new unexplored dimensions for materials synthesis. As shown by the pioneering study of the Nobel prize-winning Bridgman [1,2], «pressure» opens up an additional dimension, both for the synthesis of new classes of materials with outstanding properties, and for «pressure tuning» physico-chemical features to understand the relationships between structure and the resulting properties. This new dimension has generated great enthusiasm recently because the changes in chemical bonds and properties induced by pressure surpass those due to temperature or even chemical substitution. Hence, the pressure can completely overpass the expectations of traditional chemistry and the potential of high-pressure synthesis is thus immense.

From a fundamental point of view, as an intensive thermodynamic parameter, pressure has a tremendous effect on materials synthesis. Shear stresses, produced during strongly non-equilibrium (and non-hydrostatic) compression, can also be interesting for materials design, although they do not allow getting reliable well-crystallized solids and have not been studied so far in situ using large-volume apparatuses. Pressure can play a

crucial role in: (1) preventing the decomposition of thermally unstable chemical precursors; (2) enhancing chemical reactivity and hence decreasing synthesis temperature or reaction time; (3) strengthening chemical bonds and promoting new dense crystal structures.

Such modifications have proven promising in the formation of a large variety of new inorganic compounds with outstanding properties, which are currently unattainable through any other conventional methods. High pressure as an effective industrial technology emerged in the 1950s of the past century after the synthesis of artificial diamond [3,4]—the hardest known material—and the discovery of superhard cubic boron nitride c-BN [5], synthesized a couple of years later. Since the success of these pioneering studies, high-pressure synthesis promoted a large number of new classes of materials with outstanding properties, recoverable at ambient conditions. The most remarkable are: (1) new superhard phases [6] with electrical conductivity like c-BC₅ [7] or even with non-carbon composition—like nanostructured phases of c-BN [8,9] and high pressure boron allotrope γ -B [10]; (2) new multiferroic materials (like BiMnO₃, BiAlO₃, BiGaO₃, BiFeO₃ [11]); (3) new thermoelectric compounds (silicon clathrates [12] or CoSb_{2.75}Te_{0.20}Sn_{0.05} [13]); (4) original semiconductors (e.g., open-framework silicon allotrope Si₂₄ [14]); (5) novel energy storage materials (e.g., magnesium carbides [15,16] or polymerized CO compound [17]); and (6) new superconductors (Ba-based silicon clathrates and clathrate-like carbon-framework analogues [12,18,19] or a series of new iron (nickel)-based compounds [20]). All these materials, which are impossible or very difficult to synthesize by conventional-chemistry methods, have great values for potential technological applications.

In the past century, the design of a new material using high pressure and high temperature (HP-HT)—like artificial diamond—required many years of intensive experimental work of academic or industrial research institutes. Nowadays, a couple years of research can be sufficient to propose and optimize a new high-pressure material with its full physical characterizations. If the characterization methods of materials science are basically the same, what has changed during the last years is the possibility to probe the transformations in the chemical systems by in situ X-ray probes using synchrotron radiation such as X-ray diffraction (XRD). Actually, synchrotron sources are necessary because X-rays generated by these facilities are characterized by very high flux and brilliance (about 10¹³ and 10¹⁵ times higher in 3rd and 4th generation synchrotrons respectively than in X-ray conventional laboratory set-ups) that allows X-rays passing through the high-pressure assemblies and to perform X-ray diffraction in real time during HP-HT experiments

Such in situ HP-HT probing overcomes the intrinsic limitations of the last century ex situ ‘cook and look’ time-consuming methodology. The real-time observation of the precursor evolution has become essential. It allows to find (and optimize) the (P,T) conditions required for the synthesis by tackling the mechanisms and the kinetics of structural and chemical changes.

Two directions are actually developing for high-pressure design of new crystalline materials. One consists of exploring very high pressures beyond the industrial limits ($P > 20$ GPa) in order to reach significantly unusual solids (for example room temperature superconductor [21], or polymerization of CaC₂ [22]) that would allow understanding the links between advanced properties and crystal structure/composition, which we will not consider in this paper. Another methodological approach, more pragmatic but still promising, consists of the in situ exploration of “traditional” industrial pressure scale for the design of new stable or metastable compounds by also playing with kinetics (e.g., for nanostructuring) and nucleation-growth mechanism for phase selection [23]. Fixing this “industrial limit” to 20 GPa, what we are actually doing in this review, is quite challenging, but it remains industrially accessible, for example, in advanced technology of production of sintered nanodiamond with advanced mechanical and optical properties [24]. This “industrial limit” justifies our focus on large volume presses technologies (designed for in situ X-ray diffraction) where sufficient amounts of a high-pressure material can be produced and, hence, commercialized.

Additionally, to meet the challenge of sustainable growth it is obvious that the new materials designed by high-pressure synthesis should be composed by the most immediately available chemical elements in the Earth's crust. It is interesting to note that more than 99% of the atoms that we can find on the surface of the Earth are necessarily included in a shortlist of 10 light elements which are (approximate % by weight) [25]: oxygen (46.6%), silicon (27.7%), aluminum (8.1%), iron (5.0%), calcium (3.6%), magnesium (2.1%), sodium (2.8%), potassium (2.6%), titanium (0.6%), and carbon (0.2%). That is why in this review, we aim to focus on recent examples of new light compounds (composed mainly with the light elements aforementioned) synthesized recently under high pressure by the assistance of in situ X-ray diffraction with synchrotron radiation.

This paper is organized as follows. In Section 2, we will provide an in-time comprehensive review of the recent advances in the development of high-pressure devices which are adapted to X-ray diffraction in many beamlines of synchrotrons, so that the non-specialist readers can get a clear idea of the methods widely employed at present time. The use of these devices in the last twenty years for exploring new materials has led to new successful in situ high-pressure syntheses of light-element compounds that are presented in Section 3. Finally, some perspectives regarding the current challenges and future directions are given in Section 4. The materials syntheses described in our review principally concern (quasi-) hydrostatic synthesis conditions that allows producing well-crystallized powders and crystals (at high temperatures, melt or supercritical fluid form at each synthesis described).

2. Methods

There is a wide range of means to generate static HP-HT conditions for synthesis under extreme conditions (here under "static" we understand those that can be maintained from few minutes to few weeks). Typically, heating does not create significant problems for in situ studies, so we will not discuss it in detail, while creation of high pressure does. The majority of HP devices are based on the same principle: the force needed to generate high pressure is created by the application of a primary pressure, from a few tens to several thousand bars, on the piston's surface of a hydraulic or pneumatic press. Applied on (at least) 2 anvils, this force is transmitted on the experimental assembly, including a gasket, the chemical precursors, and most often a pressure-transmitting medium. The surface of this assembly is much smaller than the surface of the piston on which the primary pressure is applied, this has the effect of generating a pressure multiplied on the sample according to the "principle of intensification". If this principle is general, however, this type of device can fall into two main categories, according to the sample volume brought under high pressure: diamond anvil cells (DAC) and large volume devices.

2.1. Diamond Anvil Cell

The DAC is a compact opposed-anvils device, used as early as 1959 [26], and typically measuring only ~60 mm in diameter for a weight of a few hundred grams (more details and schematic drawings can be found in ref. [27]). It can generate pressure of around 100 GPa routinely and at most 600 GPa (with the risk of irreversible breakage of diamonds at decompression). The principle of a DAC is simple: it involves compressing the sample, previously placed in a hard metallic gasket (general case), between the truncated ends (culets) of a pair of opposite diamonds. For this, one of the diamonds is placed on the fixed body of the cell, in which a moving piston is adjusted and driven by a primary force, together with second mounted-on diamond. The experimental volume is therefore reduced to the hole in the metallic gasket (typically around a hundred microns in diameter or 1/3 of culet diameter), in which the sample, the pressure gauge, and a pressure transmitting medium are housed. The pressure is typically measured by visible fluorescence of a known standard (e.g., ruby [28]); alternative methods can also be used (e.g., P-V equations of state or piezospectroscopic methods [29]). The heating of the sample inside DAC (unfortunately, together with diamonds) may be provided by resistive furnaces surrounding the diamonds

for temperatures below 1200 K. To reach higher temperatures (up to 7000 K), mainly the beam of a powerful infrared laser (YAG or CO₂) is used. Temperature measurement is usually done by thermocouple (for resistive heating) or optical pyrometer (above 1500 K). The main advantages of a diamond anvil cell are, in addition to the ability of obtaining very high pressures and temperatures, the transparency of the diamonds which, with its small size, allows the device to be adapted to a wide variety of structural and spectroscopic techniques. In particular, DAC is widely used for academic in situ studies by X-ray diffraction of synchrotron radiation on the synthesis of new room-temperature superconducting materials (for example, carbonaceous sulfur hydride above 200 GPa [21]) or novel high-energy-density materials beyond 40 GPa (for example LiN₅ [30]).

Nevertheless, DAC also presents a major drawback for synthesis experiments because the sample volume studied (and especially recovered) is tiny (of the order of 10⁻⁵ mm³), which in principle prohibits any very advanced physical and chemical characterization. Additionally, no reliable study of interactions in mixtures and construction of binary phase diagram is possible. Obtaining very high temperatures under high pressure is particularly difficult, because of the unavoidable high thermal gradients even in the case of very small sample volumes. In addition, chemical reactions (under such extreme pressures and temperatures) with the metallic gasket or the pressure-transmitting medium, as well as carbon diffusion from diamond, are quite frequent, making the exploitation of the results very complicated. Finally, the use of precursor samples of fine chemistry and/or of overly complex properties (e.g., solvent synthesis) is technically quasi-impossible in DAC. Any industrial perspective of a DAC synthesis is still challenging to consider. Thus far in situ DAC synthesis research, although of great fundamental interest, is limited to “exotic” materials under very high pressures, beyond the “industrial limit” situated at ~20 GPa.

2.2. Large Volume Devices

Large volume presses (LVP) are already widely used in the industrial environment, and they are constantly developing in several countries, particularly in China at the present time. LVPs (more details can be found in reviews [31,32]) are able to compress few-millimeter samples (and larger) to pressures beyond 1 GPa. Some of these devices are only suitable for ex situ experiments because their sample/reaction-volume environment is opaque to X-rays (piston-cylinder, Belt, Bridgman or Drickamer apparatus), whereas multi-anvil and Paris–Edinburgh cell (Cf. Section 2.2.3) devices have been mainly (re)designed and used during these last few years in conjunction with in situ X-ray diffraction studies at synchrotron facilities.

2.2.1. Multi-Anvil Devices

Multi-anvil presses (MAP) are generally classified according to the number of anvils they use and therefore depend on the shape of the polyhedral space in which the pressure transmitting medium is inserted. Thus, the tetrahedral, cubic, and octahedral presses have 4, 6, and 8 anvils, respectively. When the anvils are brought together, they apply a more “hydrostatic” pressure (in fact, in contrast to uniaxial DAC compression, in the case of MAP the compression is homogeneous in all three space directions) on the pressure-transmitting medium. This allows generating the highest pressure inside the sample assembly (typically of cylindrical shape), i.e., in the reaction volume where synthesis occurs.

The anvils can be driven either by an individual ram or by using guide blocks and applying uniaxial pressure. MAPs generally use automatic pumps to control primary pressure on one or more hydraulic rams which will effectively compress the anvils. Since the force must be sufficient, given the size of these anvils, large presses weighing several tons must be used. The first multi-anvil devices were developed in the middle of the 20th century with pioneering Hall’s tetrahedral MAP in 1958, with four hydraulic rams [33]. Later, von Platen developed a cubic device with spherical anvils submerged in oil [34], while Kawai was the first to propose an octahedral device [35]. The Kawai-type press was then greatly improved, first by introducing a new two-stage compression [36]: the

octahedral pressure medium was inserted into an assembly of eight tungsten carbide (WC) cubes pressed by six primary anvils. In 1990, Walker et al. [37] simplified the first compression stage by introducing the removable “hatbox design”, allowing ordinary presses to be converted into MAPs. Such a type of multi-anvil module is called Walker’s module. The two-stage compression design and Kawai octahedral HP cells can also be used in cubic devices of the DIA type devices, i.e., when the force on the WC-cube assembly is applied by six primary anvils.

Nowadays, the most commonly used MAPs are DIA and Walker types. Figure 1 shows a schematic view and the differences of both press geometries.

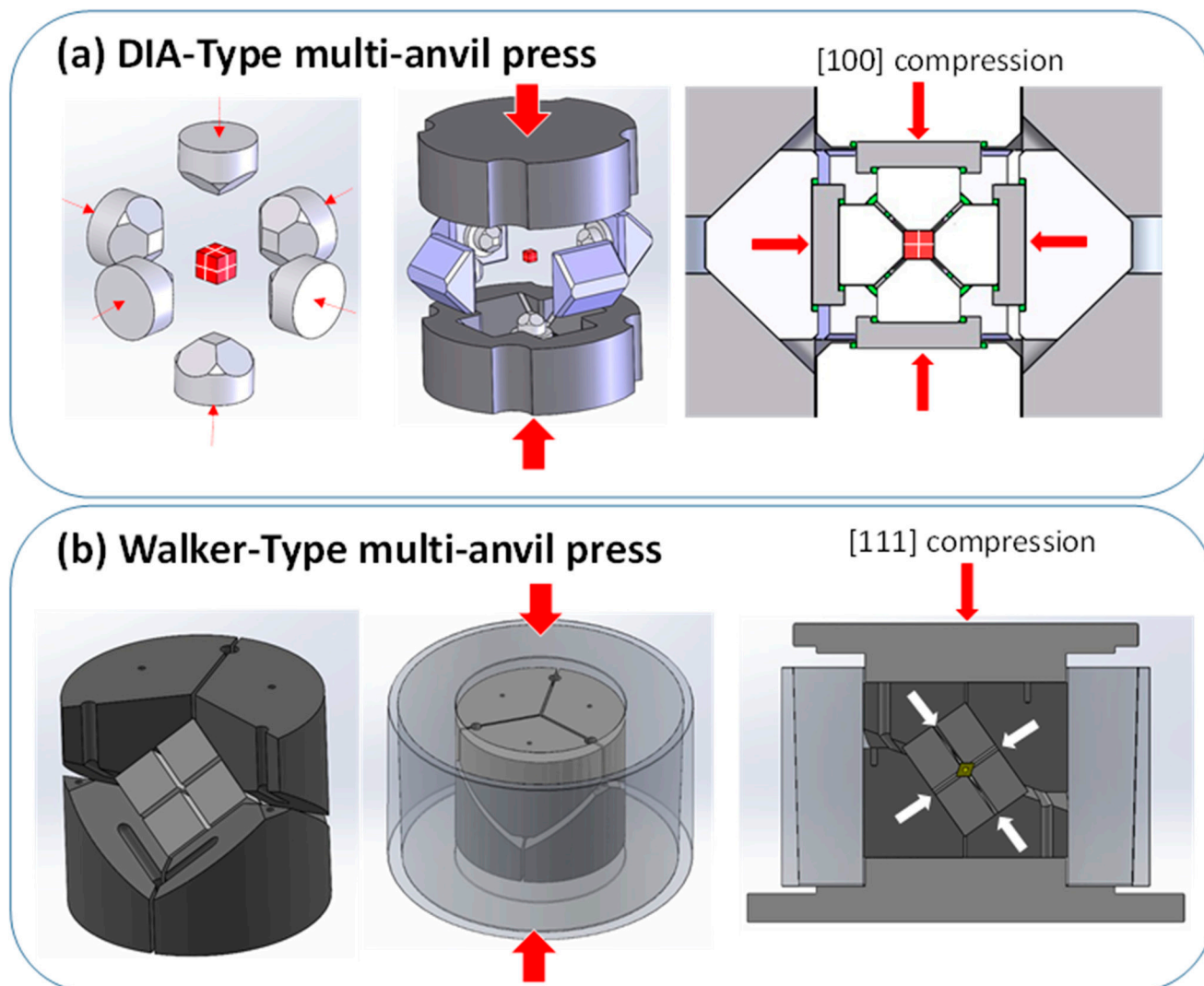


Figure 1. (a) Schematic view of the DIA geometry, in which the compression of the primary anvils takes place along the [001] directions of cubic assemblage of secondary WC cubic anvils. (b) Schematic view of the Walker geometry, in which the primary anvils are inserted in a cylindrical vessel and the primary compression happens along the [111] direction of the WC-cubes secondary-anvil assembly.

Both MAP have double anvils stage arrangement: primary and secondary anvils. Convention is that we count the stages from “outside”, which means that the outer six hard-steel anvils are called primary anvils, whereas the eight cubes are secondary anvils. The Walker’s module has a cylindrical cavity filled with the six hard steel primary anvils, three facing up and three facing down. These 6 anvils form a cubic cavity dedicated for the secondary anvils. On the contrary, in the DIA module, there is no cylinder and the first stage anvils consists of four independent moveable equatorial anvils and bottom and

top anvils (Cf. Figure 1) that apply forces perpendicular to the cube's surfaces. Hence, the main difference between the DIA and the Walker MAP module stands in the orientation of the cubic cavity in relation to compression axis, i.e., the [111] direction of the cube in the Walker module, and the [100] in the DIA one. The second stage of compression in both the DIA and Walker MAP is a set of eight cubes with truncated interior corners (Cf. Figure 2).

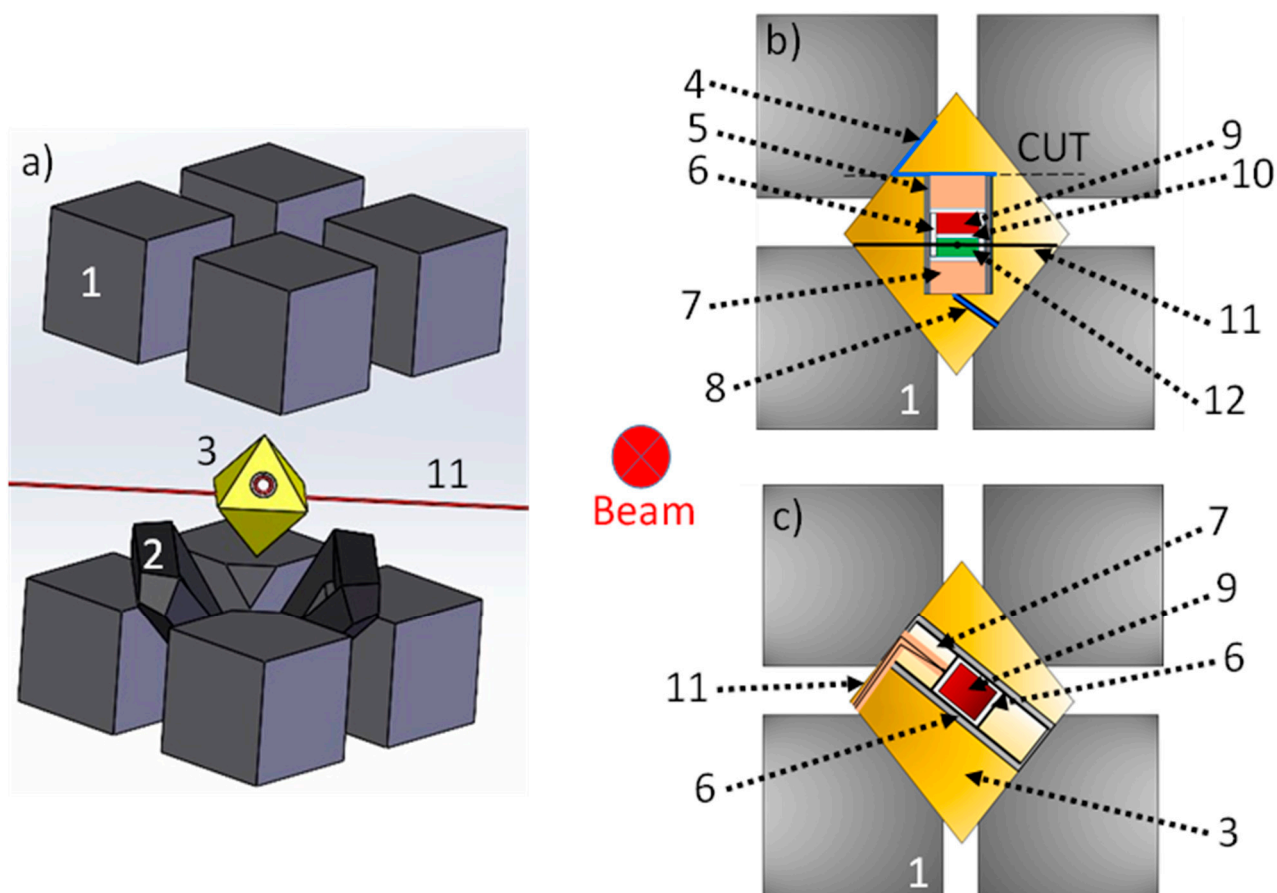


Figure 2. (a) Schematic view of the octahedral pressure medium and how it is inserted in the Kawai-type octahedral cell, made of eight truncated WC cubes. (b) Schematic view of the typical multi-anvil cell used during EDX and CAESAR experiments on PSICHE beamline at SOLEIL synchrotron. (c) Schematic view of the typical multi-anvil cell used during ADX experiments on ID06 beamline at SOLEIL synchrotron. (1) Partial view of WC cube. (2) Gaskets. (3) Octahedral pressure medium. (4) Molybdenum foil. (5) TiB₂ heater. (6) Hexagonal boron nitride (h-BN) capsule. (7) ZrO₂ rods. (8) Molybdenum powder. (9) Sample. (10) Hexagonal boron nitride (h-BN) cap. (11) Thermocouple in Al₂O₃ tubing. (12) MgO/h-BN powder pressure calibrant.

These truncations form an octahedral assembly cavity. The usual material of this second stage is tungsten carbide (WC), although the use of cubic boron nitride (c-BN) or sintered diamond (SD) cubes is also possible, although more expensive. Only two of these eight cubes have electrical contacts with primary anvils. These cubes are located diagonally opposite to each other and are in contact with furnace ends of the sample assembly. The truncations are directly in contact with the octahedral pressure medium and by varying their size and hence the size of the octahedron, it is possible to attain different pressures. The assemblies are thus defined by the octahedral edge length (OEL) and the truncation edge length (TEL). The standard OEL/TEL assemblies are: 18/11, 14/8, 10/5, 10/4, 8/3 that can provide the synthetic volumes of 12 mm³ at 4–10 GPa, 5–8 mm³ at 11–16 GPa, 3 mm³ at 17–21 GPa and 1 mm³ at 22–26 GPa, 0.5 mm³ at 30–35 GPa, respectively.

In both DIA and Walker modules, the sample assembly has thus a cylindrical shape inside the octahedral pressure medium. The usual octahedron is made of magnesium

oxide MgO with often small additions of Al₂O₃, Cr₂O₃, etc. Before using the octahedron in high-pressure experiments, it is often fired above 900 °C during a few hours. This procedure results in harder octahedron, permitting to reach higher pressures. The hole inside the octahedron, dedicated for the sample assembly with furnace and thermocouple, usually passes through two opposite faces of the octahedron. These multi-anvil devices use resistive heating with an internal heater (graphite, chromite LaCrO₃, TiB₂, TiC, metallic foil, etc.) inside the octahedron to reach simultaneous high temperature and pressure (Cf. Figure 2 where two typical set-ups are shown). In addition, gaskets, prepared usually from materials with low coefficient of internal friction like pyrophyllite (this particular material has important property of increase of plasticity under compression up to maximum and subsequent decrease), fill the space between two adjacent cubes and provide electrical insulation between the secondary anvils. Temperature can be measured using thermocouple or estimated using electrical power-temperature calibration-curve method. Pressure can be also estimated with prior calibration curves (maximal or mean pressure in the reaction volume vs. applied hydraulic-oil pressure). In both cases of pressure and temperature, the larger cell assures higher reproducibility of calibration curves.

2.2.2. Adaptation of Multi-Anvil Devices to In Situ Synchrotron X-ray Diffraction

The compression efficiency in a DIA apparatus is usually less than in a Walker-type MAP, but DIA module is accessible for in situ synchrotron X-ray diffraction (XRD) while the highly X-ray absorbent steel confinement ring around the anvils of a Walker module makes X-ray diffraction impossible in this configuration. In DIA-type MAP, the four equatorial anvils of the first stage can have a horizontal groove dedicated to incoming and outgoing X-ray beams. That is why DIA multi-anvil presses are widely used in all synchrotrons around the world. Two main X-ray diffraction techniques have been developed with MAP: angle-dispersive XRD (ADX) and energy-dispersive XRD (EDX). Whereas EDX technique is used at polychromatic X-ray radiation and is generally associated with a solid-state detector at a fixed angle (2θ), ADX technique is operated only with monochromatic incident X-ray beam and 2D detector.

High quality crystallographic data can be yielded from the ADX measurements (symmetry, structure, internal coordinates of atoms, and microstructure of crystalline samples, etc.). However, the ADX has also some disadvantages, which can severely limit its use, like for example rather long acquisition time needed (compared to EDX) and requirement of a very high spatial accessibility (which is difficult with MAP's geometry).

Conversely, EDX does not generally allow a very precise quantitative crystallographic analysis of the sample studied (for example prohibiting any Rietveld refinement of crystal structure) because the relative intensities of the diffraction peaks are convoluted by the emission spectrum of the synchrotron source energy and by the energy-depending absorption (contingent also to gaskets extrusion with (P, T) conditions) along the X-ray beam path. However, EDX has some advantages over the ADX technique. The quality of the new detectors is such that recording an EDX spectrum takes a few μs or ps only. This speed makes EDX a powerful tool for rapid structural analysis (e.g., to detect intermediate phases, which are unstable or exist for a very short period) or to perform kinetics studies on the synthesis of new materials. On the other hand, the decisive advantage of EDX is the ability to obtain diffraction spectra with a point detector without the use of a goniometer. The fixed scattering angle therefore allows efficient use of diffracted X-ray collimators in order to define very precisely the detected area, resulting in the removal of the unwanted diffraction signal from the sample environment. Therefore, high spatial accessibility of the sample is not required and EDX can be applied for in situ experiments with significantly limited access to the sample. This is why this diffraction technique is mainly used for high-pressure experiments in multi-anvils. Figure 3 shows the various elements of a typical synchrotron X-ray diffraction station (EDX) associated with a multi-anvil press.

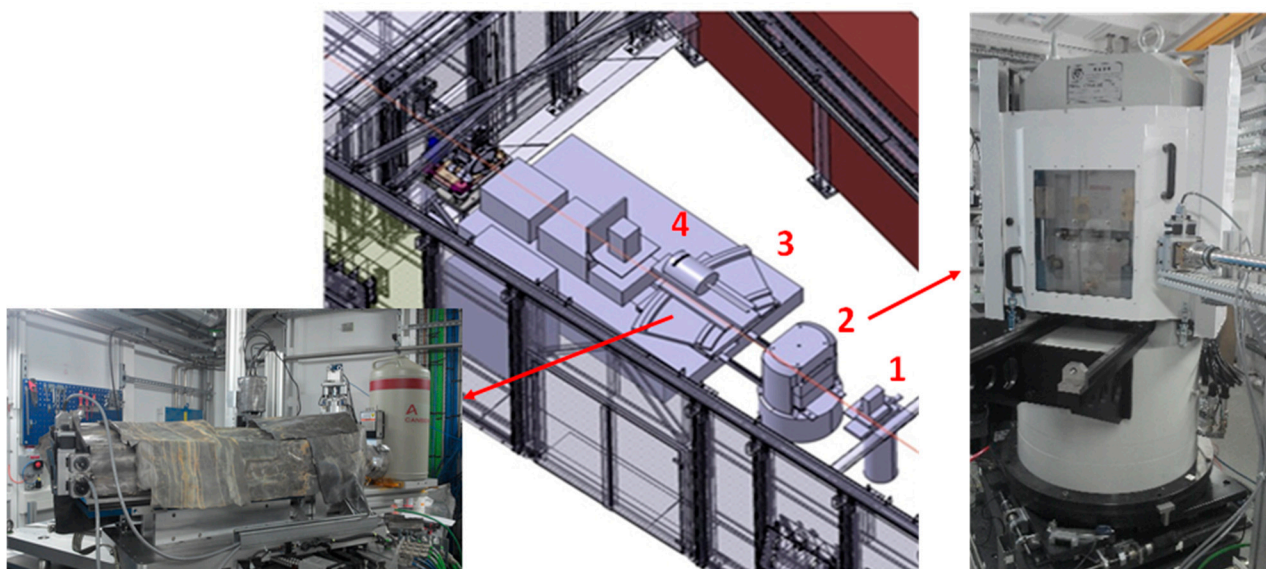


Figure 3. Optics hutch of PSICHE beamline at SOLEIL, a synchrotron X-ray diffraction station (EDX) associated with a multi-anvil press. (1) Input collimating slits. (2) Multi-anvil press. (3) CEASAR system with (4) solid-state germanium detector.

Figure 3 also allows us to present a third hybrid mode associated with X-ray diffraction: the Combined Angle and Energy-dispersive Structural Analysis and Refinement (CAESAR) method. This technique proposed by Wang et al. [38] is now in operation with MAP at PSICHE beamline of SOLEIL synchrotron in France. It consists of collecting series of one dimensional EDX patterns (intensity versus energy E) as function of diffraction angle 2θ , by varying the position of the detector and the 2 pairs of output slits (Cf. Figure 3) placed behind MAP (i.e., by keeping the same volume of sample investigated with a very small sphere of confusion). Hence, at the end of the acquisition, the entire data set contains all 2θ steps (up to 0.01°) from 0° to 30° and forms a two-dimensional array (2D diagram): Intensity ($E, 2\theta$). These intensity data can be then regrouped according to photon energies, providing a large number of angle-dispersive (intensity versus 2θ) patterns, each of which corresponds to a given photon energy. This combination of energy-dispersive and angle-dispersive enables exploring a wider region of the reciprocal space. Thus, the collection and the analysis of CAESAR data (via an algorithm that re-normalizes the intensities) allows finally to perform structural Rietveld refinement, even if performing primarily EDX.

The choice between these three different X-ray diffraction techniques involves significant modifications to the sample environment in an in situ high-pressure multi-anvil press experiment.

For ADX, like at ID06 beamline of ESRF, it is impossible to collimate the diffraction signal of each element on the beam path (Sollers slits are impossible to implement in MAP, due to the limited aperture). Hence, along the beam path, cylindrical amorphous SiBCN X-ray windows and wide amorphous boron epoxy rectangles are inserted into the octahedron and gaskets, respectively. Indeed, when using a monochromatic beam, the flux is considerably reduced. It is thus important to insert non-crystalline and low-absorbing elements along the beam path as to preserve the high quality of the diffraction data. The cross-section of the typical octahedron used in ADX at ESRF is shown in Figure 2c. It indicates the position of the various components of the sample assembly.

For EDX, as compared to ADX, the use of the polychromatic beam ensures higher flux. Additionally, the efficient use of collimators (resulting in the elimination of the unwanted diffraction signal from the sample environment) makes the use of non-crystalline and low-absorption insertions not necessary once the beam is focused on the central part of the assembly.

Additionally, to perform CAESAR acquisition, like at PSICHE beamline of SOLEIL synchrotron, the sample volume probed during the experiment should be identical at

every diffraction angle. To ensure this, the cylindrical sample assembly should be placed perpendicularly to the plan of the beam. In this way, the depth of the measured sample is invariant with respect to the azimuthal angle. We typically cut the octahedron into two parts; and the hole hosting the high-pressure assembly is drilled in the cut surface, as shown in the cross-section of the octahedron in Figure 2b.

2.2.3. Paris–Edinburgh Press

The Paris–Edinburgh press is a “two-opposed-anvil-type” large volume device. Developed 30 years ago, this press was designed preliminarily for high-pressure experiments in neutron sources such as ISIS in the United Kingdom [39]. The design idea was to generate maximum force in a minimum of space so that the press could be easily installed on any beamline without performing major work to accommodate a huge device (like multi-anvil presses). The originality of the Paris–Edinburgh press comes from its hydraulic ram, which is a key breakthrough. It has been optimized (by finite element calculations) to reduce both size and weight. The outcome is a ram with a high capacity (from 500 kN to 4500 kN) which weighs only a few kilograms (from 10 to 90 kg depending on the version) and fits into a 40 cm cube. The press is also easily removable, with parts not exceeding 20 kg, which facilitates its handling and transport. This compactness made it possible to adapt the Paris–Edinburgh press in various synchrotrons or neutron sources as well as in many academic laboratories all over the World (Cf. below).

As shown in Figure 4, depending on the version, the Paris–Edinburgh press can have 2 or 4 columns: generally, notation VX is used to designate a Paris–Edinburgh press with 2 columns (thus allowing a wider angular opening) [40] and V—a Paris–Edinburgh press with 4 columns.

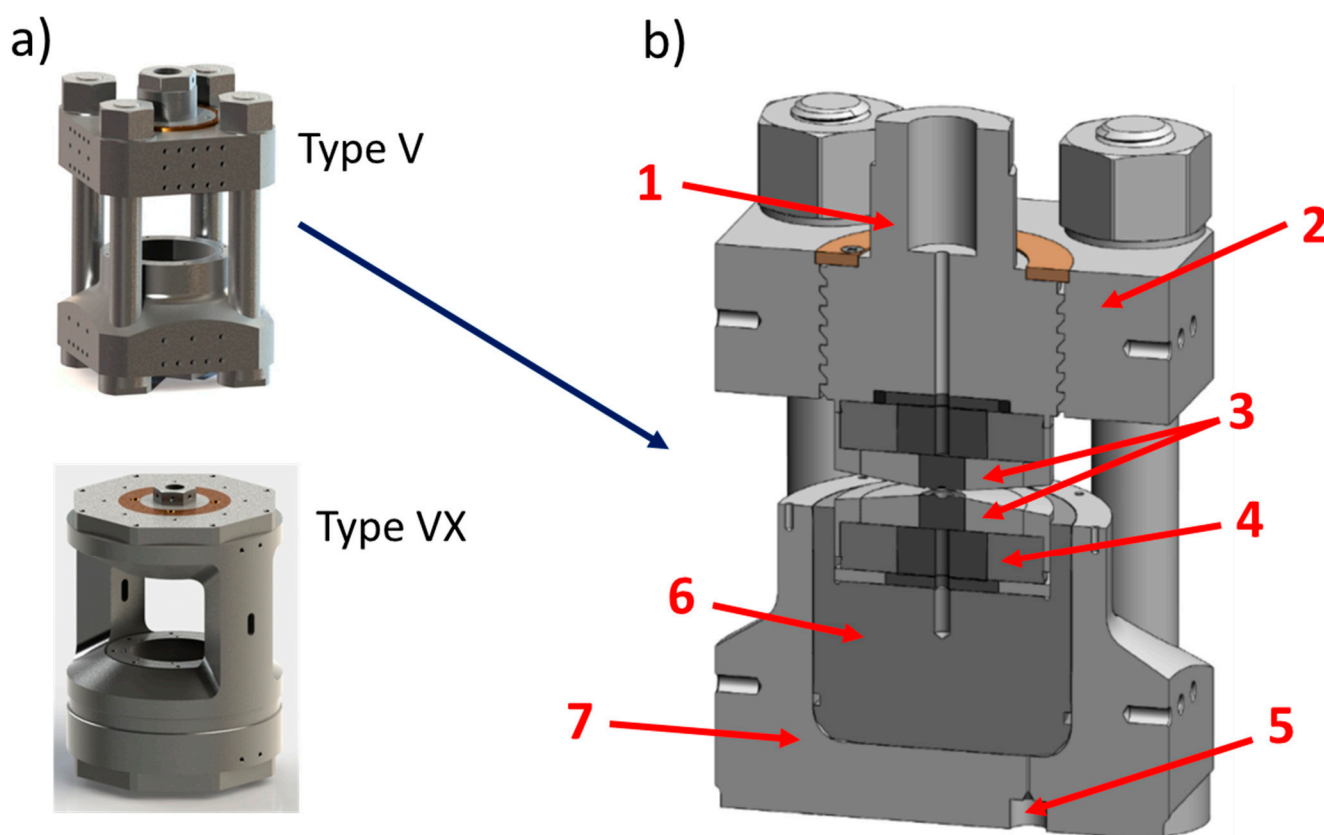


Figure 4. (a) The two types of Paris–Edinburgh (PE) press with 4 (type V) and 2 columns (type VX). (b) Cross-section of the V3 PE press: (1) breech, (2) top platen, (3) anvils, (4) seat, (5) hydraulic fluid inlet, (6) hydraulic piston, (7) ram.

This Figure 4 also shows a sectional view of a Paris–Edinburgh press V3 and allows to simply illustrate its principle of operation: a hydraulic fluid or gas pressure is applied to the base of the piston via a high-pressure generator (automatic compressor, hand pump, etc.) connected to the press ram by a high-pressure flexible tube. The top part of the press is fixed. The piston then pushes a tungsten carbide seat, fretted in a steel part (with a radial stress of 1 GPa), which transmits the force to 2 opposed anvils: the high-pressure part is located between the anvils. These anvils can have several shapes, permitting to provide HP-HT experiments in various pressure ranges. In their standard design, these tungsten carbide (WC) anvils (but for reaching higher pressures, sintered diamond (SD) anvils could be used), also fretted with hard steel, have a circular high-pressure cavity with a quasi-conical profile, dedicated for gasket and sample assembly. The gasket is characterized by the value of its external diameter (ED) and of its central hole (where the sample assembly is housed), corresponding to the flat surface of this high-pressure cavity (FS). Various geometries ED/FS exist. For instance, 12/5, 10/3.5, 7/2.4, and 5/1.5 geometries correspond (with SD anvils) to the maximum reachable pressures of 6, 8, 10, and 17 GPa, respectively [41]. For ex situ or in situ neutrons diffraction studies, gaskets (or pressure medium) are made of baked pyrophyllite. Nevertheless, pyrophyllite absorbs too much X-rays and cannot be used for synchrotron techniques. That is why for in situ X-ray diffraction studies, amorphous boron-epoxy gasket, which is almost transparent to X-rays, is used. Occasionally, an additional Teflon (or PolyEtherEtherKetone PEEK) ring can be positioned around the gasket in order to moderate the gasket flow under compression.

Inside the gasket, the sample assembly consists of the usual various parts of traditional high-pressure components: sample capsule, cylindrical heater, insulating ceramics, thermocouple, etc. Depending on the experiment's requirements, these parts can be prepared from various materials. Furthermore, some parts can be either removed or added. Figure 5 shows a basic sample assembly associated with the 10/3.5 geometry.

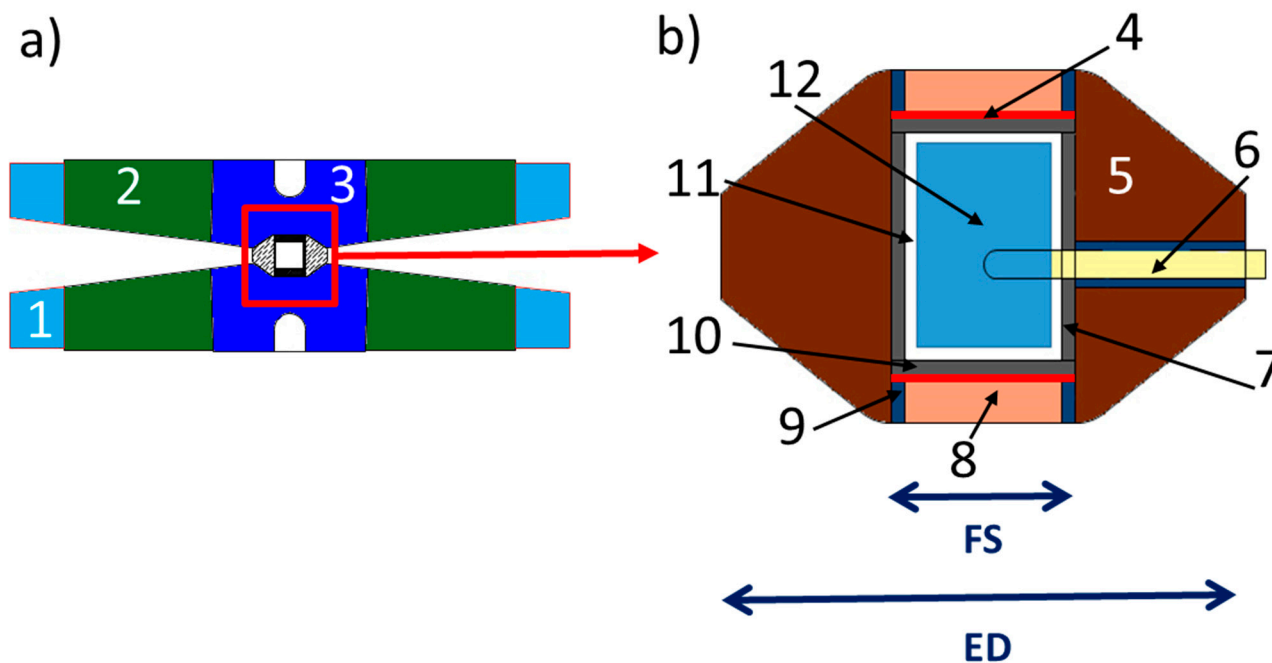


Figure 5. Schematic diagram of two-opposed anvils (a) and sample assembly (b) of the large volume Paris–Edinburgh press for in situ X-ray diffraction studies (here for ED = 10 mm and FS = 3.5 mm). (1) Cooling device. (2) Steel binding ring. (3) Tungsten carbide WC anvils. (4) Molybdenum disk. (5) Amorphous boron epoxy gasket (pressure medium). (6) Coaxial thermocouple. (7) Graphite heater. (8) Insulating ceramic. (9) Electrical contacts. (10) Graphite disk. (11) h-BN or MgO capsule. (12) Sample.

As in multi-anvil press, temperature is generated by Joule effect (resistive heating). Sample temperature is measured with a coaxial thermocouple, with no correction for the pressure effect on the thermocouple electromotive force. In case of thermocouple failure, the sample temperature can be also well estimated by an established power-temperature relation, which depends mainly on the gasket's geometry. In off-line experiments, pressure is also estimated with prior calibration curves where the sample pressure is plotted as a function of the controlled applied primary (oil) pressure on the piston.

2.2.4. Adaptation of Paris–Edinburgh Press to In Situ Synchrotron X-ray Diffraction

Thanks to its compactness, the Paris–Edinburgh press has been adapted during the last years for a wide range of in situ high (P,T) measurements such as neutron and X-ray diffraction [42,43], extended X-ray absorption fine structure (EXAFS) [44], Compton scattering [45], inelastic neutron and X-ray scattering [46], ultrasonic [47], or tomographic studies [48]. For X-ray diffraction, this press is widely used in almost all synchrotrons in the world and can be adapted to all the diffraction geometries mentioned above in Section 2.2.2: ADX, EDX or CAESAR measurements. In particular, the ADX mode has been largely developed thanks to the exceptional angular opening of the press (140° for a VX3) and the development of an original Sollers slits system [49]. Actually, as shown in Figure 6, in a X-ray diffraction beamline like ID27 of ESRF, the diffracted beam can be easily collimated by a Sollers slit system, installed on translations and allowing alignment of the central slit on the incident beam.

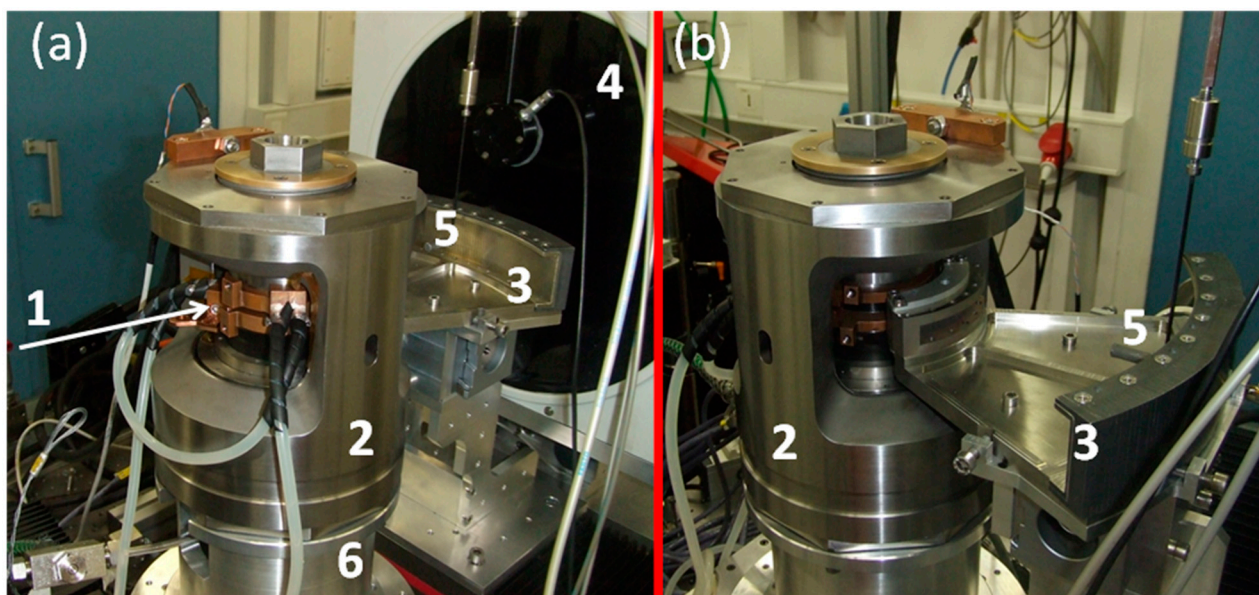


Figure 6. Front (a) and rear (b) views of the Paris–Edinburgh press installed on the ID27 beamline of ESRF. (1) Incoming beam. (2) Paris–Edinburgh press. (3) Sollers slits system. (4) Image-plate detector. (5) Motorized beamstop. (6) Press-positioning x-y-z motors.

This multichannel collimator consists of two concentric sets of 75 fine slits (WC blades) at 0.8° angle from each other to cover a total angle of 60° . Both arrays are located 50 and 200 mm, respectively, from the sample (centered on the rotation axis of this multichannel collimator). Slit widths of the inner and outer arrays (0.05 and 0.20 mm, respectively) are designed in order to minimize the volume seen by the two-dimensional detector and maximize the signal detected. These slits are mechanically aligned with high precision on a base-plate made of Invar to prevent from any variation of the system dimensions in case of temperature fluctuation in the experimental hutch. By oscillating the slits at a constant speed during data collection, background scattering coming from the material surrounding the sample can be effectively removed and homogeneous angle dispersive data can be

collected using a 2D detector (like MAR CCD detectors or hybrid pixel detectors) with large input surface of more than 150 mm diameter. Exposure times are typically between 20 and 100 s (depending on the sample) for a single ADX pattern.

Hence, the Paris–Edinburgh press combined with a multi-channel collimator permits in situ ADX and allows collecting rich crystallographic data sets for samples at extreme pressures and temperatures.

3. In Situ Large-Volume High-Pressure Syntheses

As already explained in the previous section, in contrast to DAC experiments, in situ large-volume-pressure experiments reproduce real industrial conditions for high (P,T) synthesis of new materials. In the following, we will present recent successful in situ high-pressure syntheses of light-element compounds in various systems, performed at synchrotron facilities using multi-anvil or Paris–Edinburgh presses.

3.1. Diamond and *c*-BN

Graphite-to-diamond transformation in graphitic phases of various light-elements (e.g., B-C-N-O) compounds inspired high-pressure synthesis experiments for decades [50–52], and for most diamond-like phases, the main hot topic concerned their existence and purity. Graphite, h-BN, and graphitic BC_x and BC_xN phases have been studied in situ in DAC at HP, both at room temperature and HT [53]. Numerous direct phase transformations were observed [54,55], a number of advanced superhard materials were revealed and patented [7,56], and new mechanisms of HP-HT graphite-to diamond transformation developed [57,58]. However, most of the results remain in the field of explorative materials science. They allow understanding deep links between structure, composition, and functional properties at an extended range (e.g., hardness [59,60], superconductivity [61,62], etc.), rather than applying them immediately in industry.

At the same time two of them, diamond and cubic BN, are well-known industrial materials whose formation has been thoroughly studied at HP-HT conditions in large volume apparatuses, primary by ex situ since the 1950s, and in situ in the late 1990s methods [63–65]. Both materials have a simple diamond-like structure, and, subsequently, a simple XRD pattern that can be easily identified (Figure 7). This fact makes it easy to observe the onset temperature of diamond or *c*-BN formation in a typical experiment of heating at various chemical systems at stable pressure (in fact, only external oil pressure applied on anvils can be maintained, the sample pressure can—and often does—change with temperature and transformation degree). In situ probing of these materials allowed getting the methodology for constructing the reliable phase diagrams under extreme conditions, as well as understanding the kinetics, mechanism and dynamics of industrial crystallization processes. Some pioneering results of in situ observations of crystallization mechanisms for diamond (in typical ferrous-metal environment) and *c*-BN (in supercritical B-N-H fluid) under conditions close to industrial are presented in Figure 7.

The data presented in Figure 7a allowed us to study the kinetics of fast crystallization of diamond for the first time; activation energy $E_A = 148 (47) \text{ kJ}\cdot\text{mol}^{-1}$, with mechanism implying the 3-D diffusion growth and continuous nucleation [65]. The time scale of full diamond crystallization at ~5 GPa, in the 1500–1600 K range in the presence of Fe-Ni-C solvent was estimated as a few minutes (4 min. correspond to the temperature range of Figure 7a).

Based on the data of Figure 7b, the mechanism of *c*-BN crystallization in the presence of supercritical B-N-H fluid was established that include equilibria between NH₃-intercalated BN disordered layered compound (X), whose role could not be established without in situ observations [64]. This intermediate phase X cannot be recovered at ambient conditions, and this study revealed the impossibility to suggest the correct mechanism of HP-HT crystallization of *c*-BN without in situ methods. Therefore, studied supercritical synthesis is very efficient for high doping degree of *c*-BN, e.g., by Si or Be, and recently high-temperature semiconductors (operating up to 875 K) were reported [66].

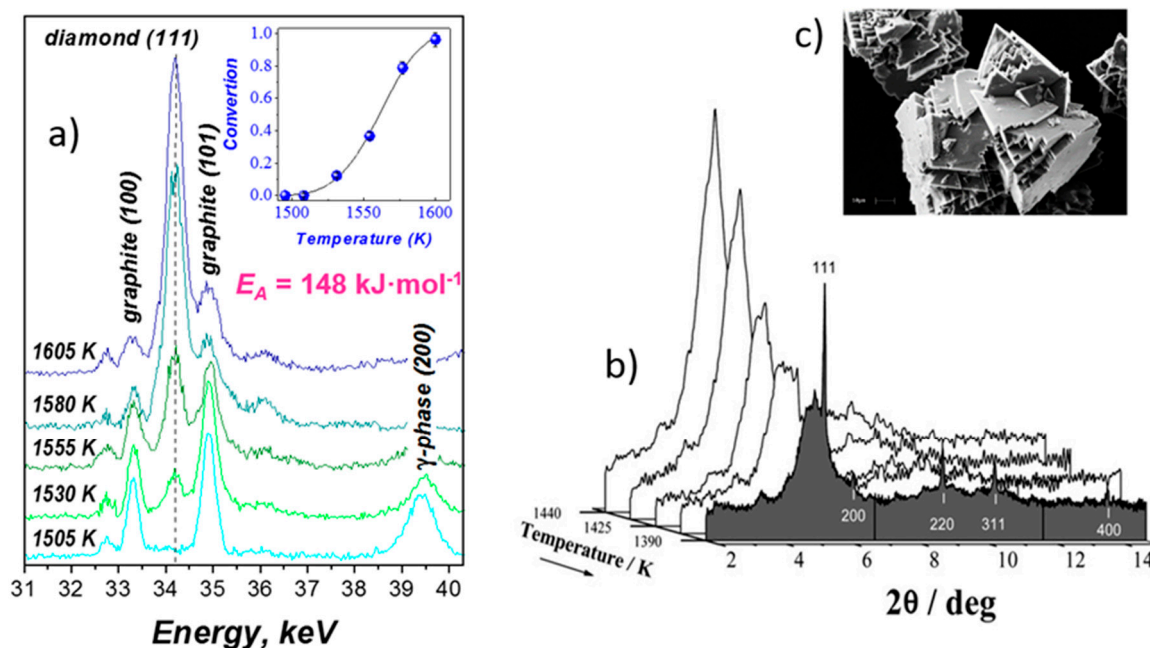


Figure 7. In situ observation of synthesis of diamond and c-BN from their graphitic precursors using a Paris–Edinburgh press at ESRF. (a) Graphite-to-diamond transformation in the presence of Fe–Ni–C liquid: energy dispersive X-ray diffraction patterns taken at 5.2 GPa with heating rate 25 K/min [65]. Insert: Kinetic curve of graphite-to-diamond transformation. Temperature changes linear with time, the full curve correspond to ~ 4 min. (b) Crystallization of c-BN from B–N–H supercritical fluid: sequence of angle-dispersive X-ray diffraction patterns taken at 2.1 GPa in the course of cooling the supercritical solution (57 mol.% BN) from 1460 to 1390 K [64]. (c) Scanning electron micrograph of as-grown c-BN crystals (2500 \times) (reproduced from [64] with permission from the PCCP Owner Societies).

3.2. Boron-Rich Compounds

Boron-rich compounds attracted much attention in the past years for the design of new useful materials combining high hardness, toughness, and resistance to extreme mechanical, thermal and radiation conditions [6,67]. In particular, numerous attempts have been made to fulfill the hardness gap between two reference superhard materials, i.e., polycrystalline diamond ($H_V \sim 80\text{--}120$ GPa, which is a typical value range of good-quality sintered samples) and two times less harder c-BN ($H_V \sim 40\text{--}60$ GPa for polycrystalline ingots, also these hardness values for diamond and c-BN can be higher for single crystal faces and nanostructured ingots) [67]. Among icosahedral boron-rich solids, the record hardness has been achieved in the case of high-pressure boron allotrope, γ -B [68–70]; while most of the icosahedral boron rich compounds remain at the lower boundary of superhardness, i.e., at $\sim H_V$ of c-BN [67].

At the same time, such complicated crystal structures with large unit cells have more numerous reflections in XRD patterns [53] as compared to simple diamond and graphite structures, which render them difficult to observe and identify among the diffraction of the HP-cell environment. Numerous explorative in situ studies of the boron-rich part of the B–C–N–O–X system at HP-HT conditions were performed and led (i) to the discovery of new compounds in B–N [71], B–Si, and B–Se systems [72], (ii) to construction of B–O [73], B–N [74], and B–N–O [75] phase diagrams, as well as (iii) to understanding the difficulties of HP synthesis of stoichiometric compounds in corresponding systems [76].

Rhombohedral boron subnitride $B_{13}N_2$ is a boron rich solid with relatively simple XRD pattern known for icosahedral borides (similar to B_4C and B_6O of α -Boron type). It can be synthesized by crystallization from the B–BN melt at 5 GPa [71,76] and is the only stable compound in the system at this pressure [74]. The phase forms reddish crystals, similar to boron suboxide B_6O , and is predicted to be superhard with $H_V \sim 40$ GPa and has the highest incompressibility (or bulk modulus) in “ α -Boron family”. At the same time,

in contrast to B_6O , $B_{13}N_2$ never forms as a single phase in the B-BN system. Only in situ studies and construction of phase diagrams explained this fact.

Figure 8a shows the in situ synthesis of $B_{13}N_2$. Initial boron, β -B allotrope, is also observed, but cannot be a priori recognized. The temperatures of transformations at given pressure, T_1 and T_2 , can be estimated from the pattern sequence (linear heating controlled by thermocouple). In the hypothesis that transformation occurs immediately after the thermodynamic conditions have been achieved (this is often valid at high temperatures and is often used, at least for construction of the first in situ approximation), these values can be used for refinement of the parameters describing the thermodynamic model of liquid and/or solid phase(s). The calculated phase diagram explained the difficulties in synthesis of single-phase samples of $B_{13}N_2$ (peritectic-type of phase diagram), as compared to B_6O (simple eutectic type).

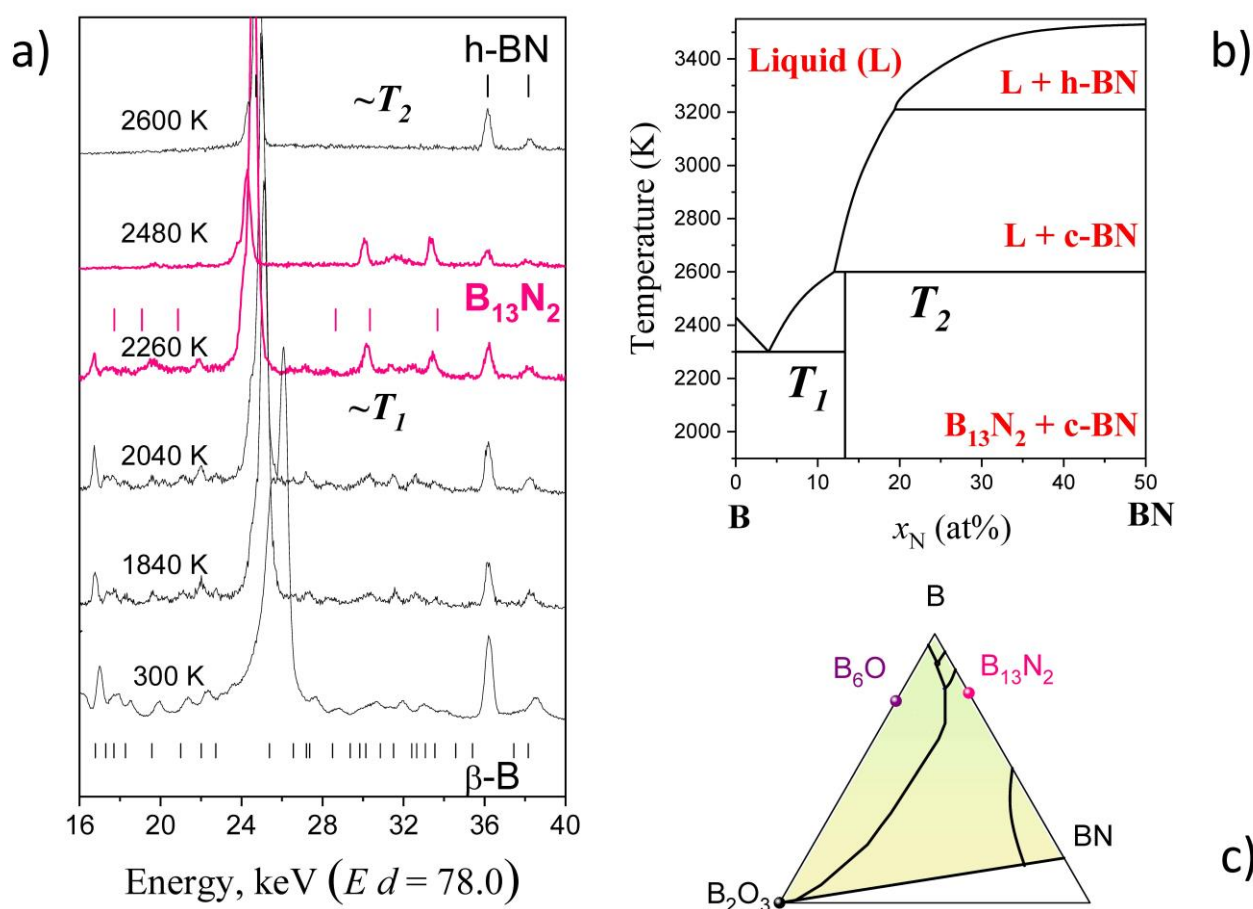


Figure 8. (a) In situ observation of synthesis of icosahedral boron-rich compound $B_{13}N_2$ by chemical reaction of boron (β -B allotrope) with h-BN using a multi-anvil system MAX80 at HASYLAB-DESY [77]. Typical sequence of the energy-dispersive X-ray diffraction patterns taken at 5 GPa in the course of heating of the B-BN mixture to 2600 K [74]. The stars represent the h-BN escape line, while vertical bars show the positions of the phase reflections. The β -B lines disappear between 2040 and 2260 K ($T_1 \sim 2300$ K). The reflections of $B_{13}N_2$ appear at 2260 K and are observed at temperatures below 2600 K ($T_2 \sim 2600$ K). (b) Isobar section ($P = 5$ GPa) of calculated B-BN phase diagram with temperatures T_1 and T_2 as the elements of the calculated phase diagrams [74]. Insert: Large ($\sim 200 \mu\text{m}$) reddish crystal of $B_{13}N_2$ in boron matrix [58]. (c) Projection of melting phase diagram on the concentration triangle of the B-N-O system [75]. The ternary phase diagram has been established by combining in situ and ex situ data.

3.3. Magnesium Carbides

Magnesium carbides have been attempted many times to be placed on the Mg-C phase diagram, which is one of the systems that is interesting for diamond synthesis, both single crystals and B-doped semiconductors. However, the experimental data were controversy [78,79] and inconsistent with thermodynamic consideration [80,81].

In situ studies allowed to shed the light on the crystallographic diversity of magnesium carbides that form at high pressure, i.e., β -Mg₂C₃ [16] and Mg₂C [15], both having p-T-x domains of thermodynamic stability (above 5 GPa) [82]. These high-pressure phases can be recovered at ambient conditions and remain metastable for long time. β -Mg₂C₃ is a yellow powder, while Mg₂C has a dark grey color.

Figure 9a shows the sequence of powder XRD patterns collected at 6 GPa during the heating of a mixture of Mg and C. In contrast to ex situ XRD experiments (powder patterns of multiphase samples), in situ data allowed estimating unambiguously the individual reflections of unknown magnesium carbide phase. Chemical analysis indicated the Mg₂C₃ composition with C₃⁴⁻ anions, while ab initio evolutionary simulations [83] predicted a number of unit cells for such composition, and one of them was successful, as the monoclinic unit cell was refined using Rietveld analysis of in situ XRD data [16]. Conventional ex situ techniques were very time-consuming to accomplish the characterization of Mg-C system (competing crystallization of low-symmetry phases), even simple cubic antiferite carbide Mg₂C was recognized and characterized after in situ HP-HT studies using DAC at HPCAT beamline of synchrotron APS (Chicago, IL, USA) [15]. For monoclinic β -Mg₂C₃ phase, the in situ synthesis of large volume samples was crucial [16].

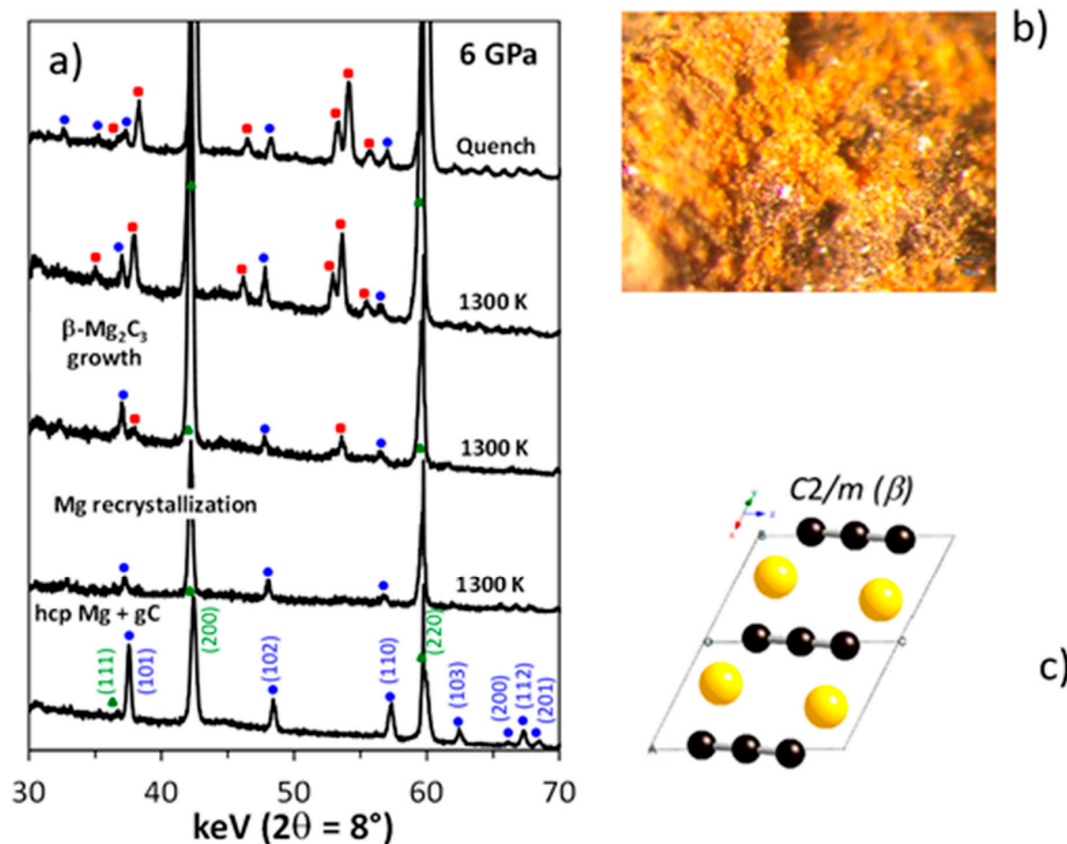


Figure 9. (a) In situ observation of synthesis of Mg₂C₃ (red circles) by chemical reaction of Mg (blue circles) with powder of glassy carbon using energy-dispersive XRD with white beam of synchrotron radiation in a Paris–Edinburgh-type press at SOLEIL [16]. Green circles show the MgO capsule material. (b) Optical microscope picture of as synthesized β -Mg₂C₃ powder. (c) Monoclinic crystal structure of β -Mg₂C₃ resolved by combination of in situ powder XRD and evolutionary structural algorithm USPEX [16]. Yellow balls indicate the position of Mg atoms, while black balls—of C atoms. (Figure adapted with permission from [16]. Copyright 2014 American Chemical Society).

3.4. Silicon

Si-I with diamond structure is a low-pressure semiconductive allotrope that passes into metallic Si-II (β -Sn structure), stable above ~ 10 GPa in all temperature ranges up to melting. A large variety of phases were observed at higher pressures [84,85] and on decompression (Si-III with BC8 structure [86] and Si-XII with R8 structure [87] considered as rhombohedrally distorted BC8), but again, it is not clear whether these phases have a domain of thermodynamic stability. Heating of Si-III gives Si-IV with hexagonal diamond structure [88], which serves an excellent example of synthesis of an advanced material by using high pressure to produce a precursor, not a final product. The diversity of silicon crystalline forms is very promising for both theory and advanced applications in solar cells and photonics [89,90].

Crystal structures of silicon are much simpler as compared to boron, but more complicated than those of carbon. Their observation is easier because Si scattering factor for the X-rays is much higher.

In situ HP-HT chemical route to Si-III has been discovered for Na-Si system (initial mixtures: Na + Si; Na_4Si_4 + Si or simply $\text{Na}_{30}\text{Si}_{136}$) using both multi-anvil and Paris-Edinburgh techniques [91] (Figure 10a–c). The phase-pure samples have been synthesized at significantly reduced pressure in the Na-Si system at 9.5 GPa by quenching from high temperatures ~ 1000 K. Pure sintered polycrystalline ingots with dimensions ranging 0.05 to 0.5 mm can be easily recovered at ambient conditions. In situ control of the synthetic protocol, using synchrotron radiation, has allowed observing the underlying mechanism of chemical interactions and phasing transformations in the Na-Si system, as well as pressure-temperature (-time) profiles of synthetic protocols (Figure 10c). The “chemical” samples show better crystal perfection as compared to the samples obtained by direct phase transformation (Figure 10d,e).

3.5. Sodium Silicide Clathrates and Open-Framework Allotropes

Sodium silicide clathrates are promising compounds for the design of open-framework silicon allotropes that are predicted to be ideal materials for solar cell applications [92]. Compounds like $\text{Na}_4\text{Si}_{24}$ [93] or $\text{Na}_{30.5}\text{Si}_{136}$ [94] were discovered by exploring high-pressure chemistry of Na-Si system and are the promising precursors for synthesis of open framework Si_{24} and Si_{136} allotropes with quasi-direct bandgap. However, contrary to many other high-pressure syntheses, the $\text{Na}_4\text{Si}_{24}$ compound cannot be easily obtained; the in situ studies indicated that it is due to complicated nucleation mechanism [23].

$\text{Na}_{8-x}\text{Si}_{46}$ (structure I), $\text{Na}_{24-y}\text{Si}_{136}$ (structure II) have been first obtained under high vacuum from sodium silicide Na_4Si_4 [95]. However, depending on stoichiometry (i.e., x and y), nominal stability extends from negative pressures (~ -4 GPa for hypothetical Si_{46} and ~ -3 GPa for known metastable Si_{136}) [96] to high pressures (stoichiometric $\text{Na}_8\text{Si}_{46}$, $\text{Na}_4\text{Si}_{24}$, and $\text{Na}_{30.5}\text{Si}_{136}$ with two sodium atoms per largest clathrate cage) [93,94]. All the structures are presented in Figure 11.

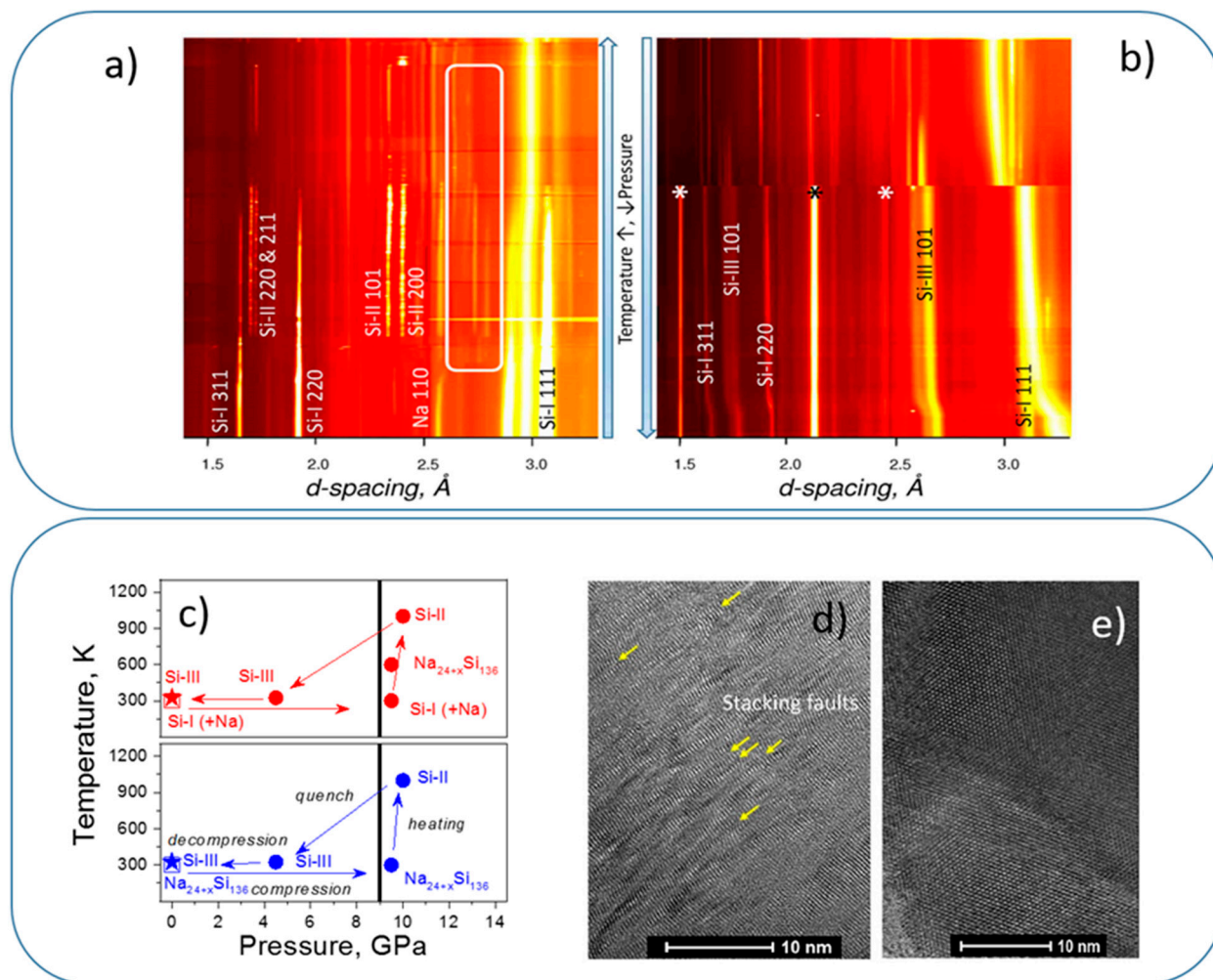


Figure 10. Sequences of XRD diffraction patterns of the Na + Si system at 9.5 GPa during (a) heating, and (b) quench and decompression using multi-anvil press (ESRF, ID06 beamline) [91]. White contour delimits the reflections that appear during interactions (Na₄Si₄ and clathrates), asterisks show the “noise” reflections from the environment that do not move with pressure change (gasket material, etc.). (c) Pressure-temperature evolution during Si-III synthesis from the Na/Si mixture (red) in comparison with decomposition of Na₃₂Si₁₃₆ clathrate (sII-HP) at high temperature (blue) [91]. Vertical lines indicate the low-limit pressures where Si-III has been observed and can be easily extracted in pure form. (d,e) TEM images of Si-III sample obtained by direct transformation at HP-HT sample (d) and in Na-Si system (e). The latter does not show stacking faults, typical for direct-transformation sample [91]. (Figure adapted with permission from [91]. Copyright 2016 American Chemical Society).

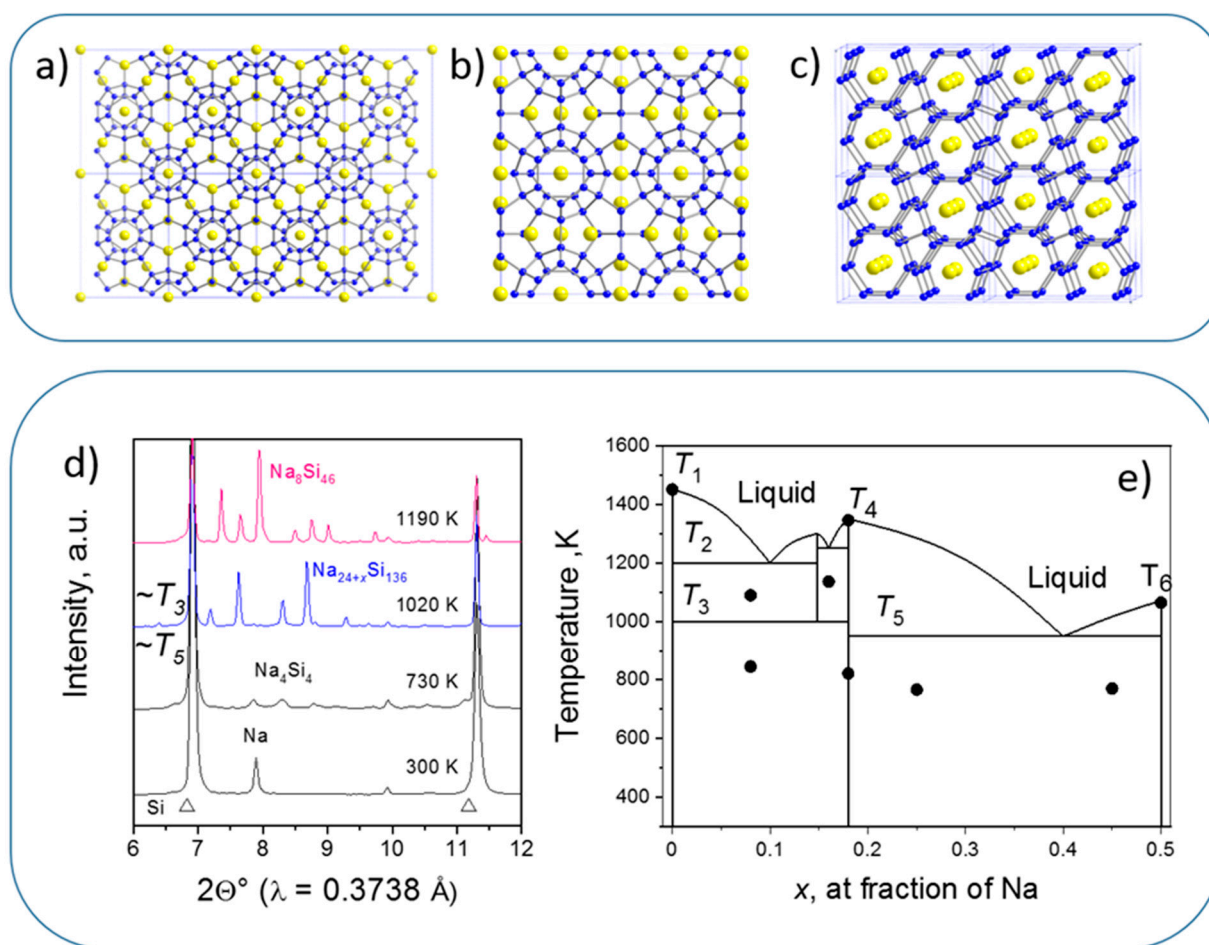


Figure 11. (a–c) Crystal structures of Na-Si stoichiometric clathrates: (a) $\text{Na}_{24}\text{Si}_{136}$ —structure II or sII, (b) $\text{Na}_8\text{Si}_{48}$ —structure I or sI, (c) $\text{Na}_4\text{Si}_{24}$ or NaSi_6 . Blue balls indicate the atomic positions of Si atoms, while yellow balls—of Na. (d) In situ XRD data on phase/chemical transformations in the Na + Si mixture (~15 at % of Na) during heating at 4 GPa obtained at ID27 with Paris–Edinburgh press (ESRF) [97]. (e) First (experimental) approximation of phase diagram of the Na-Si system in the 5–8 GPa range that reflects in situ and ex situ observations [98]. Solid circles indicate experimental observations using either ex situ (phase compositions) or in situ (temperatures) techniques.

In situ studies [97] (e.g., Figure 11d) allowed to observe the following features of phase transformations in Na-Si system: (i) the Na-Si equilibrium phases are Na_4Si_4 , $\text{Na}_8\text{Si}_{46}$ (sI), and $\text{Na}_{30}\text{Si}_{136}$ (sII-HP), stoichiometric compounds without solid solutions; (ii) sII-HP coexists with Si-I at “low” temperatures, while sI (or $\text{Na}_4\text{Si}_{24}$) becomes stable at high temperature (if Si is not in excess); (iii) high Na content makes sII-HP stable up to melting temperatures and sII-HP melts congruently; (iv) co-existence of sI and sII-HP (without Si-I) is possible. Such observations are typical for in situ XRD probing of the synthesis; this information together with XRD and electrical in situ data on T_1 [99], T_4 [98], and T_6 [100], allowed drawing the experimental approximation of phase diagram in the 5–8 GPa range [98] (Figure 11e).

Once obtained at high pressure, Na-Si clathrates can be used as precursors for preparation of corresponding Si allotropes, two silicon frameworks remain after sodium removal, i.e., Si_{24} [14] and Si_{136} . These allotropes can also, in their turn, be considered as precursors for producing other advanced silicon forms, for example Si_{24} passes into microcrystalline hexagonal silicon 4H during heating in air [101]. At our in situ example presented in Figure 12a, clathrate $\text{Na}_{30.5}\text{Si}_{136}$ (sII-HP) loses Na atoms starting from 473 K, and passes into Si open-framework structure at ~773 K. At higher temperatures, this open-framework allotrope passes into stable Si-I phase with diamond structure. These observations illustrate quite rare “in situ” synthesis using conventional diffractometry equipped with

high-temperature oven chamber HTK 1200 N (Anton Paar). This allows us to make efficient syntheses with precious high-pressure samples without synchrotron facility, at IMPMC laboratory (Paris, France).

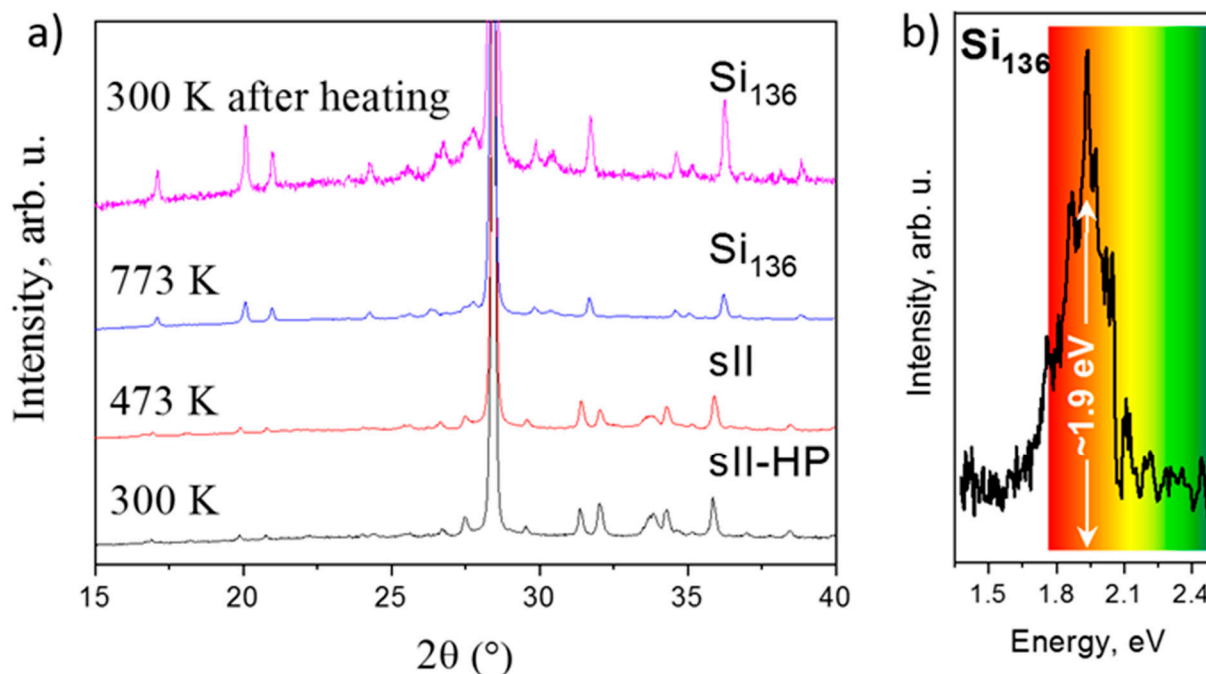


Figure 12. (a) In situ synthesis of quasi-direct bandgap allotrope of Si, Si₁₃₆ from sII-HP clathrate performed at IMPMC laboratory using conventional diffractometry and high-temperature oven chamber (Anton Paar). Principal intensive Si-I reflection is located at ~27°. All other peaks correspond to Na_{30.5}Si₁₃₆ at 300 K and, displaced to the left contrary expected thermal expansion, to Si₁₃₆ at 775 K (our data). (b) Photoluminescence spectra of silicon allotrope with (quasi)direct bandgap c-Si₁₃₆ in match with predicted value of quasi-direct bandgap ~2 eV (our data).

Theoretical predictions [102] and previous optical absorption [103] and photoluminescence [104] measurements on Si₁₃₆ and semiconductive Na₅Si₁₃₆ phase, respectively, confirmed a fundamental gap close to 2 eV. Figure 12b illustrates the PL signal of Si₁₃₆ sample produced via HP-HT route, well in agreement with previous results.

4. Current Challenges and Future Directions

In situ high-pressure synthesis of new outstanding materials is nowadays a flourishing field of research that may lead to the patenting of many novel industrially important materials. This field is still at an initial stage but it is obvious that many discoveries will appear soon and will be useful to meet the societal challenges of the century. To this end, if the methodological tools will remain broadly similar to those mentioned in Section 2 of this review, several improvements related to the experimental and theoretical tools of the domain will open up new horizons.

Actually, while high-pressure techniques seem to be well optimized for this industrial pressure range, the constant improvement of X-ray brilliance, optics, X-ray detectors associated with the various upgrades currently being made by the 3rd generation synchrotrons will make it possible to carry out in situ synthesis experiments that will be more and more accurate and fast. Hence, various kinetics studies which are now at the limit of current X-ray technologies will be easily achievable in future years. Additionally, new possibilities opened up by the combination of diffraction and imaging or tomography under extreme conditions [48] will allow better understanding of the physical processes involved in the high-pressure synthesis of new materials. For example, recently, combined X-ray diffraction and X-ray Computed Tomography have been used to study the crystal growth kinetics of LaMn₇O₁₂ quadruple perovskite. The idea was to determine the optimized

growth conditions and preferred orientations of single crystals of large size under extreme conditions. This study provides new insights regarding the growth kinetics, orientations, and crystal shape/size characteristics of the high-pressure $\text{LaMn}_7\text{O}_{12}$ phase, which are relevant to the field of multiferroic [105]. Such nondestructive in situ X-ray monitoring can also be used to tailor materials with outstanding mechanical or thermal properties by a quantitative microstructure analysis of transformation at high pressure and temperature, as demonstrated recently by a pioneering study on iron under extreme conditions [106].

Additionally, the progress of new precursor chemistry will take an important place in future in situ high pressure synthesis. With this development, new complex materials could become potential targets for such research. It is already the case for nanocomposites whose complex structural organization of the initial chemical reactant involves that of the ending material, synthesized in situ under high pressures and high temperatures conditions. For example, recently, the original combination of solution-phase synthesis of inorganic nanomaterials with subsequent high-pressure conditions was used to synthesize innovative nanocomposites with the in situ synchrotron probe by X-ray diffraction [107,108]. This approach paves the way to advanced multifunctional materials made of several phases not reachable at ambient conditions, which could combine the best functional properties for advanced electronic, thermal, and optical applications.

Finally, in the coming years, in situ high-pressure synthesis will also benefit from improvements of theoretical predictions which now greatly impact the ways this research can be performed. The simulations are developing with the emergence of many algorithms [83,109] and are now crucial in the design of advanced materials. These algorithms can be used not only to generate crystal structures of materials with desired outstanding properties, but also to select the most appropriate P-T conditions and paths for the materials synthesis. Therefore, before any synthesis, they can directly “guide” in situ high-pressure experiments [109]. These advances promise to optimize the process of scientific discovery of new materials by efficient ab initio-assisted in situ high-pressure synthesis. In the framework of this combined methodology, fast tests of new ideas will be possible with minimal production of waste matter as compared to classical studies.

Author Contributions: Conceptualization, Y.L.G. and A.C.; writing—review and editing, Y.L.G. and A.C. All authors have read and agreed to the published version of the manuscript.

Funding: This work was supported by Agence Nationale de Recherche (project ANR-17-CE08-0038).

Data Availability Statement: No new data were created or analyzed in this study. Data sharing is not applicable to this article.

Acknowledgments: We are grateful for assistance in synchrotron in situ experiments to W. Crichton & M. Mezouar (ESRF) and N. Guignot (SOLEIL). The authors also thank B. Baptiste and C. Renero-Lecuna for help with in situ XRD experiments with conventional diffractometry at IMPMC (Figure 12a) and V. Timoshenko for help with PL measurements (Figure 12b). We strongly appreciate the input to this review from our former master and PhD students E. Prével, I. Touloupas and S. Pandolfi.

Conflicts of Interest: The authors declare no conflict of interest.

References

1. Bridgman, P.W. The physics of high pressure. In *International Text-Books of Exact Science*; George Bell and Sons: London, UK, 1931; Volume 7, p. 398.
2. Bridgman, P.W. *Collected Experimental Papers*; Harvard University Press: Cambridge, MA, USA, 1964.
3. Bundy, F.P.; Hall, H.T.; Strong, H.M.; Wentorf, R.H. Man-made diamonds. *Nature* **1955**, *176*, 51–55. [[CrossRef](#)]
4. Liander, H. Artificial diamonds. *ASEA J.* **1955**, *28*, 97.
5. Wentorf, H.R.J. Cubic form of boron nitride. *Chem. Phys.* **1957**, *26*, 956. [[CrossRef](#)]
6. Le Godec, Y.; Courac, A.; Solozhenko, V.L. High-pressure synthesis of superhard and ultrahard materials. *J. Appl. Phys.* **2019**, *126*, 151102. [[CrossRef](#)]
7. Solozhenko, V.L.; Kurakevych, O.O.; Andrault, D.; Le Godec, Y.; Mezouar, M. Ultimate metastable solubility of boron in diamond: Synthesis of superhard diamondlike BC5. *Phys. Rev. Lett.* **2009**, *102*, 015506. [[CrossRef](#)]

8. Solozhenko, V.L.; Kurakevych, O.O.; Le Godec, Y. Creation of nanostructures by extreme conditions: High-pressure synthesis of ultrahard nanocrystalline bulks of cubic boron nitride. *Adv. Mater.* **2012**, *24*, 1540–1544. [CrossRef]
9. Dubrovinskaia, N.; Solozhenko, V.; Miyajima, N.; Dmitriev, V.; Kurakevych, O.O.; Dubrovinsky, L. Superhard nanocomposite of dense polymorphs of boron nitride: Noncarbon material has reached diamond hardness. *Appl. Phys. Lett.* **2007**, *90*, 101912. [CrossRef]
10. Oganov, A.R.; Chen, J.; Gatti, C.; Ma, Y.; Ma, Y.; Glass, C.; Liu, Z.; Yu, T.; Kurakevych, O.O.; Solozhenko, V. Ionic high-pressure form of elemental boron. *Nature* **2009**, *457*, 863–867. [CrossRef] [PubMed]
11. Gilioli, E.; Ehm, L. High pressure and multiferroics materials: A happy marriage. *IUCrJ* **2014**, *1*, 590–603. [CrossRef]
12. Yamanaka, S. Silicon clathrates and carbon analogs: High pressure synthesis, structure, and superconductivity. *Dalton Trans.* **2010**, *39*, 1901–1915. [CrossRef]
13. Jiang, Y.; Jia, X.; Ma, H. The thermoelectric properties of CoSb₃ compound doped with Te and Sn synthesized at different pressure. *Mod. Phys. Lett. B* **2017**, *31*. [CrossRef]
14. Kim, D.Y.; Stefanoski, S.; Kurakevych, O.O.; Strobel, T.A. Synthesis of an open-framework allotrope of silicon. *Nat. Mater.* **2014**, *14*, 169–173. [CrossRef] [PubMed]
15. Kurakevych, O.O.; Strobel, T.A.; Kim, D.Y.; Cody, G.D. Synthesis of Mg₂C: A magnesium methanide. *Angew. Chem. Int. Ed.* **2013**, *52*, 8930–8933. [CrossRef] [PubMed]
16. Strobel, T.A.; Kurakevych, O.O.; Kim, D.Y.; Le Godec, Y.; Crichton, W.; Guignard, J.; Guignot, N.; Cody, G.D.; Oganov, A.R. Synthesis of β-Mg₂C₃: A monoclinic high-pressure polymorph of magnesium sesquicarbide. *Inorg. Chem.* **2014**, *53*, 7020–7027. [CrossRef] [PubMed]
17. Lipp, M.J.; Evans, W.; Baer, B.J.; Yoo, C.-S. High-energy-density extended CO solid. *Nat. Mater.* **2005**, *4*, 211–215. [CrossRef] [PubMed]
18. Blase, X.; Bustarret, E.; Chapelier, C.; Klein, T.; Marcenat, C. Superconducting group-IV semiconductors. *Nat. Mater.* **2009**, *8*, 375–382. [CrossRef]
19. Yamanaka, S.; Enishi, E.; Fukuoka, H.; Yasukawa, M. High-pressure synthesis of a new silicon clathrate superconductor, Ba₈Si₄₆. *Inorg. Chem.* **1999**, *39*, 56–58. [CrossRef] [PubMed]
20. Shirage, P.; Miyazawa, K.; Ishikado, M.; Kihou, K.; Lee, C.-H.; Takeshita, N.; Matsuhata, H.; Kumai, R.; Tomioka, Y.; Ito, T.; et al. High-pressure synthesis and physical properties of new iron (nickel)-based superconductors. *Phys. C Supercond.* **2009**, *469*, 355–369. [CrossRef]
21. Snider, E.; Dasenbrock-Gammon, N.; McBride, R.; Debessai, M.; Vindana, H.; Vencatasamy, K.; Lawler, K.V.; Salamat, A.; Dias, R.P. Room-temperature superconductivity in a carbonaceous sulfur hydride. *Nat. Cell Biol.* **2020**, *586*, 373–377. [CrossRef]
22. Zheng, H.; Wang, L.; Li, K.; Yang, Y.; Wang, Y.; Wu, J.; Dong, X.; Wang, C.-H.; Tulk, C.A.; Molaison, J.J.; et al. Pressure induced polymerization of acetylide anions in CaC₂ and 107-fold enhancement of electrical conductivity. *Chem. Sci.* **2016**, *8*, 298–304. [CrossRef]
23. Guerette, M.; Ward, M.D.; Lokshin, K.A.; Wong, A.T.; Zhang, H.; Stefanoski, S.; Kurakevych, O.; Le Godec, Y.; Juhl, S.J.; Alem, N.; et al. Synthesis and properties of single-crystalline Na₄Si₂₄. *Cryst. Growth Des.* **2018**, *18*, 7410–7418. [CrossRef]
24. SUMITOMO. Sumidia Binderless NPD10/Sumidia D A90, 2015. Available online: <https://www.sumitool.com/en/products/cutting-tools/cbn-pcd/npd10-da90.html> (accessed on 21 July 2021).
25. Lutgens, F.K.; Tarbuck, E.J. *Essentials of Geology*; Pearson Prentice Hall: New Jersey, NJ, USA, 2006; p. 504.
26. Weir, C.E.; Lippincott, E.R.; Van Valkenburg, A.; Bunting, E.N. Infrared studies in the 1-to 15-micron region to 30,000 atmospheres. *J. Res. Nat. Bur. Stand. Sect. A* **1959**, *63*, 55. [CrossRef] [PubMed]
27. Shen, G.; Mao, H.K. High-pressure studies with X-rays using diamond anvil cells. *Rep. Prog. Phys.* **2016**, *80*, 016101. [CrossRef] [PubMed]
28. Mao, H.K.; Bell, P.M.; Shaner, J.T.; Steinberg, D.J. Specific volume measurements of Cu, Mo, Pd, and Ag and calibration of the ruby R₁ fluorescence pressure gauge from 0.06 to 1 Mbar. *J. Appl. Phys.* **1978**, *49*, 3276–3283. [CrossRef]
29. Popov, M. Pressure measurements from Raman spectra of stressed diamond anvils. *J. Appl. Phys.* **2004**, *95*, 5509. [CrossRef]
30. Laniel, D.; Weck, G.; GaiFFE, G.; Garbarino, G.; Loubeyre, P. High-pressure synthesized lithium pentazolate compound metastable under ambient conditions. *J. Phys. Chem. Lett.* **2018**, *9*, 1600–1604. [CrossRef]
31. Huppertz, H. Multianvil high-pressure/high-temperature synthesis in solid state chemistry. *Z. Krist. Cryst. Mater.* **2004**, *219*, 330–338. [CrossRef]
32. Liebermann, R.C. Multi-anvil, high pressure apparatus: A half-century of development and progress. *High Press. Res.* **2011**, *31*, 493–532. [CrossRef]
33. Hall, H.T. Some high-pressure, high-temperature apparatus design considerations: Equipment for use at 100,000 atmospheres and 3000 C. *Rev. Sci. Instr.* **1958**, *29*, 267–275. [CrossRef]
34. Von Platen, B. A multiple piston, high pressure, high temperature apparatus. In *Modern Very High-Pressure Techniques*; Wentorf, R.H., Ed.; Butterworths: London, UK, 1962; pp. 118–136.
35. Kawai, N. A static high-pressure apparatus with tapering multi-pistons forming a sphere. *Proc. Jpn. Acad.* **1966**, *42*, 385–388. [CrossRef]
36. Kawai, N.; Endo, S. The generation of ultrahigh hydrostatic pressures by a split sphere apparatus. *Rev. Sci. Instrum.* **1970**, *41*, 1178–1181. [CrossRef]

37. Walker, D.; Carpenter, M.; Hitch, C. Some simplifications to multianvil devices for high pressure experiments. *Am. Miner.* **1990**, *75*, 1020–1028.
38. Wang, Y.; Uchida, T.; Von Dreele, R.; Rivers, M.L.; Nishiyama, N.; Funakoshi, K.-I.; Nozawa, A.; Kaneko, H. A new technique for angle-dispersive powder diffraction using an energy-dispersive setup and synchrotron radiation. *J. Appl. Crystallogr.* **2004**, *37*, 947–956. [[CrossRef](#)]
39. Besson, J.; Nelmes, R.; Hamel, G.; Loveday, J.; Weill, G.; Hull, S. Neutron powder diffraction above 10 GPa. *Phys. B Condens. Matter* **1992**, *180*, 907–910. [[CrossRef](#)]
40. Klotz, S.; Hamel, G.; Frelat, J. A new type of compact large-capacity press for neutron and x-ray scattering. *High Press. Res.* **2004**, *24*, 219–223. [[CrossRef](#)]
41. Morard, G.; Mezouar, M.; Rey, N.; Poloni, R.; Merlen, A.; Le Floch, S.; Toulemonde, P.; Pascarelli, S.; San-Miguel, A.; Sanloup, C.; et al. Optimization of Paris-Edinburgh press cell assemblies for in situ monochromatic X-ray diffraction and X-ray absorption. *High Press. Res.* **2007**, *27*, 223–233. [[CrossRef](#)]
42. Le Godec, Y.; Dove, M.; Redfern, S.A.; Tucker, M.G.; Marshall, W.G.; Syfosse, G.; Besson, J.-M. A new high P-T cell for neutron diffraction up to 7 GPa and 2000 K with measurement of temperature by neutron radiography. *High Press. Res.* **2001**, *21*, 263–280. [[CrossRef](#)]
43. Mezouar, M.; Le Bihan, T.; Libotte, H.; Le Godec, Y.; Häusermann, D. Paris-Edinburgh large-volume cell coupled with a fast imaging-plate system for structural investigation at high pressure and high temperature. *J. Synchrotron Radiat.* **1999**, *6*, 1115–1119. [[CrossRef](#)]
44. Katayama, Y.; Mezouar, M.; Itié, J.P.; Besson, J.M.; Syfosse, G.; Le Fevre, P.; Di Cicco, A. High-pressure high-temperature XAFS investigation on HgTe. *J. Phys. Colloq.* **1997**, *7*, 1011. [[CrossRef](#)]
45. Hämäläinen, K.; Huotari, S.; Laukkanen, J.; Soininen, A.; Manninen, S.; Kao, C.-C.; Buslaps, T.; Mezouar, M. Free electron gas under high pressure. *Phys. Rev. B* **2000**, *62*, R735–R738. [[CrossRef](#)]
46. Klotz, S.; Besson, J.M.; Schwoerer-Böhning, M.; Nelmes, R.J.; Braden, M.; Pintschovius, L. Phonon dispersion measurements at high pressures to 7 GPa by inelastic neutron scattering. *Appl. Phys. Lett.* **1995**, *66*, 1557–1559. [[CrossRef](#)]
47. Debord, R.; Leguillon, D.; Syfosse, G.; Fischer, M. A finite element study of a high-pressure/high-temperature cell for simultaneous X-ray and ultrasonic measurement. *High Press. Res.* **2003**, *23*, 451–463. [[CrossRef](#)]
48. Philippe, J.; Le Godec, Y.; Mezouar, M.; Berg, M.; Bromiley, G.; Bergame, F.; Perrillat, J.-P.; Alvarez-Murga, M.; Morand, M.; Atwood, R.; et al. Rotating tomography Paris-Edinburgh cell: A novel portable press for micro-tomographic 4-D imaging at extreme pressure/temperature/stress conditions. *High Press. Res.* **2016**, *36*, 512–532. [[CrossRef](#)]
49. Mezouar, M.; Faure, P.; Crichton, W.; Rambert, N.; Sitaud, B.; Bauchau, S.; Blattmann, G. Multichannel collimator for structural investigation of liquids and amorphous materials at high pressures and temperatures. *Rev. Sci. Instrum.* **2002**, *73*, 3570–3574. [[CrossRef](#)]
50. Hall, H.T. Periodic compounds: Syntheses at high pressures and temperatures. *Science* **1965**, *148*, 1331–1333. [[CrossRef](#)]
51. Teter, D.M.; Hemley, R.J. Low-compressibility carbon nitrides. *Science* **1996**, *271*, 53–55. [[CrossRef](#)]
52. Lowther, J.E. Potential super-hard phases and the stability of diamond-like boron-carbon structures. *J. Phys. Condens. Matter* **2005**, *17*, 3221–3229. [[CrossRef](#)]
53. Kurakevych, O.O. Superhard phases of simple substances and binary compounds of the B-C-N-O system: From diamond to the latest results (a review). *J. Superhard Mater.* **2009**, *31*, 139–157. [[CrossRef](#)]
54. Mao, W.L.; Mao, H.-K.; Eng, P.J.; Trainor, T.P.; Newville, M.; Kao, C.-C.; Heinz, D.L.; Shu, J.; Meng, Y.; Hemley, R.J. Bonding changes in compressed superhard graphite. *Science* **2003**, *302*, 425–427. [[CrossRef](#)]
55. Meng, Y.; Mao, H.-K.; Eng, P.J.; Trainor, T.P.; Newville, M.; Hu, M.Y.; Kao, C.; Shu, J.; Häusermann, D.; Hemley, R.J. The formation of sp³ bonding in compressed BN. *Nat. Mater.* **2004**, *3*, 111–114. [[CrossRef](#)]
56. Solozhenko, V.; Andraut, D.; Fiquet, G.; Mezouar, M.; Rubie, D.C. Synthesis of superhard cubic BC₂N. *Appl. Phys. Lett.* **2001**, *78*, 1385–1387. [[CrossRef](#)]
57. Solozhenko, V.L.; Kurakevych, O.O. Reversible pressure-induced structure changes in turbostratic BN-C solid solutions. *Acta Crystallogr. Sect. B Struct. Sci.* **2005**, *61*, 498–503. [[CrossRef](#)]
58. Kurakevych, O.O.; Solozhenko, V.L. High-pressure design of advanced BN-based materials. *Molecules* **2016**, *21*, 1399. [[CrossRef](#)] [[PubMed](#)]
59. Mukhanov, V.; Kurakevych, O.; Solozhenko, V. Hardness of materials at high temperature and high pressure. *Philos. Mag.* **2009**, *89*, 2117–2127. [[CrossRef](#)]
60. Kvashnina, Y.A.; Kvashnin, A.G.; Popov, M.Y.; Kulnitskiy, B.A.; Perezhogin, I.A.; Tyukalova, E.V.; Chernozatonskii, L.A.; Sorokin, P.B.; Blank, V.D. Toward the ultra-incompressible carbon materials. Computational simulation and experimental observation. *J. Phys. Chem. Lett.* **2015**, *6*, 2147–2152. [[CrossRef](#)] [[PubMed](#)]
61. Li, Q.; Wang, H.; Tian, Y.; Xia, Y.; Cui, T.; He, J.; Ma, Y.; Zou, G. Superhard and superconducting structures of BC₅. *J. Appl. Phys.* **2010**, *108*, 023507. [[CrossRef](#)]
62. Moussa, J.E.; Cohen, M.L. Constraints on T_c for superconductivity in heavily boron-doped diamond. *Phys. Rev. B* **2008**, *77*, 064518. [[CrossRef](#)]
63. Solozhenko, V.; Turkevich, V. High pressure phase equilibria in the Li₃N-BN system: In situ studies. *Mater. Lett.* **1997**, *32*, 179–184. [[CrossRef](#)]

64. Solozhenko, V.L.; Le Godec, Y.; Klotz, S.; Mezouar, M.; Turkevich, V.Z.; Besson, J.-M. In situ studies of boron nitride crystallization from BN solutions in supercritical N-H fluid at high pressures and temperatures. *Phys. Chem. Chem. Phys.* **2002**, *4*, 5386–5393. [[CrossRef](#)]
65. Solozhenko, V.L.; Turkevich, V.Z.; Kurakevych, O.O.; Crichton, W.A.; Mezouar, M. Kinetics of diamond crystallization from the melt of the Fe-Ni-C system. *J. Phys. Chem. B* **2002**, *106*, 6634–6637. [[CrossRef](#)]
66. Mukhanov, V.A.; Courac, A.; Solozhenko, V.L. The effect of doping on the lattice parameter and properties of cubic boron nitride. *J. Superhard Mater.* **2020**, *42*, 377–387. [[CrossRef](#)]
67. Mukhanov, V.A.; Kurakevych, O.O.; Solozhenko, V.L. Thermodynamic model of hardness: Particular case of boron-rich solids. *J. Superhard Mater.* **2010**, *32*, 167–176. [[CrossRef](#)]
68. Solozhenko, V.L.; Kurakevych, O.O.; Oganov, A.R. On the hardness of a new boron phase, orthorhombic γ -B28. *J. Superhard Mater.* **2008**, *30*, 428–429. [[CrossRef](#)]
69. Oganov, A.R.; Solozhenko, V.L.; Gatti, C.; Kurakevych, O.O.; Le Godec, Y. The high-pressure phase of boron, γ -B₂₈: Disputes and conclusions of 5 years after discovery. *J. Superhard Mater.* **2011**, *33*, 363–379. [[CrossRef](#)]
70. Oganov, A.R.; Chen, J.; Gatti, C.; Ma, Y.; Ma, Y.; Glass, C.W.; Liu, Z.; Yu, T.; Kurakevych, O.O.; Solozhenko, V. Ionic high-pressure form of elemental boron. *Nature* **2009**, *460*, 292. [[CrossRef](#)]
71. Kurakevych, O.O.; Solozhenko, V.L. Rhombohedral boron subnitride, B₁₃N₂, by X-ray powder diffraction. *Acta Crystallogr. C* **2007**, *63*, i80–i82. [[CrossRef](#)]
72. Cherednichenko, K.A.; Mukhanov, V.A.; Wang, Z.; Oganov, A.R.; Kalinko, A.; Dovgaliuk, I.; Solozhenko, V. Discovery of new boron-rich chalcogenides: Orthorhombic B₆X (X = S, Se). *Sci. Rep.* **2020**, *10*, 1–8. [[CrossRef](#)] [[PubMed](#)]
73. Solozhenko, V.L.; Kurakevych, O.O.; Turkevich, V.; Turkevich, D.V. Phase diagram of the B-B₂O₃ System at 5 GPa: Experimental and theoretical studies. *J. Phys. Chem. B* **2008**, *112*, 6683–6687. [[CrossRef](#)] [[PubMed](#)]
74. Solozhenko, V.L.; Kurakevych, O.O.; Turkevich, V.; Turkevich, D.V. Phase diagram of the B–BN system at 5 GPa. *J. Phys. Chem. B* **2010**, *114*, 5819–5822. [[CrossRef](#)] [[PubMed](#)]
75. Solozhenko, V.L.; Turkevich, V.Z.; Kurakevych, O.O.; Turkevich, D.V.; Taniguchi, T. Phase equilibria in the B-BN-B₂O₃ system at 5 GPa. *J. Phys. Chem. C* **2013**, *117*, 18642–18647. [[CrossRef](#)]
76. Solozhenko, V.L.; Kurakevych, O.O. Chemical interaction in the B-BN system at high pressures and temperatures. Synthesis of novel boron subnitrides. *J. Solid State Chem.* **2009**, *182*, 1359–1364. [[CrossRef](#)]
77. Shimomura, O. Current activity of max80 at the photon factory. *Phys. B C* **1986**, *139*, 292–300. [[CrossRef](#)]
78. Shul'zhenko, A.A.; Ignat'eva, I.Y.; Bel'avina, N.N.; Belousov, I.S. Constitution diagram of magnesium-carbon system at 7.7 GPa. *J. Superhard Mater.* **1988**, *6*, 3–5.
79. Kovalenko, T.V.; Ivakhnenko, S.A. Properties of diamonds seed-grown in the magnesium-carbon system. *J. Superhard Mater.* **2013**, *35*, 131–136. [[CrossRef](#)]
80. Irmann, F. Zur Kenntnis der Magnesiumcarbid. *Helv. Chim. Acta* **1948**, *31*, 1584–1602. [[CrossRef](#)] [[PubMed](#)]
81. Rueggeberg, W.H.C. The carbides of magnesium. *J. Amer. Chem. Soc.* **1943**, *65*, 602–607. [[CrossRef](#)]
82. Kurakevych, O.O.; Le Godec, Y.; Strobel, T.A.; Kim, D.Y.; Crichton, W.A.; Guignard, J. High-pressure and high-temperature stability of antiferromagnetic Mg₂C by in situ X-ray diffraction and ab initio calculations. *J. Phys. Chem. C* **2014**, *118*, 8128–8133. [[CrossRef](#)]
83. Oganov, A.R.; Glass, C.W. Crystal structure prediction using ab initio evolutionary techniques: Principles and applications. *J. Chem. Phys.* **2006**, *124*, 244704. [[CrossRef](#)] [[PubMed](#)]
84. Hu, J.Z.; Merkle, L.D.; Menoni, C.S.; Spain, I.L. Crystal data for high-pressure phases of silicon. *Phys. Rev. B* **1986**, *34*, 4679–4684. [[CrossRef](#)]
85. Hu, J.; Spain, I. Phases of silicon at high pressure. *Solid State Commun.* **1984**, *51*, 263–266. [[CrossRef](#)]
86. Wentorf, R.H.; Kasper, J.S. Two new forms of silicon. *Science* **1963**, *139*, 338–339. [[CrossRef](#)]
87. Piltz, R.O.; Maclean, J.R.; Clark, S.; Ackland, G.; Hatton, P.D.; Crain, J. Structure and properties of silicon XII: A complex tetrahedrally bonded phase. *Phys. Rev. B* **1995**, *52*, 4072–4085. [[CrossRef](#)] [[PubMed](#)]
88. Pandolfi, S.; Renero-Lecuna, C.; Le Godec, Y.; Baptiste, B.; Menguy, N.; Lazzeri, M.; Gervais, C.; Spektor, K.; Crichton, W.A.; Kurakevych, O.O. Nature of hexagonal silicon forming via high-pressure synthesis: Nanostructured hexagonal 4H polytype. *Nano Lett.* **2018**, *18*, 5989–5995. [[CrossRef](#)] [[PubMed](#)]
89. Kurakevych, O.O.; Le Godec, Y.; Crichton, W.A.; Strobel, T.A. Silicon allotropy and chemistry at extreme conditions. *Energy Procedia* **2016**, *92*, 839–844. [[CrossRef](#)]
90. Kurakevych, O.O.; Le Godec, Y.; Strobel, T.A.; Kim, D.Y.; Crichton, W.A.; Guignard, J. Exploring silicon allotropy and chemistry by high pressure-high temperature conditions. *J. Phys. Conf. Ser.* **2017**, *950*, 42049. [[CrossRef](#)]
91. Kurakevych, O.O.; Le Godec, Y.; Crichton, W.A.; Guignard, J.; Strobel, T.A.; Zhang, H.; Liu, H.; Diogo, C.C.; Polian, A.; Menguy, N.; et al. Synthesis of bulk BC₈ silicon allotrope by direct transformation and reduced-pressure chemical pathways. *Inorg. Chem.* **2016**, *55*, 8943–8950. [[CrossRef](#)] [[PubMed](#)]
92. Linghu, J.; Shen, L.; Yang, M.; Xu, S.; Feng, Y.P. Si₂₄: An efficient solar cell material. *J. Phys. Chem. C* **2017**, *121*, 15574–15579. [[CrossRef](#)]
93. Kurakevych, O.O.; Strobel, T.A.; Kim, D.Y.; Muramatsu, T.; Struzhkin, V.V. Na-Si clathrates are high-pressure phases: A melt-based route to control stoichiometry and properties. *Cryst. Growth Des.* **2012**, *13*, 303–307. [[CrossRef](#)]

94. Yamanaka, S.; Komatsu, M.; Tanaka, M.; Sawa, H.; Inumaru, K. High-pressure synthesis and structural characterization of the type II clathrate compound $\text{Na}_{30.5}\text{Si}_{136}$ encapsulating two sodium atoms in the same silicon polyhedral cages. *J. Am. Chem. Soc.* **2014**, *136*, 7717–7725. [[CrossRef](#)]
95. Kasper, J.S.; Hagemuller, P.; Pouchard, M.; Cros, C. Clathrate structure of silicon $\text{Na}_8\text{Si}_{46}$ and $\text{Na}_x\text{Si}_{136}$ ($x < 11$). *Science* **1965**, *150*, 1713–1714.
96. McMillan, P.F. New materials from high-pressure experiments. *Nat. Mater.* **2002**, *1*, 19–25. [[CrossRef](#)] [[PubMed](#)]
97. Jouini, Z.; Kurakevych, O.O.; Moutaabbid, H.; Le Godec, Y.; Mezouar, M.; Guignot, N. Phase boundary between Na-Si clathrates of structures I and II at high pressures and high temperatures. *J. Superhard Mater.* **2016**, *38*, 66–70. [[CrossRef](#)]
98. Jouini, Z. Synthesis of Clathrates in the Silicon-Sodium System under High Pressure and High Temperature. Ph.D. Thesis, Sorbonne Université, Paris, France, Université de Carthage, Carthage, Tunisia, 2018.
99. Kubo, A.; Wang, Y.; Runge, C.E.; Uchida, T.; Kiefer, B.; Nishiyama, N.; Duffy, T.S. Melting curve of silicon to 15 GPa determined by two-dimensional angle-dispersive diffraction using a Kawai-type apparatus with X-ray transparent sintered diamond anvils. *J. Phys. Chem. Solids* **2008**, *69*, 2255–2260. [[CrossRef](#)]
100. Courac, A.; Le Godec, Y.; Renero-Lecuna, C.; Moutaabbid, H.; Kumar, R.; Coelho-Diogo, C.; Gervais, C.; Portehault, D. High-pressure melting curve of zintl sodium silicide Na_4Si_4 by in situ electrical measurements. *Inorg. Chem.* **2019**, *58*, 10822–10828. [[CrossRef](#)]
101. Shiell, T.B.; Zhu, L.; Cook, B.A.; Bradby, J.E.; McCulloch, D.G.; Strobel, T.A. Bulk crystalline 4H-silicon through a metastable allotropic transition. *Phys. Rev. Lett.* **2021**, *126*, 215701. [[CrossRef](#)] [[PubMed](#)]
102. Connétable, D. First-principles calculations of carbon clathrates: Comparison to silicon and germanium clathrates. *Phys. Rev. B* **2010**, *82*. [[CrossRef](#)]
103. Gryko, J.; McMillan, P.F.; Marzke, R.F.; Ramachandran, G.K.; Patton, D.; Deb, S.K.; Sankey, O.F. Low-density framework form of crystalline silicon with a wide optical band gap. *Phys. Rev. B* **2000**, *62*, R7707–R7710. [[CrossRef](#)]
104. Grigorian, L.; Eklund, P.; Fang, S. Clathrate Structure for Electronic and Electro-Optic Applications. U.S. Patent No. 6,103,403, 15 August 2000.
105. Srinu Bhadram, V.; IMPMC, Sorbonne Université Pierre and Marie Curie Campus, Paris, France. Unpublished work. 2021.
106. Boulard, E.; Denoual, C.; Dewaele, A.; King, A.; Le Godec, Y.; Guignot, N. Following the phase transitions of iron in 3D with X-ray tomography and diffraction under extreme conditions. *Acta Mater.* **2020**, *192*, 30–39. [[CrossRef](#)]
107. Grosjean, R.; Le Godec, Y.; Delacroix, S.; Gouget, G.; Beaunier, P.; Ersen, O.; Ihiwakrim, D.; Kurakevych, O.O.; Chaneac, C.; Portehault, D. A high-pressure pathway toward boron-based nanostructured solids. *Dalton Trans.* **2018**, *47*, 7634–7639. [[CrossRef](#)]
108. Grosjean, R.M. Boron-Based Nanomaterials under Extreme Conditions. Ph.D. Thesis, Université Pierre et Marie Curie, Paris, France, 2016.
109. Pietrucci, F. Strategies for the exploration of free energy landscapes: Unity in diversity and challenges ahead. *Rev. Phys.* **2017**, *2*, 32–45. [[CrossRef](#)]

Review

A Review of Binderless Polycrystalline Diamonds: Focus on the High-Pressure–High-Temperature Sintering Process

Jérémy Guignard *, Mythili Prakasam * and Alain Largeteau * 

UMR 5026, ICMCB, CNRS, Université Bordeaux, F-33600 Pessac, France

* Correspondence: jeremy.guignard@icmcb.cnrs.fr (J.G.); mythili.prakasam@icmcb.cnrs.fr (M.P.); alain.largeteau@u-bordeaux.fr (A.L.)

Abstract: Nowadays, synthetic diamonds are easy to fabricate industrially, and a wide range of methods were developed during the last century. Among them, the high-pressure–high-temperature (HP–HT) process is the most used to prepare diamond compacts for cutting or drilling applications. However, these diamond compacts contain binder, limiting their mechanical and optical properties and their substantial uses. Binderless diamond compacts were synthesized more recently, and important developments were made to optimize the P–T conditions of sintering. Resulting sintered compacts had mechanical and optical properties at least equivalent to that of natural single crystal and higher than that of binder-containing sintered compacts, offering a huge potential market. However, pressure–temperature (P–T) conditions to sinter such bodies remain too high for an industrial transfer, making this the next challenge to be accomplished. This review gives an overview of natural diamond formation and the main experimental techniques that are used to synthesize and/or sinter diamond powders and compact objects. The focus of this review is the HP–HT process, especially for the synthesis and sintering of binderless diamonds. P–T conditions of the formation and exceptional properties of such objects are discussed and compared with classic binder-diamonds objects and with natural single-crystal diamonds. Finally, the question of an industrial transfer is asked and outlooks related to this are proposed.

Keywords: diamonds; binderless; synthesis; sintering; high pressure; high temperature; physical properties



Citation: Guignard, J.; Prakasam, M.; Largeteau, A. A Review of Binderless Polycrystalline Diamonds: Focus on the High-Pressure–High-Temperature Sintering Process. *Materials* **2022**, *15*, 2198. <https://doi.org/10.3390/ma15062198>

Academic Editors: Alexander Obraztsov and Dina Dudina

Received: 22 December 2021

Accepted: 16 February 2022

Published: 16 March 2022

Publisher's Note: MDPI stays neutral with regard to jurisdictional claims in published maps and institutional affiliations.



Copyright: © 2022 by the authors. Licensee MDPI, Basel, Switzerland. This article is an open access article distributed under the terms and conditions of the Creative Commons Attribution (CC BY) license (<https://creativecommons.org/licenses/by/4.0/>).

1. Introduction

Carbon (C) is the fourth most abundant element in the universe and is mainly produced in massive stars during thermonuclear fusion of three He atoms. On Earth, carbon is the fifteenth most abundant element in crust; however, its total estimate is still under debate [1] due to its ubiquity in higher atmosphere layers to inner core under various forms.

Indeed, carbon can be present as organic (e.g., oil, coal), inorganic (CO₂, CO) and pure (C) components. Under its pure form, only three natural structures are reported: graphite, lonsdaleite and diamond, whereas a lot of synthetic carbon phases have been created over the last decades, e.g., graphene, fullerene, nanotubes, glassy carbon, amorphous carbon, Q-carbon and others.

Due to its electronic structure of 1s²2s²2p², pure carbon can adopt sp² and sp³ hybridization, conferring the possibility to be bonded with three or four neighbors, respectively. Hence, graphite (sp²)–diamond (sp³) phase transition, without any catalyst, needs a very high activation energy in the form of high pressure and high temperature in the orders of 10 GPa and several hundred degrees, respectively, compared to the transition line. This difference in hybridization type also explains the huge difference in their physical properties.

Diamonds have always fascinated people and scientists, first because natural diamonds are rare and are used as luxury products. In spite of being such a simple component,

natural diamonds offer the best mechanical and optical properties and very advanced thermal and electrical properties. Therefore, scientists have put a lot of effort into reproducing diamonds in the laboratory since the late nineteenth century. All these efforts have produced a lot of technical developments in high-pressure research, with a wide range of applications in Earth and material science [2–4]. Additionally, these efforts have produced a new desire in diamond geological settings as well as in mineral physics to determine and understand this phase transition.

The goal of this review is two-fold: (i) provide a brief overview of natural and synthetic diamonds as well as their properties and uses and (ii) provide a state of the art of synthesis/sintering techniques of binderless diamonds under high-pressure–high-temperature (HP–HT) conditions. These synthetic diamond compacts have received a lot of attention in the last two decades since the first success of direct conversion sintering (DCS) of graphite at 20 GPa and $T > 2000$ °C [5]. Indeed, these new synthetic diamonds offer a wide range of applications based on their exceptional mechanical, optical and electrical properties that can surpass those of classical polycrystalline diamond compact (PDC) and even those of natural diamonds. Therefore, the focus of this review will be on technical improvements over the decades as well as on the research of material with ultimate properties, in more reasonable conditions, in order to consider a potential industrial transfer.

2. The Different Forms of Pure Carbon

2.1. Natural

In nature, pure carbon exists only under three different crystalline structures: graphite, which is stable at ambient pressure and temperature, and two high-pressure–high-temperature minerals (lonsdaleite and diamond) (Figure 1, Table 1).

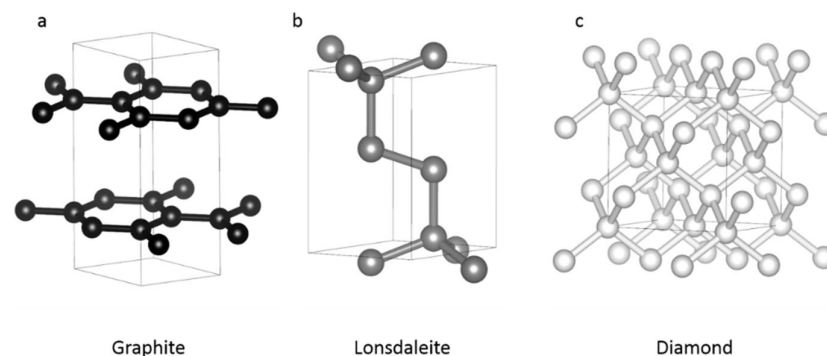


Figure 1. Crystal structures of the three natural forms of carbon. From left (a) to right (c), i.e., with increasing pressure and temperature, (a) graphite (black), (b) lonsdaleite (dark grey) and (c) diamond (light grey). Graphite and lonsdaleite have hexagonal structure, whereas diamond is cubic. Graphite has a sp^2 hybridization, whereas lonsdaleite and diamond have an sp^3 one.

Table 1. Lattice parameter of the three natural forms of carbon.

	Occurrence	Lattice	Space Group	Unit Cell (Å)	Density (g/cm ³)	Hybridization
Graphite	Ambient conditions	Hexagonal	(194) $P6_3/mmc$	$a = b = 2.456$ $c = 6.696$ ¹	2.26	sp^2
Lonsdaleite	HPHT	Hexagonal	(194) $P6_3/mmc$	$a = b = 2.51$ $c = 4.12$ ²	⁴ 3.30– ⁵ 3.52	sp^3
Diamond	HPHT	Cubic	(227) $Fd\bar{3}m$	$a = 3.56679$ ³	3.51	sp^3

^{1,3} from [6] ² from [7] ⁴, measured ⁵, calculated.

Graphite has a hexagonal structure (Table 1, space group # 194, $a = b = 2.456$ Å, $c = 6.696$ Å, [6]) and is formed by a staking of layers composed of regular hexagons of

carbon (Figure 1a). Each atom of a given layer is covalently bonded to three others, making an sp^2 hybridization type, whereas between layers, bonds are weaker and could be of Van der Waals type. This would be the reason for the low hardness of graphite (1–2 on Mohs scale).

Lattice structure of lonsdaleite (also called hexagonal-diamond) is also hexagonal (Table 1, space group # 194, $a = 2.51 \text{ \AA}$, $c = 4.12 \text{ \AA}$, [7]). This kind of intermediate structure between graphite and diamond has an sp^3 hybridization (Figure 1b). This form of carbon was discovered in Canyon Diablo (Arizona) meteor crater. Lonsdaleite is very rare and mostly found in meteorites and craters [8], even though it was also reported in ultra-high-pressure context on Earth [9]. It is therefore a high-pressure high temperature form of carbon but its stability field, if any, is still poorly constrained [10]. Main difference with diamond is the stacking of atoms, with an AB–AB sequence. Properties of lonsdaleite are also debated, and there are discrepancies between measured and calculated [11] physical properties, such as for density (3.3 and 3.52 g/cm^3), hardness (7–8 and 12 on Mohs scale) and indentation resistance (predicted to be 152 GPa). If these properties were confirmed, lonsdaleite would be harder than diamond.

Diamond, the hardest known phase among natural and synthetic materials, has a face-centered cubic lattice (Table 1, space group # 227, $a = 3.56679 \text{ \AA}$, [6]). In this compact structure ($\rho = 3.51 \text{ g/cm}^3$), atoms are covalently bonded with three others with an average bond length of $\sim 1.54 \text{ \AA}$, due to sp^3 orbitals hybridization (Figure 1c). Hence, atoms form tetrahedral structure (Figure 1c) confer incredible physical properties to this mineral. Stacking sequence is of ABC–ABC–ABC type, making a complex suite of polytypes between lonsdaleite (2H) and diamond (3C). Diamond stability field covers a wide range of P–T conditions that can be enlarged due its metastability field.

2.2. Synthetic

High-purity carbon forms were fabricated over the last decades with their own properties, and several hundred allotropes were predicted through calculation. A lot of reviews were focused on this topic, including synthetic and predicted forms ([12] and reference therein). This section will focus on the brief description of common synthetic forms of carbons and those that are also commonly used (other than graphite) as starting materials for the synthesis and/or sintering of high-pressure phases such lonsdaleite and diamonds. In most cases, these precursors are either highly disordered or contain already a certain amount of sp^3 bonds. These two features could play a role to decrease the P–T conditions of formation of diamonds compared to graphite (high order, only sp^2 bonds). More details on this respect are given in Section 5.

Graphene corresponds to a mono-layer of graphite, constituting a 2D structure of hexagons. In graphene sheets, each atom of carbon is covalently bonded to its three nearest neighbors. Graphene is known for its exceptional electronic (high electric conductivity), optical, thermal (high conductivity) and mechanical (highest young modulus) properties.

Pyrolytic carbon is a synthetic form of carbon, close to graphite, produced by the pyrolysis of hydrocarbon. The main difference with graphite is the presence of covalent bonds between graphene layers, making pyrolytic carbon a highly orientated structure with unusual physical properties, e.g., higher thermal conductivity than graphite, and magnetic levitation. Pyrolytic carbon is mainly used for military, plastics, metallurgy, electronic and medicine.

Fullerenes and carbon nanotubes (CNTs) have similar bonds to graphene but are 3D bodies with spherical and cylindrical shapes, respectively. In these structure, carbon atoms and bonds form, in addition to the classic hexagons, pentagons and/or heptagons that prevent a 2D structure as in graphene. These two compounds form two big families, with more or less complex structure, e.g., from C₂₀ to C₇₀ for fullerenes and from single (SWCNTs) to multi-wall nanotubes (MWCNTs). In most cases, they were fabricated by vaporization of carbon at high temperature and neutral atmosphere (He or Ar). Nanotubes were also synthesized using CVD method. Due to their physical and chemical proper-

ties, fullerenes and nanotubes are the second most used nanoparticles, after silver [13]. Fullerene applications are widespread, including for pharmacy, medicine, cosmetics and electronics [14]. Applications of CNTs are more recent and are still under development but are already used as composite fibers in polymers [15,16] and could be also promising in electronics [17,18], environment [19] and medicine [20]. It has to be noted that fullerene exists in nature, particularly in space. However, it was first synthesized in lab before being identified as fullerene in space.

Amorphous carbon (aC) is a carbon allotrope that does not have a crystalline structure [21]. In mineralogy, this term is used for coal that is, in reality, a mixture of very fine polycrystalline graphite. For the past few decades, it has been possible to synthesize thin films of aC using CVD [22] or arc deposition [23] methods. Atomic bond lengths and distances are unique compared to all other carbon allotropes. According to the synthesis methods, the ratio sp²-sp³ hybridization can be controlled. Applications are wide and concern textiles, healthcare, water filtering and food packaging [24]. More recently, a new form of aC was synthesized by a process of surfusion: the Q-Carbon (QC), which seems to exhibit physical properties at least similar to those of diamonds [25,26].

Glassy- (or vitreous) carbon (GC) is a non-graphitizing, non-graphitizable form of carbon that is fabricated through the carbonization of polymeric precursors at high temperature (>1200 °C). Staking of disorientated graphite layers, a huge disordered structure and a high level of closed micro-porosity, are the main “lattice” features of GC, conferring a low density of 1.5 g/cm³. GC has unique properties, e.g., high temperature and chemical resistance, impermeability to gases and liquid, low friction and low electrical resistance. GC is mainly used as electrode in electrochemistry and as crucible in high-temperature experiments.

Other precursors can be used to synthesize high-pressure phases of carbon. However, they are organic compounds such as polycyclic aromatic hydrocarbons (PAH), stearic acid, diamondoids, methane (CH₄) and even explosives charges (Trinitrotoluene TNT or Hexogen RDX).

3. Natural Diamonds: Geological Settings and Classification

3.1. Natural Diamonds: Some Geological Settings

Natural diamonds occur in various sources such as Earth mantle [27,28], crater impact [29,30], meteorites [31] and even interstellar environment [32], as evidenced by diamond presolar grains.

Conditions of formation of natural diamonds on Earth are very well documented and mainly based on mineralogy and chemistry of diamond inclusions. It has been shown that 99% of diamonds originated from subcontinental lithospheric mantle (up to 200–250 km depth), with the last percent corresponding to a deeper rare origin in the sublithospheric mantle (up to at least 700 km depth) (Figure 2a). In the former case; i.e., lithospheric diamonds, three groups can be distinguished: peridotitic (65%), eclogitic (33%) and websteritic (2%) diamonds ([33], Figure 2b). Among the peridotitic suite, another three-part subdivision, according to the paragenese, was also made between harzburgitic (56% of all natural diamonds), lherzolitic (8%) and wherlitic (0.7%) diamonds origin ([33], Figure 2c). Based on the geothermobarometry of minerals constituting diamond inclusions, pressure–temperature conditions of diamond formations were estimated around 5–6 GPa and 1000–1200 °C, with few variations according to their environment of formation [33].

Hence, diamonds could form from various mechanisms such as (i) direct conversion through the graphite–diamond phase transition at relevant conditions, (ii) precipitation from a fluid or melt saturated with carbon and (iii) oxidation-reduction reactions involving methane and/or carbonates. The first mechanism is the most unlikely as it has been shown experimentally that an overpressure of at least 10 GPa is needed to directly transform graphite to diamond (>15 GPa and ~2000 °C, [5]), conditions that are far from natural conditions of formation. Therefore, the presence of melts (metallic, carbonate or silicate) and/or fluids (COH) associated with relevant oxygen fugacity conditions is required to

precipitate diamonds in conditions recorded by their inclusions, i.e., closer to the graphite–diamond boundary [33].

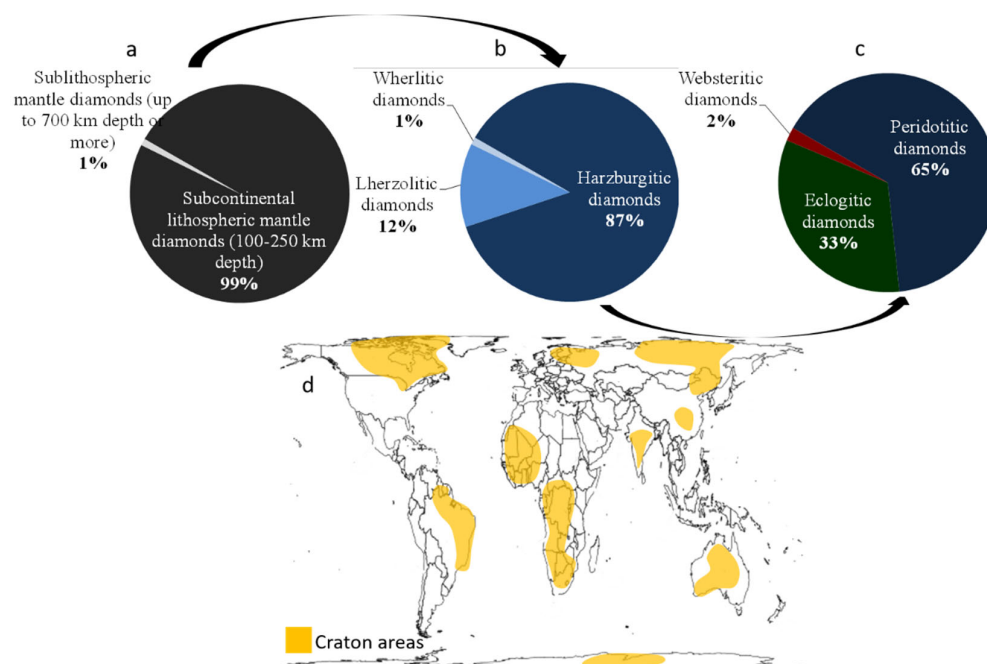


Figure 2. Main geological settings for the formation of natural diamonds. (a) Different setting as a function of depth of formation. (b) Geological settings for the lithospheric mantle diamonds. (c) Parageneses observed for the most common peridotitic diamonds. (d) World map for the localization of the main cratons on Earth. These cratons are the main diamond deposits.

Polycrystalline natural diamonds can also be found but are very rare. One of them is the enigmatic carbonado diamond, which is mined for industrial purpose [34]. Briefly, carbonados are black and porous, with 1 micrometer grain size of randomly orientated diamonds and with silicate and metal inclusions as well as a high number of Poly-Aromatic Hydrocarbons (PAH). It is found in Brazil, Central African Republic and Siberia. Origin of carbonados is still being debated and could be either from cold subducting slab [35], from regional metamorphism in Earth’s crust [36] or from seed-heating by fission of radiogenic elements [37]. The last potential origin is formation from meteoritic shocks as polycrystalline diamonds (with nanograins) have been also found near impact craters [30].

Diamond deposits are usually two-fold: primary or magmatic and secondary or alluvial [38,39]. P–T conditions for the formation of diamonds are easily reached in the Earth’s upper mantle. However, there are only few diamond deposits that are in close proximity to ancient cratons, with very stable (no tectonic) old thick continental crust with mantle keel beneath (Figure 2d, [40]).

In most cases, these deposits (primary) are related to kimberlites, a volcanic rock with an ultrabasic composition that is very rich in volatiles (H_2O and CO_2), leading to very explosive eruptions. Diamonds are thus upwarped by these brutal eruptions, i.e., by very fast magma ascent, and are concentrated in subsurface pipes and dikes that are exploited today as mines. These deposits are mostly located in Africa, Russia, Canada and Australia, making these regions the biggest natural diamond producers (Figure 3). Other types of primary deposit exist, such as basalt/eclogite in subduction zone, lithospheric mantle and convecting mantle for deep diamonds. Alluvial deposits (secondary) are directly related to primary ones because erosion of these latter would accumulate diamonds in sedimentary traps. Finally, impact-induced diamond formation and ultra-high-pressure crustal diamonds are more anecdotal.

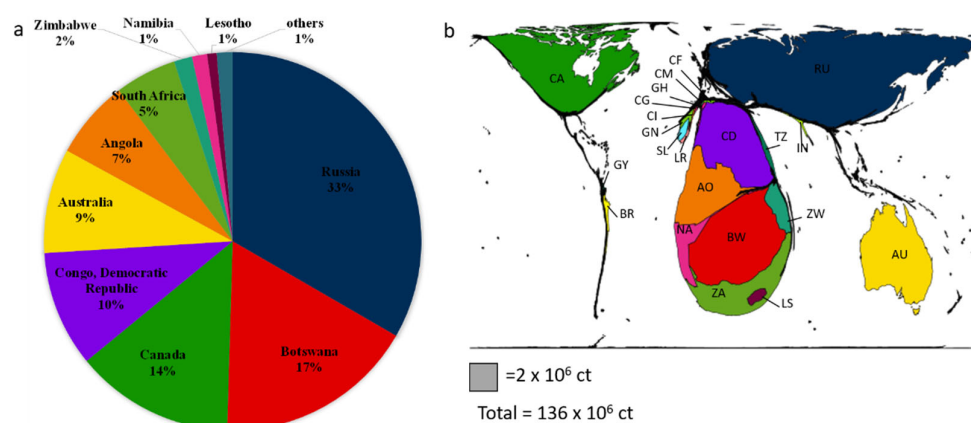


Figure 3. Localization of the main countries producing diamonds through their mines. (a) Among the top ten diamond mining countries, seven are from Africa, which reflects the cratonic geological setting. Others represented countries from place 11 to 22 are Sierra Leone, Tanzania, Guinea, Brazil, Liberia, Guyana, Ghana, India, Central African Republic, Ivory Coast, Cameroon and Congo. Once again, Africa is largely represented. Total of diamonds from mine was ~136 Million Carats in 2019. Source: [41]. (b) Cartogram representing these 22 biggest natural diamond mining producers, realized thanks to [42] algorithm. RU = Russia, BW = Botswana, CA = Canada, CD: Congo, Republic Democratic, AU = Australia, AO = Angola, ZA = South Africa, ZW = Zimbabwe, NA= Namibia, LS = Lesotho, SL = Sierra Leone, TZ = Tanzania, GN = Guinea, BR = Brazil, LR = Liberia, GY = Guyana, GH = Ghana, IN = India, CF = Central African Republic, CI = Ivory Coast, CM = Cameroon and CG = Congo. It is of note that this map is almost perfectly correlated with the localization of the main craton area.

In 2019, about 136 million carats, i.e., 27 tons (1 ct = 0.2 g), was extracted from different mines all over the world [41]. Most of this extraction comes from primary deposits, but the yield in such environment is very low and typically in the order of 1ct for 10 tons of rocks. This is, for example, lower than gold deposits, which are around few grams per ton of rock. Among the 10 biggest producers of natural diamonds, seven countries are from Africa (Figure 3). In addition to having an important environmental impact [43], diamond extraction also has huge societal consequences in these countries, where “conflict diamonds” or “blood diamonds” caused wars, corruption, underdevelopment and death [44,45].

3.2. Diamond Classification

Diamonds can be classified according different features that were primarily established for jewelry. Here, we will briefly describe the 4-C rule (carat, clarity, color and cut) and a usual classification based on optical properties (the type classification).

3.2.1. The 4-C Classification

The 4-C rule applies essentially in jewelry. The first C refers to “carat”, the unit that measures the weight of diamonds, with 1 carat equal to 0.2 g. The second C is for “color” and is based on 23 levels (from D to Z), from colorless to light yellow diamond. This can be related to the type classification too (cf. below). The third C is “clarity”, which describes the level of impurity potentially contained in diamonds. Each level is denoted by letters and numbers. Finally, the fourth C characterizes the “cut” of diamonds that will reveal all the brightness and scintillation.

3.2.2. The Type Classification

This classification refers to the optical properties of diamonds and therefore to their impurities as substitutions for their lattice. It has to be noted that this classification suits both natural and synthetic diamonds. Thus, two different types were determined based on the presence or absence of Nitrogen (N) in the lattice, i.e., the most common impurity found

in diamonds. For more details about type classification, the reader can refer to Section 6.1 and [46].

Type I: In type I diamonds, nitrogen (N) is present in the lattice to a level that can be measured using IR absorption spectroscopy (>500 ppm). Nitrogen in diamond lattice usually gives a yellowish color. This category was also divided into two subgroups according to the arrangement of Nitrogen atoms in the lattice. Hence, Type Ia are characterized by aggregated N impurities in the lattice, either in N-pairs (type IaA) or $4N + V$ (V for vacancy, type IaB), whereas in type Ib, nitrogen atoms are isolated from one another in the lattice. Most of natural diamonds are type Ia (~98%), and, more specifically, IaA, whereas most of synthetic diamonds using HP–HT techniques are Ib.

Type II: In this type of diamond, there is no detectable nitrogen impurity, at least by spectroscopic techniques (<2 ppm). Again, two subgroups were created based on the absence of detectable impurities (Type IIa) or by the presence of isolated Boron (B) in the lattice (Type IIb). Hence, type IIa is considered to be the purest type of diamond; it is also an electrical insulator and is very rare in nature, whereas most synthetic diamonds by CVD techniques are of this type. The boron contained in type IIb gives a blueish color to this diamond, resulting in specific electrical properties that are very rare in nature and in synthetic diamonds.

4. HP–HT C-Phase Diagram and the Graphite–Diamond Equilibrium Line

The first HP–HT carbon phase diagram as well as the notion of stability field of graphite and diamonds was provided using thermodynamics [47]. It was then adapted using the principle of metastability [48], which is still under consideration more than a century later.

Still using thermodynamic and specifically calculation of heat of formation [49] and reaction kinetics with temperature [50], the diamond/graphite equilibrium line was estimated. This latter study proposed the conditions for direct transition as well as the effect of using a metal catalyst [50]. The melting temperature of graphite at ambient pressure was also estimated at 4273 °C, a value relatively close to real one.

In 1940s and 1950s, the focus was on the Clapeyron slope of the graphite–diamond equilibrium line with very contradictory results [3,51,52]. It was only in the mid-1950s and early 1960s that graphite-to-diamond phase transition was experimentally observed by ASEA AB [53,54] and GE Company [55,56]. The success of these two experiments was possible after huge instrumental development to reach pressure up to 8–10 GPa and temperature of 2000 °C. In this way, two different high-pressure apparatuses were used by the two teams: a 6-anvil spherical and the famous “Hall” belt-type [4] press (Figure 4). The 6-anvil spherical set up was quickly given up due to handling difficulties and high level of anvil mechanical failure during experiments (Figure 4a,b). On the other hand, the “belt” type apparatus is easy to manipulate, with limited risk of failure and higher reproducibility, making this press the most used for industrial applications (Figure 4c,d). These experiments were performed using iron catalyst and no seeds, resulting in the formation of diamond grains of few hundred microns (inset Figure 4b,c). The very first direct catalyst-free conversion from graphite to diamond occurred a few years later [56], after an important instrumental development allowing pressure of almost 20 GPa and temperature of nearly 5000 °C to be reached using flash-heating techniques. The triple point was determined to be at 12.5 GPa and 4373 °C, and diamonds were recovered from different experiments even though the yield was lower than 60%.

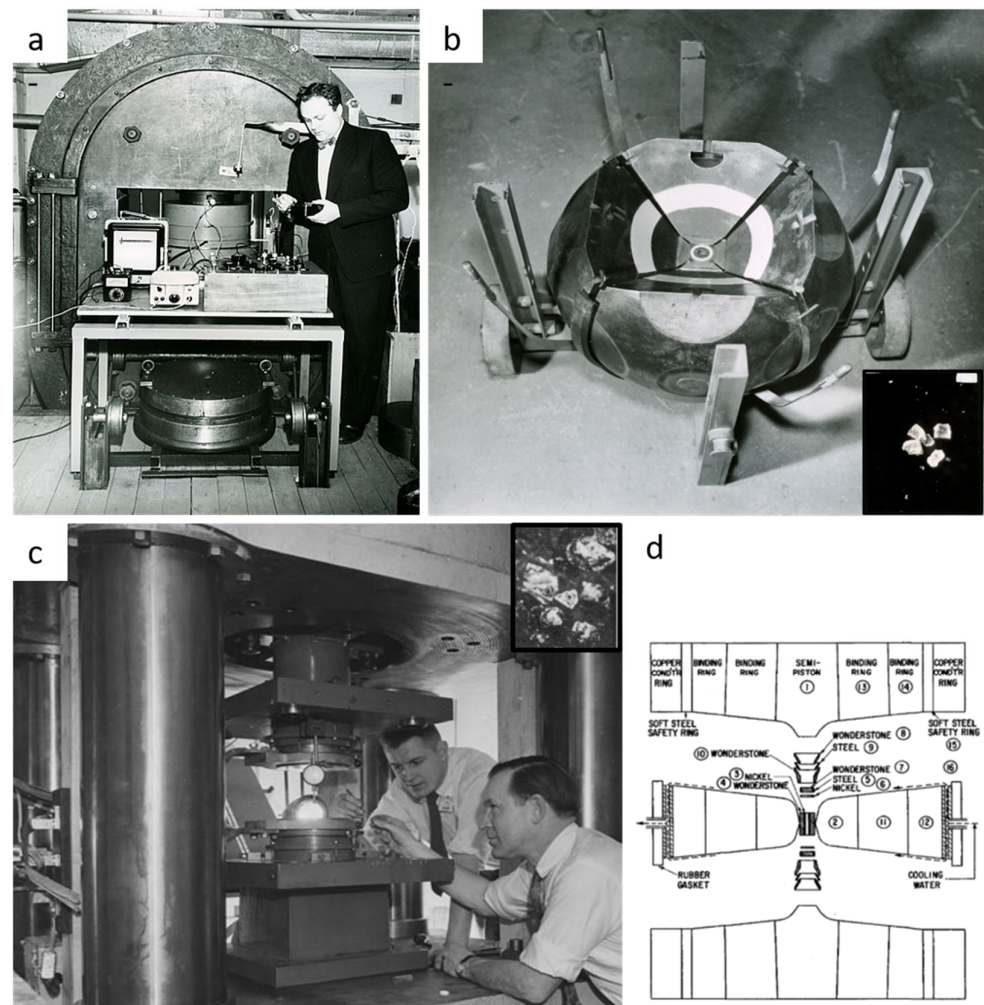


Figure 4. The historical first successful experiments of synthetic diamonds. (a,b) From ASEA company (Sweden) using the 6-anvils sphere apparatus [53,54]; a-picture from https://commons.wikimedia.org/wiki/File:ASEA_Quintus_press_for_diamonds_1953.jpg (accessed on 1 December 2021), b-Reproduced from [54], with the permission of AIP Publishing (c,d) From GE company in 1955 using the famous Hall “belt”-type apparatus [4,55,56]; pictures from <https://www.ge.com/news/reports/diamonds-werent-forever-in-the-ge-store-but> (accessed on 1 December 2021). Inset are shown the recovered diamond after experiments with a typical size of few hundred microns. These few studies mark the starting point of the development of diamond synthesis for scientific and industrial purposes (Section 5) as well as the building of more and more precise HP–HT phase diagram of carbon (Figure 5).

In the 1960s and 1970s, studies of mineral inclusions (HP–HT phases, compositions) trapped in natural diamonds also produced constraints on graphite–diamond equilibrium line (Section 3). Discovery of lonsdaleite in 1967 added complexity to C-phase diagram at high pressure and temperature, and today it is still unclear if this phase is stable or not (Figure 5).

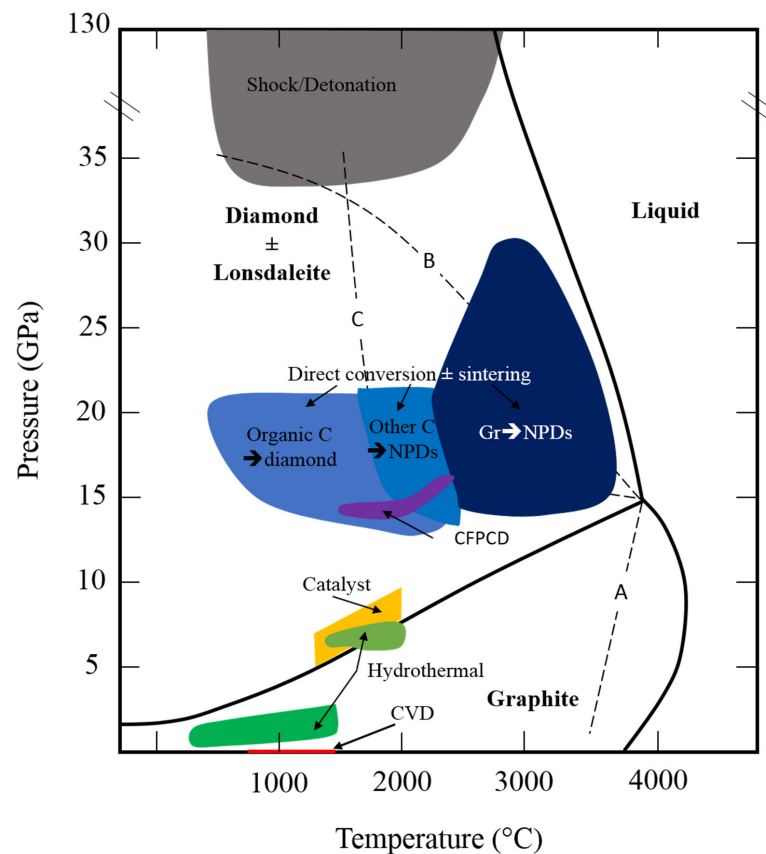


Figure 5. P–T phase diagram of carbon are adapted from [57]. Solid lines are the limits between stability fields. A and B dashed represent the limits between metastability fields, respectively, graphite + metastable diamond and diamond + metastable graphite. C dashed line represents a hypothetical limit between lonsdaleite and diamond stability field. Colored areas show the P–T conditions for the synthesis of diamonds according to the different techniques used.

More recently, it was reported that diamonds could be stable up to 2 TPa [58], a pressure at which other stable phases were predicted [59]. This question of diamond stability and/or metastability is thus more than ever under debate and depends on much more parameters than previously thought. Such metastability field is the basis of a lot of different processes for the synthesis and sintering of diamonds under disequilibrium conditions (Section 5).

5. On the Way to Catalyst-Free/Binderless Synthetic Diamonds

Since late ninetieth and early twentieth centuries, the original experiments from [2,60,61] tried to synthesis and sinter diamonds in laboratory. A large variety of experimental and analytical set-ups were developed toward this aim that allowed for the refinement of the P–T phase diagram of carbon as well as better understanding of graphite-to-diamond transition mechanisms and their exceptional diamond properties (Figure 5).

The main strategy to fabricate synthetic diamonds was to mimic the natural conditions of formation of diamonds in laboratory, i.e., high-pressure–high-temperature (+/– fluids, static or dynamic/shock) and under low pressure (LP) conditions in H₂ atmosphere (as an analogue of interstellar environment). The main experimental processes, i.e., static HP–HT, dynamic HP–HT, and LP, to synthesize diamonds, were all developed in the 1950s–1960s, respectively, by [55,62,63]. Static HP–HT and LP (also called CVD) are the only two processes that allow one to sinter diamonds, i.e., to fabricate diamond compact. The other processes, such as shock/detonation, can only produce powders with different purities, sizes and distributions.

More recently, in the 1990–2000s, other experimental strategies, based on the metastability features of diamonds, synthesis and sinter diamonds, were deployed in very unexpected P–T conditions (SPS, hydrothermal or other unconventional set-ups) (see below). Despite the notable originality of these experiments, only diamond powders were produced with highly variable yields and grain sizes (see below).

Nowadays, production of synthetic diamonds (also called man-made or lab-grown diamond) is far higher than that of natural diamonds, with worldwide production ~18 billion of carats, i.e., 3600 tons, in 2019, essentially for industrial uses [64]. China largely dominates the world market of synthetic diamonds, with more than 50% of the global production, followed by India and USA (Figure 6a). HP–HT and CVD (LP) are the major techniques used. HP–HT techniques are the leading techniques in synthetic diamonds production. However, CVD process has become increasingly popular following the recent developments to fabricate large pure diamonds [65]. Natural diamonds are essentially used as gems in jewelry (99%), and only 1% are used in industrial applications, whilst synthetic diamonds are widely used for industrial applications and are also employed in various applications [66] (Figure 6c). Among them, about 60% are dedicated to stone and building materials processing, 15% for electromechanical industry and 2% for geological drilling. The last 20% are dedicated to more restrictive applications that are very different, such as military and defense, medical testing, in pharmacy, cosmetic, electronics, high-pressure science, optics and electronics.

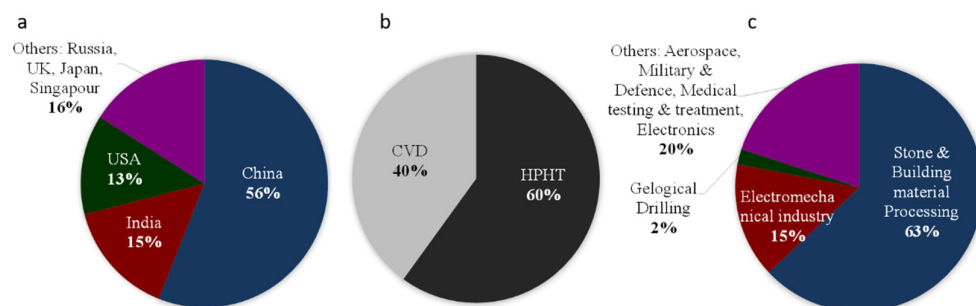


Figure 6. Synthetic diamond production in 2019 represents ~18 billion carats [64,65]. (a) By country, China accounts for more than the half of the worldwide production. (b) By technique, similar amount is produced using HPHT and CVD. It is of note that China represents 98% of the HPHT synthesis of diamonds. (c) By application, from usual tools (e.g., grit, abrasives and drilling) to new technology uses (e.g., in electronics, medicine). Note that synthetic diamond production for jewelry is negligible.

In this section, the different experimental techniques for the sintering of binderless diamonds are described, based on a pressure scale, from low to ultra-high pressure. For each of these techniques, starting materials and P–T conditions are described as well mechanisms of formation of diamonds. The yield is also very important and is discussed along with the capabilities of sintering. Special focus is made on HP–HT processes (Section 5.3), techniques that are the most promising for the sintering of big pieces of binderless diamonds.

Indeed, the role of high pressure in synthesis and sintering processes is fundamental [67–69]. Concerning synthesis, pressure can stabilize phases at lower temperature or simply phases that do not exist at atmospheric pressure. Typically, in Earth sciences, it concerns all phases present in deep interiors of planets. In materials sciences, high pressure (\pm high temperature) is used to synthesize and recover new phases with specific mechanical, optical, electrical or thermal properties that can have many applications.

In terms of sintering, it is known that application of an external pressure on a powder enhances its densification. Indeed, pressure allows for the better packing of grains that can deform and slide to fill free space. Moreover, pores are easily closed by the pressure and therefore the influence of pores' surface tension becomes negligible. Finally, by applying pressure, other sintering parameters such as temperature and time can be decreased in order to avoid grain growth and obtain objects with better properties.

5.1. Low Pressure Processes: CVD Diamonds

CVD technique is, with HP-HT, the only technique that transforms a gaseous carbonaceous compound (CH_4) to diamond and that leads to a dense body with millimeter thickness. Important developments have been made in the last 30 years to obtain large crystals in terms of surface and thickness (up to few 3–4 mm), with high purity (higher than HP-HT). However, sizes of CVD diamonds remain clearly smaller than those of HP-HT diamonds, either with binder or not. Hence, commercialization of CVD diamonds now represents a large market of synthetic diamonds (Figure 6b).

Briefly, CVD process is a low-pressure–medium-temperature (LP–MT) process that involves ionized gases to allow deposition on pre-existing seeds. Monocrystalline and polycrystalline diamonds can be made with this technique based on the substrate preparation. The first synthesis of CVD diamonds was made by William Eversole at Union carbide in early 1950s using hydrocarbons and carbon monoxide, but the project was given up [70]. The modern origin of CVD techniques was in the early 1960s in three independent labs in USA, USSR and Japan, respectively [63,71]. With these studies, the major role of hydrogen was discovered for synthesis of diamonds by CVD. These studies led to understanding that hydrogen maintains unreconstructed diamond surface structure, i.e., makes possible deposition of new carbon atom (from CH_4 in most cases) and growth of diamonds crystals at 40 Pa and 1050 °C [62]. During next few decades, it was only possible to grow very thin diamond layers. In the 1980s–1990s, growth rate steeply increased thanks to new technological development of wide range variety of plasma and electric discharges. Thus, four techniques for growing diamonds at low pressure exist [72,73]. All these techniques have their own advantages and potential applications.

Hot Filament or Foil CVD (HFCVD). In this case, a metallic filament (W, Ta, Mo or Re, for example) is used to dissociate gases and form radicals suitable for diamond growth. With this technique, the growth rate is typically very low (0.1 to 1 $\mu\text{m}/\text{h}$) but may be increased by the increase of gas flow (as for all techniques).

Chemical Activation CVD (CACVD). Using a combustion flame that permits an exothermic chemical conversion of gases. Here, the growth rate is much higher than in the case of HFCVD and is from 10 to 100 $\mu\text{m}/\text{h}$.

Electromagnetic Induced CVD. There are three types of wavelengths used: radiofrequency (RF), microwave (MW) and laser-induced plasma (LIP). A very wide range of growth rates was observed with this technique, from 0.01 to 100 $\mu\text{m}/\text{h}$.

Electrical induced CVD. This technique is based on direct-current (DC) plasma discharge between two electrodes. This technique shows the most efficient rate, with most of values between 10 and 1000 $\mu\text{m}/\text{h}$.

Until now, CVD diamonds were the purest diamonds that could be synthesized. Indeed, contrary to HP-HT diamonds, CVD diamonds are type II, i.e., with the absence of nitrogen (see Section 3.2.2). With this aim of purity, recent development has been made to increase the growth rate and control the abundance and nature of chemical and physical defects [74]. Finally, by coupling high growth rate and high purity, fields of application have become important for CVD diamonds, especially for new technologies (e.g., thermal bridges, quantum, and optic windows) rather than in building or cutting tools, which are more dedicated to HPHT diamonds.

5.2. Medium Pressure Processes: SPS and Hydrothermal Diamonds

5.2.1. SPS Diamonds

Spark Plasma Sintering (SPS) is a technique involving a pulsed direct current that passes through a powder inserted in a graphite mold ($P_{\text{max}} = 100 \text{ MPa}$, very high temperature), more rarely in tungsten carbide ($P_{\text{max}} = 1 \text{ GPa}$, $T_{\text{max}} = 500 \text{ °C}$). There is a huge literature on this technique to understand densification mechanisms on conducting and insulating samples [75,76]. Briefly, the sample is heated by Joule effect and the current density in the sample produces a “plasma” between particles. This promotes the formation of neck and grain boundaries between them and densifies the powder [77]. This is valid for

conducting and insulating material. Therefore, using SPS sintering conditions (temperature, time) to obtain a fully dense body is drastically less effective than the classic hot-pressing techniques [75,76].

With the development and democratization of the Spark Plasma Sintering (SPS) technique at the beginning of 21st century, few studies from one lab have synthesized/sintered diamond at relatively low-pressure–high temperature [78–85].

In their studies, no catalyst or diamond seed was used and different precursors were tested for both the synthesis and sintering of diamonds. It was observed that carbon nanotubes (MWCNTs) and C60 transform partially to diamond at very unusual conditions, i.e., at pressure around 50–80 MPa and temperature above 1150 °C in the vacuum SPS chamber. Using MWCNTs with different purity degrees leads to formation of very fine-grained diamonds, i.e., <10 µm but with unclear evidences from Raman and/or XRD analysis [78–80]. Transition from C60 is more obvious, with a yield of 30%, and is thought to be direct, without any intermediate product, and due to some sp³ hybrids present in the C60 [82]. Once all the sp³ bonds of the C60 are converted to diamonds, reaction stops and no more formation and/or growth of diamonds is observed, limiting this process. This typically leads to diamond size of 250 microns in minor content, with the rest of C60 being transformed into graphite, the main element. In any case, no sintering of diamonds particles is observed, and the diamonds are present only as isolated grains. Sintering and stability of nanodiamonds prepared from detonation was also tested using SPS at 60 MPa and up to 1400 °C [84]. It was shown that nanodiamonds remain stable up to 950 °C, but the recovered sample was a loose powder. At higher temperature, nanodiamonds start to destabilize to carbon onion and are fully transformed at 1400 °C. Once destabilized, graphite sintering occurs. This highlights the real difficulty of both stabilizing and sintering diamonds in metastable conditions. More pressure is probably the first parameter to consider.

Either using MWCNT, C60 or nanodiamonds, classic SPS method seems difficult to transfer at the industrial scale. Indeed, the starting materials are expensive, and even though sample size could be large in SPS chamber (>cm²) and P–T conditions are very low, transformation is very limited and has not been improved, even using Fe-Ni catalyst [81,85]. Finally, there is a need to isolate diamonds from graphite using strong chemical reagents.

In conclusion, by combining SPS and carbon sources that have already some sp³ bonding, such as C60, a transformation into diamonds particles is possible at unexpected P–T conditions ($P \leq 100$ MPa, $T \sim 1200$ – 1300 °C), i.e., at very disequilibrium conditions. However, no conversion from sp² bonds is observed in such conditions. In this context, only isolated nano- to micro- crystals are synthesized without any sintering evidence. A point of interest would be to use other carbon sources as starting materials with a much greater number of pre-existing sp³ bonds such as diamondoids (fourth bullet of Section 5.3.3). This would probably increase the yield of diamond formation and start the sintering between grains.

5.2.2. Hydrothermal Diamonds

Synthesis of diamonds using hydrothermal techniques was motivated since it was shown that C-H-O fluid could play an important role in the formation of natural diamonds [33,86]. This field of research was of significant interest in late 1990s and early 2000s in order to constrain mechanisms of formation of diamonds in such environments.

From a general point of view, two different techniques were used: a classic hydrothermal treatment at low-medium pressure (LP, MP) and temperatures (LT, MT) ($P < 1$ GPa, $T < 800$ °C) and high-pressure–high-temperature conditions ($P > 5$ GPa and $T > 1200$ °C) (Figure 3).

Concerning usual hydrothermal conditions for diamond syntheses, three different starting materials can be distinguished, as follows.

The first one consists of mixing diamond seeds with different liquids such as 10 M NaOH, C-H-O rich, water, 1,1,1-trichloroethane, hexachlorocyclohexane or dichloromethane. These experiments were mostly performed in piston cylinder (1–2 GPa) (Figure 7a) or

Roy-Tuttle autoclave (few hundred MPa) at temperatures up to 1450 °C (mostly to 300 °C) and for duration between 1 and 21 days, mostly 3 days [87–94]. In all these studies, it is unclear if diamonds grow on seeds or not.

The second type of precursor is to use SiC and water, typically under pressure of 100–500 MPa, and temperature between 300 and 800 °C, in a Tuttle-Roy autoclave [95–98]. In any case, hydrolysis of SiC produced new phases that may be amorphous carbon, graphite and diamonds. It is worth noting too that the diamond yield is very low and that a combination of different analytics was necessary to determine its presence (XRD, RAMAN, SEM and TEM), mostly under nanograins form.

A more anecdotal synthesis of diamonds was to mix in an autoclave at 200 °C for 12 h EDTA, hydrochloric acid (pH = 3) and deionized water [99]. After centrifugation, an almost amorphous phase was recovered, corresponding to approximately 5-nm-sized diamonds.

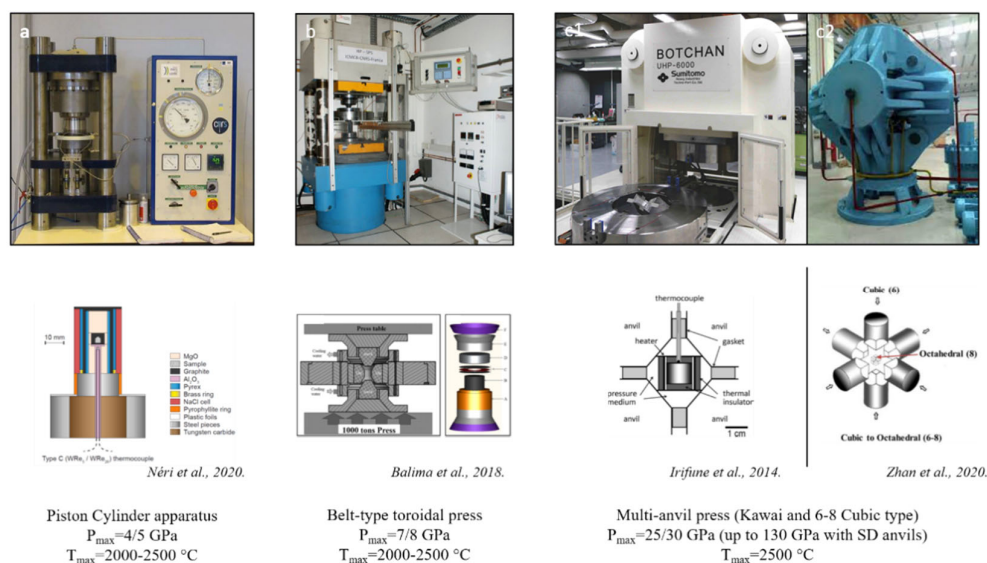


Figure 7. High-pressure devices commonly used for diamond synthesis under high-pressure–high-temperature (HPHT) conditions. From left to right, the maximum pressure achievable increases from 4–5 GPa in Piston cylinder (a) to 25–30 GPa in conventional multi-anvil press (c1,c2). In between (b), “belt”-type toroidal press is the most common apparatus used by industrial manufacturer. (a) Personal picture, assembly adapted from [100]; (b) personal picture, assembly adapted from [101]; (c1) picture from <http://www.grc.ehime-u.ac.jp/legacy/news79.html> (accessed on 1 December 2021), assembly adapted from [102]; and (c2) adapted from [103]. (a,b) are suitable for catalyst-diamond synthesis, whereas (c1,c2) have been developed more recently for the synthesis and sintering of large volume of binderless diamonds. (See Section 5 for more details).

In all these studies, even though diamond formation was difficult to assess, a range of composition in the C-H-O system was determined for diamond formation. This range of composition was extended under oxidizing conditions [94].

In HP–HT hydrothermal synthesis, graphite was used as precursor and mixed with various fluid generated substances such as water, silver oxalate, oxalic acid, and anthracene [104–109]. Similar pressure and temperature conditions have been used in all studies, i.e., $P = 5.7\text{--}7.7 \text{ GPa}$ and $T = 1200\text{--}2000 \text{ }^{\circ}\text{C}$, and experiments were performed either in “belt”-type or split-sphere multi-anvil apparatus (Figures 4 and 7b,c1,c2). In all these studies, diamond crystals were obtained. Further, diamond formation depends on usual thermodynamic conditions (P&T), on fluid compositions and on duration. Briefly, it was observed that under 5.7 GPa and 1150–1420 °C and under 7.7 GPa and 1400–1600 °C, graphite and diamonds coexist. Moreover, diamond growth rate was almost exponentially temperature-dependent, being hundreds of hours to few minutes between 1150 and 2000 °C [107–109]. Diamond crystallization depends also on fluid composition. Indeed, the crystallization

rate of diamond decreases according to the following fluid composition: $(K_2CO_3(Na_2CO_3)-H_2O-CO_2-C) > (CO_2-C) \approx (H_2O-CO_2-C) \approx (H_2O-C) \approx (CaMg(CO_3)_2-H_2O-CO_2-C) > (CH_4-H_2O-C-CH_4-H_2-C)$ [108]. This wide-range fluid composition was also responsible of colored diamonds (colorless, yellow, brown and gray). Finally, yield of diamond crystallization was reported to also be time-dependent with a strong nonlinear dependence [104–106]. This suggests that diamond crystallization is due to graphite dissolution to saturation and fast precipitation as diamonds. These studies help one to better understand fluid-assisted natural diamond formation.

5.3. High-Pressure Processes: Towards Large Binderless Diamond Objects

5.3.1. Origin in the 1960s

As mentioned above (Section 4), in the mid-1950s early 1960s, two labs succeeded to synthesize diamond from direct conversion of graphite at high pressure and high temperature [53,55]. Later, two studies provided more complete sets of experiments [56,110]. In both studies, graphite was used as a starting material and submitted to pressure between 12 and 15 GPa and temperature up to 3500 °C, by direct heating through the sample by electric current, for very short times (μ s) (Figure 5). Recovered samples showed partial transformation to diamond with a yield up to 60%. According to heating method, diamonds were either nano- (20–50 nm) or micro-polycrystalline (10–20 μ m). It is to be noted that [56] tried to synthesize diamonds with amorphous carbon, leading to the formation of gray-white polycrystalline diamond, most likely with a higher yield and purity.

This research area was quickly given-up since the role of metal catalyst (Ni based) and the drastic decrease of P–T conditions to synthesize diamonds were discovered contemporaneously [56].

5.3.2. A Brief Description of Catalyst Synthesis of Diamonds and PDC

For the last 50 years, diamond industry has been dominated by catalyst diamonds and associated PDC. Even though it is not within the scope of the present review, a brief description of this process is given.

Indeed, after the discovery of [56], two other studies from General Electric Company detailed the C–Ni phase diagram at high pressure and high temperature [111,112]. These two studies defined the graphite–diamond equilibrium line that was later refined from 4.7 GPa, 1100 °C to 6.1 GPa and 1620 °C [113] (Figure 5). With such low conditions, industrial transfer was possible with low-cost large-volume apparatuses such as Toroid press and piston cylinder. It is noted that other catalysts were developed and used (Cu, Zn and Ge [114,115]) until recently with more focus on color center (Mg, Ge, [116,117]). Catalyst diamonds are then recovered from the metallic matrix using acid leaching and are used for grinding, polishing, as cutting wheels or as PDC (polycrystalline diamond compact) for drilling machine or anvils in high-pressure research. In the case of PDC fabrication, catalyst diamonds are then sintered using a binder (mostly Co) at 5 GPa and 1500 °C [118]. This technique is ideal to produce big object of few cm³. The amount of binder, as well as the grains size of diamonds, is important for mechanical properties and thermal stability [119–121] (Section 6). Typically, hardness of PDC is around 70 GPa and thermal stability is 400–500 °C, which are not sufficient when cutting new materials or drilling rocks.

Therefore, new routes to synthesize binderless diamond compact are necessary but technical, and cost difficulties remain regarding a potential industrial transfer, due to the very high-pressure and high-temperature conditions of synthesis and sintering.

5.3.3. Development in the Last Two Decades

In the last two decades, a lot of technical developments have been achieved in order to reach higher pressure and temperature conditions. Thus, binderless diamonds synthesis and sintering was studied a lot in order to fabricate diamonds from different precursors with the aim to obtain large samples with exceptional properties (Figure 8, Table 2).

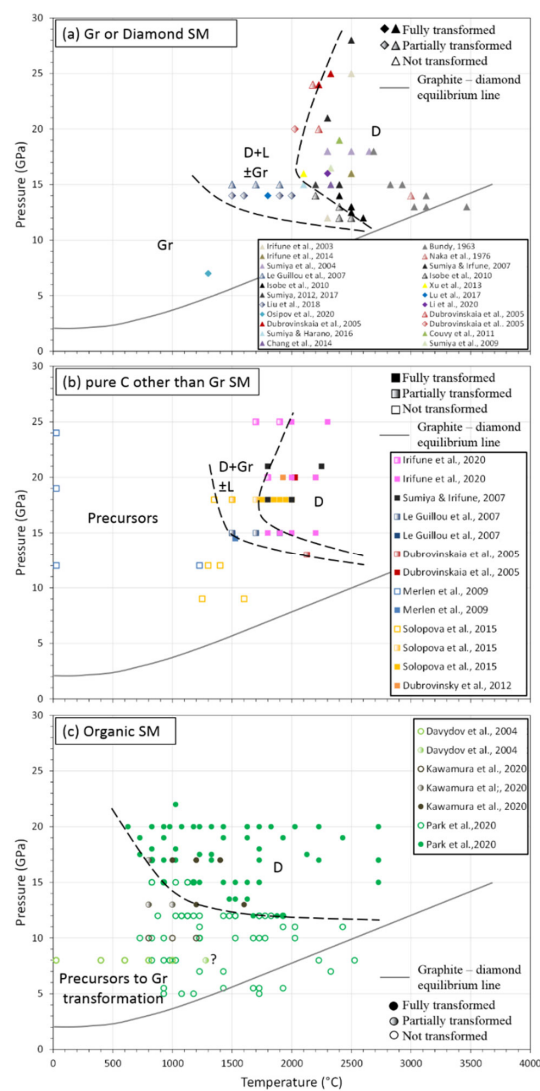


Figure 8. Pressure–Temperature diagram and data compilation of direct transformation of carbon compounds to diamonds at high pressure and high temperature. SM is for starting materials, C for carbon, Gr for graphite, L for lonsdaleite and D for diamond. Filled symbols are for total conversion to diamonds; open symbols are for no transformation; and color gradient is for incomplete, i.e., with SM remaining or for the presence of L in the sample. Triangle and diamonds are for Gr and D SM (a), square for other than Gr or D pure carbon SM (b), and circles are for organic compounds as SM (c). Grey solid line is for the graphite–diamond equilibrium as defined in Figure 5. Black dashed lines are guide for the eyes to note the transition to diamond. It is of note that this transition is favored with organic compounds (c) compared to other pure C form (b) and to graphite precursor (a). Additionally, lonsdaleite appears with pure carbon precursors and seems to be more present with higher crystallinity graphite (see text for more details). References: (a) [5], Irifune et al., 2003; [56], Bundy, 1963; [102], Irifune et al., 2014; [110], Naka et al., 1976; [122], Sumiya et al., 2004; [123], Sumiya & Irifune, 2007; [124], Sumiya & Irifune, 2008; [125], Le Guillou et al., 2007; [126], Isobe et al., 2010; [127], Xu et al., 2013; [128], Sumiya, 2012; [129], Sumiya, 2017; [130], Sumiya & Harano, 2016; [131], Couvy et al., 2011; [132], Chang et al., 2014; [133], Sumiya et al., 2009. (b) [134], Lu et al., 2017; [135], Liu et al., 2018; [136], Li et al., 2020; [137], Osipov et al., 2020; [138,139], Dubrovinskaia et al., 2005a,b; [140], Irifune et al., 2020; [141], Merlen et al., 2009; [142], Solopova et al., 2015; [143], Dubrovinsky et al., 2012. (c) [144], Davydov et al., 2004; [145], Kawamura et al., 2020; [146], Park et al., 2020.

Table 2. Experimental conditions for the synthesis and/or sintering of binderless diamonds.

Study	Apparatus	Starting Material (SM)			Pressure (GPa)	Temperature (°C)	Time (Min)	Yield (%)	Remarks
		Phase	Type	Grains Size (μm)					
Bundy, 1963	Belt-type press	Gr, SC, Gr, aC	R	-	11.8–15	up to 3900	-10^{-7}	-	1st direct transition reported
Naka et al., 1976	-	Gr	R	-	14	up to 3500	4	60	10–20 μm diamond grain recovered
Iriune et al., 2003	Kawai type MAA	Gr	R	-	12–25	2300–2500	-	up to 100	10–200 nm grain size in NPD
Davydov et al., 2004	Toroid Press	PAH	P	-	8	1500	1	60	5–40 μm monocrystals, 100% yield for T > 1350 °C, and graphitization step
Sumiya et al., 2004	Kawai type MAA	Gr	R	-	18	2300–2700	0.2–170	100	Microstructure: homogenous fine structure + lamellar structure
Dubrovinskaia et al., 2005	Kawai type MAA	C60	P	-	20	2200	-	100	Diamonds nanorods aggregated 5–20 nm Ø, >1 mm length, compact body of 1.8 mm Ø and 3 mm high
Dubrovinskaia et al., 2005	Kawai type MAA	C60 aC Gr D	P	-	13–20 20 20–25 20	27–2127 2027 2177–2327 2027	<90	up to 100	5–12 nm grain size of diamond, lonsdaleite often present
Le Guillou et al., 20,007	Kawai type MAA	QAS CB HTCB pGr HOPG	-	-	30–100 × 10 ⁻³ 30–100 × 10 ⁻³ 0.5–1 >1	1500 1500–1700–1900 1500–1700 1500–1700–1900 1700	15–60	up to 100	Transformation path highly dependent on the nature of the precursors, especially their crystallinity. Lonsdaleite can be present
Sumiya and Irifune, 2007, 2008	Kawai type MAA	Gr aC GC C60	R P P P	- - - -	15–28 18–21 18–21 18	2300–2500 1800–2000 2000–22,500 1800–2000	0.2–10 10–20 6–20 30–35	100	Lower hardness for other C precursors than graphite
Merlen et al., 2009	DAC, PE, MAA	SWCNT +/– I	P	-	12–25	25–1527	60–120	up to 100	Graphitization step
Isobe et al., 2010	Kawai type MAA	Gr	R	-	12–14	2200–2600	5–30	up to 100	Minimum condition for NPD. Higher pressure means lower T to complete transformation.
Couvy et al., 2011	Kawai type MAA	Gr	R	-	19	2400	0.5	100	-
Dubrovinsky et al., 2012	Kawai type MAA	GC	B	20–50	20	1927	<15	100	Nano polycrystalline (50 nm) balls of 15–40 microns, presence of NaCl or Na2CO3 to make microballs.
He et al., 2013	Hinge-type cubic press	μD	P	-	8–20	1400–2500	1–30	no need	-
Xu et al., 2013	Hinge-type cubic press	Gr +/– milled	P	5–20	16	2500	1–10	100	Reaction at lower T with ball-milled Gr
Chang et al., 2014	Kawai type MAA	Gr	R	-	15	2327	20	100	NPD shaped in anvil, cylinder or sphere
Solopova et al., 2015	Kawai type MAA	GC	B	20–50	18	1850–2000	1–5	up to 100	Nano polycrystalline balls of 15–40 microns, presence of NaCl or Na2CO3 to make microballs
Lu et al., 2017	Hinge-type cubic press	μD	P	0.5	14	2000	1	no need	Cylinder of 3 mm Ø & high at the end. Some backtransformation in graphite. Final grain size of 170 nm
Liu et al., 2018	Hinge-type cubic press	μD	P	8–12	14	1000–2000	-	no need	-
Zhan et al., 2020	Hinge-type cubic press	μD	P	8–12	14	up to 1900	-	no need	Cylinder 11 mm Ø, 6 mm high. Not transparent at all. There may be pores and/or cracks
Li et al., 2020	Hinge-type cubic press	μD	P	8–12	16	2300	10	no need	Same size body as above, 10-micron final grain size
Osipov et al., 2020	Toroid press	nD	P	25 × 10 ⁻³	7	1300	0.2	no need	Purification + sintering using ethanol at HPHT
Kawamura et al., 2020	Kawai type MAA	C ₁₈ H ₃₆ O ₂	P	-	10–13–17	600–1600	5–180	up to 100	Graphitization step, 10 nm grain at the end, control fO ₂ in some exp and remove water during exp
Park et al., 2020	DAC	C ₁₀ H ₁₆ /C ₁₄ H ₂₀ /C ₁₈ H ₂₄	P	0.5–2 × 10 ⁻³	5–22	627–2727	-10^{-7}	up to 100	Lower transition than with pure C source. Direct transformation, no graphitization step
Irifune et al., 2020	Kawai type MAA	GC	R	-	15–25	1700–2300	20	up to 100	Grain size dependence on P,T. P,T limits to keep nanograin

Gr = graphite, SCGr = single-crystal graphite, PAH = PolyAromatic Hydrocarbon, aC = amorphous Carbon, D = diamond, QAS = quasi amorphous carbon, CB = carbon black, HTCB = high-temperature carbon black, pGr = pyrolytic Graphite, HOPG = highly orientated pyrolytic graphite, SWCNT = single-wall carbon nano tube, μD = microdiamond, nD = nanodiamond, R = rods, P = powder, and B = balls. MAA = multi-anvil apparatus.

- Binderless Diamond from Graphite: NPDs (Nano-Polycrystalline Diamonds)

Graphite is the obvious precursor to think about when diamond synthesis and sintering want to be performed.

The first report of binderless diamond compact synthesis and sintering from the direct conversion of graphite is relatively recent [5]. These compacts were fabricated using a multi-anvil apparatus to reach pressure up to 25 GPa and very high temperature of 2500 °C (Table 2, Figures 5, 7 and 8a). The ingenious idea was to use directly dense graphite rods as starting materials that allow for pre-shaping of the resulting diamond compact and avoid cold compression texture/delamination. It is of note that all the following studies have kept this idea (Table 2). A transparent diamond compact was recovered, with limited dimensions of 0.1 mm diameter and 0.3 mm thickness, composed of nano-grains (NPD for nano-polycrystalline diamonds). These compacts showed exceptional mechanical, optical and thermal properties. Therefore, a wide range of applications could be considered (see below). This first study marks the starting of an important collaboration in Japan between Geodynamics Research Center (GRC) represented by Pr. T. Irifune, and Sumitomo Electric Industry (SEI) represented by Dr. H. Sumiya, head of the Advanced Materials Laboratory [147]. Indeed, important technical developments were made and numerous scientific studies were published in order to understand the mechanisms of this direct conversion sintering. With these new technical developments, bigger dimensions were obtained, and today, it is possible to recover samples of ~1 cm³. It is of note that, still today, synthesis, sintering and characterization of NPD from graphite are almost exclusively performed by these two Japanese labs.

NPDs microstructures sintered between 15–18 GPa and 2300–2700 °C were studied (Table 2, Figure 8a), mostly by TEM and associated techniques, to understand mechanisms of the direct conversion sintering diamond body [122]. This study revealed the almost systematic presence of lonsdaleite in the final product. However, its abundance depended on sintering temperature essentially and was detected either with XRD or by electron diffraction using TEM, respectively, at low or high temperatures. Nevertheless, NPDs had a mixed texture of homogenous fine or lamellar structure, the former being composed of randomly orientated 10 nm grains, the latter being inherited from originally deformed graphite. This lamellar structure was most likely responsible for NPD's hardness compared to sample without this structure (Section 6, see below, [123,124]). This lamellar structure disappears at very high temperatures when grain growth becomes efficient and new grain boundaries are formed. This dual texture was explained by two different mechanisms of transformation, respectively, by diffusion and by martensitic process. To go further with understanding of transition mechanisms, the authors of [125] characterized transformation from graphite and different precursors submitted at 15 GPa and between 1500 and 1900 °C (Table 2, Figure 8a and third bullet of this section). It was shown that the presence of lonsdaleite is highly dependent on the ordered structure, i.e., crystallinity of the precursors, i.e., the most ordered the structure, the more lonsdaleite was present. In all products, nano-diamonds were formed, but the degree of transparency depends on P–T conditions. Transformation mechanisms were determined by using different type of starting graphite (more or less orientated grains in the rod). These mechanisms mostly act simultaneously and are diffuse and related to defects and restacking.

Many different experimental conditions were tested to determine the lowest P–T conditions of this direct conversion sintering from graphite. It was shown that transition could occur at relatively low pressure of 12 GPa, but it needs temperature as high as 2600 °C and that therefore higher pressure means lower temperature (Table 2, Figure 8a, [126]). Moreover, in most of these “low”-pressure range experiments, lonsdaleite was found, except at very high temperatures (Table 2, Figure 8a). At high temperatures, grain growth was also present and the lamellar structure disappeared, making lower hardness compacts as suggested previously [123,124]. Another study tried to decrease P–T conditions of this direct conversion sintering from graphite to diamond by comparing NPDs from

crystalline graphite and milled graphite after sintering at 16 GPa and up to 2500 °C (Table 2, Figure 8a, [127]). From crystalline graphite, lonsdaleite was always present, whereas it was absent using milled graphite [127], confirming that the structure ordering is of major importance, as also underlined by other precursors (third bullet of this section). A thermodynamic and kinetic process were considered to explain this difference with different transition states according to the precursors, and therefore low overpressure was necessary to start the transition.

The best conditions for this direct conversion sintering from graphite to give transparent NPDs with very high mechanical properties were then defined (Table 2, Figure 8a) and are $P > 15$ GPa and $2100 < T < 2400$ °C [128,129]. Lower temperatures produce too much lonsdaleite and insufficient densification, and higher temperatures promote grain growth and disappearance of lamellae texture. Even though mechanisms of transformation can be slightly different as already exposed, the main feature is the presence of lamellar texture in final samples, a structure that is only observable with graphite precursors, even if lonsdaleite is present.

- Sintering from Diamonds Precursors

Twenty years ago, Voronov, associated with the DMI Company, proposed to sinter diamond compact without any binder using only diamond powders [148]. The main goal was to use binderless polycrystalline diamonds (BPCD) for drilling applications and thus avoid thermal problem of conventional PCD (presence of Co-Binder). Accordingly, a 300-ton toroid press was used and an important development of the anvil materials (nano-grained WC/Co was made to support pressure up to 15 GPa and temperature up to 2000 °C. However, with the aim of an industrial transfer, all experiments were performed between 7–9 GPa and 1000–2000 °C and for duration between 1 and 100 seconds. An important work on precursors was made [148]. Different types of diamond (natural, HP-HT and detonation) with different grains size (1 nm to 50 µm) and purity (0.1 to 20 wt% of contamination, i.e., in most cases Fe, Ni, Cu, Mn, Si O, N and H) were tested, as well as the mixing of different grain-size populations. Thus, pellets of 100 mm³ (6 mm diameter and 3 mm high) were synthesized and characterized using XRD, SEM and EDS. Even though dense bodies were recovered ($\rho = 3.1\text{--}3.5$ g/cm³), analysis not only showed diamonds in the aggregates. Indeed, in XRD pattern, an important background to the lower angle was visible, suggesting the presence of an amorphous phase that could be a carbon phase. This was confirmed by SEM and EDS analysis, which revealed the presence of ashes in the aggregates with composition rich in C and metal elements. Finally, no Raman spectra were shown for the presence and/or absence of graphite, which is an unavoidable analysis to characterize diamonds. These first binderless PCDs had similar properties than conventional PCD, e.g., a thermal stability up to 1200 °C in Ar atmosphere, a thermal conductivity to 600 W/m.K, a Vickers Hardness of 75 GPa, a strength of 3.8–4.2 GPa and a limited abrasive wear, making them not much better.

This protocol was retried only by two different teams almost twenty years later, which were distinct due to the choice in their starting powders and conditions of sintering.

Recently, a lab from Sichuan University, China put a lot of effort into directly sintering micrometer-sized diamond powders into dense bodies with several mm³ volume. These bodies are referred as MPD (micro polycrystalline diamond) or CFPCD (Catalyst-Free PolyCrystalline Diamonds), meaning binder-free. All these compacts have been synthesized in hinge-type cubic press (Figure 7c).

The first study from this lab used high-purity commercial diamond powder with initial grain size of 0.5 µm, which was substantially re-purified. Sintering at 14 GPa and up to 2000 °C has shown that temperature is very critical regarding the diamonds back transformation to graphite, even for sintering time of 1 min (Table 2, Figure 8a, [134,149]). With this patent [149] and first study [134], mm³ diamond pieces have been achieved with very high hardness and grain size of 170 nm, showing the milling of diamond powders during compression.

More recently, further developments were made to better control and identify the sintering mechanisms. Using previously purified 8–12 μm grain size of diamonds that were pre-compacted into a pellet with a relative density of 75%, it was shown that fully dense diamonds compacts could be sintered at 14 GPa and 1600 °C [135]. By covering a wide range of temperatures, it was shown that graphite appears at 1500 °C and above (Table 2, Figure 8a), especially at triple junction. These areas are thought to be low-pressure zone between high-stress diamonds grains, allowing a back-transformation to graphite. However, temperature had to be higher to avoid brittle behavior, even at high pressure, and to allow plastic deformation of diamonds grains and therefore creation of grain boundaries. Region around these newly formed grain boundaries had shown high level of dislocation, twin boundaries, stacking fault and a lot of diamonds lamellae, guaranteeing a high level of sintering. Triple junction zone contained nano-diamonds grains in turbostratic graphite and amorphous carbon matrix. This is probably the reason why these diamond compacts are opaque compared to that sintering by direct transformation of graphite (first bullet of this section). There is therefore a subtle balance in the temperature control to avoid too much graphite in triple junction but to allow the formation of strong grain boundaries.

The two other studies span the P–T range and focus on the P–T path (Table 2); the final size of the bodies; and the mechanical, abrasive and cutting properties of these diamond compacts [103,136]. For instance, samples up to $\sim 500 \text{ mm}^3$ (10 mm diameter and 6 mm high) were synthesized using similar set-up and at pressure and temperature up to 16 GPa and 2300 °C [136]. The final product was optically dark, with 10 μm grain size and with the presence of micro cracks. Moreover, XRD and Raman spectra appear very clean, suggesting high-purity samples.

Another lab from St. Petersburg, Russia, tried to directly sinter diamond compact from diamonds powders but using nano-diamonds powders of $\sim 25 \text{ nm}$ from detonation synthesis, i.e., with TNT/RDX (Section 5.4) as starting materials [137]. The main goal focused on nitrogen-vacancy-nitrogen-center diamonds for biomedical applications. A precise procedure of purification of the starting materials was developed to remove residual metals and amorphous carbon in the polycrystalline nano-diamonds powders. A mixture of this powder (50–70 wt%) and ethanol (30–50 wt%) was then packed in a graphite cylinder (4 mm diameter and 5.5 mm high) and put into a toroid-press (Figure 7b and [150]). Sintering conditions were $P = 7 \text{ GPa}$ and $T = 1300 \text{ °C}$ for 10 s, lower than all other methods of binderless diamonds sintering (Table 2, Figure 8a). With this method, no dense bodies were sintered, but sintering of several grains was observed, and with the presence of ethanol, purity was highly enhanced, which was observable in the change in color from grey/black for the precursors to white/transparent after sintering.

- Sintering from Other Pure Carbon Forms

Other sources of pure carbon were used to synthesize diamonds at high pressure-and high temperature. The main goal of these studies was twofold: first, try to decrease P–T conditions for the formation of dense bodies and then provide new constraints on the mechanism of diamond formation and precise the P–T phase diagram (Table 2, Figure 8b). Thus, during the last 15 years, numerous studies have been reported with these precursors.

Two different types of experiments have been performed.

C60 was the first other pure carbon form to be tested for the synthesis and sintering of diamond compact [138]. P–T conditions were similar to those used with graphite precursor [5], i.e., 20 GPa and 2200 °C for 60 min. Therefore, no difference was observed in the final product, i.e., pure diamond. However, the transparent aggregate (1.8 mm diameter and 3 mm high) was composed of diamond nano-rods of 20 nm of diameter and 1 μm length. This first study was immediately followed by a more complete investigation of another pure carbon source [139]. C60, amorphous carbon (aC) was used under various P–T conditions, i.e., 13–20 GPa and 27–2127 °C, for 60 min (Table 2, Figure 8b). Except at ambient temperature where C60 remains stable even at pressure to 20 GPa, all other C60 precursors had transformed to nano-polycrystalline diamonds, and small abundance of 6H polytype that corresponds to another stacking of C-tetrahedra was present. Moreover, it

appears that diamonds forming from C60 have a higher thermal stability, up to 1627 °C, i.e., 300 °C higher than that sintered from pure graphite. Starting with aC leads to the formation of diamond and lonsdaleite at 20 GPa and 2027 °C. Mechanisms of transformation from other pure carbon sources were also established [125]. By using QAC (quasi amorphous carbon), CB (carbon black ± heat treated) and two types of graphite (first bullet of this paragraph) as starting materials and submitted to 15 GPa, at 1500–1700–1900 °C and between 15 and 60 min, it was proposed that the degree of ordering in the precursor was of major importance for the resulting products (Table 2, Figure 8b). Globally, for given P–T conditions, disordered precursors react faster, without any graphitization step, achieve higher transformation rate and are more easily transparent. Under these conditions, nucleation is the dominant mechanism, and these precursors mostly evolve according to a diffusion-limited reconstructive mechanism, which originates from the precursor structural defects. Moreover, even though some reactions were incomplete, in no other phase were diamonds or residual precursors found, i.e., there was no lonsdaleite (Figure 8b). Here [123], aC, GC and C60 were submitted to 18–21 GPa, 1800–2250 °C, for 6 to 35 min (Table 2, Figure 8b). All were 100% transformed to nano-polycrystalline diamonds, with grain size 5–200 nm depending on annealing time. However, TEM observations did not show the presence of lamellar as in diamonds obtained from graphite (first bullet of this section, [123]). Finally, a recent study based exclusively on GC constrained grain size evolution of NPD as a function of P–T conditions and discussed related mechanical properties [140]. It was shown that full transformation temperature increases from 1700 to 1900 °C with the increasing of pressure, from 15 to 25 GPa (Table 2, Figure 8b). Moreover, grain size evolution after 20 min of annealing is highly inhibited at 25 GPa compared to 15 GPa. Therefore, to keep the exceptional properties of NPD with grain size less than 10 nm, very high pressure resulted in lowering temperature and thus limited grain growth. Again, with such other pure carbon starting materials, no lonsdaleite was observed (Figure 8b).

One of the lowest transitions to diamond with pure carbon precursors was established using SWCNT at 14.5 GPa and 1527 °C ([141]; Table 2, Figure 8b). In this study, micro-grain size diamonds formed, and an intermediate step of graphitization to highly disordered structure occurred before transition to diamonds. Again, this disordered structure seems to be the source of a lower and direct transition to diamonds.

Other studies, mostly from BGI lab (Bayerisches GeoInstitut), used different precursors to synthesize diamond micro sphere to be used further as double-stage in diamond anvil cell (DAC). These experiments were performed in large volume press in order to mix precursor powders and pressure medium powders of NaCl, MgO or Na₂CO₃ [142]. This mixture helped shape the resulting diamond. Only glassy carbon (GC) (20–50-micron size) was used in these experiments. Up to 20 GPa and 2000 °C, GC transformed more or less into pure diamond without any trace of lonsdaleite (Figure 8b), most likely due to the disordered structure of the starting materials, as suggested by others studies [123,125]. The resulting micro-balls of diamonds (10–50 µm) were nano- to micro-polycrystalline and were used in double-stage DAC to reach pressure of 600 GPa [143].

To sum up, diamond transition using other pure carbon precursors occurs at lower P–T conditions than diamonds fabricated from graphite. Moreover, a narrower field of lonsdaleite is observed compared to the one observed with pure graphite as starting material (Figure 8b). These two features (lower P–T conditions and narrow lonsdaleite field) are due to the disordered structure of the precursors that decrease activation energy of nucleation.

- Sintering from Carbonaceous Organic Compounds

Organic compounds transformation were studied a lot, first at high temperature [151] and then at pressure that did not exceed 1 GPa [152], revealing the steps of carbonization and graphitization.

More recently, high-pressure–high-temperature experiments were performed on different types of organic precursors. Here is given a brief overview of three complete

studies [144–146] that span over a wide range of pressure–temperature conditions (Table 3, Figure 8c).

Table 3. Common physical properties of diamond.

Mechanical Properties	
Poisson's ratio	0.1
Young's modulus (GPa)	1050
Fracture toughness K1C (MPa.m ^{0.5})	
Natural single crystal	5
Synthetic polycrystalline (NPDs)	8.5
Fracture strength (GPa)	
Natural single crystal	2.5–3.0
Synthetic polycrystalline (NPDs)	0.2 to 1.1
Transverse rupture strength (GPa)	
Natural single crystal	1.0–2.0
Synthetic polycrystalline (binder)	2.5 up to 400 °C, 0.5 at 500 °C
Synthetic polycrystalline (NPDs)	3.0 up to 1000 °C
Flank wear width/cutting length (µm/m)	
Natural single crystal	11.25
Synthetic polycrystalline (binder)	0.50
Synthetic polycrystalline (NPDs)	0.16
Knoop hardness (GPa)	
Natural single crystal	70 to 120 according to orientation
Synthetic polycrystalline (binder)	50–80 according to binder content
Synthetic polycrystalline (binderless)	
From graphite or diamond	125–145
From other C-precursors	80–100
Friction coefficient (µ)	0.05 to 0.15 according to orientation
Optical properties	
Color (see type classification)	colorless to various
Transparency	(X-ray) UV to IR
Absorption	2.5–6 µm
Fluorescence	UV
Refractive index	2.417 (0.044 dispersion)
Electrical properties	
Conductivity (Ω.m)	
Most natural diamonds	Insulator, 10 ¹¹ to 10 ¹⁸
Type IIb (boron-doped, natural and synthetic)	Semiconductor, superconductor at 4 K
Electronic gap	5.5 eV
Dielectric constant	5.58 at 35 GHz
Thermal properties	
Expansion coefficient (10 ⁻⁶ × K ⁻¹)	1.0 at 600 °C, 4.4 at 1300 °C
Conductivity (W/(m.K))	
Natural single crystal	2200
Synthetic (¹² C enriched)	up to 3200
Stability at 1 bar	700 °C in air up to 1600 °C in Ar

Different PAH (polycyclic aromatic hydrocarbons), i.e., naphthalene, anthracene, perylene and coronene, were submitted to 8 GPa and up to 1500 °C for 60 s in a toroid type

press [144] (2, Figures 7b and 8c). Special care was taken for the choice of container. Graphite was chosen instead of metal to avoid any catalyst action and to allow produced gas to escape due to the porosity of graphite. XRD, SEM and Raman results did not show that any difference based on the PAH used. In any case, a step of graphitization occurred at 800 °C and diamond transformation started around 1280 °C, which was incomplete transformation. Typically, diamond grains of 5–40 µm were formed. A crystallographic link was observed for the graphite-to-diamond transformation, with diamond facets perpendicular to the graphite platelets. Such conditions of transformation are the lowest known without any catalyst to date.

Experiments in multi-anvil press using stearic acid (C₁₈H₃₆O₂) were performed at P = 10–17 GPa and T = 800–1600 °C and for 5 to 180 min [145] (Table 2, Figure 8c). The main goal was to fabricate at lower conditions nano-polycrystalline diamond (NPD) compact with similar quality (grain size, transparency) to those classically formed using graphite (first bullet of this section). In order to obtain dense bodies without any pores, water from stearic acid dehydration has to be removed from the sample using MgCO₃ porous powders under the sample that allows percolation. With this set-up, transition to diamond started at 13 GPa and T = 800 °C and was achieved at 1200 °C, clearly lower than NPD from graphite (T > 2000 °C) (Figure 8a). Moreover, no lonsdaleite was observed, which was in agreement with an intermediate, highly disordered, amorphous graphite stage during heating that promoted the formation of diamonds. Thus, activation energy of transition was reduced, even more by the presence of CH₄ and H₂O.

Different diamondoids (adamantane, diamantane and triamantane) were tested to be transform into diamonds [146,153,154]. Diamondoids are very small H-terminated carbon cages (few nm) with a lattice structure of diamond. Pioneering works by [153] showed that diamondoids transformed to diamonds at 12.5 GPa and 200 °C, values that were clearly lowered to 8–9 GPa and 1300–1600 °C [154]. Using laser-heating DAC and time-resolved XRD (<19 µs), these phases were submitted to pressure between 5 and 22 GPa and temperatures between 627 and 2727 °C (Table 2, Figure 8c) [146]. No obvious difference was observed for the different precursors, and transition to diamond occurred at 12 GPa and 1727 °C and 20 GPa and 627 °C for the lower limit in pressure and temperature, respectively (Figure 8c). No graphitization step was observed for the mechanism of transition, but further ab initio calculations have suggested that once diamondoids were dehydrogenated, they bond together in the diamond structure. This is therefore a direct sp³-sp³ reconstruction.

It therefore looks quite easily to form diamonds from organic compounds. Indeed, transition is largely lowered compared to graphite or other pure C precursors. Moreover, transition is direct, without any lonsdaleite field, again probably due to the disordered structure of the pressurized starting materials. However, to the best of our knowledge, no data exist on the mechanical, optical and thermal properties of these bodies.

5.4. Ultra High Processes: Shock and Detonation Diamonds

Diamonds produced by shock and detonation were studied in order to understand observed diamond in both impact crater and some meteorites and thus provide constraints on their conditions of formation. The first report of diamond formation by shock from graphite was made by [61] at 30 GPa for 1 µs, with a relatively low recovery, but diamonds particles observed were <10 µm diameter and well identified using XRD. Moreover, due to the very fast shock wave, the mechanism of transition was thought to be diffusionless and most likely due to the compression of c-axis leading to atom rearrangement through the cubic diamond form.

This pioneering study was the starting point of production of diamonds by shock using mainly three different techniques that will be shortly described below. The main applications of these shocked diamonds concern polishing using nanograins [155] and more recently have been devoted to bioapplications [156].

The first technique uses a shock wave that is produced either by an explosion, by a projectile or by a laser. In most cases, precursor was graphite with different grade/crystallinity [157–160]. Other materials such as fullerene [161], black carbon, amorphous carbon, adamantane [162] and even rock containing graphite [163] were also used. In all these experiments, the yield of dense phases was always very low, i.e., 5–10% maximum. In experiments containing graphite with different crystallinity and at pressure between 20 and 228 GPa (Figure 5), it was shown that lonsdaleite is preferentially formed if graphite is pyrolytic, whereas diamond forms even with more disordered graphite. Moreover, lonsdaleite formation seems to be favored when graphite basal plane is perpendicular to the shock wave, whereas diamonds are formed regardless of graphite crystals orientation [159]. Transition was most likely martensitic as the shock wave was very fast, and a resolution of 10 ns was allowed to follow these transitions [159]. However, lonsdaleite remained unstable as temperature increased in favor of stable cubic diamond ($T > 3000$ K). With other precursors, only diamonds were formed, with micrometer size (6–10 μm).

Second method involved using the carbon contained in explosives, which was transformed into nano-diamonds in a closed system that generated suitable conditions of formation for diamonds. It has to be noted that there was no lonsdaleite form in these experiments due to the low degree of crystallinity of these explosives. The pioneering experiments by [114] have shown that, according to the explosive (TH50/50 or TNT) used, the yield for diamond recovery varies from <5% to 40–50%. In this study [164], $P = 18\text{--}19$ GPa and $T \sim 3700$ °C, and the transformation occurred in 0.5 μs (Figure 5). It was also proposed that transformation involved kinetics processes rather than equilibrium ones. In order to control this kind of transformation by explosion, especially concerning grain size and distributions, several technical developments were proposed in the last two decades. For example, inert gas was replaced by water in confinement bag that allowed for a rapid cooling that avoided back transformation to graphite [162]. In that case, the yield reached 60% when using TNT/RDX +/– HMX/TNT. A lot of efforts were also made on the best ratio TNT/XRD as well as on the nanostructure of these explosives in order to produce the smallest particles (down to 3 nm) with a very narrow distribution involving diffusive processes [165,166] that can influence optical properties [167]. Purification procedures were also developed to increase the yield [165]. Other explosives (BTF, $\text{C}_6\text{N}_6\text{O}_6$) were also tested to produce hydrogen-free nano diamonds [168] in order to access specific properties.

Last but not least, the third method involves sintering diamond (12 mm diameter and 5 mm thick pellets) from diamond powder using shock without any binder [169]. To avoid the problem of cracks, shock residual temperature had to be controlled as well as the starting grain size. The development of cracks increased with the increase of grain size, and relative density reached 90% for bigger grain size.

A final attempt was to produce nanodiamond using laser techniques [170]. This process is similar to a shock but differs by the fact that the high energy laser is focused on the solid target that is placed in a liquid (mainly water). This technique is very common for a lot of metal and ceramics. For nanodiamonds synthesis, the interaction between the laser and the graphite (i.e., the target) vaporized this later. Crystallization occurred in contact with the liquid at HP-HT, synthesizing nanodiamonds with grain size from few to hundreds of nm.

5.5. Other Unconventional Experimental Set-Ups

This section describes original unconventional techniques in which diamond formation was reported for different conditions of pressure and/or temperature. However, these new findings have to be confirmed since only single study was devoted to a given technique.

Ultrasound cavitation was used to synthesize micro-grain (6–9 μm) diamonds from graphite (100–200 μm) in various organic solvents, with a significant yield up to 10% [171]. Although authors claimed that synthesis was made at 1 bar and 120 °C, real local conditions inside the cavitation chamber are most likely to be thousands of degrees Celsius and several GPa. One of the main advantages of this technique was the fast transformation,

around 10 min. The mechanism of transformation in this method was “probabilistic” and based on the number of cavities that collapsed normally onto the graphite basal plane. This kind of “probabilistic” approach makes it unsuitable for an industrial transfer, even though this technique seems to be energetically favorable to synthesize diamond, similar to HP-HT and clearly better than CVD [171]. No other work was reported to demonstrate the reproducibility of this phenomena, inducing certain reservations with regard to the technique.

Diamond nanorods were also fabricated from carbon nanofibers using pulsed laser annealing [172]. Once again, authors claimed that transformation occurred at ambient pressure and temperature, whereas this conversion involves melting of carbon nanofibers under a super undercooled state. Pressure was also most likely high due to repeated laser pulse that controlled the rate of transformation. Complete transformations occurred using this technique, and resulting diamond nanorods can be used as seed for further CVD diamonds synthesis [172]. Additionally, in this case, no other works were reported to demonstrate the reproducibility of this phenomena, inducing certain reservations with regard to its reproducibility, although it was reported to have a significant yield of 100%.

High shear strain, using a rotational anvil apparatus, under ambient temperature and pressure below 1 GPa (0.4–0.7 GPa), allowed for the direct formation of diamond from graphite powder [173]. In this study, lonsdaleite was also observed. In any case, transformation was far from being complete (most likely ~1% yield), diamond crystals formed were smaller than 50 nm and a lot of phases coexisted. Moreover, sample thickness did not exceed 50 μm . Interestingly, the mechanisms of formation at such low pressure and temperature came from the concentration of high stress at the limit of lattice instability, which promoted phase transition.

Decomposition of SiC using chlorine-containing gases at 1 bar and 1000 °C in a quartz sealed tube allowed for the formation of nano- and micro-crystalline diamonds [86]. These diamonds were produced as very thin layer, and the interface of SiC and Carbon had hardness properties of 50 GPa and Young modulus of 800 GPa. In this set-up, hydrogen was assumed to stabilize the conversion of SiC to diamond.

6. Diamonds Properties and Uses

6.1. General Properties

Diamond structure is the basis of all of its properties and therefore of its associated uses. Indeed, all is in its tetrahedral covalent bonding forming sp^3 hybridization as well as its compacted *fcc* lattice. The level of impurities and defects in the lattice is also of great importance for specific optical or mechanical applications. These features may be altered in natural diamonds or during the synthesis and sintering processes (Sections 3 and 5).

Diamond has exceptional mechanical properties (Table 3) such as very high hardness, elastic properties, low friction coefficient and low wettability. Specifically, a body of synthetic diamonds called “compact” without binder has higher hardness than natural single crystal due to the presence of grain boundary and especially if the grains are very small (Hall-Petch relation) (Section 6.2, Table 3). Moreover, the recent development of binderless diamond compact with nano-grains (nano-polycrystalline diamonds NPD) shows exceptional wear resistance, transverse rupture strength (TRS) compared to conventional PCD (containing Co-binder), and temperature of 1000–1200 °C (compared to 400 °C for PCD) [130] (Section 6.2, Table 3).

Diamonds are also known to be good electrical insulators [174] (Table 3). Exceptions are for type IIb diamonds (boron impurities between 5 and 10 ppm) [175], either natural or synthetic, that are semiconductors, with a transition to superconductivity around 4 K [176]. Despite their electrical insulator feature for most of diamonds, they also have high thermal conductivity that can be modified in synthetic diamonds (Table 3).

Diamond also possesses the highest thermal conductivity, even higher than copper [177]. This is even truer for synthetic diamond enriched in ^{12}C compared to natural ones [178,179] (Table 3). Indeed, this property depends essentially on defects that are

present in the crystal (e.g., minor phase, dislocation, lattice substitution, and vacancy) and that can be controlled in synthetic diamonds, especially in CVD ones. Coupled with its high electrical resistivity, this makes diamonds the best materials for heat sink applications in high-power electronic devices.

Optically [180], diamond is transparent from UV to far IR, with an absorption band between 2.5 and 6 μm . It is also transparent to X-ray and hyperfrequency domain. Thus, it is highly used for optical windows and polarizers. For such uses, the compact may not contain any physical defects such as porosity.

By combining its high resistivity, high thermal conductivity and electric properties, diamonds can be used for specific devices such as sensors and detectors [181].

6.2. Specific Properties of Binderless Diamonds

Mechanical, optical and thermal properties of these NPDs have been extensively studied over the last decade, and a Special Issue on high-pressure research has been dedicated recently concerning scientific application (HPR, 2020) (Table 3). When possible, comparison with MPD (binderless diamonds sintered from diamond powder) and classic PCD are provided.

• Mechanical properties

When talking about mechanical properties and especially hardness measurements of materials, one has to be aware that determined values depend a lot on the method used, i.e., Vicker's [182] vs. Knoop's [183] vs. Nano's Hardness [184] vs. ultrasonic spectroscopy [185], as they measure these properties at various spatial scales [186].

A lot of studies have focused on elastic properties and hardness of NPDs. Each time, these studies have brought new data on sintering conditions and also constrain mechanical properties on these NPDs.

Knoop hardness (H_k) was one of the first measured properties on the NPDs [124,125]. Its mean value was determined to be $H_k \sim 120\text{--}130$ GPa, which was higher than single crystal and higher than other NPDs sintered from other pure C precursors ($H_k \sim 70\text{--}120$ GPa) (Table 3) (third bullet of the Section 5.3.3). Such high hardness was directly related to lamellar microstructure observed only in samples fabricated from graphite. Moreover, such high hardness was weakly temperature-dependent compared to single crystal, in which, according to orientation, a stark decrease in H_k was observed around 200–300 $^\circ\text{C}$ [129]. It is of note here that MPD (second bullet of the Section 5.3.3) has hardness at least the same as diamond single crystal (SC) ($H_k \geq 120$ GPa) as indenters have been broken very often [103]. Moreover, they have similar hardness ($H_k \geq 120$ GPa) to the more studied NPDs (Table 3) [129].

Ref. [131] measured young modulus (E) and nano-hardness (H_N) of previously sintered NPDs using nano-indentation technique [131]. NPDs fabricated at 19 GPa and 2400 $^\circ\text{C}$ for 30 sec (Table 3, Figure 8a) were very dense and transparent and led to $E = 707$ GPa and $H_N = 62$ GPa, which was harder than other commercially available polycrystalline diamonds. Other elastic properties (bulk modulus: K_s , shear modulus: G , and Young's modulus: E) were determined by using ultrasonic measurements (P and S-wave velocity: V_p , V_s) [132] on the three NPDs sintered at 15 GPa, 2327 $^\circ\text{C}$ and for 20 min (Table 3, Figure 8a). This bulk method of characterization gave a relative density $\rho > 99.94\%$ and values of V_p , V_s , K_s , G and E , which were very close to those of single-crystal diamond (Table 3).

Other techniques, non-destructive, can be used to determine elastic properties of diamonds and more specifically of synthetic diamonds. The main advantage of these methods is that they measure properties of bulk samples and only of a small area, as for the hardness measurements. For example, ultrasonic methods (RUS: [187] and pulsed-echo: [188]) were used to measure elastic moduli on both natural and synthetic diamonds. These two studies pointed that crystallographic directions have higher elastic properties than others despite the fact that diamonds have cubic lattice, and that polycrystalline diamonds can exhibit similar elastic properties to single crystal. Concerning NPDs, measurement of NPDs stiff-

ness by Brillouin scattering confirmed higher properties than single-crystal diamond [189]. It is of note that in this study, ab initio calculations show that lonsdaleite could be even stiffer than NPDs, a conclusion that has to be confirmed with experiments.

- Thermal properties

Thermal properties of NPDs are at least as high as single-crystal (SC) diamonds, as revealed by XRD up to 1500 °C–1600 °C [128]. At this temperature and under inert atmosphere, NPDs and SC start to destabilize, whereas binder PDCs start to deteriorate at 400–500 °C with the appearance of cracks, and at 700 °C with the appearance of graphite.

Thermal stability of MPDs was shown to be very high, with a starting transformation to graphite at 1200 °C, at least 200 °C above all other natural or synthetic diamonds (single crystal, NPDs . . .) and twice the thermal stability of common binder PDC [103].

Transverse rupture strength (TRS or flexural strength) of NPDs were measured at both ambient temperature and up to 1200 °C and compared with other diamond materials such single crystal (SC) or PDCs [128–130]. At ambient temperature, TRS of NPDS was about 3 GPa, i.e., 15–20% higher than PDCs, and was twice that of single crystal. With increasing temperature, TRS of PDCs drastically decreased to 0 at 500 °C, whereas in the case of NPDs, stable TRS remained up to 1000 °C and tended to increase above.

- Machining and Cutting properties

Plastic behavior of NPDs compared to conventional PDCs was studied at HP–HT using D-DIA press coupled with X-ray radiography and diffraction [190–192]. Deformation of PDCs was highly dependent on the binder content and resulted in strong work hardening. However, strength of PCDs was weaker than that of single crystal due to the presence of binder, which acted as a lubricant. On the other hand, NPDs showed a strength 2–3 times higher than conventional PCDs, and mechanisms of deformation were completely different and were dominated by nano-twinning instead of by classic dislocation slip.

Cutting and abrasive properties have shown that NPDs always offer better wear resistance than SC or PDCs. For instance, the wear rate decreases from 200–1000 µm/m to 50–500 µm/m for PCDs and SC, respectively, and down to 10 µm/m for NPDs [128]. As another example, the flank wear of NPDs is reduced by a factor of 2–3 compared to PCDs, and by a factor 20 compared to SC [129,130] (Table 3).

Fracture toughness of MPD has been determined to be higher than the one of SC, and the wear/abrasion resistance to be 2 to 3 times higher than the best PDC [103].

- Optical properties

Optical properties of NPDs were also extensively studied using IR, UV and photoluminescence spectroscopy [128,133]. By combining these techniques, structural defects were revealed, such as the presence of nitrogen, small abundance of lonsdaleite, presence of a few dislocations and the absence of residual strain. Moreover, NPDs have larger bandgap than that of single-crystal diamond [193].

- Uses

Prior to considering these uses of NPDs, a great instrumental effort was made to be able to fabricate large pieces of ~1 cm³ [102]. This was possible due to the development of a 6000-ton Kawai-type multi anvil, as well as the selection of adapted grade of WC anvils and heater elements (Figure 7c). Thus, with such high-load apparatus, very high pressure was attainable even for very large volume samples.

Due to the exceptional properties of NPDs, they have potential applications in various industrial fields (cutting, drilling and electronics) and in new technologies. However, the industrial transfer for the fabrication of these NPDs seems extremely difficult. Indeed, the extreme high conditions of pressure and temperature (20 GPa, T > 2000 °C) needed for such synthesis require very high-pressure apparatuses that are very expensive (~1 M\$) and very different from classic Toroid press usually used at much lower conditions (P < 8 GPa, T < 2000 °C). Moreover, these very high-pressure apparatuses are not easy to install and not easy to use, with a high risk of failure (so called blow-out).

Therefore, the main use for this NPD is limited to scientific fields, especially in high pressure research, either for their mechanical or optical properties. A Special Issue was published recently in *High-Pressure Research* (2020) in order to provide the main uses of NPDs on different scientific topics. A brief description is given below.

Mostly, NPDs are used in diamond anvil cell (DAC) combined with X-ray spectroscopic techniques such as XAS and EXAFS. Indeed, NPDs anvils have the advantage to produce a weak background in the signal and to not produce any glitch in the signal compared to conventional single-crystal anvils [194–198]. Thus, very fine local structure in the samples can be determined over a wide range of pressure. Similarly, NPDs were also used as anvils for neutron diffraction studies [199,200]. These recent developments have shown that pressure up to 80 GPa can be reached with a very “clean” neutron diffraction pattern, making NPDs anvils suitable materials for in situ studies of low Z materials at high pressure.

NPDs are also used to go further under high pressure combined with these spectroscopic techniques. Double stage DAC (ds-DAC) was also used with NPDs balls as double stage anvils, as first proposed by [143]. According to the shape and size of the double stage, pressure up to 400 GPa has been reached with a still acceptable XAS signal [201,202]. Concerning this ds-DAC set-up, there is still a debate on the value of the high pressures reached, basically due to pressure scaling problems at Mbar [203]. Again, in the same idea, in Paris–Edinburgh press (PE), NPDs were used as a new opposed type double stage to reach pressure up to 130 GPa [204]. The NPD double stage was inserted into the first stage of PE. With this method, sample size could be 100 times bigger than corresponding pressure obtained using conventional DAC. However, no temperature test was performed, making this set-up relatively limited for Earth sciences purposes.

Optical properties were investigated and have shown that NPDs are suitable as pressure and hydrostaticity/isostaticity sensors in high-pressure apparatuses combined with X-Ray/neutron sources [205].

7. Summary and Outlook

Diamond synthesis has always fascinated scientists since the beginning of the last century. A lot of different techniques were developed to mimic natural conditions of diamond formation (Figure 2, Figure 5, Table 4). Basically, there are five main different ways to synthesize/sinter diamonds that cover wide ranges of pressure and temperature, typically from few Pa (in CVD) to several hundreds of GPa (in shock) and from 800–1000 °C (in hydrothermal) to 2000–2500 °C (in HPHT) (Table 4). Each of these techniques has their own advantages and disadvantages based on their P–T conditions, field of applications, technical difficulties and industrial transfer capabilities. From a synthesis point of view, all these five techniques are able to fabricate diamonds, but the yield is very variable, from a few percent (in hydrothermal and SPS) to fully transformed samples (in CVD, HPHT or shock). Moreover, grain size produced is highly variable, from nanometer- to several-hundred-micrometer grains, according to the different techniques, and even within the same techniques but using different P, T and t conditions. Among these techniques, only two are able to sinter diamonds to objects of few mm² (in CVD and HPHT), up to 1 cm² (in HPHT), and to single-crystal or polycrystalline objects. These techniques are CVD and HPHT (Table 4), whereas SPS, hydrothermal or shock produces isolated grains, as powder, with a wide range of grain sizes, from nm to several hundred μm.

In terms of applications, diamond powders are mainly devoted to abrasives whereas compact objects have many more application fields. In detail, due to their smaller sizes and higher purity, CVD diamonds are used as optic windows or thin tips on cutting tools, whereas HPHT diamonds are used as cutting tools for building or drillings.

Table 4. Summary of P–T conditions of the different techniques to synthesize and/or sinter diamonds.

Techniques	Pressure (GPa)	Temperature (°C)	Synthesis	Yield	Sintering	Size of Sintered Objects
CVD	10^{-8} – 10^{-9}	800–1500	✓	very high	✓	few mm ³
SPS	0.1	1500–1600	✓	low	×	-
Hydrothermal						
LP-LT(MT)	0.1–2	300–1200	✓	very low	×	-
HP-HT(MT)	3–8	1000–2000	✓	low	×	-
HPHT						
Catalyst	4–5	1400–1500	✓	high	✓	cm ³
Binderless	15–25	2000–2500	✓	very high	✓	cm ³
Shock	>30	>2000	✓	very high	×	-

Finally, among all of these techniques, HP–HT process is the most used and has experienced the most developments since the mid-1950s, and the first synthetic diamonds. Indeed, diamond objects were, for decades, synthesized and sintered using binders (called PCD), in metallic matrix for the synthesis and using mostly cobalt for the sintering, in order to decrease P–T conditions of formations to few GPa (4–5) and medium temperature (1400–1500 °C) suitable for industrial transfer. This process is able to produce objects with mechanical properties adapted to cutting and drilling, but their duration is limited (hardness only 70 GPa and thermal stability up to 400 °C, a temperature easily reached in drilling due to friction).

Today and after two decades of technical developments using multi-anvil press, HP–HT process is able to synthesize and sinter diamond bodies (up to 1 cm²) without any binder at 20–25 GPa and 2000–2500 °C. This process, called direct conversion sintering (DCS), produces polycrystalline diamonds (mostly with nanometer grain size) that have exceptional mechanical properties, even better than single-crystal diamonds. A lot of work has been made to constrain mechanisms of this DCS as well as to improve the quality of the final product. However, an industrial transfer seems difficult as pressure and temperature remain very high, such that apparatuses are expensive and not easy to use. The next step would be therefore to lower conditions of sintering and keeping exceptional properties.

Indeed, as shown in the phase diagram of carbon (Figure 5), there is an important gap between the synthesis/sintering of diamonds using CVD process (low-pressure–medium-temperature, LP–MT) and those sintered by multi-anvil press (HPHT). Thus, preliminary works were made on the direct sintering of diamond objects from micrometer-grain-size diamond powders, either natural or synthetic (e.g., [131,134]). In this way, the energy delivered by high pressure and high temperature is only devoted to the formation of grain boundaries instead of graphite-to-diamond transition and formation of grain boundaries in the DCS process. Encouraging results show that diamond objects could be obtained at pressure around 12–15 GPa and 2000 °C, still far from conditions achievable in the industry.

The future challenges would be therefore to discover a way or different ways to lower these conditions of synthesis/sintering binderless diamonds compact. Indeed, even though the phase diagram of C is relatively well known and well constrained in terms of P–T stability fields, others parameters could be crucial to reach more “metastable conditions” at which the procedures of synthesis and/or sintering would be efficient. For example, heating and cooling rates, compression and decompression rates, control of grain size and distribution, control of hydrostaticity/isostaticity during the cold compression, and purity of precursors are among the possibilities to explore. Among these potential parameters to tune with, grain size seems to be of primary importance. Indeed, the reactivity of powder is extremely sensitive to the average grain size, its distribution and its purity. For example, it is known that the maximum packing of spheres is only ~75%; therefore, mixing powders with different grain sizes would help to compact the powder with limiting grain fragmentation and high level of stress during cold compression [131,206]. These potential damages

have to be repaired at high temperatures, demanding higher conditions of sintering. It can be concluded from the present literature review that high-pressure–high-temperature conditions have high potential in yielding diamonds.

Finally, analytical progress should be made to characterize the mechanical properties of such hard materials, e.g., the development of non-destructive methods. Finally, the debate on lonsdaleite as a recoverable phase and on its potential higher mechanical properties than diamonds should be continued.

Author Contributions: J.G. contributed to investigation, formal analysis, data curation, validation and writing—original draft preparation. M.P. contributed to conceptualization, supervision, editing, formal analysis and project co-administration. A.L. contributed to conceptualization, methodology, investigation, resources, supervision, writing—review and editing and project administration. All authors have read and agreed to the published version of the manuscript.

Funding: The authors thank CNRS prématuration project DiamCeram (prematuration 2020/AL 12 20) for funding this study.

Institutional Review Board Statement: Not applicable.

Informed Consent Statement: Not applicable.

Data Availability Statement: Data sharing is not applicable in this article (no new data were created or analyzes in this study).

Acknowledgments: The authors thank Stéphane TOULIN (ICMCB, UMR5026) for providing us with assistance with bibliography, Corinne MONNIER (CNRS INNOVATION) and Paola TORRES (CNRS, DR15) for their efficient and helpful contribution.

Conflicts of Interest: The authors declare no conflict of interest.

References

1. Fischer, R.A.; Cottrell, E.; Hauri, E.; Lee, K.K.M.; Le Voyer, M. The carbon content of Earth and its core. *Proc. Natl. Acad. Sci. USA* **2020**, *117*, 8743–8749. [[CrossRef](#)]
2. Parsons, C.A. Experiments of the Artificial Production of Diamond. *Phil. Trans. Roy. Soc.* **1918**, *A220*, 67–106. [[CrossRef](#)]
3. Bridgman, P.W. An experimental contribution to the problem of diamond synthesis. *J. Chem. Phys.* **1947**, *15*, 92. [[CrossRef](#)]
4. Hall, H.T. Ultra-high pressure, high-temperature apparatus: The “Belt”. *Rev. Sci. Instrum.* **1960**, *31*, 125–131. [[CrossRef](#)]
5. Irifune, T.; Kurio, A.; Sakamoto, S.; Inoue, T.; Sumiya, H. Ultrahard polycrystalline diamond from graphite. *Nature* **2003**, *421*, 599–601. [[CrossRef](#)] [[PubMed](#)]
6. Wyckoff, R.W. *Crystal Structures 1*, 2nd ed.; Interscience Publishers: New York, NK, USA, 1963; pp. 7–83.
7. Frondel, C.; Marvin, U.B. Lonsdaleite, a Hexagonal Polymorph of Diamond. *Nature* **1967**, *214*, 587–589. [[CrossRef](#)]
8. Ross, A.; Steele, A.; Fries, M.D.; Kater, L.; Downes, H.; Jones, A.P.; Smith, C.L.; Zolensky, M.E.; Shaddad, M.H. MicroRaman spectroscopy of diamond and graphite in Almahata Sitta and comparison with other ureilites. *Meteorit. Planet. Sci.* **2011**, *46*, 364–378. [[CrossRef](#)]
9. Godard, G.; Frezzotti, M.L.; Palmeri, R.; Smith, D.C. Origin of high-pressure disordered metastable phases (Lonsdaleite and amorphized quartz) in metamorphic rocks: Geodynamic shock or crystal-scale overpressure? In *Ultrahigh-Pressure Metamorphism; 25 years after the discovery of coesite and diamond*; Elsevier: Amsterdam, The Netherlands, 2011; pp. 125–148. [[CrossRef](#)]
10. Utsumi, W.; Yagi, T.; Taniguchi, T.; Shinomura, O. In situ X-ray observation of the graphite-diamond transition using synchrotron. In *Proceedings of the 3rd NIRIM International Symposium on Advanced Materials*, Tsukuba, Japan, 4–8 March 1996; pp. 257–261. [[CrossRef](#)]
11. Pan, Z.; Sun, H.; Zhang, Y.; Chen, C. Harder than diamond: Superior indentation of wurtzite BN and Lonsdaleite. *Phys. Rev. Lett.* **2009**, *102*, 055503. [[CrossRef](#)]
12. Sundqvist, B. Carbon under pressure. *Physic Rep.* **2021**, *909*, 1–73. [[CrossRef](#)]
13. McIntyre, R.A. Common nano-materials and their use in real world application. *Sci. Prog.* **2012**, *95*, 1–22. [[CrossRef](#)]
14. Murayama, H.; Tomonoh, S.; Alford, J.M.; Karpuk, M.E. Fullerene production in tons and more: From science to industry. *Fuller. Nanotub. Carbon Nanostructures* **2004**, *12*, 1–9. [[CrossRef](#)]
15. Pagni, J. Amroy aims to become nano-leader. *European Plastic News*, 5 March 2010.
16. Zhu, Z.; Lu, L.; Yao, X.; Zhang, W.; Liu, W. Carbon nanotube tape stays sticky in extreme temperatures. In *Nanowork Newsletter*; American Chemical Society: Washington, DC, USA, 2019.
17. Noyce, S.G.; Doherty, J.L.; Cheng, Z.; Han, H.; Bowen, S.; Franklin, A.D. Electronic Stability of Carbon Nanotube Transistors Under Long-Term Bias Stress. *Nano Lett.* **2019**, *19*, 1460–1466. [[CrossRef](#)] [[PubMed](#)]

18. Belkin, A.; Hubler, A.; Bezryadin, A. Self-Assembled Wiggling Nano-Structures and the Principle of Maximum Entropy Production. *Sci. Rep.* **2015**, *5*, 8323. [CrossRef] [PubMed]
19. Tan, C.W.; Tan, K.H.; Ong, Y.T.; Mohamed, A.R.; Sharif, H.S.Z.; Tan, S.H. Energy and environmental applications of carbon nanotubes. *Environ. Chem. Lett.* **2012**, *10*, 265–273. [CrossRef]
20. Tucker, A. Jack Andraka, the Teen Prodigy of Pancreatic Cancer. *Smithsonian Magazine*, 1 December 2012.
21. Robertson, J. Diamond-like amorphous carbon. *Mater. Sci. Eng. R Rep.* **2002**, *37*, 129–281. [CrossRef]
22. Grill, A.; Meyerson, B.S.; Patel, V.V. Diamondlike carbon films by RF plasma-assisted chemical vapor deposition from acetylene. *IBM J. Res. Dev.* **1990**, *34*, 849–857. [CrossRef]
23. Polo, M.C.; Andújar, J.L.; Hart, A.; Robertson, J.; Milne, W.I. Preparation of tetrahedral amorphous carbon films by filtered cathodic vacuum arc deposition. *Diam. Relat. Mater.* **2000**, *9*, 663–667. [CrossRef]
24. Ho, M.P.; Lau, A.K.-T. Amorphous carbon nanocomposites. *Fill. Reinf. Adv. Nanocompos.* **2015**, *12*, 309–328. [CrossRef]
25. Narayan, J.; Bhaumik, A. Q-carbon discovery and formation of single-crystal diamond nano- and microneedles and thin films. *Mater. Res. Lett.* **2016**, *4*, 118–126. [CrossRef]
26. Narayan, J.; Bhaumik, A.; Gupta, S.; Haque, A.; Sachan, R. Progress in Q-carbon and related materials with extraordinary properties. *Mater. Res. Lett.* **2018**, *6*, 353–364. [CrossRef]
27. Shirey, S.B.; Cartigny, P.; Frost, D.J.; Keshav, S.; Nestola, F.; Nimis, P.; Graham Pearson, D.; Sobolev, N.V.; Walter, M.J. Diamonds and the geology of mantle carbon. *Rev. Mineral. Geochem.* **2013**, *75*, 355–421. [CrossRef]
28. Shirey, S.B.; Shigley, J.E. Recent advances in the understanding the geology of diamonds. *Gems Gemol.* **2013**, *49*, 188–232. [CrossRef]
29. Hough, R.M.; Gilmour, I.; Pillinger, C.T.; Arden, J.W.; Gilkes, K.W.R.; Yuan, J.; Milledge, H.J. Diamond and silicon carbide in impact melt rock from the Ries impact crater. *Nature* **1995**, *378*, 41–44. [CrossRef]
30. Ohfuji, H.; Irifune, T.; Litasov, K.D.; Yamashita, T.; Isobe, F.; Afanasiev, V.P.; Pokhilenko, N.P. Natural occurrence of pure nano-polycrystalline diamond from impact crater. *Sci. Rep.* **2015**, *5*, 14702. [CrossRef] [PubMed]
31. Nabiei, F.; Badro, J.; Dennenwaldt, T.; Oveisi, E.; Cantoni, M.; Hébert, C.; El Goresy, A.; Barrat, J.-A.; Gillet, P. A large planetary body inferred from diamond inclusions in a ureilite meteorite. *Nat. Commun.* **2018**, *9*, 1327. [CrossRef] [PubMed]
32. Lodders, K.; Amari, S. Presolar grains from meteorites: Remnants from the early times of the solar system. *Chem. Erde* **2005**, *65*, 93–166. [CrossRef]
33. Stachel, T.; Luth, R.W. Diamond formation—Where, when and how? *Lithos* **2015**, 220–223, 200–220. [CrossRef]
34. McCall, G.J.H. The carbonado diamond conundrum. *Earth-Sci. Rev.* **2009**, *93*, 85–91. [CrossRef]
35. Robinson, D.N. The characteristics of natural diamond and their interpretation. *Miner. Sci.* **1978**, *10*, 55–72.
36. Frantsesson, E.V.; Kaminskiy, F.V. Carbonado, a diamond variety of nonkimberlitic origin. *Akademiya Nauk SSSR Doklady. Earth Sci. Sect.* **1974**, *219*, 117–119.
37. Kagi, H.; Takahashi, K.; Hidaka, H.; Masuda, A. Chemical properties of Central American carbonado and its implications. *Geochim. Cosm. Acta* **1994**, *58*, 2629–2638. [CrossRef]
38. Mitchell, R.H. Kimberlites and Lamproites: Primary sources of diamond. *Geosci. Can.* **1991**, *18*, 1–16.
39. Marshall, T.R.; Baxter-Brown, R. Basic principles of alluvial diamond exploration. *J. Geochem. Explor.* **1995**, *53*, 277–292. [CrossRef]
40. King, S.D. Archean cratons and mantle dynamics. *Earth Planet. Sci. Lett.* **2005**, *234*, 1–14. [CrossRef]
41. US Geological Survey. *Mineral Commodity Summaries 2020: US Geological Survey*; US Geological Survey: Reston, VA, USA, 2020; 200p. [CrossRef]
42. Gastner, M.T.; Seguy, V.; More, P. Fast flow-based algorithm for creating density-equalizing map projections. *Proc. Natl. Acad. Sci. USA* **2018**, *115*, 2156–2164. [CrossRef] [PubMed]
43. Yelapaala, K.; Ali, S.H. Multiple scales of diamond mining in Akwatia, Ghana: Addressing environmental and human development impact. *Resour. Policy* **2005**, *30*, 145–155. [CrossRef]
44. Lujala, P.; Gleditsch, N.P.; Gilmore, E. A diamond curse? Civil war and a lootable resource. *J. Confl. Resolut.* **2005**, *49*, 538–562. Available online: <https://www.jstor.org/stable/30045130> (accessed on 1 December 2021). [CrossRef]
45. Le Billon, P. Diamond wars? Conflict diamonds and geographies of resource wars. *Ann. Assoc. Am. Geogr.* **2008**, *98*, 345–372. [CrossRef]
46. Breeding, C.M.; Shigley, J.E. The “type” classification system of diamonds and its importance in gemology. *Gems Gemol.* **2009**, *45*, 96–111. [CrossRef]
47. Roozeboom, B. Die heterogenen Gleichgewichte. *Braunschweig* **1901**, *1*, 180.
48. Tamman, G. Crystal forms which are stable only at high pressures. *Z. Phys. Chem.* **1909**, *69*, 569.
49. Rossini, F.D.; Jessup, R.S. Heat and free energy of formation of carbon dioxide and the transition between graphite and diamond. *J. Res. Natl. Bur. Stand. US* **1938**, *21*, 491. [CrossRef]
50. Leipunskii, O.I. Synthetic diamonds. *Usp. Khim.* **1939**, *8*, 1519.
51. Lijebblad, R. Equilibrium pressure for the different temperatures between graphite and diamonds. *Ark. Kemi.* **1955**, *8*, 423.
52. Berman, R.; Simon, F. The graphite-diamond equilibrium. *Z. Electrochem.* **1955**, *59*, 333. [CrossRef]
53. Liander, H.; Lundblad, E. Some observations on the synthesis of diamonds. *Ark. Kemi.* **1960**, *16*, 139–149.
54. Lundblad, E.G. High-pressure synthesis of diamond in Sweden in 1953. *AIP Conf. Proc.* **1994**, *309*, 503–506. [CrossRef]
55. Bundy, F.P.; Hall, H.T.; Strong, H.M.; Wentorf, R.H., Jr. Man-made diamonds. *Nature* **1955**, *176*, 51–55. [CrossRef]

56. Bundy, F.P. Direct conversion of graphite to diamond in static pressure apparatus. *J. Chem. Phys.* **1963**, *38*, 631–643. [CrossRef]
57. Bundy, F.P. The P, T phase and reaction diagram for elemental carbon, 1979. *J. Geophys. Res.* **1980**, *85*, 6930–6936. [CrossRef]
58. Lazicki, A.; McGonegle, D.; Rygg, J.R.; Braun, D.G.; Swift, D.C.; Gorman, M.G.; Smith, R.F.; Heighway, P.G.; Higginbotham, A.; Suggit, M.J.; et al. Metastability of diamond ramp-compressed to 2 terapascals. *Nature* **2021**, *589*, 532–535. [CrossRef] [PubMed]
59. Benedict, L.X.; Driver, K.P.; Hamel, S.; Militzer, B.; Qi, T.; Corraera, A.A.; Saul, A.; Schwegler, E. A Multiphase equation of state for carbon addressing high pressures and temperatures. *Phys. Rev. B* **2014**, *89*, 224109. [CrossRef]
60. Scientific American. *How Mr. Hannay Made his Diamonds*; Munn & Company: New York, NY, USA, 1880; p. 83.
61. Moissan, H. *Le Four Electrique*; G. Steinheil: Paris, France, 1897.
62. DeCarli, P.S.; Jamieson, J.C. Formation of diamond by explosive shock. *Science* **1961**, *133*, 1821–1822. [CrossRef] [PubMed]
63. Angus, J.C.; Will, H.A.; Stanko, W.S. Growth of diamond seed crystals by vapor deposition. *J. Appl. Phys.* **1968**, *39*, 2915–2922. [CrossRef]
64. Available online: <https://statista.com> (accessed on 1 December 2021).
65. Available online: <https://www.alliedmarketresearch.com> (accessed on 1 December 2021).
66. Expertmarketresearch. Global Industrial Diamond Market Outlook. 2020. Available online: <https://www.expertmarketresearch.com/reports/industrial-diamond-market> (accessed on 1 December 2021).
67. German, R.M. *Sintering Theory and Practice*; Wiley-VCH: Weinheim, Germany, 1996; p. 568.
68. German, R.M. Sintering: From empirical observations to scientific principles. In *Chapter Ten—Sintering with External Pressure*; Butterworth-Heinemann: Oxford, UK, 2014; pp. 305–354. [CrossRef]
69. Antou, G.; Guyot, P.; Pradeilles, N.; Vandenhende, M.; Maitre, A. Identification of densification mechanisms of pressure-assisted sintering: Application to hot pressing and spark plasma sintering of alumina. *J. Mater. Sci.* **2015**, *50*, 2327–2336. [CrossRef]
70. Eversole, W.G. Synthesis of Diamond. U.S. Patents 3,030,187, 3,030,188, 23 July 1958.
71. Angus, J.C. Diamond synthesis by chemical vapor deposition: The Early years. *Diam. Relat. Mater.* **2014**, *49*, 77–86. [CrossRef]
72. Angus, J.C.; Hayman, C. Low-pressure, metastable growth of diamond and “diamondlike” phases. *Science* **1988**, *241*, 913–921. [CrossRef]
73. Schwander, M.; Partes, K. A review of diamond synthesis by CVD processes. *Diam. Relat. Mater.* **2011**, *20*, 1287–1301. [CrossRef]
74. Tallaire, A. Ingénierie des Défauts Multidimensionnels dans le Diamant Synthétisé par Dépôt Chimique en Phase Vapeur Assisté par Plasma. Ph.D. Thesis, Matériaux, Université Paris 13—Sorbonne Paris Cité, Paris, France, 2017.
75. Munir, Z.A.; Anselmi-Tamburini, U.; Ohyanagi, M. The effect of electric field and pressure on the synthesis and consolidation of materials: A review of the Spark Plasma Sintering method. *J. Mater. Sci.* **2006**, *41*, 763–777. [CrossRef]
76. Kumar, D.B.; Babu, S.; Aravind Jerrni, K.M.; Joseph, N.; Jiss, A. Review of spark plasma sintering process. *IOP Conf. Ser. Mater. Sci. Eng.* **2020**, *993*, 012004. [CrossRef]
77. Chaim, R. Densification mechanisms in Spark Plasma Sintering of nanocrystalline ceramics. *Mater. Sci. Eng. A* **2007**, *443*, 25–32. [CrossRef]
78. Zhang, F.; Shen, J.; Sun, J.; Zhu, Y.Q.; Wang, G.; McCartney, G. Conversion of carbon nanotubes to diamond by spark plasma sintering. *Carbon* **2005**, *43*, 1254–1258. [CrossRef]
79. Zhang, F.; Shen, J.; Sun, J.; McCartney, G. Direct synthesis of diamond from low purity carbon nanotubes. *Carbon* **2006**, *44*, 3113–3148. [CrossRef]
80. Zhang, F.; Mihoc, C.; Ahmed, F.; Lathe, C.; Burkel, E. Thermal stability of carbon nanotubes, fullerene and graphite under spark plasma sintering. *Chem. Phys. Lett.* **2011**, *510*, 109–114. [CrossRef]
81. Zhang, F.; Adam, M.; Ahmed, F.; Otterstein, E.; Burkel, E. Pulsed electric field induces diamond synthesis from carbon nanotubes with solvent catalysts. *Diam. Relat. Mater.* **2011**, *20*, 853–858. [CrossRef]
82. Zhang, F.; Ahmed, F.; Holzhüter, G.; Burkel, E. Growth of diamond from fullerene C60 by spark plasma sintering. *J. Cryst. Growth* **2012**, *340*, 1–5. [CrossRef]
83. Zhang, F.; Ahmed, F.; Bednarcik, J.; Burkel, E. Diamond synthesis through the generation of plasma during spark plasma sintering. *Phys. Status Solidi A* **2012**, *209*, 2241–2246. [CrossRef]
84. Zhang, F.; Fan, K.; Yu, J.; Saba, F.; Sun, J. Pulsed direct current field-induced thermal stability and phase transformation of nanodiamonds to carbon onions. *RCS Adv.* **2019**, *9*, 14360. [CrossRef]
85. Zhang, F.; Burkel, E. Synthesis of diamond using spark plasma sintering. In *Sintering of Ceramics—New Emerging Techniques*; Arunachalam, L., Ed.; InTech: London, UK, 2012; ISBN 978-953-51-0017-1. [CrossRef]
86. Nickel, K.G.; Kraft, T.; Gogotsi, Y.G. Hydrothermal synthesis of diamond. In *Handbook of Ceramics and Hard Materials*; Wiley: New York, NY, USA, 2000; Chapter 3. [CrossRef]
87. Szymanski, A.; Abgarowicz, E.; Bakon, A.; Niedbalska, A.; Salacinski, R.; Sentek, J. Diamond formed at low pressures and temperatures through liquid-phase hydrothermal synthesis. *Diam. Relat. Mater.* **1995**, *4*, 234–235. [CrossRef]
88. Roy, R.; Ravichandran, D.; Ravindranathan, P.; Badzian, A. Evidence for hydrothermal growth of diamond in the C-H-O and C-H-O halogen system. *J. Mater. Res.* **1996**, *11*, 1164–1168. [CrossRef]
89. Zhao, X.-Z.; Roy, R.; Cherian, K.A.; Badzian, A. Hydrothermal growth of diamond in metal-C-H₂O systems. *Nature* **1997**, *385*, 513–515. [CrossRef]
90. Szymanski, A. On the possibility of bulk large diamond single crystal synthesis with hydrothermal process. *J. Miner. Soc. Korea* **1997**, *10*, 18–32.

91. Gogotsi, Y.G.; Kraft, T.; Nickel, K.; Zvanut, M.E. Hydrothermal behavior of diamond. *Diam. Relat. Mater.* **1998**, *7*, 1459–1465. [[CrossRef](#)]
92. Yokosawa, K.; Korablov, S.; Tohji, K.; Yamasaki, N. The possibility of diamond sintering by hydrothermal hot pressing. *AIP Conf. Proc.* **2006**, *833*, 100–103. [[CrossRef](#)]
93. Korablov, S.; Yokosawa, K.; Korablov, D.; Tohji, K.; Yamasaki, N. Hydrothermal formation of diamond from chlorinated organic compounds. *Mater. Lett.* **2006**, *60*, 3041–3044. [[CrossRef](#)]
94. Korablov, S.; Yokosawa, K.; Sasaki, T.; Korablov, D.; Kawasaki, A.; Ioku, K.; Ishida, E.H.; Yamasaki, N. Synthesis of diamond from a chlorinated organic substance under hydrothermal conditions. *J. Mater. Sci.* **2007**, *42*, 7939–7949. [[CrossRef](#)]
95. Roy, R.; Ravichandran, D.; Badzian, A.; Breval, E. Attempted hydrothermal synthesis of diamond by hydrolysis of β -SiC powder. *Diam. Relat. Mater.* **1996**, *5*, 973–976. [[CrossRef](#)]
96. Gogotsi, Y.G.; Kofstad, P.; Yoshimura, M.; Nickel, K.G. Formation of sp^3 -bonded carbon upon hydrothermal treatment of SiC. *Diam. Relat. Mater.* **1996**, *5*, 151–162. [[CrossRef](#)]
97. Gogotsi, Y.; Weiz, S.; Ersoy, D.A.; McNallan, M.J. Conversion of silicon carbide to crystalline diamond-structured carbon at ambient pressure. *Nature* **2001**, *411*, 283–287. [[CrossRef](#)]
98. Basavalingu, B.; Byrappa, K.; Madhusudan, P. Hydrothermal synthesis of nanosized crystals of diamond under sub-natural conditions. *J. Geol. Soc. India* **2007**, *69*, 665–670.
99. Zhang, W.; Fan, B.; Zhang, Y.; Fan, J. Hydrothermal synthesis of well crystallized C8 and diamond monocrystals and pH-controlled C8-Diamond phase transition. *CrystEngComm* **2017**, *19*, 1248–1252. [[CrossRef](#)]
100. Néri, A.; Guignard, J.; Monnereau, M.; Bystricky, M.; Perillat, J.-P.; Andraut, A.; King, A.; Guignot, N.; Tenailleau, C.; Duployer, B.; et al. Reevaluation of metal interconnectivity in a partially molten silicate matrix using 3D microtomography. *Phys. Earth Planet. Inter.* **2020**, *308*, 106571. [[CrossRef](#)]
101. Balima, F.; Belin, F.; Michau, D.; Viraphong, O.; Poulon-Quintin, A.; Chung, U.-C.; Dourfaye, A.; Largeteau, A. High pressure pulsed electric current activated equipment (HP-SPS) for material processing. *Mater. Des.* **2018**, *139*, 541–548. [[CrossRef](#)]
102. Irifune, T.; Isobe, F.; Shinmei, T. A novel large-volume Kawai-type apparatus and its application to the synthesis of sintered bodies of nano-polycrystalline diamond. *Phys. Earth Planet. Inter.* **2014**, *228*, 255–261. [[CrossRef](#)]
103. Zhan, G.D.; Moellendick, T.E.; Li, B.; Gooneratne, C. New ultra-strong and catalyst-free PDC cutting element technology. In Proceedings of the International Petroleum Technology Conference, Dhahran, Saudi Arabia, 13 January 2020. [[CrossRef](#)]
104. Akaishi, M.; Yamaoka, S. Crystallization of diamond from C-H-O fluid under high-pressure and high-temperature conditions. *J. Cryst. Growth* **2000**, *209*, 999–1003. [[CrossRef](#)]
105. Akaishi, M.; Shaji Kumar, M.D.; Kanda, H.; Yamaoka, S. Formation process of diamond from supercritical H_2O - CO_2 fluid under high pressure and high temperature conditions. *Diam. Relat. Mater.* **2000**, *9*, 1945–1950. [[CrossRef](#)]
106. Akaishi, M.; Shaji Kumar, M.D.; Akaishi, M.; Yamaoka, S. Formation of diamond from supercritical H_2O - CO_2 fluid at high pressure and high temperature. *J. Cryst. Growth* **2000**, *213*, 203–206. [[CrossRef](#)]
107. Sokol, A.G.; Pal'yanov, Y.N.; Pal'yanova, G.A.; Khokhryakov, A.F.; Borzdov, Y.M. Diamond and graphite crystallization from C-O-H fluids under high pressure and high temperature conditions. *Diam. Relat. Mater.* **2001**, *10*, 2131–2136. [[CrossRef](#)]
108. Sokol, A.G.; Pal'yanov, Y.N.; Pal'yanova, G.A.; Tomilenko, A.A. Diamond crystallization in fluid and carbonate-fluid systems under mantle P-T conditions: 1. Fluid composition. *Geochem. Int.* **2004**, *42*, 830–838.
109. Sokol, A.G.; Pal'yanov, Y.N. Diamond crystallization in fluid and carbonate-fluid systems under mantle P-T conditions: 2. An analytical review of experimental data. *Geochem. Int.* **2004**, *42*, 1018–1032.
110. Naka, S.; Horii, K.; Takeda, Y.; Hanawa, T. Direct conversion of graphite to diamond under static pressure. *Nature* **1976**, *259*, 38–39. [[CrossRef](#)]
111. Strong, H.M.; Hanneman, R.E. Crystallization of diamond and graphite. *J. Chem. Phys.* **1967**, *46*, 3668–3676. [[CrossRef](#)]
112. Strong, H.M.; Chrenko, R.M. Further studies on diamond growth rates and physical properties of laboratory-made diamond. *J. Chem. Phys.* **1971**, *75*, 1838–1843. [[CrossRef](#)]
113. Kennedy, C.S.; Kennedy, G.C. The equilibrium boundary between graphite and diamond. *J. Geophys. Res.* **1976**, *81*, 2467–2470. [[CrossRef](#)]
114. Wakatsuki, M. New catalysts for synthesis of diamond. *Jpn. J. Appl. Phys.* **1966**, *5*, 337. [[CrossRef](#)]
115. Kanda, H.; Akaishi, M.; Yamaoka, S. New catalysts for diamond growth under high pressure and high temperature. *Appl. Phys. Lett.* **1994**, *65*, 784–786. [[CrossRef](#)]
116. Polyanov, Y.N.; Kupriyanov, I.N.; Borzdov, Y.M.; Surovtsev, N.V. Germanium: A new catalyst for diamond synthesis and a new optical active impurity in diamond. *Sci. Rep.* **2015**, *5*, 14789. [[CrossRef](#)]
117. Polyanov, Y.N.; Kupriyanov, I.N.; Khokhryakov, A.; Borzdov, Y.M. High pressure crystallization and properties of diamond from magnesium-based catalyst. *CrystEngComm* **2017**, *19*, 4459–4475. [[CrossRef](#)]
118. Katzman, H.; Libby, W.F. Sintered diamond compacts with a cobalt binder. *Science* **1971**, *171*, 1132–1134. [[CrossRef](#)]
119. Liu, C.; Kou, Z.; He, D.; Chen, Y.; Wang, K.; Hui, B.; Zhang, R.; Wang, Y. Effect of removing internal residual metallic phases on wear resistance of polycrystalline diamond compacts. *Int. J. Refract. Met. Hard Mater.* **2012**, *31*, 187–191. [[CrossRef](#)]
120. Westraadt, J.E.; Sigalas, I.; Neethling, J.H. Characterization of thermally degraded polycrystalline diamond. *Int. J. Refract. Met. Hard Mater.* **2015**, *48*, 286–292. [[CrossRef](#)]

121. Gu, J.; Huang, K. Role of cobalt of polycrystalline diamond compact (PDC) in drilling process. *Diam. Relat. Mater.* **2016**, *66*, 98–101. [[CrossRef](#)]
122. Sumiya, H.; Irifune, T.; Kurio, A.; Sakamoto, S.; Inoue, T. Microstructure features of polycrystalline diamond synthesized directly from graphite under static high pressure. *J. Mater. Sci.* **2004**, *39*, 445–450. [[CrossRef](#)]
123. Sumiya, H.; Irifune, T. Hardness and deformation microstructures of nano-polycrystalline diamonds synthesized from various carbons under high pressure and high temperature. *J. Mater. Res.* **2007**, *22*, 2345–2351. [[CrossRef](#)]
124. Sumiya, H.; Irifune, T. Microstructure and Mechanical Properties of High-Hardness nanopolycrystalline diamonds. *SEI Tech. Rev.* **2008**, *66*, 85–91.
125. Le Guillou, C.; Brunet, F.; Irifune, T.; Ohfuji, H.; Rouzaud, J.-L. Nanodiamond nucleation below 2273 K at 15 GPa from carbons with different structural organizations. *Carbon* **2007**, *45*, 636–648. [[CrossRef](#)]
126. Isobe, F.; Irifune, T.; Shinmei, T.; Suga, S.; Nishiyama, N.; Sumiya, H. Lowering P, T Boundary for Synthesis of pure nano-polycrystalline diamond. *J. Phys. Conf. Ser.* **2010**, *215*, 012136. [[CrossRef](#)]
127. Xu, C.; He, D.; Wang, H.; Guan, J.; Liu, C.; Peng, F.; Wang, W.; Kou, Z.; He, K.; Yan, X.; et al. Nano-polycrystalline diamond formation under ultra-high pressure. *Int. J. Refract. Met. Hard Mater.* **2013**, *36*, 232–237. [[CrossRef](#)]
128. Sumiya, H. Novel development of high-pressure synthetic diamonds “Ultra-hard Nano-polycrystalline Diamonds”. *SEI Tech. Rev.* **2012**, *74*, 15–23.
129. Sumiya, H. Novel superhard nanopolycrystalline materials synthesized by direct conversion sintering under high pressure and high temperature. *MRS Bull.* **2017**, *42*, 729–733. [[CrossRef](#)]
130. Sumiya, H.; Harano, K. Innovative Ultra-hard materials: Binderless nano-polycrystalline Diamond and nano-polycrystalline Cubic Boron Nitride. *SEI Tech. Rev.* **2016**, *81*, 21–26.
131. Couvy, H.; Lahiri, D.; Chen, J.; Agarwal, A.; Sen, G. Nanohardness and Young’s modulus of nanocrystalline diamond. *Scr. Mater.* **2011**, *64*, 10419–11022. [[CrossRef](#)]
132. Chang, Y.-Y.; Jacobsen, S.D.; Kimura, M.; Irifune, T.; Ohno, I. Elastic properties of transparent nano-polycrystalline diamond measured by GHz-ultrasonic interferometry and resonant sphere methods. *Phys. Earth Planet. Inter.* **2014**, *228*, 47–55. [[CrossRef](#)]
133. Sumiya, H.; Harano, K.; Arimoto, K.; Kagi, H.; Otake, S.; Irifune, T. Optical characteristics of nano-polycrystalline diamond synthesized directly from graphite under high pressure and high temperature. *Jpn. J. Appl. Phys.* **2009**, *48*, 120206. [[CrossRef](#)]
134. Lu, J.; Kou, Z.; Liu, T.; Yan, X.; Liu, F.; Ding, W.; Zhang, Q.; Zhang, L.; Liu, J.; He, D. Submicron binderless polycrystalline diamond sintering under ultra-high pressure. *Diam. Relat. Mater.* **2017**, *77*, 41–45. [[CrossRef](#)]
135. Liu, J.; Zhan, G.; Wang, Q.; Yan, X.; Liu, F.; Wang, P.; Lei, L.; Peng, F.; Kou, Z.; He, D. Superstrong micro-grained polycrystalline diamond compact through work hardening under high pressure. *Appl. Phys. Lett.* **2018**, *112*, 061901. [[CrossRef](#)]
136. Li, Q.; Zhan, G.; Li, D.; He, D.; Moellendick, T.E.; Gooneratne, C.P.; Alalayednassir, A.G. Ultrastrong catalyst-free polycrystalline diamond. *Sci. Rep.* **2020**, *10*, 22020. [[CrossRef](#)]
137. Osipov, V.Y.; Shakhov, F.M.; Bogdanov, K.V.; Takai, K.; Hayashi, T.; Treussart, F.; Baldycheva, A.; Hogan, B.T.; Jentgens, C. High-quality green-emitting nanodiamonds fabricated by HPHT sintering of polycrystalline shockwave diamonds. *Nanoscale Res. Lett.* **2020**, *15*, 209. [[CrossRef](#)]
138. Dubrovinskaia, N.; Dubrovinsky, L.; Crichton, W.; Langenhorst, F.; Richter, A. Aggregated diamond nanorods, the densest and least compressible form of carbon. *Appl. Phys. Lett.* **2005**, *87*, 083106. [[CrossRef](#)]
139. Dubrovinskaia, N.; Dubrovinsky, L.; Langenhorst, F.; Jacobsen, S.; Liebske, C. Nanocrystalline diamond synthesized from C60. *Diam. Relat. Mater.* **2005**, *14*, 16–22. [[CrossRef](#)]
140. Irifune, T.; Ueda, C.; Ohshita, S.; Ohfuji, H.; Kunimoto, T.; Shinmei, T. Synthesis of nano-polycrystalline diamond from glassy carbon at pressures up to 25 GPa. *High Press. Res.* **2020**, *40*, 96–106. [[CrossRef](#)]
141. Merlen, A.; Toulemonde, P.; Le Floch, S.; Montagnac, G.; Hammouda, T.; Marty, O.; San Miguel, A. High pressure-high temperature synthesis of diamond from single-wall pristine and iodine doped nanotube bundles. *Carbon* **2009**, *47*, 1643–1651. [[CrossRef](#)]
142. Solopova, N.A.; Dubrovinskaia, N.; Dubrovinsky, L. Synthesis of nanocrystalline diamond from glassy carbon balls. *J. Cryst. Growth* **2015**, *412*, 54–59. [[CrossRef](#)]
143. Dubrovinsky, L.; Dubrovinskaia, N.; Prakapenka, V.B.; Abakumov, A.M. Implementation of micro-ball nanodiamond anvils for high-pressure studies above 6 Mbar. *Nat. Commun.* **2012**, *3*, 1163. [[CrossRef](#)]
144. Davydov, V.A.; Rakhmanina, A.V.; Agafonov, V.; Narymbetov, B.; Boudou, J.-P.; Szwarc, H. Conversion of polycyclic aromatic hydrocarbons to graphite and diamond at high pressures. *Carbon* **2004**, *42*, 261–269. [[CrossRef](#)]
145. Kawamura, H.; Ohfuji, H. Nano-polycrystalline diamond synthesized through the decomposition of stearic acid. *High Press. Res.* **2020**, *40*, 162–174. [[CrossRef](#)]
146. Park, S.; Abate, I.I.; Liu, J.; Wang, C.; Dahl, J.E.P.; Carlson, R.M.K.; Yang, L.; Prakapenka, V.B.; Greenberg, E.; Devereaux, T.P.; et al. Facile diamond synthesis from lower diamondoids. *Sci. Adv.* **2020**, *6*, eaay9405. [[CrossRef](#)]
147. Irifune, T. A brief history of nano-polycrystalline diamond. *High Press. Res.* **2020**, *40*, 1–2. [[CrossRef](#)]
148. Voronov, O.; Tompa, G.; Sadangi, R.; Kear, B.; Wilson, C.; Yan, P. *Superhard Nanophase Cutter Materials for Rock Drilling Applications*; Diamond Materials Inc.: Piscataway, NJ, USA, 2000. [[CrossRef](#)]
149. Duanwei, H.; Chao, X.; Haikuo, W. Method for Preparing High-Performance Polycrystalline Diamond by Utilizing Hinge-Type Cubic Press. Patent CN103331129A, 2013.

150. Shakhov, F.M.; Abyzov, A.M.; Takai, K. Boron doped diamond synthesized from detonation nanodiamond in C-O-H fluid at high pressure and high temperature. *J. Solid State Chem.* **2017**, *256*, 72–92. [[CrossRef](#)]
151. Fischbach, D.B. The kinetics and mechanism of graphitization. In *The Chemistry and Physics of Carbon 7*; Walker, P.L., Ed.; Marcel Dekker: New York, NY, USA, 1971; pp. 1–154.
152. Bonijoly, M.; Oberlin, M.; Oberlin, A. A possible mechanism for natural graphite formation. *Int. J. Coal Geol.* **1982**, *1*, 283–312. [[CrossRef](#)]
153. Wentorf, R.H., Jr. The behavior of some carbonaceous materials at very high pressures and high temperatures. *J. Phys. Chem.* **1965**, *9*, 3063–3069. [[CrossRef](#)]
154. Ekimov, E.A.; Kudryavtsev, O.S.; Mordinova, E.; Lebedev, O.I.; Vlasov, I.I. High-pressure synthesis of nanodiamonds from adamantane: Myth or Reality. *Chem. Nanomater.* **2018**, *4*, 269–273. [[CrossRef](#)]
155. Bergmann, O.R.; Bailey, N.F.; Coverly, H.B. Polishing performance of polycrystalline diamond produced by explosive shock wave synthesis. *Metallography* **1982**, *15*, 121–139. [[CrossRef](#)]
156. Schrand, A.M.; Ciftan Hens, S.A.; Shenderova, O.A. Nanodiamond particles: Properties and perspectives for bioapplications. *Crit. Rev. Solid State Mater. Sci.* **2009**, *34*, 18–74. [[CrossRef](#)]
157. Erksine, D.J.; Nellis, W.J. Shock-induced martensitic phase transformation of orientated graphite to diamond. *Nature* **1991**, *349*, 317–319. [[CrossRef](#)]
158. Kurdyumov, A.V.; Britun, V.F.; Yarosh, V.V.; Danilenko, A.I.; Zelyavski, V.B. The influence of the shock compression conditions on the graphite transformation into lonsdaleite and diamond. *J. Superhard Mater.* **2012**, *34*, 19–27. [[CrossRef](#)]
159. Kraus, D.; Ravasio, A.; Gauthier, M.; Gericke, D.O.; Vorberger, J.; Frydrych, S.; Helfrich, J.; Fletcher, L.B.; Schaumen, G.; Nagler, B.; et al. Nanosecond formation of diamond and lonsdaleite by shock compression of graphite. *Nat. Commun.* **2016**, *7*, 10970. [[CrossRef](#)]
160. Volt, T.J.; Gupta, Y.M. Graphite to diamond transformation under shock compression: Role of orientational order. *J. Appl. Phys.* **2019**, *125*, 245902. [[CrossRef](#)]
161. Epanchintsev, O.G.; Zubchenko, A.S.; Korneyev, A.E.; Simonov, V.A. Highly-efficient shock-wave diamond synthesis from fullerenes. *J. Phys. Chem. Solids* **1997**, *58*, 1785–1788. [[CrossRef](#)]
162. Donnet, J.B.; Fousson, E.; Wang, T.K.; Samirant, M.; Baras, C.; Pontier Johnson, M. Dynamic synthesis of diamonds. *Diam. Relat. Mater.* **2000**, *9*, 887–892. [[CrossRef](#)]
163. Kenkmann, T.; Hornemann, U.; Stöffler, D. Experimental shock synthesis of diamonds in a graphite gneiss. *Meteorit. Planet. Sci.* **2005**, *40*, 1299–1310. [[CrossRef](#)]
164. Titov, V.M.; Anisichkin, V.F.; Mal'kov, I.Y. Synthesis of ultradispersed diamond in detonation waves. *Fizika Goreniya I Vzeryva* **1989**, *25*, 117–126. [[CrossRef](#)]
165. Pichot, V.; Comet, M.; Fousson, E.; Baras, C.; Senger, A.; Le Normand, F.; Spitzer, D. An efficient purification method for detonation nanodiamonds. *Diam. Relat. Mater.* **2008**, *17*, 13–22. [[CrossRef](#)]
166. Pichot, V.; Risse, B.; Schnell, F.; Mory, J.; Spitzer, D. Understanding ultrafine nanodiamond formation using nanostructured explosives. *Sci. Rep.* **2013**, *3*, 2159. [[CrossRef](#)] [[PubMed](#)]
167. Pichot, V.; Muller, O.; Seve, A.; Yvon, A.; Merlat, L.; Spitzer, D. Optical properties of functionalized nanodiamonds. *Sci. Rep.* **2017**, *7*, 14086. [[CrossRef](#)]
168. Batsanov, S.S.; Osavchuk, A.N.; Naumov, S.P.; Efimov, A.E.; Mendis, B.G.; Apperley, D.C.; Batsanov, A.S. Synthesis and properties of hydrogen-free detonation diamond. *Propellants Explos. Pyrotech.* **2015**, *40*, 39–45. [[CrossRef](#)]
169. Akira, B.S.; Takamatsu, M.; Akashi, T. Shock compression synthesis of diamonds. *Adv. Mater.* **1994**, *6*, 346–354. [[CrossRef](#)]
170. Zousman, B.; Levinson, O. Pure nanodiamonds produced by laser-assisted technique. In *Nanodiamond*; Williams, O., Ed.; RSC Nanoscience & Nanotechnology: London, UK, 2014; Chapter 5.
171. Khachatryan, A.; Aloyan, S.G.; May, P.W.; Sargsyan, R.; Khachatryan, V.A.; Baghdasaryan, V.S. Graphite-to-diamond transformation induced by ultrasound cavitation. *Diam. Relat. Mater.* **2008**, *17*, 931–936. [[CrossRef](#)]
172. Narayan, J.; Bhaumik, A.; Sachan, R.; Haque, A.; Gupta, S.; Pant, P. Direct conversion of carbon nanofibers and nanotubes into diamonds nanofibers and the subsequent growth of large-size diamonds. *Nanoscale* **2019**, *11*, 2238–2248. [[CrossRef](#)]
173. Gao, Y.; Ma, Y.; An, Q.; Levitas, V.; Zhang, Y.; Feng, B.; Chaudhuri, J.; Goddard III, W.A. Shear driven formation of nano-diamonds at sub-gigapascals and 300 K. *Carbon* **2019**, *146*, 364–368. [[CrossRef](#)]
174. Fromentin, S. Resistivity of Carbon, Diamond. In *The Physics Factbook*; Elert, G., Ed.; 2004. Available online: <https://hypertextbook.com> (accessed on 1 December 2021).
175. Bormashov, V.S.; Tarelkin, S.A.; Buga, S.G.; Kuznetsov, M.S.; Terentiev, S.A.; Semenov, A.N.; Blank, V.D. Electrical properties of the high quality boron-doped single crystal diamonds grown by the temperature gradient method. *Diam. Relat. Mater.* **2013**, *35*, 19–23. [[CrossRef](#)]
176. Ekimov, E.A.; Sidorov, V.A.; Bauer, E.D.; Mel'nik, N.N.; Curro, N.J.; Thompson, J.D.; Stishov, S.M. Superconductivity in diamond. *Nature* **2004**, *428*, 542–545. [[CrossRef](#)] [[PubMed](#)]
177. Burgemeister, E.A. Thermal conductivity of natural diamond between 320 and 450 K. *Phys. B+C* **1978**, *93*, 165–179. [[CrossRef](#)]
178. Olson, J.R.; Pohl, R.O.; Vandersande, J.W.; Zoltan, A.; Anthony, T.R.; Banholzer, W.F. Thermal conductivity of diamond between 170 and 1200 K and the isotope effect. *Phys. Rev. B* **1993**, *47*, 14850. [[CrossRef](#)] [[PubMed](#)]

179. Wei, L.; Kuo, P.K.; Thomas, R.L.; Anthony, T.R.; Banholzer, W.F. Thermal conductivity of isotopically modified single crystal diamond. *Phys. Rev. Lett.* **1993**, *70*, 3764. [[CrossRef](#)] [[PubMed](#)]
180. Zaitseez, A.M. Optical properties of diamond. In *A Data Handbook*; Springer: Berlin/Heidelberg, Germany, 2001.
181. Gicquel, A.; Hassouni, K.; Silva, F.; Achard, J. CVD diamond film: From growth to applications. *Curr. Appl. Phys.* **2001**, *1*, 479–496. [[CrossRef](#)]
182. Smith, R.L.; Sandland, G.E. An accurate method of determining the hardness of metals, with particular reference to those of a high degree of hardness. *Proc. Inst. Mech. Eng.* **1922**, *102*, 623–641. [[CrossRef](#)]
183. Knoop, F.; Peters, C.G.; Emerson, W.B. A sensitive pyramidal-diamond tool for indentation measurements. *J. Res. Natl. Bur. Stand.* **1939**, *23*, 39–61. [[CrossRef](#)]
184. Fischer-Cripps, A.C. *Nanoindentation*, 3rd ed.; Springer: Berlin/Heidelberg, Germany, 2004.
185. Migliori, A.; Sarrao, J.L.; Vissler, W.M.; Bell, T.M.; Lei, M.; Fisk, Z.; Leisure, R.G. Resonant ultrasound spectroscopic techniques for measurement of the elastic moduli of solids. *Phys. B* **1993**, *183*, 1–24. [[CrossRef](#)]
186. Ben Ghorbal, G.; Tricoteaux, A.; Thuault, A.; Louis, G.; Chicot, D. Comparison of conventional Knoop and Vickers hardness of ceramic materials. *J. Eur. Ceram. Soc.* **2017**, *37*, 2531–2535. [[CrossRef](#)]
187. Migliori, A.; Ledbetter, H.; Leisure, R.G.; Pantea, C.; Betts, J.B. Diamond's elastic stiffness from 332 K to 10 K. *J. Appl. Phys.* **2008**, *104*, 053512. [[CrossRef](#)]
188. Wang, S.-F.; Hsu, Y.-F.; Pu, J.-C.; Sung, J.C.; Hwa, L.G. Determination of acoustic wave velocities and elastic properties for diamond and other hard materials. *Mater. Chem. Phys.* **2004**, *85*, 432–437. [[CrossRef](#)]
189. Tanigaki, K.; Ogi, H.; Sumiya, H.; Kusakabe, K.; Nakamura, N.; Hirao, M.; Ledbetter, H. Observation of higher stiffness in nanopolycrystalline diamond than monocrystal diamond. *Nat. Commun.* **2013**, *4*, 2343. [[CrossRef](#)] [[PubMed](#)]
190. Gasc, J.; Wang, Y.; Yu, T.; Benea, I.C.; Rosczyk, B.R.; Shinmei, T.; Irifune, T. High-pressure, high-temperature plastic deformation of sintered diamonds. *Diam. Relat. Mater.* **2015**, *59*, 95–103. [[CrossRef](#)]
191. Wang, Y.; Shi, F.; Ohfuji, H.; Gasc, J.; Nishiyama, N.; Yu, T.; Officer, T.; Shinmei, T.; Irifune, T. Strength and plastic deformation of polycrystalline diamond composite. *High Press. Res.* **2019**, *40*, 35–53. [[CrossRef](#)]
192. Wang, Y.; Shi, F.; Gasc, J.; Ohfuji, H.; Wen, B.; Yu, T.; Officer, T.; Nishiyama, N.; Shinmei, T.; Irifune, T. Plastic deformation and strengthening mechanisms of nanopolycrystalline diamonds. *ACS Nano* **2021**, *15*, 8283–8294. [[CrossRef](#)]
193. Ischii, R.; Fukuta, R.; Ischikawa, F.; Matsushita, M.; Ohfuji, H.; Shinmei, T.; Irifune, T.; Funato, M.; Kawakami, Y. Deep-ultraviolet near band-edge emissions from nano-polycrystalline diamond. *High Press. Res.* **2019**, *40*, 140–147. [[CrossRef](#)]
194. Dzielgielewski, P.; Mathon, O.; Kantor, I.; Pascarelli, S.; Shinmei, T.; Irifune, T.; Antowicz, J. High pressure atomic structure of Zr-Cu metallic glass via EXAFS spectroscopy and molecular dynamics simulations. *High Press. Res.* **2019**, *40*, 54–64. [[CrossRef](#)]
195. Rosa, A.D.; Mathon, O.; Torchio, R.; Jacobs, J.; Pasternak, S.; Irifune, T.; Pascarelli, S. Nano-polycrystalline diamond anvils: Key devices for XAS at extreme conditions: Their use, scientific impact, present status and future needs. *High Press. Res.* **2019**, *40*, 65–81. [[CrossRef](#)]
196. Elbers, M.; Sternemann, C.; Julius, K.; Paulus, M.; Surmeier, G.; König, N.; Nase, J.; Bolle, J.; Wagner, R.; Irifune, T.; et al. Pressure stability of the first hydration shell of yttrium in aqueous YCl₃ solution. *High Press. Res.* **2020**, *40*, 194–204. [[CrossRef](#)]
197. Kousa, M.; Iwasaki, S.; Ishimatsu, N.; Kawamura, N.; Nomura, R.; Kakizawa, S.; Mizumaki, M.; Sumiya, H.; Irifune, T. Element-selective elastic properties of Fe₆₅Ni₃₅ Invar alloy and Fe₇₂Pt₂₈ alloy studied by extended X-ray absorption fine structure. *High Press. Res.* **2019**, *40*, 130–139. [[CrossRef](#)]
198. Nataf, L.; Baudalet, F.; Polian, A.; Jonane, I.; Anspoks, A.; Kuzmin, A.; Irifune, T. Recent progress in high pressure X-ray absorption spectroscopy at the ODE beamline. *High Press. Res.* **2020**, *40*, 82–87. [[CrossRef](#)]
199. Komatsu, K.; Klotz, S.; Nakano, S.; Machida, S.; Hattori, T.; Sano-Furukawa, A.; Yamashita, K.; Irifune, T. Developments of nano-polycrystalline diamond anvil cells for neutron diffraction experiments. *High Press. Res.* **2020**, *40*, 184–193. [[CrossRef](#)]
200. Yamashita, K.; Komatsu, K.; Klotz, S.; Fernandez-Diaz, M.T.; Irifune, T.; Sugiyama, K.; Kawamata, T.; Kagi, H. A nano-polycrystalline diamond anvil cell with bulk metallic glass cylinder for single-crystal neutron diffraction. *High Press. Res.* **2019**, *40*, 88–95. [[CrossRef](#)]
201. Kuramochi, K.; Ishimatsu, N.; Sakai, T.; Kawamura, N.; Irifune, T. An application of NPD to double-stage diamond anvil cells: XAS spectra of rhenium metal under high pressures above 300 GPa. *High Press. Res.* **2019**, *40*, 119–129. [[CrossRef](#)]
202. Sakai, T.; Yagi, T.; Takeda, R.; Hamatani, T.; Nakamoto, Y.; Kadobayashi, H.; Mimori, H.; Kawaguchi, S.I.; Hirao, N.; Ohishi, Y.; et al. Conical support for double stage diamond anvil apparatus. *High Press. Appar.* **2019**, *40*, 12–21. [[CrossRef](#)]
203. Yagi, T.; Sakai, T.; Kadobayashi, H.; Irifune, T. Review: High pressure generation techniques beyond the limit of conventional diamond anvils. *High Press. Res.* **2019**, *40*, 148–161. [[CrossRef](#)]
204. Kono, Y.; Kenney-Benson, C.; Shen, G. Opposed type double stage cell for Mbar pressure experiment with large sample volume. *High Press. Res.* **2020**, *40*, 175–183. [[CrossRef](#)]

-
205. Barreda-Argüeso, J.A.; Gonzalez, J.; Valiente, R.; Irifune, T.; Rodriguez, F. Exploiting optical properties of nanopolycrystalline diamond in high pressure experiments. *High Press. Res.* **2019**, *40*, 107–118. [[CrossRef](#)]
 206. Guan, S.; Peng, F.; Liang, H.; Fan, C.; Tan, L.; Wang, Z.; Zhang, Y.; Zhang, Y.H.; He, D. Fragmentation and stress diversification in diamond powder under high pressure. *J. Appl. Phys.* **2018**, *124*, 215902. [[CrossRef](#)]